

Quantum Frequency Down-Conversion of Single Photons in Nonlinear Optical Waveguides

Dissertation

zur Erlangung des Grades
des Doktors der Naturwissenschaften
der Naturwissenschaftlich-Technischen Fakultät II
– Physik und Mechatronik –
der Universität des Saarlandes

von

Sebastian Zaske

Saarbrücken

2013

Tag des Kolloquiums: 24.04.2013

Dekan: Univ.-Prof. Dr. rer. nat. Christian Wagner

Mitglieder des Prüfungsausschusses: Univ.-Prof. Dr. rer. nat. Jürgen Eschner
Univ.-Prof. Dr. rer. nat. Christoph Becher
Priv.-Doz. Dr. habil. Johannes A. L’huillier
Dr. rer. nat. Marc Bienert

Optical communication and information processes will further influence the lives of people in the decades to come. Dialogue and information transfer, from person to person, from people to people, are important, nay essential, for mankind.

—Nicolaas Bloembergen (“Nobel Banquet Speech”, December 10, 1981) [1]

Abstract

In this work, we experimentally study quantum frequency conversion of single photons from the visible spectral range (input) to a wavelength that lies in one of the low-loss telecom wavelength bands around $1.3\ \mu\text{m}$ or $1.55\ \mu\text{m}$ (output). To this end, we use difference frequency generation (DFG) in nonlinear optical waveguides made of periodically poled LiNbO_3 . The DFG process is driven by a strong coherent light field that is delivered by a home-built 532-nm-pumped continuous-wave optical parametric oscillator based on bulk periodically poled LiTaO_3 . We demonstrate two efficient schemes: frequency down-conversion from 738 nm to 1560 nm and from 711 nm to 1310 nm. In the first case, we have employed faint laser pulses to emulate single photons at 738 nm and extensively investigate noise effects. An external (internal) conversion efficiency of 8 % (73 %) was achieved and spontaneous Raman scattering was identified as a main noise source. In the second case, we used true single photons from an InP quantum dot. Here the external (internal) efficiency was 32 % ($\geq 64\%$). We demonstrate the preservation of the photon lifetime and of nonclassical intensity correlations under frequency down-conversion. Compared with the first process, a much better signal-to-noise ratio was observed in the second process. The results hold great promise with regard to the implementation of on-demand telecom single-photon sources and future quantum networks.

Zusammenfassung

In dieser Arbeit wird die Quantenfrequenzkonversion einzelner Photonen aus dem sichtbaren Spektralbereich (Eingang) zu einer Wellenlänge in einem der verlustarmen Telekommbänder um $1.3\ \mu\text{m}$ oder $1.55\ \mu\text{m}$ (Ausgang) experimentell untersucht. Dazu wird Differenzfrequenzmischung (DFG) in optisch nichtlinearen Wellenleitern aus periodisch gepoltem LiNbO_3 benutzt. Der DFG-Prozess wird von einem intensiven, kohärenten Lichtfeld getrieben, welches von einem 532-nm-gepumpten optisch parametrischen Oszillator basierend auf periodisch gepoltem LiTaO_3 geliefert wird. Zwei effiziente Prozesse werden demonstriert: Frequenz-Abwärtskonversion von 738 nm nach 1560 nm und von 711 nm nach 1310 nm. Im ersten Fall wurden abgeschwächte Laserpulse benutzt, um einzelne Photonen bei 738 nm zu simulieren und Rauscheffekte zu untersuchen. Eine externe (interne) Konversionseffizienz von 8 % (73 %) wurde erreicht und spontane Ramanstreuung als Haupt-Rauschquelle identifiziert. Im zweiten Fall wurden echte Einzelphotonen von einem InP-Quantenpunkt benutzt. Hierbei lag die externe (interne) Konversionseffizienz bei 32 % ($\geq 64\%$). Die Erhaltung von Photonenlebensdauer und nichtklassischen Intensitätskorrelationen wurden demonstriert. Im Vergleich zum ersten Prozess konnte beim zweiten Prozess ein viel besseres Signal-zu-Rausch-Verhältnis beobachtet werden. Die Ergebnisse sind vielversprechend im Hinblick auf die Realisierung von Telekom-Einzelphotonenquellen und zukünftigen Quanten-Netzwerken.

Contents

1	Introduction	1
1.1	Qubits, Photons, and Quantum Communication	1
1.2	Quantum Frequency Conversion	6
1.3	Aim and Outline of this Thesis	10
2	Theoretical Background	13
2.1	Fundamentals of Nonlinear Optics	13
2.1.1	Nonlinear Polarization	13
2.1.2	Coupled Mode Equations	15
2.1.3	Phasematching	16
2.1.4	Quasi-Phasematching	18
2.2	Quantum Physical Description of Light Fields	22
2.2.1	Photon Number States	22
2.2.2	Different Types of Light	23
3	Nonlinear Optical Materials and Devices	29
3.1	Lithium Niobate and Lithium Tantalate as Nonlinear Optical Materials	29
3.1.1	Crystal Structure	29
3.1.2	Ferroelectricity and Electric Field Poling	30
3.1.3	Stoichiometry and Doping	31
3.1.4	Linear and Nonlinear Optical Properties	31
3.2	Nonlinear Optical Devices	33
3.2.1	Parametric Amplification	33
3.2.2	Optical Parametric Oscillators	34
3.2.3	Waveguide-Based Quasi-Phasematched Frequency Converters . .	41
4	Green-Pumped Continuous-Wave Optical Parametric Oscillators	55
4.1	Green-Pumped CW SRO Based on MgO:PPLN	57
4.1.1	Experimental Setup	57
4.1.2	Basic Properties of the MgO:PPLN-Based SRO	58
4.1.3	Tuning Range and Linewidths	60
4.1.4	Spectroscopy of Cesium and Frequency Stabilization	61
4.2	Green-Pumped CW SRO Based on MgO:PPLT	65

4.2.1	Basic Properties of the MgO:PPLT-Based SRO	65
4.2.2	Signal Extraction through Output Coupling	68
4.2.3	Frequency Stabilization Using a Wavemeter	70
4.3	Summary	74
5	Frequency Down-Conversion of Attenuated Laser Pulses	77
5.1	Experimental Design	78
5.1.1	Optical Setup	78
5.1.2	Zn:PPLN Waveguide Chip	80
5.2	Down-Conversion from 738 nm to the C-Band: Experimental Results	82
5.2.1	Performance of the Frequency Converter	82
5.2.2	Investigation of Raman Noise	89
5.2.3	Spectral Filtering	95
5.2.4	Conversion Efficiency with Single-Photon-Level Input	95
5.3	Successive DFG and SFG in a Double-Pass Configuration	100
5.4	Summary and Discussion	104
6	Quantum Frequency Down-Conversion of Single Photons from a Quantum Dot	107
6.1	InP Quantum Dots as Single-Photon Emitters	108
6.1.1	Semiconductor Quantum Dots: Fundamentals	108
6.1.2	Fabrication and Layout of the InP/GaInP Quantum Dot Sample	110
6.2	Experimental Setup and Preparatory Experiments	111
6.2.1	Experimental Setup	111
6.2.2	Performance of the Waveguide Chip	114
6.2.3	Preselection and Wavelength Tuning of Quantum Dots	117
6.3	QFC from 711 nm to 1313 nm: Experimental Results	121
6.3.1	Spectral Filtering	121
6.3.2	Conversion Efficiency with Single-Photon Input	124
6.3.3	Time-Correlated Single-Photon Counting	127
6.3.4	Conservation of Photon Antibunching	130
6.4	Summary and Discussion	133
7	Summary and Future Prospects	137
A	Refractive Indices of Nonlinear Materials	143
B	Supplemental Equations and Formulas	147
	Bibliography	151
	Publications	169

Chapter 1

Introduction

In 1984, inspired by an idea originally developed in the 1970's [2], Bennett and Brassard published their famous proposal for quantum key distribution (QKD) [3], now known as the BB84 protocol. In principle, it provides a method for secure communication guaranteed by the fundamental laws of quantum physics. A couple of years later, Bennett, Brassard, and co-workers managed to experimentally demonstrate QKD over a 32-cm distance in air [4]. This experiment may be considered one of the first technical applications that exploits the potential of quantum physics for data communication. Individual photons were used as information carriers.

It is fair to say that, since the first experimental demonstration of QKD, a scientific revolution has taken place. Today, quantum optics is no longer only a testbed for fundamental physics but is also more and more becoming a technological discipline. Many researchers around the world strive to exploit the nature of quantum correlations as a resource to build practical devices such as QKD systems or quantum computers—machines that have the potential to solve certain computational problems (e.g., integer factorization of large numbers) much more efficient than any classical computer [5, 6]. It is a vision that some day QKD will be possible between two far apart cities or that quantum computers on different continents get connected ('the quantum internet' [7]). However, the exchange of quantum information (QI) over large distances remains an unsolved problem so far and currently is subject to intensive research. In the following, we briefly outline the challenges associated with long-distance quantum communication (QC) and the approaches to overcome them. We start by briefly recalling some basic concepts in QC and QI.

1.1 Qubits, Photons, and Quantum Communication

Stationary vs. Flying Qubits

The quantum bit (qubit) [8] is a fundamental concept in QC and QI. In classical digital data processing, a bit is either in state '0' or '1'. These states can be represented, for example, by two different voltage levels. In contrast to that, a qubit is generally in a

coherent superposition of two quantum states, say $|0\rangle$ and $|1\rangle$, represented by

$$|\psi\rangle = \alpha |0\rangle + \beta |1\rangle. \quad (1.1)$$

As usual, α and β are two complex numbers with the property $|\alpha|^2 + |\beta|^2 = 1$. Compared with classical bits which can be stored on a hard drive for many years, qubits are very fragile due to decoherence effects. An illustrative representation of the state $|\psi\rangle$ is often given by a vector pointing to a point on the surface of a unit sphere, the Bloch sphere. To this end, the eigenstates of the two-level system $|1\rangle$ and $|0\rangle$ are chosen to lie on the north and southpole of this sphere (or vice versa), respectively, and the coefficients α and β are identified with $\alpha = \cos(\theta/2)$ and $\beta = e^{i\phi} \sin(\theta/2)$. The parameters θ and ϕ are the polar and the azimuthal angle in a spherical coordinate system. Another essential resource in QI science are entangled states, that is, quantum correlated states of two or more qubits. In the case of two qubits labeled A and B , Bell states of the form

$$|\Psi^\pm\rangle = \frac{1}{\sqrt{2}} (|0\rangle_A |1\rangle_B \pm |1\rangle_A |0\rangle_B) \quad (1.2)$$

$$\text{or } |\Phi^\pm\rangle = \frac{1}{\sqrt{2}} (|0\rangle_A |0\rangle_B \pm |1\rangle_A |1\rangle_B) \quad (1.3)$$

are examples of such entangled states. These states cannot be written as a product of two single qubit states—this is in fact the definition of entanglement. Suppose the combined system of A and B is in the $|\Psi^+\rangle$ state. A measurement on one qubit, say A , which yields the result that A is in state $|0\rangle_A$ ($|1\rangle_A$) is equivalent to a projection onto the state $|0\rangle_A |1\rangle_B$ ($|1\rangle_A |0\rangle_B$). Thus, with a probability of one, system B will be instantaneously in state $|1\rangle_B$ ($|0\rangle_B$) in the same moment as we perform a measurement on A . This strange behavior has no counterpart in classical physics and is a powerful resource for applications. Entanglement between two particles is usually tested by a violation of Bell's inequality [9] (mostly in the CHSH formulation of Clauser, Horne, Shimony, and Holt [10]). Quantum state tomography [11] can also be applied to prove entanglement. This method is experimentally more involved but has the advantage of yielding the reconstruction of the complete density matrix. It thus reveals the maximally possible information about the two-particle system. If the density matrix of the system is known, a number of entanglement measures [12] can be calculated to analyze the quality of the entangled state. We emphasize that the particles A and B need not to be identical to get entangled in some way.

In principle, qubits can be represented by any quantum two-level system. A great variety of systems are being considered to locally manipulate and store QI ('stationary qubits'). For example, electronic states of trapped atoms, nuclear spins in molecules in liquid solutions, single spins in semiconductor quantum dots (QDs), single spins of defect centers in diamond, superconducting qubits, and others have been investigated [6]. A general difficulty with all these systems is scalability. For example, the number of ion qubits that can be faithfully controlled in an ion trap is very limited; 14 ions seems to

be the current record [13]. However, for realistic computational tasks much more qubits are needed (e.g., factorization of a large number with $N = 1024$ bits requires a number of physical qubits which is on the order of 10^3 – 10^4 [14]). In a visionary paper from 1997, Cirac *et al.* [15] therefore proposed a quantum network formed by quantum nodes (i.e., units containing one or a few stationary qubits) that are connected via quantum channels (optical fibers). In the original paper, the quantum nodes are thought of as atoms in optical cavities but they could also be implemented by solid-state qubits, such as single spins in semiconductor QDs or similar. Sending photons, the ‘flying qubits’, through these channels allows for the exchange of QI between distant nodes. In analogy to stationary matter qubits, several degrees of freedom can be used to encode a qubit on a photon, for example, the polarization or the phase of the photons. In polarization coding, two orthogonal polarization states, say vertical polarization $|V\rangle$ and horizontal polarization $|H\rangle$, are chosen to represent the states $|0\rangle$ and $|1\rangle$ in Eq. (1.1) and (1.2), (1.3). In this case, the Bloch sphere is mapped to the Poincaré sphere [16] commonly used to describe arbitrary polarization states of light (see [11] for a detailed discussion). Polarization coding was actually used by Bennett *et al.* in the first QKD experiment described in the beginning. Polarization-entangled photon pairs can also be used in QKD as in the scheme proposed by Ekert [17].

Generation of Nonclassical Light States

In a quantum network, QI is transferred from a stationary qubit to a flying qubit in a coherent process. The generation of photons and the encoding of QI onto these photons happens simultaneously in a single step. In other applications, like in QKD or in some quantum repeater protocols (see next section), single photons are generated in a first step and QI is encoded onto them in a second step. Information encoding can be performed, for example, by manipulating the polarization of the photons with polarizers or by creating an entangled state between a previously generated photon and a matter qubit. The generation of single photons is not as easy as it seems since LEDs or lasers are not suitable to produce the kind of photons that are required for many QC and QI tasks. Instead, nonclassical light states are often needed, that is, single-photon states or entangled photon states (we will leave squeezed states [18] aside). For experimentalists, a single-photon state means a light field composed of pulses arriving equally spaced in time and containing exactly one photon each. Such states can be generated by pulsed excitation of an optical transition between two energy levels in a single quantum system, such as a QD [19] or a single atom [20]. Single-photon sources of this type are called triggered or on-demand single-photon sources [21]. In the ideal case, each excitation pulse will be followed by the emission of a photon from the quantum system. The quality of a triggered single-photon source is usually characterized by measuring a function known as the degree of second-order coherence $g^{(2)}(\tau)$ [18], where $0 \leq g^{(2)}(0) < 1/2$ for single quantum emitters ($g^{(2)}(0) = 0$ for a perfect source). A classical coherent light source has a constant $g^{(2)}(\tau) = 1$ and the dip at $g^{(2)}(0)$ observed for nonclassical sources is called photon antibunching [22].

A second type of single-photon sources are so-called heralded single-photon sources [21]. This usually refers to photon pairs generated via spontaneous parametric down-conversion (SPDC) in nonlinear crystals or fibers. In this process, the nonlinear material is pumped with a laser beam and, with a small probability, pump photons spontaneously split up into two photons called signal and idler photons. Energy conservation must be fulfilled such that $\omega_p = \omega_s + \omega_i$, where ω_p , ω_s , ω_i are the angular frequencies of pump, signal, and idler field, respectively. As the photons are always produced in pairs, detection of one of them can be used to herald the other. This technique enjoys great popularity since the experimental effort is moderate and it allows for the creation of entangled photon states of the type given by Eq. (1.2) or (1.3).

It was long believed that single-photon states or entangled photon states are a must for QKD. However, nowadays the conviction is growing that this is actually not the case [21]. Based on the original BB84 protocol, more sophisticated protocols have been developed (e.g., the decoy state protocol [23]) which use attenuated laser pulses but nevertheless guarantee a high level of security. QKD systems relying on such protocols have been developed and are commercially available. The laser pulses have to be attenuated such that each pulse contains less than one photon per pulse on average. Typically, an average number of 0.1 photons per pulse is chosen which means that 9 of 10 pulses contain no photon at all. This, however, can be compensated by the high repetition rate (up to 1 GHz) of the lasers employed in QKD systems. As a consequence, QKD systems based on faint laser pulses currently outperform implementations based on triggered single-photon sources or sources of entangled photon pairs. However, in a recent paper [21] Sangouard and Zbinden come to the conclusion that single photons are by no means useless since they are needed in future technologies such as device-independent QKD [21,24] or quantum repeaters. Device-independent QKD means that the security of a QKD system does not depend on any assumptions about the devices used (which may have been the original intention of the inventors). The concept of quantum repeaters is explained in the next paragraph.

Technical Challenges for Long-Distance Quantum Communication

So far, we have recalled what qubits are, how they can be encoded to photons, and how single photons or entangled pairs of photons are created in practice. We now address the question what actually limits long-distance (distances longer than ~ 100 km) fiber-based QC. In fact, polarization coding may be suitable for free-space transmission of optical qubits but it is unsuitable for long-haul transmission through an optical fiber channel. It is technically quite involved to maintain the polarization state of the photons while they propagate through a long non-polarization-maintaining telecom fiber. However, alternative techniques which are more compatible with optical fibers were invented and have been successfully applied, like phase or frequency coding [25]. The destruction of polarization states in fibers can thus be circumvented. A second more severe technical problem in terms of long-haul fiber transmission of optical qubits is fiber attenuation. To understand the heart of this problem, we recall the working principle

of classical fiber-optic communication. To send information available as a sequence of classical bits, this sequence is converted to an optical pulse pattern—‘pulse’ represents a ‘1’, ‘no pulse’ represents a ‘0’—and sent through a fiber channel. Each pulse contains a large number of photons and the quantum state of an individual photon is completely irrelevant in this classical method. Optical communication fibers are made of SiO_2 with the lowest attenuation coefficient around the so-called telecommunications wavelengths at 1310 nm (zero dispersion and local attenuation minimum) and at 1550 nm (absolute attenuation minimum).¹ But even if a wavelength around 1550 nm is chosen as the carrier wavelength, 99% of the inserted power is lost after 100 km due to fiber attenuation (typically 0.2 dB/km). This attenuation in conjunction with dispersion effects is responsible for the degradation of the pulse pattern during transmission. As a consequence, the distance after which the message can be reliably reconstructed is limited. For this reason, repeaters are incorporated into optical transmission lines every 50–100 km to recover, amplify, and re-transmit the incoming optical signals. Every optical signal that is sent through a submarine fiber cable, say from Europe to the U.S., is thus amplified many times. Unfortunately, this method cannot be applied to optical qubits because it is impossible, that means, forbidden by the laws of quantum physics, to faithfully produce a copy of any quantum system (such as the quantum state of a photon). This was proven by Wootters and Zurek and is known as the ‘quantum no-cloning theorem’ [26]. In view of this situation, Briegel *et al.* devised the idea of a ‘quantum repeater’ in 1998 [27]. Three years later, Duan, Lukin, Cirac, and Zoller came up with a proposal for an experimental implementation of such quantum repeaters, called the DLCZ protocol [28]. In these proposals, a large distance L between two remote quantum memories (devices capable of storing QI) at locations A and B is bridged by concatenating N elementary fiber links of length L/N . A quantum state carried by a photon can be ‘written’ to a quantum memory by the absorption of a photon, stored for a certain time (e.g., as a collective excitation in an ensemble of atoms [28]), and retrieved from it in a controllable way by the emission of a photon. Two or more quantum memories can be entangled in the sense that their quantum state is described by a non-separable state as in Eq. (1.2) or (1.3). Reference [29] gives an overview on physical systems that are currently investigated as candidates for quantum memories. In the DLCZ protocol, the remote systems at A and B eventually become entangled by successive so-called entanglement swapping operations between neighboring quantum memories. These entanglement swapping operations rely on the exchange and detection of single photons. Once A and B are entangled in some way, quantum information can be transferred by quantum teleportation [30]. It turns out that quantum repeater protocols, in principle, could offer a more efficient transfer of QI than direct transmission of photons. The trick is that photons only have to travel a maximum distance of L/N (the length of one elementary link) instead of the whole distance L . Meanwhile, a number of variations and improvements of the DLCZ protocol have been proposed. Some of them suggest

¹These wavelength bands are termed O-band (1260–1360 nm) and C-band (1530–1565 nm) and are perhaps best known. Further wavelength bands in fiber-optic communication are: E-band (1360–1460 nm), S-band (1460–1530 nm), L-band (1565–1625 nm), and U-band (1625–1675 nm).

to use photon pair sources or on-demand single-photon sources in combination with quantum memories. A detailed explanation of possible implementations of quantum repeater schemes and how they work is far beyond the scope of this introduction. An instructive and detailed review can be found in [31].

The quantum repeater concept is an ingenious idea which perfectly works on paper so far. Some first experimental steps have also been taken. However, to make this idea really work in practice a number of technical issues must be tackled. One difficulty, among several others, is that the individual components to establish a quantum repeated connection simply work at different wavelengths. On the one hand, the most efficient single-photon detectors and also many implementations of quantum memories operate at wavelengths shorter than $1.0\ \mu\text{m}$. On the other hand, the length of an elementary fiber link is estimated to be on the order of 100 km in realistic scenarios [31]. Therefore, photons at telecommunications wavelengths should be used to minimize losses due to fiber attenuation. Photon pair sources, as employed in some quantum repeater protocols [32], are capable of producing telecom photons. Yet, there is also a proposal for an implementation with on-demand single-photon sources [33] which would be very promising if these sources had better performance at telecom wavelengths.

1.2 Quantum Frequency Conversion

The aforementioned mismatch of wavelengths was the starting point for this thesis. We experimentally investigate a technique called quantum frequency conversion (QFC) which has the potential to become a remedy to the described wavelength compatibility problems. Simply put, QFC describes methods by which the wavelength of photons is changed without destroying their quantum state. More precisely, in a QFC device, the quantum state of an input photon at wavelength λ_a is transferred to an output photon at λ_b , whereby the photon at λ_a is annihilated and the photon at λ_b is created (in compliance with the no-cloning theorem). To this end, intrinsic optical nonlinearities in solid-state crystals, highly nonlinear optical fibers or atomic ensembles are utilized. The conversion process has to be pumped by one (three-wave mixing) or two (four-wave mixing) strong pump lasers. We refer to frequency down-conversion if the input wavelength is shorter than the output wavelength ($\lambda_a < \lambda_b$) and to frequency up-conversion if the opposite is true. It should be emphasized that quantum frequency down-conversion and SPDC are two different things.

Before we come to the concrete aim and outline of this work, we give an overview on important literature that has been published on QFC so far. This overview, while not exhaustive, should allow for a classification of the present thesis within the scientific work performed by others in the field.

Quantum Frequency Conversion—State of the Art

QFC was first proposed by Prem Kumar in 1990 [34] and experimentally demonstrated two years later by Huang and Kumar at Northwestern University [35]. In Ref. [35] twin

beams at $\lambda_a = 1064$ nm with nonclassical intensity correlations (squeezed state) were generated in a KTiOPO_4 (KTP) crystal and one of them was mixed with pulsed laser light at $\lambda_p = 1064$ nm in a second KTP crystal to generate light at $\lambda_b = 532$ nm via sum frequency generation (SFG, $\omega_b = \omega_a + \omega_p$). The authors could show nonclassical intensity correlations between the non-converted 1064-nm beam and the up-converted 532-nm beam, that is, the initial correlations between the twin beams at 1064 nm had been preserved.

In a paper from 2003, Giorgi *et al.* (De Martini group, Sapienza University of Rome) demonstrated a dual-color Mach–Zehnder interferometer (MZI) at the single-photon level [36]. This MZI uses three beamsplitters instead of two. Photons at $\lambda_a = 876.1$ nm from an attenuated continuous-wave (cw) diode laser were sent into the interferometer and split into two beams by the first beamsplitter. Then, part of the photons in both beams were frequency up-converted to $\lambda_b = 416.8$ nm by SFG in a bulk LiIO_3 crystal producing a total of four beams. A 795-nm femtosecond Ti:sapphire laser was used to pump the process. The two beams containing the non-converted IR photons were overlapped on a second beamsplitter and the beams containing the up-converted UV photons were overlapped on a third beamsplitter. By changing the optical pathlength in one arm of the MZI, the authors observed interference fringes at both wavelengths, thereby showing that first-order coherence was preserved under frequency up-conversion. Remarkably, the authors already anticipated the great potential of QFC for ‘a QI network made of heterogeneous components’ [36].

Soon thereafter, other groups (Kwiat group at University of Illinois, Wong group at MIT, Fejer group at Stanford University) investigated frequency up-conversion as a means to overcome the problem of noisy and inefficient single-photon detectors at telecom wavelengths [37–39]. The idea of up-conversion detectors had long been around in another context [40]. However, only with the advent of periodically poled lithium niobate (PPLN) as a nonlinear material, frequency conversion could be made efficient enough such that investigation of single-photon up-conversion detectors seemed worthwhile. In all three experiments, a weak input signal (μW level) at a telecom wavelength ($\lambda_a = 1550$ nm [37, 38], $\lambda_a = 1340$ nm [39]) was up-converted to an output wavelength in the red spectral range where efficient low-noise silicon detectors can be employed for detection. Frequency up-conversion was accomplished by SFG in a PPLN crystal. Different pump schemes were adopted by the three groups. Since bulk crystals were used in [37, 38], they had to apply a relatively high pump power which was accomplished by using a pulsed 1064-nm pump laser (13 kW pulse peak power [37]) or by resonant enhancement in a ring cavity (23 W cw power [38]). In Ref. [39] a cw pump power of 88 mW at 1550 nm was sufficient to reach maximum conversion efficiency because a PPLN waveguide (WG) was used. Waveguides provide a remarkable increase in conversion efficiency at relatively low pump powers due to strong spatial confinement of the interacting light fields. The first up-conversion experiments in PPLN showed that frequency conversion can be made very efficient ($\sim 90\%$ internal efficiency) but that the amount of noise generated by the strong pump field had to be reduced to make QFC a useful technique for applications in quantum technology.

In 2005, Tanzilli *et al.* (Gisin group, University of Geneva) [41] reported an experiment in which they demonstrated that energy-time entanglement between two photonic qubits was preserved in frequency up-conversion. In this pioneering work, two PPLN WGs were employed. The first WG was pumped with 712-nm light to create energy-time entangled photon pairs (one signal photon at $\lambda_a = 1312$ nm and one idler photon at 1555 nm) via SPDC. In the next step, the 1312-nm photons were sent to the second PPLN WG in which they were up-converted to $\lambda_b = 712$ nm. Using Franson-type interferometers [42], the authors could prove entanglement between the up-converted 712-nm and the 1555-nm photons. Thus, the initial entanglement between the 1312-nm and 1555-nm photons was not corrupted by the up-conversion process.

In a theoretical paper in 2008, Ou pointed out that complementary to frequency up-conversion, ‘efficient frequency down-conversion is essential in a quantum network for converting photons emitted by atoms ($\sim 0.8 \mu\text{m}$) to photons transmitted in optical fibers ($\sim 1.56 \mu\text{m}$)’ [43]. Thus far, only up-conversion had been investigated. This was probably due to the fact that nonlinear frequency down-conversion was considered to be too noisy to be useful for QFC. Yet, in a seminal experiment by Radnaev *et al.* (Kuzmich group, Georgia Tech) from 2010, both quantum frequency down- and up-conversion were investigated [44]. The experiment described in [44] is special in several ways. The authors have combined an atomic spin-wave quantum memory with telecom-wavelength conversion. For the implementation of QFC, they do not use a nonlinear crystal but employ four-wave mixing (FWM) in a cold ^{87}Rb ensemble that was prepared in a magneto-optical trap. Using the natural diamond-type level scheme of Rb, photons at $\lambda_a = 795$ nm (retrieved from the quantum memory) are converted to photons at $\lambda_b = 1367$ nm ($\lambda_b = 1530$ nm was also tested) in this process. Two pump lasers are required to drive the FWM process, one at $\lambda_{p1} = 780$ nm and one at $\lambda_{p2} = 1324$ nm ($\omega_a + \omega_{p2} = \omega_b + \omega_{p1}$). Internal conversion efficiencies (down- and subsequent up-conversion: $795 \text{ nm} \rightarrow 1367 \text{ nm}/1530 \text{ nm} \rightarrow 795 \text{ nm}$) of 54% (30%) are demonstrated for wavelength translation from 795 nm to 1367 nm (1530 nm) and back. Furthermore, quantum correlations between the memory and the telecom light field were measured (explicit violation of the CHSH Bell inequality was reported in a follow-up paper [45]). Detection at telecom wavelengths is avoided by using the two-step sequence of down- and up-conversion. The work of Radnaev *et al.* is pathbreaking as it introduces a method to efficiently interface a Rb-based quantum memory with telecom light. Although their technique seems attractive, there are also some downsides compared to a solid-state implementation (QFC in nonlinear crystals or fibers). For example, the experimental setup is rather complex and the accessible telecom wavelength is constrained by the inherent energy level configuration of Rb.

In 2010/2011, a number of down-conversion experiments in PPLN WGs have also been reported [46–49] from authors at NTT Corp., Stanford University, University of Geneva, and our group. These experiments were similar to the early up-conversion experiments in PPLN but with reversed input and output wavelengths, that is, difference frequency generation is used according to $\omega_a - \omega_p = \omega_b$ (ω_a lies in the visible spectral range, ω_b is a telecom frequency). In all experiments, attenuated laser pulses were used to emulate sin-

gle photons. The preservation of first-order coherence under frequency down-conversion was demonstrated in [46, 48] while noise issues were mainly studied in [47, 49]. In analogy to up-conversion, it turned out that down-conversion in a PPLN WG can be very efficient but, as expected, a large amount of noise photons was generated by SPDC [47] or Raman scattering [49] induced by the strong pump field.

Concerning quantum frequency up-conversion, further remarkable progress was reported in 2010 [50, 51]. In Ref. [50] a collaboration of researchers from the University of Oregon, Bell Labs, and UCSD exploit four-wave mixing in a highly nonlinear photonic crystal fiber (PCF) to implement single-photon up-conversion. Initially, photon pairs were generated in a first PCF, each pair consisting of one photon at $\lambda_a = 683$ nm and one at 989 nm. The 683-nm photons were then up-converted to $\lambda_b = 659$ nm via FWM in a second PCF. The wavelengths of the two pump lasers were at $\lambda_{p1} = 808$ nm and at $\lambda_{p2} = 845$ nm; energy conservation in this FWM process is thus expressed by $\omega_{p1} + \omega_a = \omega_{p2} + \omega_b$. The 989-nm photons created in the first process were used as a herald to trigger single-photon detection of the input and output photons in Hanbury-Brown–Twiss (HBT) interferometers. In this way, they determined the value of $g^{(2)}(0)$ for the fields at λ_a and λ_b ($g_a^{(2)}(0) = 0.21 \pm 0.02$ before and $g_b^{(2)}(0) = 0.19 \pm 0.05$ after conversion) and could thus demonstrate the preservation of photon antibunching under frequency up-conversion. The conversion efficiency in this experiment was ~ 29 %.

In Ref. [51] Rakher and co-workers (NIST, Gaithersburg, MD) report telecom-to-visible up-conversion from $1.3 \mu\text{m}$ to 710 nm in a PPLN WG ($\lambda_p \approx 1557$ nm). In contrast to all other experiments before, photons from a triggered single-photon source (an InAs QD) were used as the input to the frequency converter. Employing pulsed optical excitation of the QD, the authors recorded the full second-order intensity correlation function (instead of merely $g^{(2)}(0)$) for the up-converted field at 710 nm. This was the first time that such a measurement was performed with converted photons and it unambiguously proved that the single-photon character had been preserved during up-conversion. The NIST group achieved an over-all conversion efficiency of 21 % including detection and a signal-to-noise ratio of 7:1 at the converted wavelength. As a side effect, the authors also show that up-conversion detection can be used to improve the sensitivity in photoluminescence lifetime measurements. This is due to the better performance of silicon avalanche photodiodes (APDs) compared to direct detection of telecom photons from the QD with an InGaAs/InP APD. Unfortunately, Ref. [51] contains no comparison of the $g^{(2)}(\tau)$ functions before and after conversion.

In a recent paper by Ikuta *et al.* [52] (Imoto group, Osaka University), the authors demonstrate the preservation of photon antibunching and of polarization entanglement in a down-conversion experiment. This work can be regarded as a significantly advanced down-conversion variant of the pioneering experiment by Tanzilli *et al.* [41]. The input wavelength is tailored to quantum memories based on Rb: wavelength-degenerate polarization-entangled twin photons at $\lambda_a = 780$ nm are created in a BBO crystal by SPDC. One half of them is combined with a strong pump field at $\lambda_p = 1600$ nm in a PPLN WG. The target wavelength is $\lambda_b = 1522$ nm in this case with an internal con-

version efficiency of 62%. The value of the intensity correlation $g^{(2)}(0)$ is determined by sending the 1522-nm photons into a fiber-based HBT setup with gated InGaAs/InP detectors ($g_b^{(2)}(0) = 0.17 \pm 0.04$ after conversion). These detectors are triggered by detection events of a free running silicon APD which are caused by the other unconverted half of 780-nm photons. To investigate the entanglement conservation, a method was applied that transforms polarization entanglement into time-bin entanglement and vice versa [53–55]. One half of the original photons is sent through a MZI prior to conversion. This transforms the polarization-entangled state into a kind of hybrid polarization/time-bin entangled state. After conversion, the 1522-nm photons are sent through a MZI for a second time to restore the polarization entanglement. This smart technique avoids the problem that the PPLN WG can only convert one polarization in a single pass. A quantum state tomography was performed to reconstruct the density matrix for the two-photon state consisting of one original and one down-converted photon. By comparison to the density matrix of the original two-photon state, the authors prove the conservation of polarization entanglement under frequency down-conversion. The calculated fidelity with respect to the $|\Phi^+\rangle$ Bell state, however, drops from 0.95 ± 0.01 before to 0.75 ± 0.06 after conversion which is attributed to anti-Stokes Raman scattering induced by the strong pump at 1600 nm. The work of the Japanese group is outstanding in the sense that it is the first QFC experiment in which quantum state tomography was applied. A similar experiment was performed later by Ramelow *et al.* (Zeilinger group, Vienna) using up-conversion from 810 nm to 532 nm [56]. Ramelow and co-workers used two bulk periodically poled KTP (PPKTP) crystals rotated by 90° against each other to convert both horizontal and vertical polarizations. The latest results on single-photon QFC from the groups at NIST [57] and at Stanford University [58, 59] are not included in this introduction. These results will be discussed at the end in Chap. 7. This seems more appropriate because it allows for comparison with the achievements presented in this thesis.

1.3 Aim and Outline of this Thesis

The main goal of this thesis was to achieve visible-to-telecom frequency conversion of photons emitted by an on-demand solid-state single-photon source and to show that photon antibunching is preserved in this process—apparently from the above literature review this had not been demonstrated so far. To this end, we have studied difference frequency mixing in PPLN WGs according to $(1/\lambda_a - 1/\lambda_p)^{-1} = \lambda_b$. Two different schemes were investigated: (i) down-conversion from $\lambda_a = 738$ nm (emission wavelength of SiV centers in diamond [60]) to the telecom C-band ($\lambda_b = 1557$ nm) and (ii) down-conversion from $\lambda_a = 711$ nm (emission wavelength of InP QDs) to the telecom O-band ($\lambda_b = 1313$ nm). The wavelengths needed to pump these processes lie around 1400 nm (i) and 1550 nm (ii). Currently, to our knowledge, there is no tunable laser on the market which covers both of these wavelengths and provides enough power (some 100 mW). To perform this task, we have thus built and tested two continuous-

wave optical parametric oscillators (OPOs). The pump sources are always indispensable components in frequency conversion setups and some interesting results could be obtained with these OPOs which are also discussed in detail.

The present thesis is organized as follows. Chapters 2 and 3 are theoretical while experimental work is presented in Chap. 4, 5, and 6. In Chap. 2 we start with the theoretical concepts of nonlinear optics (Sect. 2.1) and quantum states of light (Sect. 2.2). In Sect. 3.1 we then proceed by discussing material properties of the nonlinear crystals that are used in this work, namely periodically poled LiNbO_3 and LiTaO_3 . In Sect. 3.2 we discuss the principles of two devices that are based on these materials and that are important in our experiments: OPOs and WG-based frequency converters. In Chap. 4 the results obtained with the OPOs are presented and compared. Two devices were investigated, one OPO based on MgO:PPLN (Sect. 4.1) and one based on MgO:PSSLT (Sect. 4.2). Chapters 5 and 6 are devoted to the frequency down-conversion experiments. In Chap. 5 we investigate process (i). First, in Sect. 5.1, we introduce the setup employed for frequency down-conversion and the WG chip used to implement process (i). The results obtained with this setup are presented in Sect. 5.2 with a particular focus on noise issues and conversion efficiency. Further, in Sect. 5.3, we briefly discuss a two-step frequency conversion process, that is, down-conversion and subsequent up-conversion. This scheme might be helpful for down-conversion of arbitrary polarization states using a single WG crystal. In the experiments described in Chap. 5, attenuated laser pulses were used to emulate single photons at 738 nm. In contrast, we use true single photons from a semiconductor QD in the experiments presented in Chap. 6 in which we study process (ii). In Sect. 6.1 we first review general properties of semiconductor QDs as single-photon sources and discuss the fabrication of the particular InP QD sample that we have employed. After that, we describe the experimental setup and investigate the performance of the second WG chip used to realize process (ii) (Sect. 6.2). In Sect. 6.2 we also explain how single QDs can be selected and how their emission wavelength can be tuned. Then, in Sect. 6.3, we present the most important experiments and results of this thesis: single photons from a QD are frequency down-converted to a telecom wavelength while preserving their nonclassical properties. Finally, in Chap. 7, a summary of the thesis is given and future prospects are discussed.

Chapter 2

Theoretical Background

This chapter provides the theoretical basis for the experiments presented in this work. Since the topic of this thesis is at the interface of nonlinear optics and quantum optics, a brief introduction into the relevant concepts of both realms is given. Section 2.1 deals with nonlinear optics while Sect. 2.2 is about the quantum properties of light fields. An extensive treatment on nonlinear optics can be found, for example, in the textbook of Boyd [61]. The quantum optics section is inspired by the book of Loudon [18].

2.1 Fundamentals of Nonlinear Optics

2.1.1 Nonlinear Polarization

If an external electric field \mathbf{E} is applied to a dielectric medium, a polarization \mathbf{P} is induced. In general, the connection between the i -th Cartesian component of \mathbf{P} and the components of \mathbf{E} is established by the power series

$$P_i = \underbrace{\epsilon_0 \chi_{ij}^{(1)}}_{P_i^{(1)}} E_j + \underbrace{\epsilon_0 \chi_{ijk}^{(2)}}_{P_i^{(2)}} E_j E_k + \underbrace{\epsilon_0 \chi_{ijkl}^{(3)}}_{P_i^{(3)}} E_j E_k E_l + \dots, \quad (2.1)$$

where ϵ_0 is the permittivity of free space and the $\chi^{(n)}$ are tensors of rank $n + 1$ which are called the n th-order susceptibilities. Note that the Einstein summation convention is used in Eq. (2.1). We now write \mathbf{E} as an expansion of plane waves with angular frequencies ω_n

$$\mathbf{E} = \sum_n \mathbf{A}_n e^{i(\mathbf{k}_n \cdot \mathbf{r} - \omega_n t)} + \text{c.c.}, \quad (2.2)$$

where \mathbf{A}_n is the amplitude and \mathbf{k}_n is the wavevector associated with each frequency component ω_n . Equation (2.2) is a general way of writing the electric field and we do not make any specific assumptions on the angular frequencies ω_n at this point. The index n takes the positive integer values 1, 2, 3, ... and ‘c.c.’ denotes the complex conjugate. Defining

$$\mathbf{E}(\omega_n) \equiv \mathbf{A}_n e^{i\mathbf{k}_n \cdot \mathbf{r}} \quad (2.3)$$

and extending the range of indices to negative integers $n = \pm 1, \pm 2, \pm 3, \dots$ (with the convention $\omega_{-n} = -\omega_n$) allows to write Eq. (2.2) in the more convenient form

$$\mathbf{E} = \sum_n \mathbf{E}(\omega_n) e^{-i\omega_n t}. \quad (2.4)$$

When we insert (2.4) into (2.1), the first two polarization terms read:

$$P_i^{(1)} = \epsilon_0 \sum_j \sum_n \chi_{ij}^{(1)}(\omega_n) E_j(\omega_n) e^{-i\omega_n t}, \quad (2.5)$$

$$P_i^{(2)} = \epsilon_0 \sum_{jk} \sum_{nm} \chi_{ijk}^{(2)}(\omega_n + \omega_m; \omega_n, \omega_m) E_j(\omega_n) E_k(\omega_m) e^{-i(\omega_n + \omega_m)t}. \quad (2.6)$$

The linear polarization $P_i^{(1)}$ contains only terms that oscillate at the same angular frequencies ω_n as the original components of the electric field. If the higher-order terms $P_i^{(2)}, P_i^{(3)}, \dots$ are small compared to the linear term $P_i^{(1)}$, they can be neglected and the polarization is given by Eq. (2.5). This is the regime of linear optics. When electric fields and/or higher-order susceptibilities become large, the nonlinear terms $P_i^{(\text{NL})} \equiv P_i^{(2)} + P_i^{(3)} + \dots$ come into play. Then, nonlinear optical effects can be observed. In this thesis, we will particularly investigate second-order nonlinear effects. In the following, we thus ignore terms of order $n > 2$. Obviously, the second-order nonlinear polarization given by Eq. (2.6) is responsible for three-wave mixing processes. Working out the sum in (2.6) for the simple case of two frequencies ω_1 and ω_2 produces terms proportional to $e^{\pm i2\omega_1 t}$ (second harmonic generation of ω_1 , SHG), $e^{\pm i2\omega_2 t}$ (second harmonic generation of ω_2 , SHG), $e^{\pm i(\omega_1 + \omega_2)t}$ (sum frequency generation, SFG), $e^{\pm i(\omega_1 - \omega_2)t}$ (difference frequency generation DFG), and e^0 (optical rectification, OR).

The notation $\chi_{ijk}^{(2)}(\omega_n + \omega_m; \omega_n, \omega_m)$ in expression (2.6) indicates that each of the susceptibilities depends on three frequencies. This represents the most general case. For simplicity, we now assume that the χ_{ijk} are frequency independent. Instead of the second-order nonlinear susceptibility ($\chi_{ijk}^{(2)}$), it is common to use the nonlinear coefficient $\mathbf{d} \equiv (d_{ijk})$ given by the relation $d_{ijk} = \chi_{ijk}^{(2)}/2$. At first sight, the number of independent tensor elements d_{ijk} is $3 \times 3 \times 3 = 27$. This number can be reduced to 10 by using Kleinman's symmetry [62]

$$d_{ijk} = d_{ikj} = d_{kij} = d_{kji} = d_{jki} = d_{jik}. \quad (2.7)$$

If the \mathbf{d} tensor is contracted according to the scheme suggested by Table 2.1 [63], it can be conveniently written in form of a 3×6 matrix with 10 independent elements. The three components of the second-order nonlinear polarization in (2.6) are then obtained by the multiplication of a 3×6 matrix with a 6-component column vector [62, 64]. For instance, when we write the polarization in the same way as the electric field in (2.4),

$$\mathbf{P} = \sum_n \mathbf{P}(\omega_n) e^{-i\omega_n t}, \quad (2.8)$$

Table 2.1: Scheme for the contraction of indices.

jk	11	22	33	23, 32	31, 13	12, 21
l	1	2	3	4	5	6

the frequency component of the nonlinear polarization at $\omega_3 = \omega_1 + \omega_2$ is given by [64]

$$\mathbf{P}^{(2)}(\omega_3) = 4\epsilon_0 \begin{pmatrix} d_{11} & d_{12} & d_{13} & d_{14} & d_{15} & d_{16} \\ d_{16} & d_{22} & d_{23} & d_{24} & d_{14} & d_{12} \\ d_{15} & d_{24} & d_{33} & d_{23} & d_{13} & d_{14} \end{pmatrix} \begin{pmatrix} E_x(\omega_1)E_x(\omega_2) \\ E_y(\omega_1)E_y(\omega_2) \\ E_z(\omega_1)E_z(\omega_2) \\ E_y(\omega_1)E_z(\omega_2) + E_z(\omega_1)E_y(\omega_2) \\ E_x(\omega_1)E_z(\omega_2) + E_z(\omega_1)E_x(\omega_2) \\ E_x(\omega_1)E_y(\omega_2) + E_y(\omega_1)E_x(\omega_2) \end{pmatrix}. \quad (2.9)$$

The relation (2.9) is convenient for practical purposes.

2.1.2 Coupled Mode Equations

As a starting point, we consider the wave equation in a lossless, nonmagnetic (relative permeability $\mu_r = 1$), optically nonlinear dielectric [61]

$$-\nabla^2 \mathbf{E} + \frac{\epsilon_r}{c^2} \frac{\partial^2 \mathbf{E}}{\partial t^2} = -\mu_0 \frac{\partial^2 \mathbf{P}^{(\text{NL})}}{\partial t^2}, \quad (2.10)$$

where μ_0 is the permeability and c is the speed of light in free space. In general, the relative permittivity $\epsilon_r = 1 + \chi^{(1)}$ is a tensor. Here we will assume the special case of an isotropic medium. Then, the relative permittivity becomes a scalar which is connected with the refractive index via $\sqrt{\epsilon_r} = n$. Equation (2.10) can be derived from Maxwell's equations using the slowly varying amplitude approximation [61]. Because of the term containing $\mathbf{P}^{(\text{NL})}$ on the right-hand side, it is an inhomogeneous wave equation. In the following, we will again restrict ourselves to second-order nonlinear effects, i.e., we neglect terms with $n > 2$ in Eq. (2.1). For simplicity, we make an ansatz of three scalar electric fields E_m ($m = 1, 2, 3$),

$$E_m(z, t) = A_m(z) e^{i(k_m z - \omega_m t)} + \text{c.c.}, \quad (2.11)$$

describing plane waves with z -dependent amplitudes A_m . In practice, we will often deal with more complex spatial field distributions (e.g., Gaussian light beams or modes in a WG). However, the use of plane waves at this point is justified by the fact that it illustrates the most important principles without unnecessary complexity. The effects of spatially confined field modes in waveguided nonlinear interactions will be discussed later in Sect. 3.2.3. The fields in Eq. (2.11) are oscillating at angular frequencies ω_1 , ω_2 , and $\omega_3 = \omega_1 + \omega_2$ and propagate along the z axis. The medium has refractive

indices $n(\omega_m) \equiv n_m$ and the dispersion relation reads $c|\mathbf{k}_m| = n_m\omega_m$. The intensity is proportional to $|A_m(z)|^2$ and, with our definition of the fields (2.11), is given by [61]

$$I_m = 2\epsilon_0 n_m c |A_m(z)|^2. \quad (2.12)$$

Inserting (2.11) into (2.10) we obtain, after some calculation, the coupled mode equations [61]

$$\frac{\partial A_1(z)}{\partial z} = -i\kappa_1 A_2^*(z) A_3(z) e^{-i\Delta k' z}, \quad (2.13)$$

$$\frac{\partial A_2(z)}{\partial z} = -i\kappa_2 A_1^*(z) A_3(z) e^{-i\Delta k' z}, \quad (2.14)$$

$$\frac{\partial A_3(z)}{\partial z} = -i\kappa_3 A_1(z) A_2(z) e^{+i\Delta k' z}, \quad (2.15)$$

which govern the evolution of the amplitudes $A_m(z)$ along the propagation direction. The coupling constants κ_i are given by $\kappa_i = \frac{2\omega_i d_{\text{eff}}}{n_i c}$, where we have introduced the scalar effective nonlinear coefficient d_{eff} that can be calculated from the \mathbf{d} tensor if the propagation and polarization directions of all three fields are known [65]. The parameter

$$\Delta k' = k_3 - k_1 - k_2 \quad (2.16)$$

is the so-called wavevector mismatch. Usually, for vector fields, $\Delta k'$ is also a vector. However, for our needs it is sufficient to assume that the \mathbf{k}_m are collinear and thus $\Delta k'$ is always a scalar. The coupled differential equations (2.13)–(2.15) are central to all second-order nonlinear interactions. Depending on the actual value of $\Delta k'(k_1, k_2, k_3)$ the processes that can take place are either SHG, SFG, DFG, or OR as we shall see in the next section.

2.1.3 Phasematching

The wavevector mismatch $\Delta k'$ is a crucial parameter for the efficiency of nonlinear processes, as the following example for DFG shows (analog arguments are valid for SFG and SHG). We assume that two frequencies ω_3 and ω_1 are incident on a nonlinear medium and interact to create a third frequency $\omega_2 = \omega_3 - \omega_1$ via DFG. If both amplitudes A_3 and A_1 do not change significantly during this process, we can make the approximations $\partial A_3/\partial z \approx 0$, $\partial A_1/\partial z \approx 0$ and treat A_3 and A_1 as constants. The solution of Eq. (2.14) at $z = L$ is then obtained by integration

$$A_2(L) = -i\kappa_2 A_1^* A_3 \int_0^L e^{-i\Delta k' z} dz = -i\kappa_2 A_1^* A_3 \frac{e^{-i\Delta k' L} - 1}{-i\Delta k'}. \quad (2.17)$$

We take the squared modulus of (2.17) which is proportional to the intensity¹

$$I_2(L) \propto (\kappa_2 |A_1| |A_3|)^2 \left| \frac{e^{-i\Delta k' L} - 1}{\Delta k'} \right|^2 = (\kappa_2 |A_1| |A_3|)^2 L^2 \text{sinc}^2(\Delta k' L/2). \quad (2.18)$$

The sinc^2 function is characteristic for second-order nonlinear interactions. A plot of this function is shown in Fig. 2.1. It attains its global maximum when the argument

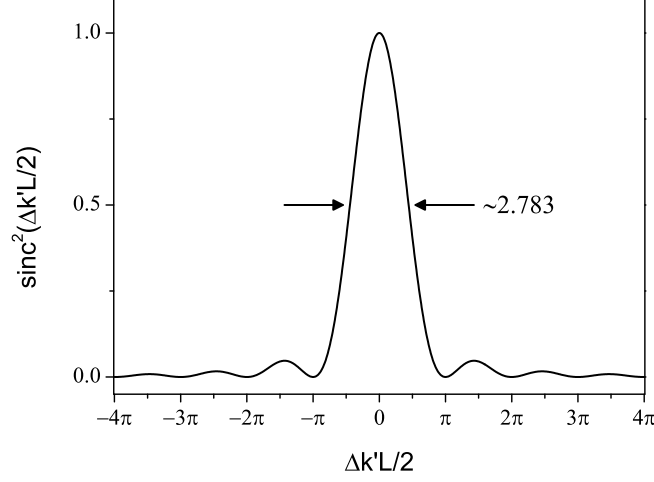


Figure 2.1: The sinc^2 function which describes the efficiency of second-order nonlinear processes as a function of the wavevector mismatch $\Delta k'$. Arrows indicate the FWHM width of the central peak.

vanishes. Therefore,

$$\Delta k' \stackrel{!}{=} 0 \quad (2.19)$$

is required to maximize the generated intensity $I_2(L)$. Equation (2.19) is known as the phasematching condition. Since the linear momentum for photons is given by $p = \hbar k$, (2.19) represents the conservation of momentum in the photon picture. Naturally, also energy conservation must be fulfilled in nonlinear optical processes which is expressed by the relation

$$\omega_3 = \omega_1 + \omega_2. \quad (2.20)$$

In practice, it is not trivial to satisfy (2.19) and (2.20) simultaneously because of material dispersion. With the vacuum wavelengths λ_m condition (2.19) reads

$$\Delta k' = 2\pi \left(\frac{n(\lambda_3)}{\lambda_3} - \frac{n(\lambda_1)}{\lambda_1} - \frac{n(\lambda_2)}{\lambda_2} \right), \quad (2.21)$$

¹We make use of the relation [61]

$$\left| \frac{e^{-i\Delta k' L} - 1}{\Delta k'} \right|^2 = L^2 \frac{\sin^2(\Delta k' L/2)}{(\Delta k' L/2)^2} \equiv L^2 \text{sinc}^2(\Delta k' L/2).$$

or, using $\lambda_m = 2\pi c/\omega_m$,

$$\Delta k' = \frac{1}{c}(n_3\omega_3 - n_1\omega_1 - n_2\omega_2) = 0. \quad (2.22)$$

Note that n_3 , n_2 , and n_1 usually also depend on the temperature of the nonlinear material. We neglect this fact for now but will come back to it later in the context of OPOs (see Sect. 3.2.2). Inspection of (2.20) and (2.22) reveals that, in general, conservation of energy and momentum are not satisfied simultaneously and no efficient frequency conversion takes place. Inserting (2.20) into (2.22) yields

$$\Delta k' = \frac{1}{c}[(n_3 - n_1)\omega_1 + (n_3 - n_2)\omega_2]. \quad (2.23)$$

Under the reasonable assumption of normal dispersion, $n_3 > n_1, n_2$ holds—anomalous dispersion occurs in spectral regions with strong absorption which is not desirable in practical devices. Thus, $n_3 - n_1 > 0$ and $n_3 - n_2 > 0$ which implies $\Delta k' > 0$. To achieve $\Delta k' = 0$ anyway, a number of phasematching techniques have been developed [66]. The two methods which are most commonly applied in nonlinear optical devices are known as birefringent phasematching (BPM) and quasi-phasematching (QPM). BPM exploits the birefringence of many nonlinear crystals to satisfy the phasematching condition. QPM is based on a periodic modulation of the nonlinear coefficient d_{eff} . The modulation is specifically engineered to phasematch a desired process. Since QPM is exclusively used throughout this thesis we will only explain this type of phasematching (see next section). Treatments of BPM can be found, for example, in Refs. [61, 65].

2.1.4 Quasi-Phasematching

To explain the QPM technique, we follow the Fourier transform approach of the review paper by Fejer *et al.* [67]. In QPM, the effective nonlinear coefficient d_{eff} is not constant but is a periodic function in z . We take account of this fact by replacing d_{eff} by $d(z)$ in (2.13)–(2.15). Under the same assumptions as in the previous section, Eq. (2.17) then becomes

$$A_2(L) = -i \frac{\kappa_2}{d_{\text{eff}}} A_1^* A_3 \int_0^L d(z) e^{-i\Delta k' z} dz \quad (2.24)$$

$$= \Gamma d_{\text{eff}} \int_0^L g(z) e^{-i\Delta k' z} dz \quad (2.25)$$

$$= \Gamma d_{\text{eff}} LG(\Delta k'). \quad (2.26)$$

In Eq. (2.25) we have used the definitions $\Gamma \equiv -i \frac{\kappa_2}{d_{\text{eff}}} A_1^* A_3$ and $g(z) \equiv d(z)/d_{\text{eff}}$, where $g(z)$ is the normalized nonlinear coefficient. In Eq. (2.26),

$$G(\Delta k') = \frac{1}{L} \int_0^L g(z) e^{-i\Delta k' z} dz \quad (2.27)$$

denotes the Fourier transform of $g(z)$. Since $g(z)$ is assumed to be periodic in z , it can be written as a Fourier series

$$g(z) = \sum_{m=-\infty}^{\infty} G_m e^{iK_m z}. \quad (2.28)$$

The G_m are Fourier coefficients, $K_m = 2\pi m/\Lambda$ is called the m th-order grating vector, and Λ is known as the QPM grating period. Inserting (2.28) into (2.27) yields

$$G(\Delta k') = \frac{1}{L} \int_0^L \sum_{m=-\infty}^{\infty} G_m e^{-i(\Delta k' - K_m)z} dz \quad (2.29)$$

$$\approx \frac{1}{L} \int_0^L G_m e^{-i(\Delta k' - K_m)z} dz \quad (2.30)$$

$$= \frac{G_m}{L} \frac{e^{-i\Delta k L} - 1}{-i\Delta k}. \quad (2.31)$$

The approximation (2.30) is valid if only one term with $\Delta k' \approx K_m$ significantly contributes to the series which is a good assumption for many realistic cases. In the last step, we have introduced the total wavevector mismatch for QPM:

$$\Delta k \equiv \Delta k' - K_m \stackrel{(2.21)}{=} 2\pi \left(\frac{n(\lambda_3)}{\lambda_3} - \frac{n(\lambda_1)}{\lambda_1} - \frac{n(\lambda_2)}{\lambda_2} - \frac{m}{\Lambda} \right). \quad (2.32)$$

Finally, by combining (2.26) and (2.31), we obtain

$$A_2(L) \approx i\Gamma d_Q \frac{e^{-i\Delta k L} - 1}{\Delta k}. \quad (2.33)$$

The quantity $d_Q \equiv d_{\text{eff}} G_m$ can be considered the effective nonlinear coefficient for m th-order QPM. Note that expression (2.33) is identical to (2.17) when the substitutions $d_{\text{eff}} \rightarrow d_Q$ and $\Delta k' \rightarrow \Delta k$ are applied. This implies that, by using these replacements, the coupled mode equations (2.13)–(2.15) remain valid for QPM interactions. In practice, the case where $g(z)$ is a Λ -periodic rectangular function that can take the values ± 1 is particularly important. The intervals with $g(z) = +1$ shall have length l . This corresponds to a periodic sign reversal of d_{eff} in the nonlinear material and is illustrated in Fig. 2.2. Assuming that $K_m = \Delta k'$ for a specific m (which is achieved by choosing an appropriate period Λ), the Fourier coefficient G_m is given by²

$$G_m = \frac{2}{\pi m} \sin(\pi m D), \quad (2.34)$$

²A possible representation of the function $g(z)$, as shown in Fig. 2.2, is [68]

$$g(z) = -A + 2AD + \sum_{m=-\infty}^{\infty'} \frac{2A}{\pi m} \sin(\pi m D) \exp\left(i \frac{2\pi m}{\Lambda} z\right), \text{ with } A = 1.$$

The primed sum \sum' means that the term with $m = 0$ is omitted in the summation.

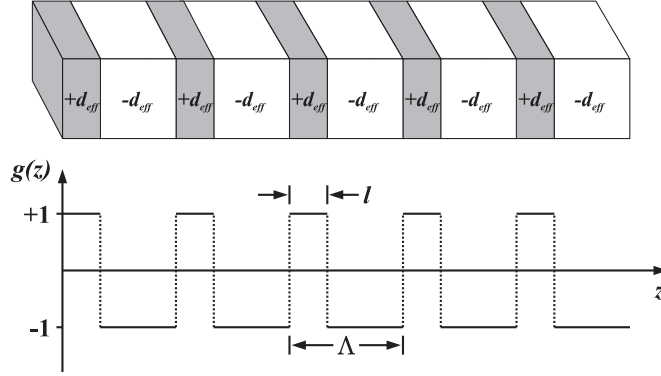


Figure 2.2: The periodic domain structure in a nonlinear material with alternating signs of d_{eff} is described by a rectangular function $g(z)$ with period Λ . l is the length of the intervals with $g(z) = +1$.

where $D = l/\Lambda$ denotes the duty cycle. The nonlinear coefficient for QPM $d_Q = d_{\text{eff}}G_m$ is maximized for $\sin(\pi mD) = 1$ which, for odd m , is accomplished by $D = 0.5$. In this case, the nonlinear coefficient for QPM becomes $d_Q = 2d_{\text{eff}}/(\pi m)$. This important result means that, compared to a perfectly phasematched interaction, d_{eff} is reduced by a factor of $2/(\pi m)$ for QPM. Hence, to maximize d_Q , it is desirable to choose $m = 1$ and thus $D = 0.5$. This is called first-order QPM. All nonlinear devices described in this thesis are based on it.

QPM was proposed independently by Bloembergen *et al.* [69] and by Franken and Ward [63] as early as 1962. Historically, nonlinear crystals with a periodic QPM structure were first realized by stacking thin plates of the material [63] with consecutive plates rotated by 180° against each other. Nowadays, given that the nonlinear crystal is also ferroelectric, periodic poling techniques [70, 71] are applied to create ferroelectric domains in which the spontaneous polarization \mathbf{P}_s periodically changes its direction (see Sect. 3.1.2). This spontaneous polarization must not be confused with the polarization \mathbf{P} introduced in Eq. (2.1). Lithium niobate (LiNbO_3), lithium tantalate (LiTaO_3) or potassium titanyl phosphate (KTiOPO_4) are important examples of nonlinear crystals where periodic poling is used to imprint QPM gratings.

Intuitive Interpretation of Phasematching and QPM

Up to now, we have only given a mathematical justification for the necessity of phasematching and the principles of the QPM technique. For a descriptive explanation of phasematching, we follow the ideas outlined in Refs. [66, 67] and consider the process of SHG, as illustrated in Fig. 2.3(a) and (b). A fundamental wave at angular frequency ω enters a nonlinear material. This fundamental wave generates a nonlinear polarization \mathbf{P} in the medium which oscillates at 2ω and causes the emission of second harmonic (SH) wavelets at each point in the medium. The total SH amplitude is obtained by a superposition of all these wavelets. In the case of perfect phasematching, the fun-

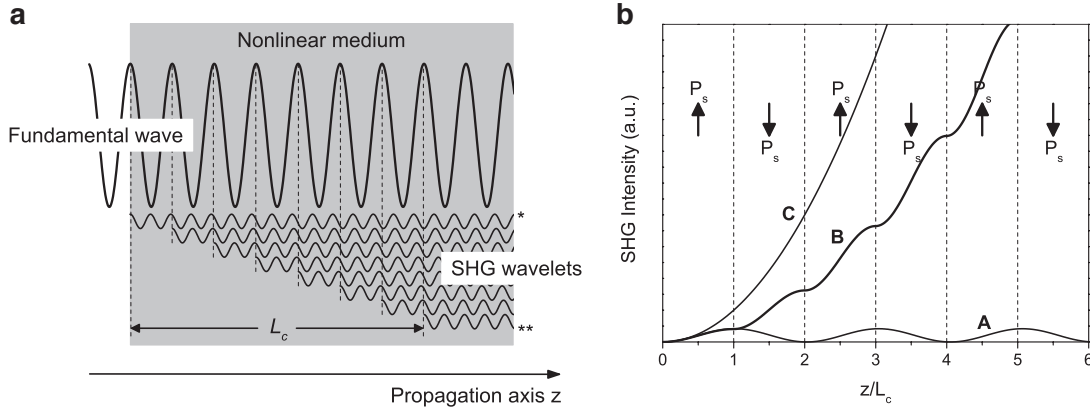


Figure 2.3: (a) Descriptive explanation of SHG in a nonlinear medium (after [66]). The fundamental wave at ω generates wavelets with frequency 2ω . Due to material dispersion (in the non-phasematched case), the fundamental and the SH wave travel at different velocities. After the coherence length L_c , the first pair of wavelets has a phase shift of π and cancels out each other (the wavelets marked with * and **). In this way, for every wavelet generated within a coherence length we can find one in the next coherence length with a phase shift of π . Thus, after $2L_c$ the SH power drops to zero again as shown by curve A in (b). (b) Evolution of the SH intensity as a function of the interaction length for different phasematching situations (after [67]). A: no phasematching, B: first-order QPM, C: perfect phasematching.

damental wave and the second harmonic wavelets travel with the same velocity, all wavelets will interfere constructively, and the SH power will grow quadratically with the propagation length z (see curve C in Fig. 2.3(b)). However, without phasematching, the refractive indices at the fundamental and at the SH frequency are not equal, i.e., $n_1 \equiv n(\omega) \neq n(2\omega) \equiv n_2$. As a consequence, the waves at both frequencies travel through the crystal with different velocities. This is the situation shown in Fig. 2.3(a). Initially, the SH power increases. But soon, after a certain length called the coherence length L_c , the wavelets have run out of phase and start to cancel out each other via destructive interference. As a consequence, the SH power decreases again and is zero at $z = 2L_c$. The described processes then repeat themselves giving rise to power oscillations along the propagation axis as indicated by curve A in Fig. 2.3(b). For practical cases, L_c is on the order of a few optical wavelengths and therefore the generated SH power is at very low levels at all positions in the crystal. Although with QPM we cannot achieve that the fundamental wave and the SH wave travel at the same velocity, it can solve this problem. In first-order QPM, the sign of d_{eff} is periodically reversed after every coherence length and thus $\Lambda = 2L_c$ for the QPM grating period. In this way, the wavelets cannot interfere destructively and the SH power increases with the propagation length in the way shown by curve B in Fig. 2.3(b). The word ‘quasi’ in QPM accounts for the fact that the phase of the interfering waves is not corrected continuously but only at certain positions (integer multiples of L_c) in the nonlinear crystal. At the end of our considerations on phasematching, we mention that QPM provides

some important advantages over BPM making it a very versatile technique. To realize a desired $\chi^{(2)}$ process using BPM, one has to rely on a fortunate combination of polarization and propagation directions of the involved light fields, i.e., the potential of BPM is limited by the dispersion and the birefringence of the chosen nonlinear crystal. In many cases, it is not possible to exploit the largest element of the \mathbf{d} tensor because the required combination of polarization and propagation directions does not satisfy the phasematching condition. Furthermore, the spectral region in which phasematching can be achieved with BPM is often much smaller than the transparency range of the crystal. In addition, spatial walk-off effects limit the interaction length in the crystal and thus the efficiency of the nonlinear process. All of the aforementioned problems are avoided using QPM since the grating period Λ can be specifically tailored to compensate for the wavevector mismatch of a desired nonlinear interaction according to Eq. (2.32). This introduces an additional degree of freedom compared to BPM and opens up interesting applications. For instance, fabrication of two consecutive sections of QPM gratings with different periods allows for the implementation of cascaded nonlinear processes such as an OPO process (see Sect. 3.2.2) in the first section and subsequent SFG in the second section [72,73]. Beyond that, QPM has the benefit of being compatible with integrated photonic structures [74].

2.2 Quantum Physical Description of Light Fields

Most experiments in nonlinear optics are performed with laser light. If the lateral intensity distribution of the laser beams is neglected, it is often sufficient to use plane waves to model the electromagnetic fields. For example, this approximation was used in the derivation of the coupled mode equations (2.13)–(2.15). The wave picture of electromagnetic fields is purely classical and cannot explain all of the phenomena we investigate in this work. In Chap. 6 we deal with single photons and, in this situation, we have to consider the particle character of light rather than its wave-like properties. Hence, we here provide a brief introduction into the quantum optical description of light fields and the peculiarities of photon statistics.

2.2.1 Photon Number States

A very important concept in quantum optics is the photon number state or Fock state $|n\rangle$ which describes a single mode of the electromagnetic field occupied by n photons. By recognizing the analogy between the electromagnetic field energy and the Hamiltonian of the quantum mechanical harmonic oscillator in the form

$$\hat{H} = \frac{1}{2}\hbar\omega \left(\hat{a}\hat{a}^\dagger + \hat{a}^\dagger\hat{a} \right) = \hbar\omega \left(\hat{a}^\dagger\hat{a} + \frac{1}{2} \right), \quad (2.35)$$

we can apply the complete formalism that has been developed for the quantum mechanical harmonic oscillator to light fields. The operators \hat{a} , \hat{a}^\dagger in Eq. (2.35) are annihilation

and creation operators for field quanta, respectively, with the properties ($n \geq 0$)

$$\hat{a}|n\rangle = \sqrt{n}|n-1\rangle, \quad (2.36)$$

$$\hat{a}^\dagger|n\rangle = \sqrt{n+1}|n+1\rangle, \quad (2.37)$$

$$[\hat{a}, \hat{a}^\dagger] = \hat{a}\hat{a}^\dagger - \hat{a}^\dagger\hat{a} = 1. \quad (2.38)$$

Note that the lowest state is the vacuum state $|0\rangle$ since $\hat{a}|0\rangle = 0$ by definition. Applying the Hamiltonian (2.35) to a Fock state yields

$$\hat{H}|n\rangle = \hbar\omega \left(\hat{a}^\dagger\hat{a} + \frac{1}{2} \right) |n\rangle = \hbar\omega \left(\hat{n} + \frac{1}{2} \right) |n\rangle = E_n|n\rangle, \quad (2.39)$$

where we have introduced the photon number operator $\hat{n} \equiv \hat{a}^\dagger\hat{a}$ with the property $\hat{n}|n\rangle = n|n\rangle$. Thus, Fock states are eigenstates of the Hamilton operator as well as of the number operator. $E_n = \hbar\omega(n + \frac{1}{2})$ is the energy of a field mode containing n quanta.

A coherent state, i.e., a state of light that can be generated by a single-mode laser, is constructed as a linear superposition of photon number states. It is represented by the relation [75]

$$|\alpha\rangle = e^{-\frac{1}{2}|\alpha|^2} \sum_{n=0}^{\infty} \frac{\alpha^n}{\sqrt{n!}} |n\rangle, \quad (2.40)$$

where α is the complex amplitude of the coherent state. The expectation value for the number operator is related to α via

$$\langle \hat{n} \rangle = \langle \alpha | \hat{n} | \alpha \rangle = |\alpha|^2. \quad (2.41)$$

2.2.2 Different Types of Light

When dealing with very low optical powers we employ single-photon detectors to measure the intensity of a light field. The operating mode of these detectors is different from other devices used to measure optical intensity, e.g., from a photodiode. A single photon that hits the detector produces a voltage pulse which is then amplified and can be registered by an electronic counter. Single-photon detectors register events (detector clicks) similar to a Geiger tube and offer the possibility to investigate the photon statistics in a light beam. It turns out that three different classes of light can be distinguished by means of the statistical properties of the intensity fluctuations. Figure 2.4 shows a representation of detector clicks that would typically occur for photons from a thermal (or chaotic) light source, a laser, and a single-photon emitter. For simplicity, we assume that the detector has 100% detection efficiency, a perfect timing resolution, and that the light intensity is sufficiently weak so that each click represents one photon impinging on the detector. Considering the photocounts in Fig. 2.4, one recognizes that the photons in Fig. 2.4(a) tend to form bunches of multiple photons (bunched light), the time separations in Fig. 2.4(b) seem to be random (random light), and the photons in Fig. 2.4(c) have more or less equal time distances (antibunched light). This

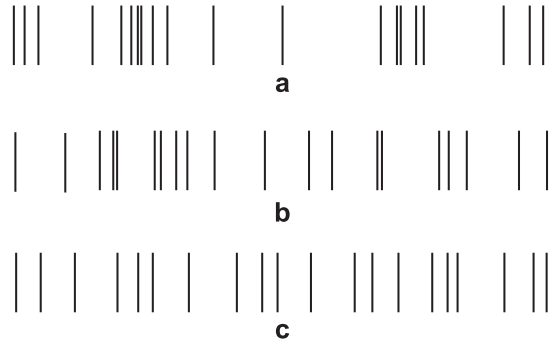


Figure 2.4: Time sequence of photocounts on a single-photon detector for (a) bunched, (b) random, (c) antibunched light (after [18]). The bars represent detection events.

phenomenon is formally described by probability distributions. For chaotic light one can show that the probability $\mathcal{P}_n(T)$ of finding n photons in a time interval of length T is given by the distribution [18]

$$\mathcal{P}(n) = \frac{\langle n \rangle^n}{(1 + \langle n \rangle)^{1+n}}. \quad (2.42)$$

This is the Planck distribution. Its variance is

$$(\Delta n_{\text{Planck}})^2 = \langle n \rangle^2 + \langle n \rangle. \quad (2.43)$$

For a coherent state described by (2.40), the photon statistics are governed by the Poisson distribution

$$\mathcal{P}(n) = |\langle n | \alpha \rangle|^2 = e^{-|\alpha|^2} \frac{|\alpha|^{2n}}{n!} = e^{-\langle n \rangle} \frac{\langle n \rangle^n}{n!}, \quad (2.44)$$

which is characteristic for random processes. The variance of the Poisson distribution is

$$(\Delta n_{\text{Poiss.}})^2 = \langle n \rangle < (\Delta n_{\text{Planck}})^2. \quad (2.45)$$

It seems reasonable to consider a perfectly coherent light source with a Poissonian photon number distribution as a reference for other light sources. With the following scheme one then classifies the three classes of intensity fluctuations by means of the root-mean-square deviation of their photon probability distribution:

- sub-Poissonian: $\Delta n < \sqrt{\langle n \rangle}$,
- Poissonian: $\Delta n = \sqrt{\langle n \rangle}$,
- super-Poissonian: $\Delta n > \sqrt{\langle n \rangle}$.

Sub-Poissonian light is also called nonclassical light as all classical light sources (light bulbs, spectral lamps, lasers, etc.) generate light with $\Delta n \geq \sqrt{\langle n \rangle}$. A quantum emitter

like a single atom or a semiconductor QD (see Sect. 6.1.1) is a source of nonclassical light, also called a single-photon source. An ideal single-photon source generates photons that are represented by a Fock state which has $\Delta n = 0$. By ‘ideal’ we mean a source with the following characteristics stated in [76]: a single photon can be emitted on-demand with a probability of one at any time specified by the user, the probability for emission of two or more photons at the same time is zero, and photons which are subsequently generated should be indistinguishable. Another desirable feature would be that the repetition rate can be made almost arbitrarily fast. In practice, the ideal case can never be completely achieved due to technical limitations. A detailed review on single-photon sources can be found in [76, 77]. The difference between the sub-Poissonian, Poissonian, and super-Poissonian distribution is well illustrated in Fig. 2.5. It shows histograms of the three distributions for different average photon numbers $\langle n \rangle$. In experimental quantum optics,

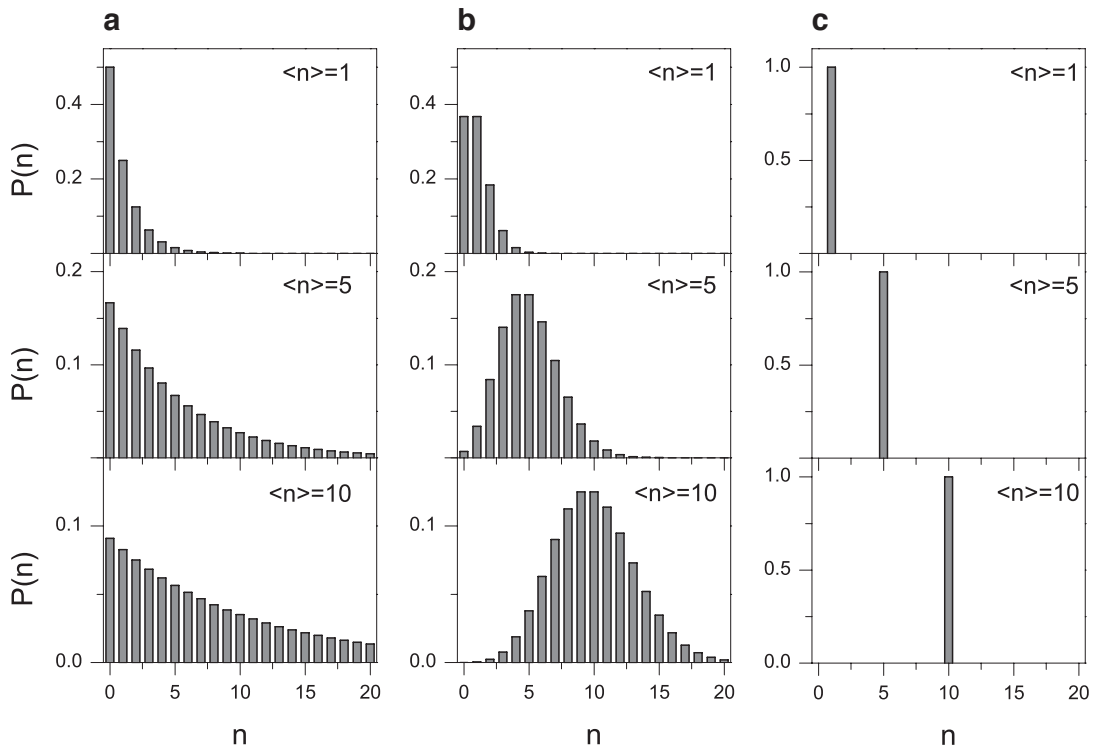


Figure 2.5: Photon number distribution for (a) super-Poissonian light as emitted by a thermal light source, (b) Poissonian light as generated by a coherent light source, (c) sub-Poissonian (nonclassical) light from a perfect single-photon source. The histogram of each distribution is shown for three different mean photon numbers $\langle n \rangle = 1, 5, 10$.

coherent states and Fock states play a central role. From the histograms in Fig. 2.5 it is evident that there exists a fundamental difference between these two states. For instance, for the Fock state $|1\rangle$, we will always (with probability 1) find exactly one photon within a certain time interval T while this is not the case for the coherent state

with $\langle n \rangle = 1$. Here we will find that 36.8% of the time intervals contain no photon, 36.8% contain one photon, 18.4% contain two photons, 6.1% contain three photons, and so on.

Degree of Second-Order Coherence

To decide whether a given light field is nonclassical, Poissonian, or super-Poissonian one could measure the photon counting statistics as illustrated in Fig. 2.5. However, this is technically very difficult since unavoidable photon losses distort the measured photon number distribution always with a tendency toward a Poissonian shape (even if it is in fact non-Poissonian). Instead, the degree of second-order coherence $g^{(2)}(\tau)$, which is much easier accessible in experiments, is usually measured (see the following section).³ For a stationary light field it is defined by [18]

$$g^{(2)}(\tau) = \frac{\langle \hat{a}^\dagger(t)\hat{a}^\dagger(t+\tau)\hat{a}(t+\tau)\hat{a}(t) \rangle}{\langle \hat{a}^\dagger(t)\hat{a}(t) \rangle^2} \quad (2.46)$$

and has the property $0 \leq g^{(2)}(\tau) \leq \infty$. The classification of light by its photon statistics that we have introduced above can also be written in terms of the value $g^{(2)}(\tau = 0)$:

- sub-Poissonian (photon number state $|n\rangle$),

$$g^{(2)}(0) = \frac{\langle n|\hat{a}^\dagger\hat{a}^\dagger\hat{a}\hat{a}|n\rangle}{\langle n|\hat{a}^\dagger\hat{a}|n\rangle^2} = 1 - \frac{1}{\langle n \rangle} \quad (2.47)$$

$(\Rightarrow 0 \leq g^{(2)}(0) < 1 \text{ for } n \geq 1),$

- Poissonian (coherent state $|\alpha\rangle$),

$$g^{(2)}(0) = g^{(2)}(\tau) = \frac{\langle \alpha|\hat{a}^\dagger\hat{a}^\dagger\hat{a}\hat{a}|\alpha\rangle}{\langle \alpha|\hat{a}^\dagger\hat{a}|\alpha\rangle^2} = 1, \quad (2.48)$$

- super-Poissonian (thermal light),

$$g^{(2)}(0) = 1 + \frac{(\Delta n)^2 - \langle n \rangle}{\langle n \rangle^2} > 1. \quad (2.49)$$

³In contrast, the degree of *first-order* (temporal) coherence in quantum optics is defined by

$$g^{(1)}(\tau) = \langle \hat{a}^\dagger(t)\hat{a}(t+\tau) \rangle / \langle \hat{a}^\dagger(t)\hat{a}(t) \rangle.$$

In classical optics this reads $g^{(1)}(\tau) = \langle E^*(t)E(t+\tau) \rangle_T / \langle E^*(t)E(t) \rangle_T$, where $\langle \dots \rangle_T$ stands for the average over a time interval T . $g^{(1)}(\tau)$ is a measure of the temporal coherence of a light field and can be determined using a Michelson or a Mach-Zehnder interferometer. From the degree of first-order coherence no statement on photon statistics can be made [78].

Relation (2.47) implies that $g^{(2)}(0) < 1$ for any number state and in particular $g^{(2)}(0) = 0$ for the single-photon state $|1\rangle$. In general, light sources that produce states which satisfy

$$1 - \frac{1}{\langle n \rangle} \leq g^{(2)}(0) < 1 \quad (2.50)$$

are called to be nonclassical. Although not correct in a strict sense, experimentalists often speak of a single-photon source when $g^{(2)}(0) < 0.5$ is fulfilled (see [79] for a detailed discussion). The situation $g^{(2)}(0) \geq g^{(2)}(\tau \neq 0)$ is known as photon bunching and $g^{(2)}(0) \leq g^{(2)}(\tau \neq 0)$ is known as photon antibunching. While photon antibunching always follows from sub-Poissonian photon statistics, the reverse conclusion is not necessarily true [80].

Measurement of the $g^{(2)}(\tau)$ Function

In principle, it would be possible to investigate the statistical properties of a stream of photons using only one single-photon detector. In practice, though not completely impossible [81], this poses some technical difficulties [82]. Real-world photon counters are often not photon-number resolving, i.e., they produce the same voltage pulse whether one, two or more photons hit the detector at the same time. Furthermore, similar to the Geiger tube, they always have a certain dead time. Thus, once a photon was detected and has generated a click no other photon can be detected in a certain time interval thereafter. To avoid these problems, the Hanbury-Brown–Twiss (HBT) intensity interferometer [83], sketched in Fig. 2.6, is commonly used for determining the $g^{(2)}(\tau)$ autocorrelation function. To measure $g^{(2)}(\tau)$, an incoming light beam is split up into

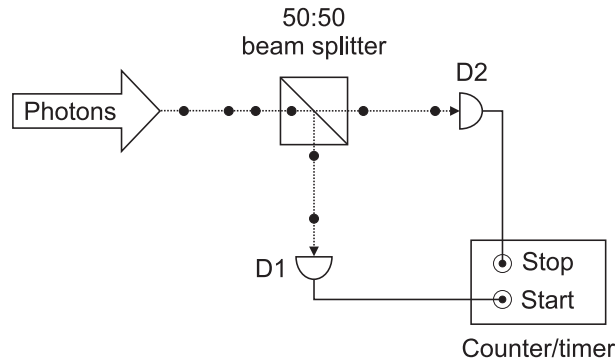


Figure 2.6: Schematic of the Hanbury-Brown–Twiss (HBT) intensity interferometer (after [84]).

two beams by a 50:50 beamsplitter and the two beams are directed to the detectors D1 and D2. The detection events are registered by special counting electronics and correlated to yield the unnormalized intensity autocorrelation function $G^{(2)}(\tau)$. Two different methods are commonly applied for data acquisition, the time-tagged method or the start-stop method [78]. For the measurements in this thesis, we have used the

first method in which the detection events are stored in two lists, one for D1 and one for D2, together with a time tag (absolute time at which the click occurred). Software-based correlation of the two lists can be performed during the measurement or at any time after and yields the unnormalized $G^{(2)}(\tau)$ function. A detailed description of the numerical procedure that is used to compute the correlation function from the measured click lists is found in [82]. The $g^{(2)}(\tau)$ function is computed by normalization of $G^{(2)}(\tau)$ with respect to a Poissonian light source [78, 82]:

$$g^{(2)}(\tau) = \frac{G^{(2)}(\tau)}{R_1 R_2 t_{\text{bin}} t_{\text{int}}}. \quad (2.51)$$

Here R_1 and R_2 are the average count rates of D1 and D2, respectively, t_{bin} is the time bin size, and t_{int} is the total integration time. For the evaluation of $G^{(2)}(\tau)$, the total integration time must be divided into small time intervals of length $t_{\text{bin}} \ll t_{\text{int}}$. Detection events are considered to happen simultaneously when they occur within a time interval of t_{bin} . This reflects the fact that the timing resolution of the electronic counters is limited.

Chapter 3

Nonlinear Optical Materials and Devices

In this chapter we review the nonlinear optical materials that are used in this work and the devices that are based on these materials. Section 3.1 discusses the relevant physical properties of lithium niobate (LiNbO_3 , LN) and lithium tantalate (LiTaO_3 , LT) which are closely related materials. Section 3.2 is dedicated to quasi-phases-matched cw OPOs and WG-based frequency converters.

3.1 Lithium Niobate and Lithium Tantalate as Nonlinear Optical Materials

3.1.1 Crystal Structure

A comprehensive overview on the crystal structure and physical properties of LN was provided by Weis and Gaylord [85]. We here partly follow their explanations. LN and LT are isomorphous crystals. They are ferroelectric at temperatures below a characteristic Curie temperature T_c ($T_c^{(\text{LN})} = 1195 \pm 15^\circ\text{C}$, $T_c^{(\text{LT})} = 610 \pm 10^\circ\text{C}$ [86]) and paraelectric for temperatures above T_c . We concentrate on the ferroelectric phase since this is of relevance for applications in nonlinear optics. A sketch of the crystal structure in the ferroelectric phase is depicted in Fig. 3.1. The crystal consists of oxygen atom layers in a (distorted) hexagonal close-packed arrangement. Li ions, Nb/Ta ions, and vacancies are sited at the octahedral interstices between the oxygen sheets. As indicated in Fig. 3.1, the ions and vacancies (V) are positioned in the order ... , Nb (Ta), V, Li, Nb (Ta), V, Li, ... along the direction defined as the crystallographic c axis. Thus, one-third of the octahedra formed by the oxygen atoms contain Li atoms, one-third Nb (Ta) atoms, and one-third vacancies. The LN (LT) crystal shows a three-fold rotation symmetry about the c axis and a mirror symmetry about three planes that form an angle of 60° . Their line of intersection coincides with the c axis. Because of these symmetry properties, LN (LT) can be classified into the point group $3m$ (trigonal crystal

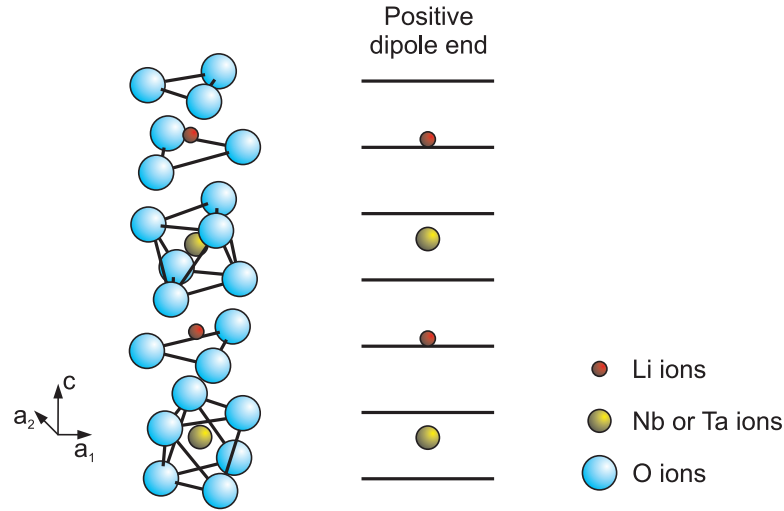


Figure 3.1: Crystal structure of LN and LT in the ferroelectric phase at $T < T_c$ (after [85,87]).

system) and a hexagonal or a rhombohedral unit cell can be chosen.

It is important to note that tensorial quantities, such as the nonlinear optical coefficient \mathbf{d} , are not stated with respect to the crystallographic axes a_1, a_2, c but with respect to Cartesian axes X, Y, Z in the literature. By convention, the Z axis is chosen to be parallel to the c axis, the Y axis lies within one of the three mirror planes, and the X axis then is perpendicular to that plane (see [85] for further details).

3.1.2 Ferroelectricity and Electric Field Poling

Without an external electric field, the energy of the Li^+ ions as a function of their position on the c axis is described by a double-well potential [66, 71]. Hence, there are two possible stable positions for the ions and they can be sited either above or below the planes defined by the oxygen triangles (in the situation sketched in Fig. 3.1, the Li^+ ions are all sited above these planes). However, at room temperature the thermal energy of the ions is not high enough to switch from one local minimum of the double-well potential to the other. The shift of Li^+ and Nb^- ions with respect to the oxygen octahedra is the reason for the ferroelectricity in LN and LT. It causes permanent electric dipole moments in each unit cell. If all Li^+ ions are shifted in the same direction within a certain volume of the crystal, the microscopic electric dipoles all point in the same direction and a macroscopic spontaneous polarization \mathbf{P}_s is observed. In analogy to ferromagnetic materials, sections where all dipoles are oriented in the same direction are called (ferroelectric) domains. A periodic modulation of the nonlinear coefficient d_{eff} for QPM in LN (LT) is achieved by periodic poling techniques [70, 71]. By applying external electric fields to a single domain crystal, a periodic domain structure with alternating directions (parallel and antiparallel to the initial $+c$ direction) of \mathbf{P}_s is induced. A domain with a flipped direction of \mathbf{P}_s is equivalent to a mirrored part of the

crystal with respect to a fixed laboratory frame. Thus, for LN and LT, the d_{31} and d_{33} tensor elements change their sign in that region. This connection between the direction of \mathbf{P}_s and the sign of the tensor elements is the foundation for the fabrication of QPM crystals via electric field poling.

3.1.3 Stoichiometry and Doping

The composition of LN and LT single crystals which are grown by the Czochralski method is usually not perfectly stoichiometric. Instead, a small fraction of Li ions is substituted by Nb ions such that the ratio of Li ions to Nb ions is not exactly 1 as would be expected from the chemical formula. In the so-called congruent composition this ratio is 0.946 [88]. Soon after the first synthesis of congruent LN (LT) single crystals, it has been noticed that these materials exhibit an effect known as photorefractive damage [89]. This term refers to optically-induced inhomogeneities in the refractive index which are observed when the material is illuminated with strong laser radiation in the visible. Photorefractive damage describes a complex mechanism involving several effects [85]. It is associated with the non-perfect stoichiometry of the crystals as Nb ions on Li sites can act as traps for electrons which play an important role in the formation of local electric fields in the crystal. These fields then lead to local fluctuations of the refractive index via the linear electro-optic effect (Pockels effect) [85]. A more detailed discussion of the physical processes that are responsible for photorefractive damage can be found in [71]. Photorefractive damage can be severely detrimental in nonlinear optical processes where visible wavelengths are involved. Further adverse effects that have been observed for LN and LT are green-induced infrared absorption (GRIIRA) [90] and blue-induced infrared absorption (BLIIRA) [91], respectively. All of these effects are strongly suppressed by using crystals that have been doped with MgO or ZnO [91–94] or/and have a near-stoichiometric (often referred to as simply ‘stoichiometric’) composition. Therefore, for the nonlinear devices presented in this work, we exclusively rely on doped crystals: congruent LN doped with MgO or ZnO and stoichiometric LT doped with MgO. Typical MgO and ZnO doping concentrations for congruent LN are 5 mol % and 7 mol %, respectively. A typical MgO doping concentration for stoichiometric LT is 1 mol %.

3.1.4 Linear and Nonlinear Optical Properties

The useful transparency range of LT spans from ~ 0.28 – $5.0 \mu\text{m}$ [98] and is thus broader than that of LN which is ~ 0.35 to $> 4 \mu\text{m}$ [99, 100]. LN and LT are birefringent materials with one optical axis (uniaxial crystals). Throughout the transparency range, the birefringence $\Delta n = n_e - n_o$ is negative for LN and changes its sign for LT (n_e, n_o are the extraordinary and ordinary refractive indices, respectively). The magnitude of the birefringence $|\Delta n|$ is much larger for LN than for LT. For this reason, LN is suitable for both BPM and QPM while phasematching in LT is only possible via QPM. For device design, it is crucial to know the dependence of the refractive indices n_e, n_o

Table 3.1: Second-order nonlinear-optical coefficients of selected crystals [pm/V].

Crystal	λ^* (μm)	d_{33}	d_{22}	d_{31}	Ref.
Congruent LiNbO ₃ (CLN)	1.313	19.5		3.2	[95]
	1.064	25.2		4.6	[95]
	0.852	25.7		4.8	[95]
	1.064	27.2	2.1	4.4	[96]
5 % MgO-doped LiNbO ₃	1.313	20.3		3.4	[95]
	1.064	25.0		4.4	[95]
	0.852	28.4		4.9	[95]
Stoichiometric LiTaO ₃ (SLT)	**	12.9	1.54	0.46	[97]
	1.313	10.7		0.85	[95]
	1.064	13.8			[95]
	0.852	15.1			[95]

* The given wavelengths are fundamental wavelengths in SHG experiments.

** In Ref. [97] a variety of nonlinear interactions has been used to determine the nonlinear coefficients.

on the wavelength and temperature with high accuracy. The refractive indices also slightly depend on the doping concentration and type of dopant. Numerous Sellmeier equations that allow to calculate $n_{e,o}(\lambda, T)$ for doped and undoped LN and LT can be found in the literature [97, 101–107]. The parameters published by Gayer *et al.* [105] for MgO-doped LN and by Dolev *et al.* [97] for stoichiometric LT have been found to match particularly well to the results obtained in our experiments. The WGs used for the experiments described in Chap. 5 and 6 are made of ZnO-doped LN. According to the manufacturer [108], a good approximation for the refractive indices of this material is obtained with an equation by Jundt [101] for congruent LN. Important Sellmeier equations and coefficients from Refs. [97, 101, 105] are summarized in App. A.

Taking into account symmetry properties of the point group $3m$, the matrix in (2.9) can be further simplified for LN (LT) and then reads [65]

$$\mathbf{d} = \begin{pmatrix} 0 & 0 & 0 & 0 & d_{31} & -d_{22} \\ -d_{22} & d_{22} & 0 & d_{31} & 0 & 0 \\ d_{31} & d_{31} & d_{33} & 0 & 0 & 0 \end{pmatrix}. \quad (3.1)$$

Numeric values for the three non-vanishing tensor elements d_{33} , d_{22} , and d_{31} of CLN, 5 % MgO:CLN, and SLT are compiled in Table 3.1. These values are often determined from SHG experiments. Numbers from different references have been included to illustrate that these quantities are not known with perfect accuracy. The d_{33} coefficient is by far the largest of the three coefficients for both crystals. It is 1.6 to 1.8 times larger for LN compared to LT. The d_{33} coefficient, which is accessible only via QPM but not via BPM, is used in all the devices described in this thesis. All three interacting light fields are always (predominantly) polarized along the Z axis such that $d_Q = 2d_{33}/\pi$. Note that the crystal coordinate system (X, Y, Z) is different from the laboratory frame

(x, y, z) which we will use to refer to the direction of light propagation (the connection between the two is illustrated in Fig. 3.2(a)). As usual in the literature, we will assume that laser beams or modes in a WG propagate along the z direction which can be chosen parallel or antiparallel to the X direction. Comparison of the numbers for undoped CLN with those for 5% MgO-doped CLN shows that MgO-doping has no large impact on the values of the nonlinear coefficients. This is supposed to be true also for ZnO doping [108]. Shoji *et al.* [95] have determined the coefficients employing different fundamental wavelengths in their SHG experiments. Their results reveal that the values of the nonlinear coefficients actually depend on the wavelength. This is usually neglected such that Kleinman's symmetry condition can be applied.

3.2 Nonlinear Optical Devices

3.2.1 Parametric Amplification

In general, an analytic solution of the coupled system (2.13)–(2.15) is not possible. However, assuming that the field E_3 is much stronger than the other two and does hardly change its amplitude (no pump depletion approximation), that is $\partial A_3/\partial z = 0$, Eq. (2.15) can be readily integrated to yield $A_3(z) = \text{const.} \equiv A_{30}$. The two remaining Eqs. (2.13) and (2.14) can then be solved analytically and we obtain [61, 66, 109]

$$A_1(z) = A_1(0)e^{i\Delta kz/2} \left[\cosh gz - \frac{i\Delta k}{2g} \sinh gz \right] + i \frac{\kappa_1 A_{30}}{g} A_2^*(0) e^{i\Delta kz/2} \sinh gz, \quad (3.2)$$

$$A_2(z) = A_2(0)e^{i\Delta kz/2} \left[\cosh gz - \frac{i\Delta k}{2g} \sinh gz \right] + i \frac{\kappa_2 A_{30}}{g} A_1^*(0) e^{i\Delta kz/2} \sinh gz. \quad (3.3)$$

With the parameter

$$\Gamma^2 \equiv \kappa_1 \kappa_2 |A_{30}|^2, \quad (3.4)$$

the gain coefficient g can be written as

$$g = \sqrt{\Gamma^2 - \left(\frac{\Delta k}{2}\right)^2}. \quad (3.5)$$

Note that Γ here is defined differently than in Sect. 2.1.4. In the following, we assume the initial conditions

$$A_1(0) = A_{10}, \quad A_2(0) = 0. \quad (3.6)$$

Equations (3.2) and (3.3) describe a process called optical parametric amplification (OPA). This term can be understood by considering the ratio of output power $P_1(L) \propto$

$|A_1(L)|^2$ to input power $P_1(0) \propto |A_1(0)|^2$:

$$\frac{P_1(L)}{P_1(0)} = \frac{|A_1(L)|^2}{|A_1(0)|^2} \quad (3.7)$$

$$= 1 + \Gamma^2 L^2 \frac{\sinh^2(gL)}{(gL)^2} \quad (3.8)$$

$$\equiv 1 + G. \quad (3.9)$$

In the last step we have defined the parametric gain $G \geq 0$. For small gain coefficient, $g \ll \frac{\Delta k}{2}$, G becomes [110]

$$G \approx \Gamma^2 L^2 \text{sinc}^2(\Delta k L/2) \xrightarrow{\Delta k=0} (\Gamma L)^2. \quad (3.10)$$

According to our initial conditions (3.6), the light fields at ω_1 and ω_3 are incident on a crystal with second-order nonlinearity. Obviously from (3.9), the power of the input field at ω_1 is amplified by a factor $1 + G$ during propagation through the nonlinear medium from $z = 0$ to $z = L$. Additionally, a third field at $\omega_2 = \omega_3 - \omega_1$ is created and its amplitude increases as well while traversing the nonlinear medium (described by Eq. (3.3)). The energy for the amplification is provided by the strong field at ω_3 which is therefore called the pump field. Furthermore, the field at ω_1 is termed the signal field and the third field at ω_2 is known as the idler field. In the context of OPOs, we will stick to this terminology and replace the indices used to label the interacting fields according to: $3 \rightarrow p$, $1 \rightarrow s$, and $2 \rightarrow i$. We here use the convention $\omega_1 < \omega_s < \omega_p$. This convention is arbitrary because the equations (3.2) and (3.3) are completely symmetric with respect to an exchange of indices $1 \leftrightarrow 2$. It is only required that $\omega_3 = \omega_p$ is the highest frequency. As an example, Fig. 3.2 illustrates OPA in a 4-cm-long MgO:PPLN crystal. Figure 3.2(b) shows $1 + G = I_s(z)/I_s(0)$ for the signal field and Fig. 3.2(c) shows the evolution of the normalized idler intensity $I_i(z)/I_s(0)$. For simplicity, we have assumed perfect phasematching $\Delta k = 0$ in these plots.

Note that, in principle, OPA and DFG describe one and the same physical process. The term OPA is used for the more specific situation when the amplification of a weak input signal by means of a strong pump field is considered. In this case, the idler wave is actually not needed, which explains the name. However, if the main objective is to generate a wave with a third frequency $\omega_2 = \omega_3 - \omega_1$ from two input fields at ω_1 and ω_3 one speaks of DFG.

3.2.2 Optical Parametric Oscillators

OPA can be exploited to build an optical parametric oscillator (OPO) which is able to generate coherent optical radiation just like a laser. One can imagine an OPO as a resonantly enhanced OPA: the nonlinear crystal is placed inside an optical cavity to provide resonant feedback for the signal and/or idler wave. In analogy to many lasers, an OPO consists of three basic elements: a pump laser, a gain medium, and an optical

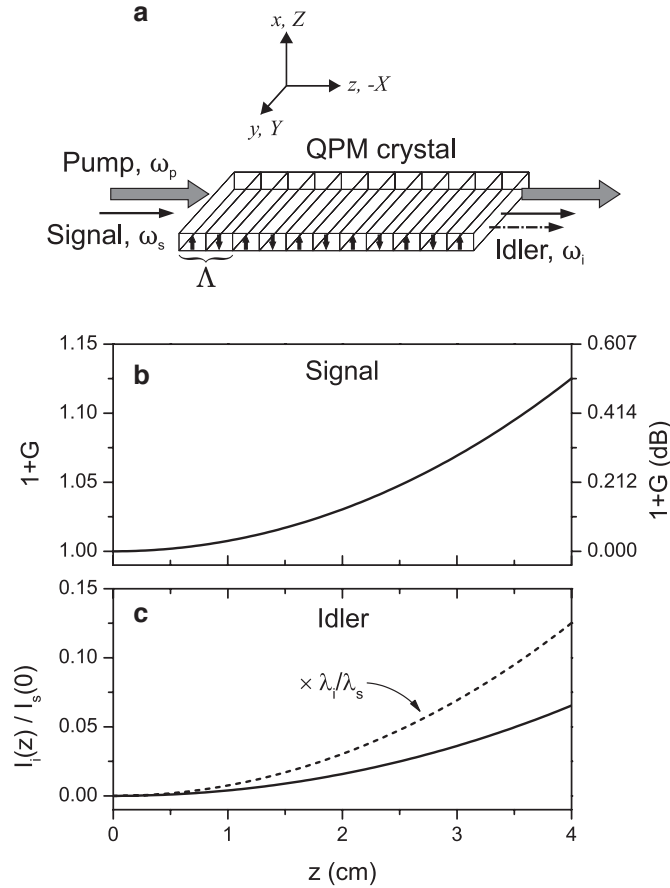


Figure 3.2: Parametric amplification in a QPM crystal. (a) Schematic of the considered OPA process: the inserted signal field is amplified with the help of the strong pump field and a third field, the idler field, is generated. The laboratory frame is denoted by lower-case letters (x, y, z) while capital letters (X, Y, Z) indicate the crystal coordinate system of LN or LT as introduced in Sect. 3.1.1. (b) Relative amplification $I_s(L)/I_s(0) = 1 + G$ of the signal intensity. (c) Solid line: idler intensity normalized with respect to the input signal intensity $I_i(L)/I_s(0)$. The generated idler intensity is smaller than the signal intensity since the number of signal and idler photons created in OPA is equal but the idler photons have less energy ($\lambda_s < \lambda_i$). Correcting the data by a factor of λ_i/λ_s results in the dashed line which shows the same course as the function in (b). Parameters used to calculate the curves: 5% MgO:PPLN, $\lambda_p = 532$ nm, $\lambda_s = 810$ nm, $\lambda_i = 1550$ nm, $n_p = 2.2246$, $n_s = 2.1668$, $n_i = 2.1307$ [105], $d_Q = 16$ pm/V, $I_P = \frac{1 \text{ W}}{\pi \times (50 \mu\text{m})^2}$.

resonator. Since the first demonstration of an OPO [111], a plethora of device designs have been developed (see [112] for a review of QPM-based OPOs). Among the criteria which are used for a classification of OPOs are: the type of pump laser, the type of radiation that is emitted (cw or pulsed), the nonlinear material, the phasematching technique (BPM, QPM, or other), and the resonator design (singly resonant, doubly

resonant, triply resonant, or other). We here only discuss the cw singly resonant OPO (cw SRO) based on QPM. Singly resonant means that the cavity mirrors are designed such that the OPO cavity is resonant only for the signal (idler) wave but not for the pump and the idler (signal) wave. A schematic of such an OPO is sketched in Fig. 3.3.

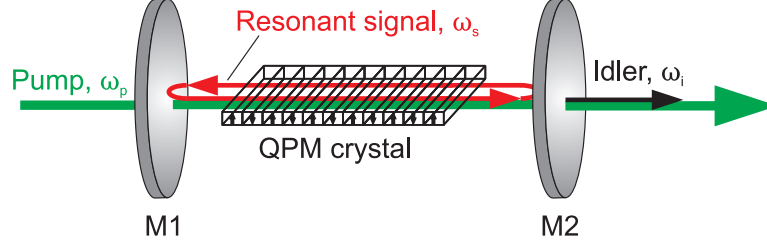


Figure 3.3: Schematic of a singly resonant OPO: a QPM crystal is placed inside an optical resonator and pumped by a laser (green). The cavity mirrors are highly reflective only for the signal wave (red). The pump light and the idler radiation (black) are transmitted by the cavity mirrors (M1, M2). As opposed to a laser, gain is only generated in one direction due to the phasematching condition $\Delta k = 2\pi(k_p - k_s - k_i - 1/\Lambda) = 0$ which must be fulfilled to generate macroscopic signal and idler power.

Start Process

It is important to note that, at the very beginning when the pump laser is switched on, the situation for an OPO is different from the initial conditions (3.6). Initially, only the pump field is incident onto the nonlinear crystal, i.e.,

$$A_p(0) = A_p, \quad A_s(0) = 0, \quad A_i(0) = 0. \quad (3.11)$$

Considering these initial conditions, the creation of photons at frequencies $\neq \omega_p$ cannot be explained by the classical coupled mode equations. In fact, the start process of an OPO is based on optical parametric fluorescence (OPF) which is a pure quantum effect (see, e.g., Ref. [113] for a mathematical treatment). This effect is also called spontaneous parametric down-conversion (SPDC). During the first pass of the pump beam through the crystal, a very small fraction of the pump photons spontaneously splits up into signal and idler photons. In an SRO, the so produced signal or idler photons are fed back by the cavity mirrors and enter the crystal again. From this point on, OPA, as discussed in the previous section, will take place in the crystal.

Oscillation Threshold

In analogy to a laser, an OPO starts when the gain per cavity round trip equals the cavity losses. Thus, optical parametric oscillation is observed only when the threshold condition $P_{p,th} < P_p$ is fulfilled, i.e., when the pump power P_p is larger than a certain threshold pump power $P_{p,th}$. Cavity losses are induced by non-perfect reflectivities of

the resonator mirrors, absorption, Fresnel reflection at interfaces, scattering, or diffraction. For simplicity, the reflectivities of all cavity mirrors at the signal (idler) frequency are modeled by a single amplitude reflection coefficient R_s (R_i). All other losses experienced by the signal (idler) wave are included in an absorption constant α_s (α_i). With $l_1 \equiv 1 - R_s e^{-\alpha_s L}$ and $l_2 \equiv 1 - R_i e^{-\alpha_i L}$, the threshold condition reads [61, 110]

$$\cosh(gL)_{\text{th}} = 1 + \frac{l_1 l_2}{2 - l_1 - l_2}. \quad (3.12)$$

This relation is obtained from Eqs. (3.2), (3.3) by requiring that the signal and idler fields reproduce themselves after each cavity round trip. It is valid both for doubly resonant and singly resonant OPOs. For a small gain coefficient g , we can write $\cosh(gL) \approx 1 + \frac{1}{2}g^2 L^2$. Further, to calculate the SRO threshold, we assume low losses for the signal frequency ($l_1 \ll 1$) and no feedback at the idler frequency ($l_2 = 1$). The threshold condition then is

$$(gL)_{\text{th}}^2 = 2l_1 = 2(1 - R_s e^{-\alpha_s L}). \quad (3.13)$$

From the above, we can directly derive a formula for the pump power at threshold [110]:

$$P_{\text{p, th}} = \{\text{beam area}\} \times \frac{\epsilon_0 n_i n_s n_p c \lambda_p^2}{\pi^2 d_{\text{eff}}^2 L^2 (1 - \delta^2)} (1 - R_s e^{-\alpha_s L}). \quad (3.14)$$

The parameter δ ($0 \leq \delta \leq 1$) is the degeneracy factor [110] determined by

$$\omega_s = \frac{1}{2}\omega_p(1 + \delta), \quad (3.15)$$

$$\omega_i = \frac{1}{2}\omega_p(1 - \delta). \quad (3.16)$$

It indicates the distance of ω_s and ω_i from the point of degeneracy $\omega_s = \omega_i = \frac{1}{2}\omega_p$. The threshold pump power has a minimum for $\delta = 0$ and increases as δ gets larger.

Equation (3.14) was derived in the plane wave approximation. In real OPO devices, the pump beam is focused into the crystal because the parametric gain scales with the pump intensity. In this situation, the interacting light fields must be treated as Gaussian beams and (3.14) has to be modified. For focused Gaussian beams, the threshold pump power is given by [110]

$$P_{\text{p, th}} = \frac{\epsilon_0 n_i n_s c \lambda_p^3}{\pi^2 d_{\text{eff}}^2 L (1 - \delta^2) \bar{h}_m(B, \xi)} (1 - R_s e^{-\alpha_s L}). \quad (3.17)$$

The function $\bar{h}_m(B, \xi)$ is the gain reduction factor according to Boyd and Kleinman [114] (see Fig. 3.5). It is discussed in the next section.

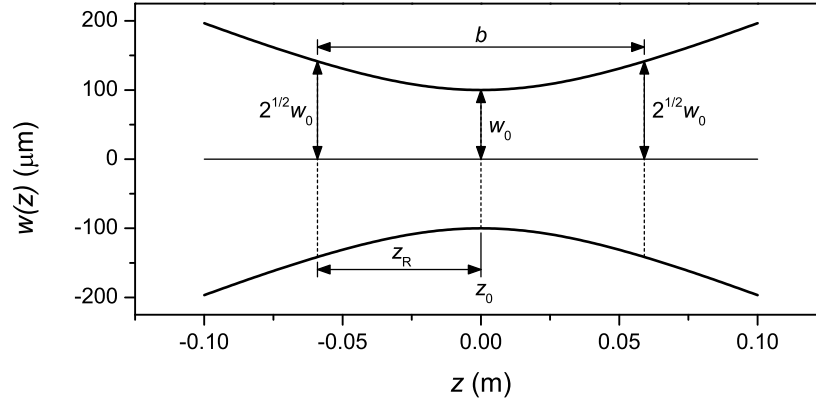


Figure 3.4: Gaussian beam. In the shown example we have assumed $\lambda = 532 \text{ nm}$ and $w_0 = 100 \mu\text{m}$.

Criteria for SRO Cavity Design

A paraxial wave equation can be derived from (2.10) for each of the frequency components ω_p , ω_s , ω_i [61]. Thus, the theory of Gaussian beams that has been developed for lasers [115] can also be applied to OPOs. Figure 3.4 shows the $1/e^2$ beam radius $w(z)$ of a Gaussian beam as a function of the distance z from the focus at $z = z_0$. The plots shown in Fig. 3.4 are given by

$$w(z) = \pm w_0 \sqrt{1 + \left(\frac{z}{z_R}\right)^2}, \quad (3.18)$$

$$\text{with } z_R = \frac{\pi w_0^2}{\lambda}. \quad (3.19)$$

In (3.18) z_R denotes the Rayleigh range, λ is the wavelength and w_0 is the beam waist at $z = z_0$. The Rayleigh range z_R is defined by the property $w(\pm z_R) = \sqrt{2}w_0$. Also shown in Fig. 3.4 is the confocal parameter $b = 2z_R$. For parametric interactions in bulk crystals, Boyd and Kleinman have shown that maximum conversion efficiency is achieved when the function $\bar{h}_m(B, \xi)$ is maximized [114]. This function must be calculated numerically, where $\xi \equiv L/b_p$ ($L =$ crystal length) is the pump focusing parameter and B accounts for double refraction ($B = 0$ for our purposes). Figure 3.5 shows a plot of the function $\bar{h}_m(B = 0, \xi)$. This function is maximized for $\xi = 2.84$ with $\bar{h}_m(0, 2.84) \approx 1$.

In order to find a (theoretically) ideal SRO cavity design, one might use the following guidelines: for a given crystal length L the pump focusing optics are chosen such that $b_p \approx L/2.84$. As seen from Fig. 3.5, the graph of $\bar{h}_m(0, \xi)$ is relatively flat around the maximum. Therefore, deviations from the ideal value can be tolerated to some extent. Once b_p is chosen, the pump beam waist w_{0p} is fixed, too, because of (3.19). The cavity design is calculated such that the resonator is stable and at the same time provides a

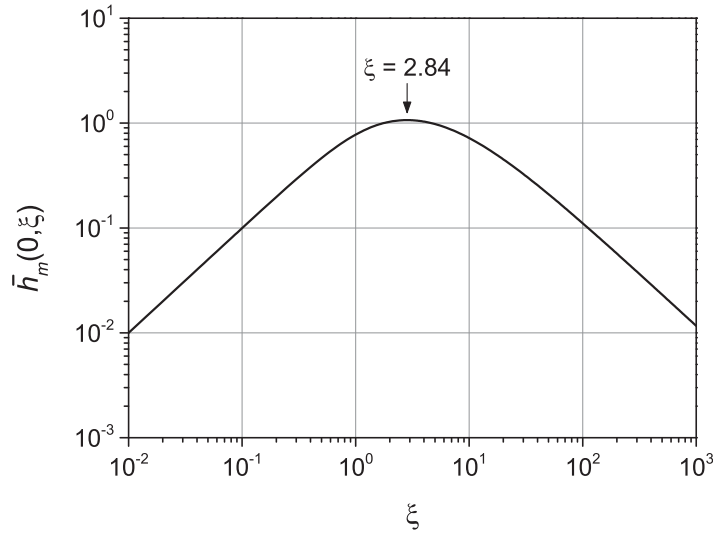


Figure 3.5: Gain reduction factor $\bar{h}_m(0, \xi)$ according to Boyd and Kleinman [114].

confocal parameter $b_s = b_p$ for the signal wave. In this way, maximum mode overlap of the pump beam and the resonant signal field is ensured.

Wavelength Tuning of QPM-Based OPOs

Controlled wavelength tuning is a prerequisite for applications of OPOs in spectroscopy (see Sect. 4.1.4) or frequency mixing experiments (see Chap. 5 and 6). A number of possibilities exist to adjust the signal and idler wavelengths of a QPM-based OPO. First of all, according to (2.32), the set of wavelengths $\{\lambda_p, \lambda_s, \lambda_i\}$ that can be phase-matched in an OPO process is determined by the grating period Λ of the QPM crystal. It is common to use crystals with multiple gratings to extend the spectral range that is accessible with a single crystal. To generate a desired signal/idler wavelength pair, one has to choose the proper grating period within the crystal. However, this does allow only for a very coarse wavelength selection. Further optimization of the crystal temperature is necessary to tune the output wavelengths in finer steps. The effect of temperature tuning is understood from relation (2.32): the refractive indices $n(\lambda, T)$ in (2.32) are temperature dependent and thus tuning the crystal temperature alters the phasematching condition and causes a wavelength shift of the signal and idler wavelength. As an example, Fig. 3.6 shows wavelength tuning curves as a function of crystal temperature for different grating periods in a MgO:PPLN crystal. Apparently, wavelength tuning via the crystal temperature in combination with multiple QPM gratings allows to cover a large spectral range. The maximum precision of temperature tuning, however, is also limited since the temperature is an experimental parameter that cannot be controlled with perfect accuracy (typically $\pm 0.01^\circ\text{C}$).

Another method of wavelength tuning can be applied when the pump laser is wavelength-

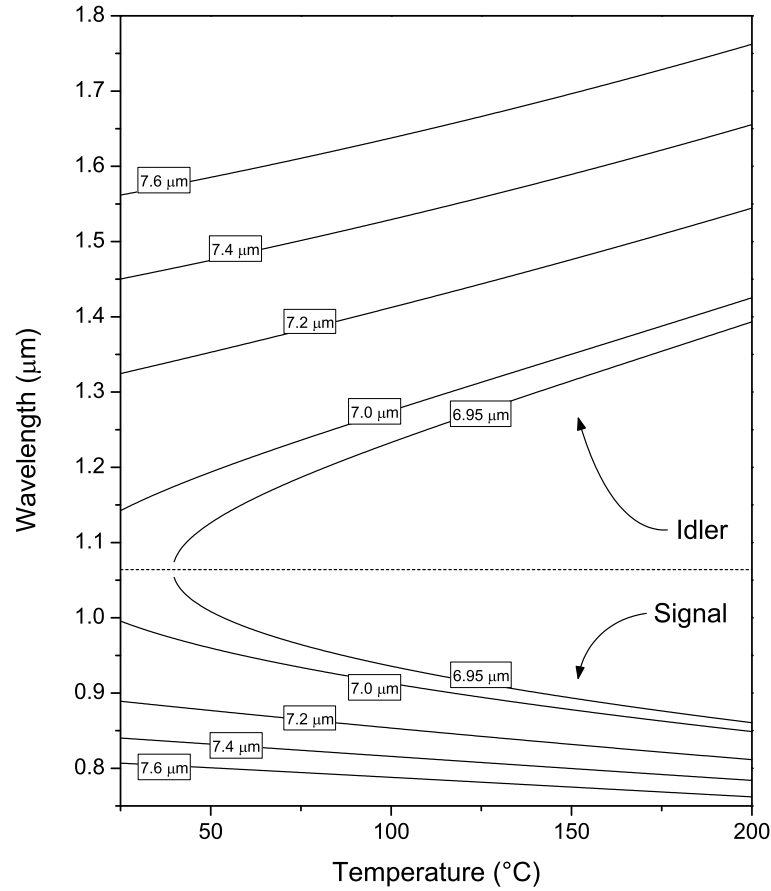


Figure 3.6: Example of OPO wavelength tuning curves as a function of crystal temperature for different QPM grating periods $\Lambda = \{6.95, 7.0, 7.2, 7.4, 7.6\} \mu\text{m}$ in MgO:PPLN. The plots were calculated for a pump wavelength of $0.532 \mu\text{m}$ with Sellmeier coefficients from [105]. The dashed line marks the point of degeneracy at $2\lambda_p = 1.064 \mu\text{m}$ which separates the branches of signal and idler tuning curves.

tunable. In this case, all other parameters in (2.32) are held constant while the wavelength of the pump laser is varied. This technique enables precise wavelength control and rapid wavelength sweeps [116].

If the pump laser is not wavelength tunable, reaching higher levels of precision requires either the possibility to scan the cavity length in a controllable manner or a frequency-selective intracavity element (such as an etalon or a diffraction grating). Scanning the cavity length can be done, e.g., by use of a piezo cavity mirror. A small relative change dL/L of the effective cavity length results in a relative frequency change of $-d\nu/\nu$. The effect of an intracavity etalon is explained in Fig. 3.7 by a typical example. In the simplest case, the etalon is a thin glass plate acting as a low-finesse Fabry–Pérot resonator. Figure 3.7(a) depicts the etalon fringes and the parametric gain profile in the nonlinear

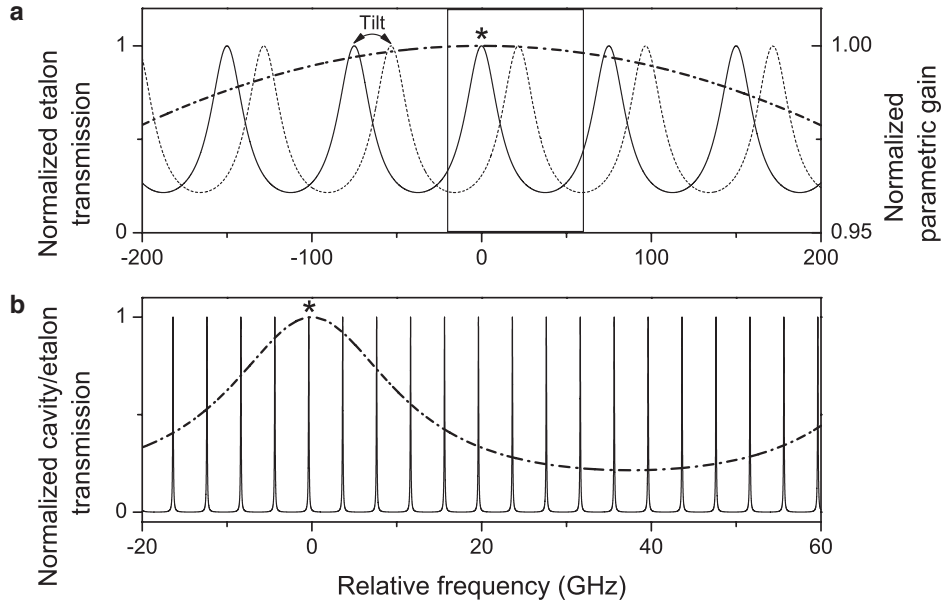


Figure 3.7: Effect of an OPO intracavity etalon. (a) Comparison of the normalized parametric gain profile (dash-dotted line) generated in the nonlinear crystal with the normalized transmission peaks of a low-finesse intracavity etalon (solid and dotted lines). The maximum of the parametric gain is chosen as the zero point of the frequency axis. The position of the etalon transmission maxima can be adjusted by tilting the etalon by a small angle. The etalon peak closest to the parametric gain maximum is marked by an asterisk. (b) Magnification of the part framed by the box in (a). The net gain (dash-dotted line) is shown together with the cavity modes of the OPO resonator (solid line). The OPO will run on the mode closest to the maximum of the net gain (marked by the asterisk). The width of the parametric gain as well as the etalon and cavity transmission fringes reflect the situation in typical experiments.

material. The etalon introduces wavelength-dependent losses in the cavity and thus modulates the net gain profile (parametric gain \times etalon transmission). By tilting the etalon, the transmission fringes and thus the maximum of the net gain can be shifted. Figure 3.7(b) depicts an enlarged view showing the maximum of the net gain and the OPO cavity modes. Similar to a laser, the OPO will oscillate on the cavity mode that experiences the highest net gain.

A more detailed survey of wavelength tuning properties of OPOs can be found in [116, 117].

3.2.3 Waveguide-Based Quasi-Phasematched Frequency Converters

Dielectric Waveguides with Rectangular Cross Section

In Sect. 2.1.2 we have introduced the coupled mode equations (2.13)–(2.15) assuming an interaction of plane waves in a nonlinear dielectric. One possibility of enhancing the efficiency of nonlinear processes is to apply resonant feedback as in an OPO resonator.

Another method is to use an optical waveguide (WG), i.e., a geometric structure that confines the light fields within a small spatial volume in two dimensions. This can be understood from the fact that $|A_m(z)|^2$ is proportional to the field intensities. For a given power, the intensity increases if the mode volume becomes smaller.

Optical fibers made of SiO_2 are perhaps the most prominent examples of optical WGs. They were actually not developed for nonlinear processes. However, nonlinear effects can be observed in these fibers as well (mostly $\chi^{(3)}$ interactions). In this thesis, we use WGs made of Zn:PPLN with a rectangular cross section. Zn:PPLN was chosen as a material because of its high nonlinear coefficient d_{33} (see Sect. 3.1) and its immunity against photorefractive damage even at visible wavelengths and at room temperature [118]. To derive the theoretical framework for understanding the propagation of light modes in a rectangular WG, we consider the situation illustrated in Fig. 3.8. The figure shows the most general case where the refractive indices for the WG core itself and for the surrounding media on all four sides of the WG can be different (while n_1 is the highest of all indices). It is not possible to find an analytic solution of Maxwell's equations for such a system. However, numerical solutions with high accuracy can be performed [119]. Here we alternatively follow the approach discussed in the book by Marcuse [120] and present an analytic approximation. The concept was originally developed by Marcatili [121] and the approximation is valid as long as the frequencies of the WG modes are far from the cut-off frequency. The cut-off frequency is the lowest frequency for which a mode can propagate through the WG. In general, two types of modes can be excited in the WG sketched in Fig. 3.8. In [120] they are termed E_{pq}^x and E_{pq}^y modes ($p, q = 0, 1, 2, \dots$). E_{pq}^x modes are polarized predominantly in the x direction while E_{pq}^y modes are mostly polarized in the y direction. One can think of these modes as 'quasi TM' and 'quasi TE' modes [122] although, in a strict sense, such modes do only exist in two very specific types of WGs (planar slab WGs and fibers with circular symmetry) [123]. Pure TM modes are characterized by $E_x, H_y, E_z \neq 0$ while all other components of the electric and magnetic field vanish. Pure TE modes have $E_y, H_x, H_z \neq 0$ and all other components vanish [120, 123]. Maxwell's equations for the \mathbf{E} and \mathbf{H} fields in regions 1–5 are given by [120]

$$E_x = -\frac{i}{K_j^2} \left[\beta \frac{\partial E_z}{\partial x} + \omega \mu_0 \frac{\partial H_z}{\partial y} \right], \quad (3.20)$$

$$E_y = -\frac{i}{K_j^2} \left[\beta \frac{\partial E_z}{\partial y} - \omega \mu_0 \frac{\partial H_z}{\partial x} \right], \quad (3.21)$$

$$H_x = -\frac{i}{K_j^2} \left[\beta \frac{\partial H_z}{\partial x} - \omega n_j^2 \epsilon_0 \frac{\partial E_z}{\partial y} \right], \quad (3.22)$$

$$H_y = -\frac{i}{K_j^2} \left[\beta \frac{\partial H_z}{\partial y} + \omega n_j^2 \epsilon_0 \frac{\partial E_z}{\partial x} \right], \quad (3.23)$$

with $K_j = \sqrt{n_j^2 k^2 - \beta^2}$. The n_j ($j = 1, \dots, 5$) are the refractive indices in regions 1–5. The propagation constant β is an effective wavenumber for a mode propagating

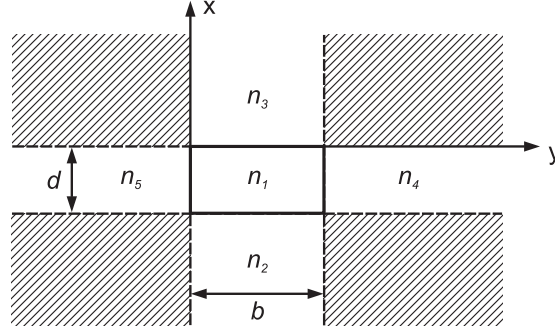


Figure 3.8: Geometry that is considered to calculate the electromagnetic field distribution in a dielectric WG with rectangular cross section $d \times b$ (after [120]). The direction of light propagation in the WG is parallel to the z axis, i.e., perpendicular to the drawing plane. The WG core material has refractive index n_1 and is surrounded on four sides by regions with refractive indices n_2, n_3, n_4 , and n_5 . In general, these indices are allowed to be different in the model. The hatched regions are ignored to enable an analytic solution of the problem.

in the WG while $k = \omega\sqrt{\epsilon_0\mu_0} = 2\pi/\lambda$ is the wavenumber in free space ($\lambda =$ vacuum wavelength). The effective index n_{eff} of the mode is defined by $n_{\text{eff}} = \beta/k$ [123]. The time and z dependence for all fields is given by the factor $\exp[i(\omega t - \beta z)]$ and is omitted in the equations (3.20)–(3.23). In Marcatili’s approximation, the solutions $\mathbf{E}(x, y)$ and $\mathbf{H}(x, y)$ to Eqs. (3.20)–(3.23) are composed of piecewise functions that are defined for each of the five regions in Fig. 3.8. For instance, the solution that describes an E_{pq}^x mode in region 1 ($-d < x < 0, 0 < y < b$), i.e., inside the core of the WG is given by

$$E_z = A \cos \kappa_x(x + \xi) \cos \kappa_y(y + \eta), \quad (3.24)$$

$$H_z = -A \sqrt{\frac{\epsilon_0}{\mu_0}} n_1^2 \frac{\kappa_y}{\kappa_x} \frac{k}{\beta} \sin \kappa_x(x + \xi) \sin \kappa_y(y + \eta), \quad (3.25)$$

$$E_x = \frac{iA}{\kappa_x \beta} (n_1^2 k^2 - \kappa_x^2) \sin \kappa_x(x + \xi) \cos \kappa_y(y + \eta), \quad (3.26)$$

$$E_y = -iA \frac{\kappa_y}{\beta} \cos \kappa_x(x + \xi) \sin \kappa_y(y + \eta), \quad (3.27)$$

$$H_x = 0, \quad (3.28)$$

$$H_y = iA \sqrt{\frac{\epsilon_0}{\mu_0}} n_1^2 \frac{k}{\kappa_x} \sin \kappa_x(x + \xi) \cos \kappa_y(y + \eta). \quad (3.29)$$

Solutions for regions 2–5 are given in App. B. We here only concentrate on E_{pq}^x modes because this class of modes is of particular importance for the experiments presented in Chap. 5 and 6. For E_{pq}^y modes the reader is referred to [120]. Numeric values for the quantities $\kappa_x, \kappa_y, \xi, \eta, \beta$ must be calculated in order to use Eqs. (3.24)–(3.29) and the other four sets of functions (regions 2–5) for practical purposes. The parameters $\kappa_x, \kappa_y, \xi, \eta, \beta$ are completely determined by the refractive indices of the five regions and the height d and width b of the WG. Using the definitions for $\gamma_2, \gamma_3, \gamma_4$, and γ_5 given

in Table 3.2, κ_x and κ_y are obtained by numerically solving the eigenvalue equations

$$\tan \kappa_x d = n_1^2 \kappa_x \frac{n_3^2 \gamma_2 + n_2^2 \gamma_3}{n_3^2 n_2^2 \kappa_x^2 - n_1^4 \gamma_2 \gamma_3} \quad (3.30)$$

and

$$\tan \kappa_y b = \frac{\kappa_y (\gamma_4 + \gamma_5)}{\kappa_y^2 - \gamma_4 \gamma_5}, \quad (3.31)$$

respectively. In general, Eqs. (3.30) and (3.31) possess multiple solutions and each

Table 3.2: Definition of the parameters $\gamma_2, \dots, \gamma_5$.

Parameter	Definition
γ_2	$[(n_1^2 - n_2^2) k^2 - \kappa_x^2]^{1/2}$
γ_3	$[(n_1^2 - n_3^2) k^2 - \kappa_x^2]^{1/2}$
γ_4	$[(n_1^2 - n_4^2) k^2 - \kappa_y^2]^{1/2}$
γ_5	$[(n_1^2 - n_5^2) k^2 - \kappa_y^2]^{1/2}$

solution corresponds to a different set of mode numbers pq . Once κ_x and κ_y are known, we can calculate the parameters ξ and η using the relations

$$\tan \kappa_x \xi = -\frac{n_3^2 \kappa_x}{n_1^2 \gamma_3}, \quad (3.32)$$

$$\tan \kappa_y \eta = -\gamma_5 / \kappa_y. \quad (3.33)$$

$$(3.34)$$

We also obtain the propagation constant of a specific mode from

$$\beta = \sqrt{n_1^2 k^2 - (\kappa_x^2 + \kappa_y^2)}. \quad (3.35)$$

The power that is transmitted through the WG is calculated by integrating the normal component of the energy flux density $\mathbf{S} \cdot \mathbf{n} = \mathbf{S} \cdot \hat{\mathbf{z}} = S_z$ (\mathbf{n} and $\hat{\mathbf{z}}$ are unit vectors) over the xy plane

$$P = \iint \mathbf{S} \cdot \hat{\mathbf{z}} \, dx dy = \iint S_z \, dx dy, \quad (3.36)$$

where

$$\mathbf{S} = \frac{1}{2} \text{Re}(\mathbf{E} \times \mathbf{H}^*) \quad (3.37)$$

is the time averaged Poynting vector. Figures 3.9(b)–(f) show some concrete examples of intensity distributions in the xy plane for several WG modes. To calculate these density plots, we have considered the special case of a WG core made of LN bonded onto a LT substrate on one side and surrounded by air on the other three sides ($n_3 = n_4 = n_5 = 1$).

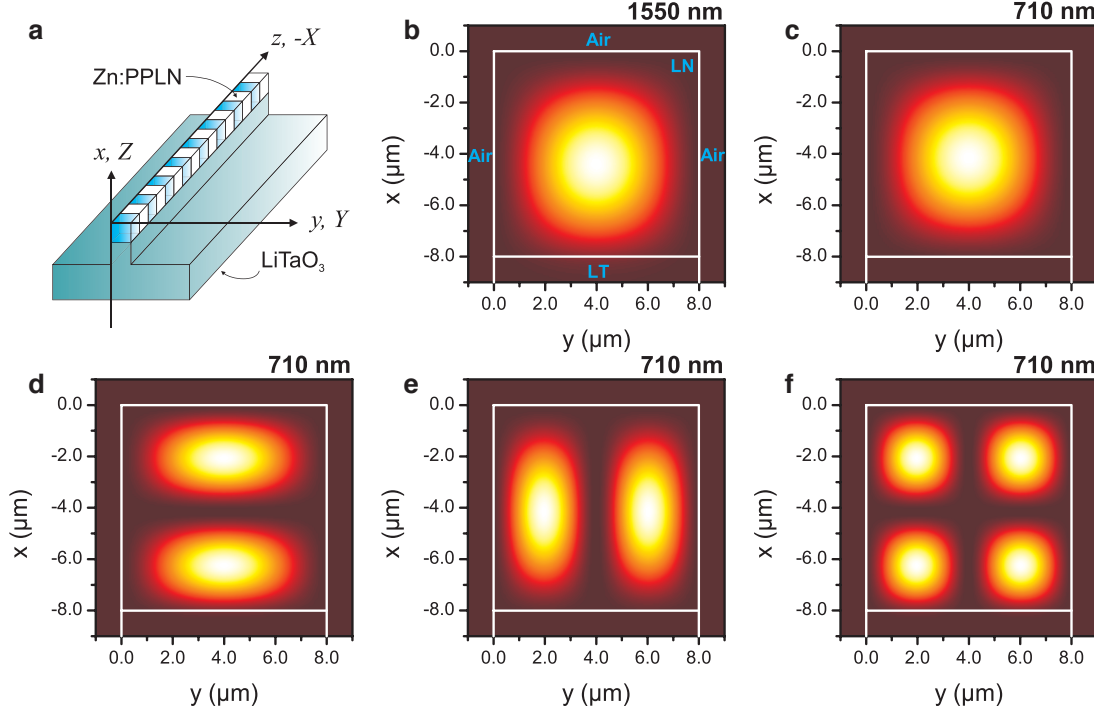


Figure 3.9: (a) Schematic of the WG. The periodic poling indicated in the drawing has no influence on the WG modes but is important for later considerations. (b)–(f) Intensity distribution (normal component S_z of the Poynting vector) for different WG modes in a LN-on-LT WG with $d \times b = 8 \times 8 \mu\text{m}^2$ cross section. (b) E_{00}^x mode for $\lambda = 1550 \text{ nm}$. (c) E_{00}^x mode, (d) E_{10}^x mode, (e) E_{01}^x mode, and (f) E_{11}^x mode (all at $\lambda = 710 \text{ nm}$). Bright areas correspond to high intensity. Refractive indices: $n_1(1550 \text{ nm}) = 2.1374$, $n_1(710 \text{ nm}) = 2.1873$, $n_2(1550 \text{ nm}) = 2.1169$, and $n_2(710 \text{ nm}) = 2.1612$.

This type of WG is used for the experiments described in this thesis (see Fig. 3.9(a) for a schematic). The refractive indices of LN and LT can be calculated for a given wavelength and temperature using published Sellmeier equations (see App. A). For the plots in Fig. 3.9, we have assumed a WG with a quadratic cross section of $d \times b = 8 \times 8 \mu\text{m}^2$. Figures 3.10(a) and (b) show cuts $S_z(x, y = b/2)$ and $S_z(x = d/2, y)$ through the centers of the E_{00}^x mode profiles for three different wavelengths 710 nm, 1310 nm, and 1550 nm. All three mode profiles have been normalized so that the integrated intensity (3.36) equals unity. Apparently, the modes are strongly confined inside the WG core, i.e., the largest fraction of the power is concentrated in the core ($> 99\%$ for all three modes). Thus, for most calculations, using only the solution for region 1 and neglecting the solutions for regions 2–5 will only introduce a small error. The asymmetry of the refractive index distribution in the x direction leads to an asymmetric intensity distribution, as seen from Fig. 3.10(a). The center of mass of the distribution is slightly shifted toward the LT substrate and the integrated intensity in region 2 (LT) is higher

than in region 3 (air). This effect is stronger for longer wavelengths and/or smaller index contrasts $\Delta n = n_1 - n_2$. Owing to the symmetric index distribution in y direction, the center of mass of the intensity distribution is not shifted and coincides with $y = b/2$ for all three wavelengths. We shall see in the next section how spatial mode overlap in the WG and nonlinear mode coupling are related.

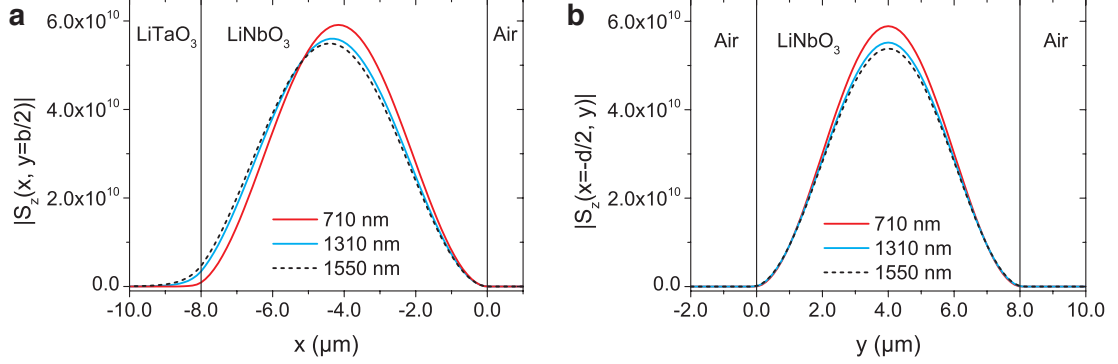


Figure 3.10: Cuts through the E_{00}^x mode profiles for three different wavelengths 710 nm, 1310 nm, and 1550 nm. (a) $S_z(x, y = b/2)$ parallel to the x axis. The center of mass of the intensity distribution is slightly shifted toward the LT substrate due to the asymmetric index distribution (LT-LN-air). (b) $S_z(x = d/2, y)$ parallel to the y axis. Here no spatial shift occurs because of the symmetric index distribution (air-LN-air).

DFG in Ridge Waveguides—Classical Treatment

In Sect. 2.1.2 we have seen how a second-order optical nonlinearity leads to a coupling of different frequency components resulting in three-wave frequency mixing. In the preceding section, we discussed the electromagnetic field modes that can be excited inside a rectangular dielectric WG. We now study DFG in ridge WGs made of LN. To this end, we consider three electric field modes

$$\mathbf{E}_m(\mathbf{r}, t) = A_m(z) \mathcal{E}_m(x, y) e^{i(\omega_m t - \beta_m z)} + c.c. \quad (m = 1, 2, 3) \quad (3.38)$$

at frequencies ω_1 , ω_2 , and ω_3 propagating in the WG. The field amplitudes are represented as a product of a scalar function $A_m(z)$ and a vector field $\mathcal{E}_m(x, y)$. $A_m(z)$ only depends on z and describes the evolution of power at ω_m along the WG (z is the propagation direction). For convenience, the dimension of $A_m(z)$ is chosen such that the power in [W] is given by $P_m = |A_m(z)|^2$ [66]. The normalized transverse intensity distribution is described by $\mathcal{E}_m(x, y)$ and depends only on x and y . For a rectangular WG, $\mathcal{E}_m(x, y)$ is obtained from Marcatili's approximation $\mathbf{E}_m(x, y)$, introduced in Sect. 3.2.3, by multiplication with a normalization factor C_m :

$$\mathcal{E}_m(x, y) = C_m \mathbf{E}_m(x, y), \quad (3.39)$$

with

$$C_m = \left[\frac{1}{2} \iint \operatorname{Re}(\mathbf{E}_m \times \mathbf{H}_m^*) \cdot \hat{\mathbf{z}} \, dx dy \right]^{-1/2}. \quad (3.40)$$

With the above definitions, the coupled mode equations governing three-wave mixing in WGs are given by [66]

$$\frac{\partial A_1}{\partial z} = -\alpha_1 A_1 - i\kappa_1 A_2^* A_3 e^{-i\Delta\beta z}, \quad (3.41)$$

$$\frac{\partial A_2}{\partial z} = -\alpha_2 A_2 - i\kappa_2 A_1^* A_3 e^{-i\Delta\beta z}, \quad (3.42)$$

$$\frac{\partial A_3}{\partial z} = -\alpha_3 A_3 - i\kappa_3 A_1 A_2 e^{+i\Delta\beta z}. \quad (3.43)$$

These equations are very similar to the relations (2.13)–(2.15) for the interaction of plane waves. However, note that three important changes were made. The $-\alpha_m A_m$ terms on the right hand side of each equation were added to account for WG attenuation. The wavevector mismatch Δk was replaced by $\Delta\beta$ since we are dealing with wave propagation in a WG now. Most importantly, the coupling constants κ_1 , κ_2 , κ_3 are different from those in (2.13)–(2.15). They depend on integrals describing the spatial overlap of the three interacting modes and are defined by

$$\kappa_1 = \frac{\omega_1 \epsilon_0}{2} \iint \boldsymbol{\mathcal{E}}_1^*(x, y) \, \mathbf{d}_Q \boldsymbol{\mathcal{E}}_3(x, y) \boldsymbol{\mathcal{E}}_2^*(x, y) \, dx dy, \quad (3.44)$$

$$\kappa_2 = \frac{\omega_2 \epsilon_0}{2} \iint \boldsymbol{\mathcal{E}}_2^*(x, y) \, \mathbf{d}_Q \boldsymbol{\mathcal{E}}_3(x, y) \boldsymbol{\mathcal{E}}_1^*(x, y) \, dx dy, \quad (3.45)$$

$$\kappa_3 = \frac{\omega_3 \epsilon_0}{2} \iint \boldsymbol{\mathcal{E}}_3^*(x, y) \, \mathbf{d}_Q \boldsymbol{\mathcal{E}}_2(x, y) \boldsymbol{\mathcal{E}}_1(x, y) \, dx dy. \quad (3.46)$$

The coupling constants κ_1 , κ_2 , κ_3 obey the relation [66]

$$\kappa_1/\omega_1 = \kappa_2/\omega_2 = \kappa_3^*/\omega_3 \equiv \kappa. \quad (3.47)$$

The integrals (3.44)–(3.46) are simplified for the interesting case of QPM in LN when we assume that only the three fundamental WG modes ($pq = 00$) interact. For example, Eq. (3.44) then becomes

$$\kappa_1 = \frac{\omega_1 \epsilon_0 d_Q}{2} \iint \mathcal{E}_{1x}^*(x, y) \mathcal{E}_{3x}(x, y) \mathcal{E}_{2x}^*(x, y) \, dx dy \quad (3.48)$$

$$= \frac{\omega_1 \epsilon_0 d_Q}{2} \underbrace{C_1 C_2 C_3 \iint E_{1x}^*(x, y) E_{3x}(x, y) E_{2x}^*(x, y) \, dx dy}_{=: \mathcal{J}_1}, \quad (3.49)$$

where use has been made of (3.39) for the second equation. Analog expressions apply for κ_2 and κ_3 .

To investigate the influence of various parameters on the performance of a WG-based

frequency converter like the one sketched in Fig. 3.9(a), we numerically solve (3.41)–(3.43) for different conditions. In later experiments, we study single-photon down-conversion via DFG. We thus assume that a weak input signal at $\omega_a = 2\pi c/\lambda_a$ and a strong pump field at $\omega_p = 2\pi c/\lambda_p$ are inserted into the WG to generate a third field at $\omega_b = \omega_a - \omega_p$. At this point, we change our notation introduced in the context of OPA/OPO. We will now use the assignment $3 \rightarrow a$, $1 \rightarrow p$ (b), $2 \rightarrow b$ (p). In this notation, ω_a and ω_p are always the angular frequencies of the fields which are inserted into the WG. Both cases, $\omega_b < \omega_p$ and $\omega_b > \omega_p$, are possible. For the solution of the coupled mode equations plotted in Fig. 3.11(a), we have set $\lambda_a = 710$ nm, $\lambda_b = 1310$ nm, and $\lambda_p = 1550$ nm with initial conditions $P_a(0) = |A_a(0)|^2 = 1$ nW, $P_b(0) = |A_b(0)|^2 = 0$, $P_p(0) = |A_p(0)|^2 = 50$ mW or 150 mW. The coupling constants κ_m have been calculated using equation (3.49) and analog expressions for κ_2 and κ_3 . With the assumed set of wavelengths, we find $|\mathcal{J}_m| \approx 0.112 \times 10^{10} \frac{1}{\text{m}} \left(\frac{\text{V}}{\text{\AA}}\right)^{3/2}$ for the overlap integrals of the three fundamental modes in the LN WG with $8 \times 8 \mu\text{m}^2$ cross section. From Fig. 3.11(a), we recognize that the input photons at 710 nm are depleted while propagating through the nonlinear WG and photons at 1310 nm are generated. At a certain position in the crystal ($z = 45.7$ mm for $P_p = 50$ mW and $z = 26.4$ mm for $P_p = 150$ mW in Fig. 3.11(a)), all power has been transferred from the ω_a mode to the ω_b mode. This point is reached at shorter interaction lengths the higher the pump power P_p is. Beyond this point, back-conversion takes place which means that the ω_b mode interacts with the strong ω_p mode via SFG to generate photons at ω_a again. In the absence of any transmission losses, these processes repeat themselves and power is mutually exchanged between modes at ω_a and ω_b . Because the power P_p of the pump field is much stronger than P_a and P_b , it is practically unaffected by these processes and remains constant for all positions z . As it is our goal to completely convert visible photons to telecom photons, it is sufficient to choose a WG length which allows for a quarter cycle of the oscillation shown in Fig. 3.11(a). The actual length of the WG chips employed in the experiments is 40 mm.

Next, we study the effect of WG attenuation (or transmission losses) which cannot be avoided in practice. To this end, we solve the system (3.41)–(3.43) for pump power values from 0–500 mW and calculate the photon-to-photon conversion efficiency $\eta = \lambda_b P_b / (\lambda_a P_a)$ at the output $z = L$ of the WG. With $L = 40$ mm fixed, we obtain the curves plotted in Fig. 3.11(b) for different attenuation coefficients α (0, 0.05, 0.1, 0.2 dB/cm). At this point, it is important to mention the relation between the amplitude loss coefficient $\alpha_{[1/\text{m}]}$ with dimension [1/m] which is used in (3.41)–(3.43) and the power loss coefficient $\alpha_{[\text{dB}/\text{cm}]}$ with dimension [dB/cm]. From

$$P(z) = |A(z)|^2 = |A(0)|^2 e^{-2\alpha_{[1/\text{m}]}z}, \quad (3.50)$$

$$P(z) = P(0) 10^{-\alpha_{[\text{dB}/\text{cm}]}z/10} \quad (3.51)$$

it follows that

$$\alpha_{[1/\text{m}]} = \frac{100}{20 \log_{10}(e)} \alpha_{[\text{dB}/\text{cm}]} \approx 11.513 \alpha_{[\text{dB}/\text{cm}]} \quad (3.52)$$

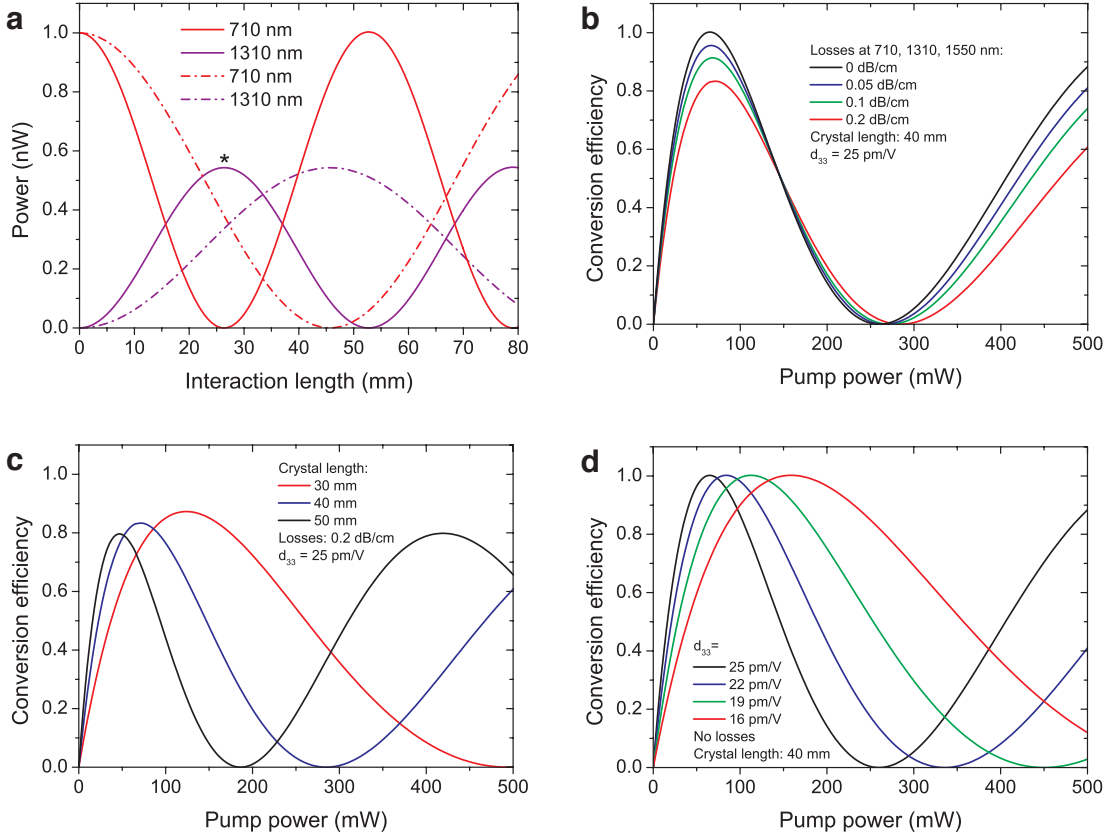


Figure 3.11: Solution of the coupled mode equations (3.41)–(3.43) under different conditions. (a) Evolution of power at $\lambda_a = 710$ nm and $\lambda_b = 1310$ nm along the propagation direction in the WG (no transmission losses). The pump power at $\lambda_p = 1550$ nm is assumed to be 50 mW (dash-dotted lines) or 150 mW (solid lines). The point marked with an asterisk at $L = 26.4$ mm corresponds to the first full conversion for $P_p = 150$ mW. (b), (c), (d) Conversion efficiency as a function of pump power for (b) different WG transmission losses (fixed interaction length and d_{33}), (c) different interaction lengths (fixed transmission losses and d_{33}), and (d) different nonlinear coefficients d_{33} (no transmission losses, fixed interaction length).

It is apparent from Fig. 3.11(b) that the pump power needed to achieve maximum conversion efficiency depends only little on α but the maximum conversion efficiency decreases for increasing losses. Theoretically, the effect of losses can be alleviated by choosing a shorter WG and increasing the pump power as illustrated in Fig. 3.11(c). However, in practice this is not always desirable because higher pump powers can favor other detrimental processes such as Raman scattering (see Sect. 5.2.2). We finish our discussion on DFG in nonlinear WG devices by studying the conversion efficiency for varying coupling constants κ_m . The κ_m depend on two quantities, d_Q and J_m , which are often not exactly known in practical cases. The tensor element d_{33} (and thus d_Q) depends on the wavelength and the values that can be found in the literature differ

depending on the reference (see Table 3.1). The calculation of the overlap integrals J_m can also be difficult if higher-order spatial modes are involved because then the total power at one frequency is distributed over different spatial modes and one has to know the fraction of power carried by each mode. For simplicity, we here only examine the influence of different nonlinear coefficients d_{33} . In practice, it is anyway difficult to decide whether a reduced conversion efficiency is due to a reduced d_{eff} or a suboptimal mode overlap. As a reference value, we have taken $d_{33} = 25 \text{ pm/V}$ which can be found in the literature for congruent LN measured using SHG of 1064 nm [95]. Figure 3.11(d) shows what happens for smaller values of d_{33} . As might be expected, the pump power required to yield maximum conversion efficiency at the WG output increases for smaller d_{33} , i.e., smaller coupling constants.

Important conclusions that can be drawn from the discussion of the plots in Fig. 3.11 are the following:

- Theoretically (in the absence of losses), a complete conversion of the visible input field to a telecom field is possible in a LN ridge WG. The required WG length to reach maximum conversion efficiency is on the order of several ten mm if moderate pump powers (100 mW order of magnitude) are applied.
- The maximum conversion efficiency that is achievable is limited by transmission losses at all three modes.
- When transmission losses are high, it might be favorable in some situations to use a shorter WG and higher pump powers.
- For a given interaction length, the pump power required to reach maximum conversion efficiency at the WG output is higher for smaller coupling constants.

The length of the WGs used in the experiments described in Chap. 5 and 6 is 40 mm. We will see that a maximum internal conversion efficiency exceeding 70 % can be achieved for pump powers between 150–250 mW (depending on actual experimental conditions).

Quantum Mechanical Model of DFG

So far, we have investigated frequency down-conversion of a weak input field from ω_a to ω_b with the help of the classical equations (3.41)–(3.43). We now introduce a simple quantum mechanical model based on the effective Hamiltonian [43]

$$\hat{H} = i\hbar\eta\hat{a}\hat{b}^\dagger A_p^* - i\hbar\eta^* A_p \hat{b}\hat{a}^\dagger, \quad (3.53)$$

where \hat{a} , \hat{b} and \hat{a}^\dagger , \hat{b}^\dagger are bosonic annihilation and creation operators, respectively (see Sect. 2.2.1). Since the pump field is assumed to be a strong classical field, it can be described by the complex amplitude A_p instead of an operator \hat{a}_p . The Hamiltonian (3.53) describes the interaction of the three field modes \hat{a} , \hat{b} and A_p coupled by the constant

η . In order to determine the time evolution of the operators \hat{a} and \hat{b} , we follow [34] and use the Heisenberg equation of motion [124]

$$\frac{d\hat{O}}{dt} = \frac{i}{\hbar}[\hat{H}, \hat{O}], \quad (3.54)$$

for an operator \hat{O} in the Heisenberg picture which is not explicitly time dependent. Identifying $\hat{O} = \hat{a}$ and $\hat{O} = \hat{b}$ and inserting (3.53) into (3.54) (see App. B for a detailed derivation) we can write down the equations of motion for the two operators:

$$\frac{d\hat{a}}{dt} = -\eta^* A_p \hat{b}, \quad (3.55)$$

$$\frac{d\hat{b}}{dt} = \eta A_p^* \hat{a}. \quad (3.56)$$

These equations are solved by

$$\hat{a}(\tau) = \hat{a}(0) \cos(|\eta A_p| \tau) - e^{-i\phi_p} \hat{b}(0) \sin(|\eta A_p| \tau), \quad (3.57)$$

$$\hat{b}(\tau) = \hat{b}(0) \cos(|\eta A_p| \tau) + e^{+i\phi_p} \hat{a}(0) \sin(|\eta A_p| \tau), \quad (3.58)$$

where τ denotes the interaction time and $e^{i\phi_p} = \eta A_p^* / |\eta A_p|$. For comparison with classical results, we must use the expectation values of the photon number operators $\hat{n}_a(\tau)$, $\hat{n}_b(\tau)$ which read (see App. B for a detailed derivation)

$$\langle \hat{n}_a(\tau) \rangle = \langle \hat{n}_a(0) \rangle \cos^2(|\eta A_p| \tau) + \langle \hat{n}_b(0) \rangle \sin^2(|\eta A_p| \tau), \quad (3.59)$$

$$\langle \hat{n}_b(\tau) \rangle = \langle \hat{n}_b(0) \rangle \cos^2(|\eta A_p| \tau) + \langle \hat{n}_a(0) \rangle \sin^2(|\eta A_p| \tau). \quad (3.60)$$

The expectation values are plotted as a function of $|\eta A_p| \tau$ in Fig. 3.12. For an interaction time of $\tau_{\text{opt}} = \pi / (2 |\eta A_p|)$, complete frequency conversion is achieved. If the input state is a single-photon Fock state $|n_a(0), n_b(0)\rangle = |1, 0\rangle$, it is converted to the state $|n_a(\tau_{\text{opt}}), n_b(\tau_{\text{opt}})\rangle = |0, 1\rangle$ after the time τ_{opt} corresponding to a complete exchange of populations in photon states, i.e., the frequency is altered while the single-photon state is preserved. To see the analogy of (3.55) and (3.56) with the classical coupled mode equations, we rewrite (3.41)–(3.43) by applying the transformations

$$A_1(z) = \frac{B_1(z)}{\sqrt{\omega_2 \omega_3}}, \quad A_2(z) = \frac{B_2(z)}{\sqrt{\omega_1 \omega_3}}, \quad A_3(z) = \frac{B_3(z)}{\sqrt{\omega_1 \omega_2}} \quad (3.61)$$

to obtain

$$\frac{\partial B_p(z)}{\partial z} = -i\kappa B_b^*(z) B_a(z), \quad (3.62)$$

$$\frac{\partial B_b(z)}{\partial z} = -i\kappa B_p^*(z) B_a(z), \quad (3.63)$$

$$\frac{\partial B_a(z)}{\partial z} = -i\kappa^* B_p(z) B_b(z). \quad (3.64)$$

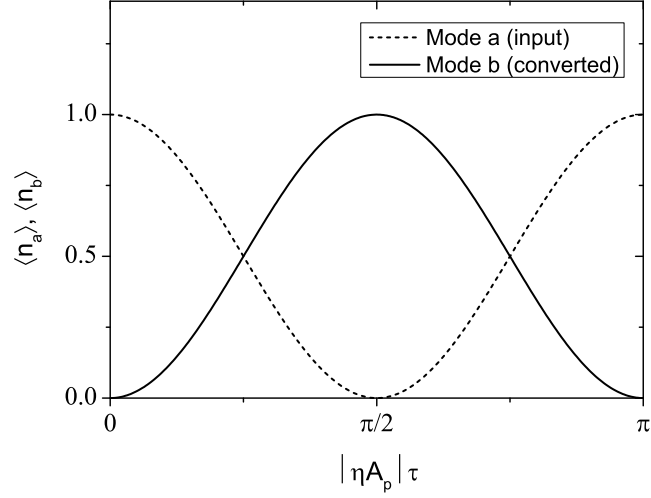


Figure 3.12: Evolution of the expectation values $\langle \hat{n}_a(\tau) \rangle$ and $\langle \hat{n}_b(\tau) \rangle$ when the input is a single-photon Fock state $|n_a, n_b\rangle = |1, 0\rangle$.

In (3.62)–(3.64) we have used the relations (3.47) and the indices 1, 2, 3 were again replaced by p, b, a, respectively. Perfect phasematching ($\Delta\beta = 0$) was assumed and WG attenuation was neglected ($\alpha_m = 0$). With the transformations (3.61), the three coupling constants $\kappa_1, \kappa_2, \kappa_3$ are replaced by the single constant κ . Given that the pump power is much stronger than the power of the other two modes, Eq. (3.62) can be approximated by $\partial B_p / \partial z \approx 0$ and integrated to yield a constant B_p . The remaining equations (3.63) and (3.64) have the same structure as the equations for the operators (3.55), (3.56), where η corresponds to $-i\kappa$. Using Eq. (3.60), we can define the conversion efficiency for a QFC device by

$$\eta_{\text{QFC}} = \frac{\langle \hat{n}_b(\tau) \rangle}{\langle \hat{n}_a(0) \rangle} = \sin^2(|\eta| \sqrt{P_p} \tau). \quad (3.65)$$

Here $|A_p|$ was replaced by $\sqrt{P_p}$ and we have again assumed $|1, 0\rangle$ to be the input state. The classical result is

$$\frac{|B_b(L)|^2}{|B_a(0)|^2} = \frac{P_b(L)}{P_a(0)} \frac{\hbar\omega_a}{\hbar\omega_b} = \sin^2(|\kappa| \sqrt{\omega_a \omega_b} \sqrt{P_p} L). \quad (3.66)$$

By defining the normalized efficiency $\eta_{\text{nor}} \equiv |\kappa|^2 \omega_a \omega_b$ and equating (3.65) and (3.66), we find [39, 125, 126]

$$\eta_{\text{QFC}} = \sin^2(\sqrt{\eta_{\text{nor}} P_p} L). \quad (3.67)$$

A remark on the model of Ou which we have used in the above derivation is necessary here. Although this model is very simple, Eq. (3.67) correctly describes the experimental observations in the case of low WG attenuation and a high signal-to-noise ratio (number of photons intentionally generated by frequency conversion vs. number of photons

generated in unwanted noise processes). Nevertheless, this model is far from giving a complete description of all the effects that possibly occur in WG-based QFC devices since all quantum noise sources are neglected. A refined model that takes into account quantum noise effects such as photon loss, Stokes and anti-Stokes Raman scattering, and pump-induced SPDC was introduced by S. Blum and G. Morigi [127]. Their model is based on Heisenberg–Langevin equations and allows to evaluate the influence of quantum noise on the statistical properties of the frequency-converted photons.

Chapter 4

Green-Pumped Continuous-Wave Optical Parametric Oscillators

Copyright Notice:

The introduction of this chapter, Sect. 4.1, and Sect. 4.3 contain material that was originally published in Ref. [128] (Copyright © Springer-Verlag 2009); with kind permission from Springer Science and Business Media.

The main goal of this thesis is frequency down-conversion of visible light emitted from a single quantum emitter to a telecom wavelength in the O- or C-band. From this objective, certain conditions for an experiment can be derived. The input wavelength λ_{in} ($= \lambda_{\text{a}}$) is determined by the choice of a particular emitter. In this work, we focus on two attractive solid-state systems, namely silicon-vacancy (SiV) centers in diamond ($\lambda_{\text{in}} \approx 738$ nm) and InP QDs ($\lambda_{\text{in}} \approx 710$ nm). The target wavelength λ_{out} ($= \lambda_{\text{b}}$) should lie within the telecom O-band (around 1310 nm) or C-band (around 1550 nm). Unlike the emission spectra of atoms, the wavelength of the emission lines of SiV centers in diamond or semiconductor QDs can vary significantly among individual centers/dots. For example, the zero-phonon lines (optical transition between two electronic energy levels without the involvement of phonons) of the SiV centers investigated in [60] lie in a wavelength range of 732–748 nm and the exciton lines (see Sect. 6.1.1) of the QDs on the sample used in this thesis are between 690 nm and 715 nm. Thus, it is necessary to deploy a widely wavelength-tunable pump source to cover a variety of possible wavelength combinations. Changing the pump source each time another set of wavelengths is investigated would be an alternative. However, we decided to keep the experimental setup as flexible as possible and to use the same pump source in all down-conversion experiments. To evaluate the desired pump tuning range, we may consider the following down-conversion schemes: 738 nm \rightarrow 1310 nm (i), 710 nm \rightarrow 1310 nm (ii), 738 nm \rightarrow 1550 nm (iii), 710 nm \rightarrow 1550 nm (iv). These processes require pump wavelengths at 1690 nm (i), 1550 nm (ii), 1409 nm (iii), and 1310 nm (iv), i.e., the pump source has to cover a spectral range that spans from the telecom O-band to the U-band

and even beyond. Furthermore, from the considerations in Sect. 3.2.3 we know that the required pump source must deliver an output power of several hundred mW to achieve a reasonable conversion efficiency in a realistic scenario. To the current state of the art, there is no laser system which combines all of the requirements mentioned above. Thus, we have chosen an alternative route and have built green-pumped cw OPOs based on QPM as pump sources for the down-conversion process. Such devices have first been demonstrated in 1995 [99] and are now established as versatile tunable coherent sources particularly in the near to mid infrared spectral range [112]. Singly resonant cw OPOs (cw SROs) are of special interest since they allow for higher output powers and feature more convenient tuning properties than doubly resonant OPOs (DROs). The vast majority of the SROs reported to date are pumped with solid-state lasers or fiber lasers emitting above $1\ \mu\text{m}$ [129–132]. Especially the combination of periodically poled LiNbO_3 and infrared pumping has turned out to be a successful concept as it unites the advantages of a high effective nonlinear coefficient ($d_Q = 16\ \text{pm/V}$ [95]) and high-power pump lasers with excellent spectral and spatial properties. This scheme allows for generating light in the wavelength range from about $1.5\ \mu\text{m}$ to $4\ \mu\text{m}$. However, the operation of such devices at even shorter signal, i.e., longer idler wavelengths, is a challenging task as the transparency of LiNbO_3 decreases at wavelengths longer than $4\ \mu\text{m}$ [133, 134]. One possible solution is provided by using a shorter pump wavelength in the visible. This naturally extends the addressable spectral range for LiNbO_3 -based SROs to shorter wavelengths which is desirable in our case. It is also interesting for a number of other applications, e.g., high-resolution spectroscopy [135] or state-insensitive optical cooling and trapping (‘magic wavelengths’) [136]. It seems convenient to use a frequency-doubled DPSS laser emitting at 532 nm as a pump laser. However, the development of green-pumped cw SROs based on undoped PPLN has long been impeded by the effects of photorefractive damage and green-induced infrared absorption (GRIIRA) [137]. Although it has been demonstrated that both effects are eliminated or at least significantly reduced when using MgO-doped PPLN (either 1%-doped stoichiometric LN or 5%-doped congruent LN) [93, 94], the material still seems to have the reputation of being unsuitable for green-pumped OPOs. Thus, in many publications, periodically poled MgO-doped stoichiometric LiTaO_3 (MgO:PPSLT) has been preferred over MgO:PPLN as the nonlinear material for green-pumped cw SROs [138–144]. On the one hand, MgO:PPSLT has a higher optical damage resistance than MgO:PPLN [138]. On the other hand, the effective nonlinear coefficient of MgO:PPSLT is by a factor of ~ 1.6 lower compared to MgO:PPLN. Both materials were tested to find out which of them is better suited for a green-pumped cw SRO. In this chapter we present two similar types of cw SROs: one is based on MgO:PPLN, the other one on MgO:PPSLT. The devices are tested with respect to their applicability as a pump source in QFC experiments. Some interesting applications that go beyond this purpose, such as Doppler-free spectroscopy of cesium, frequency stabilization, and output coupling of the resonant signal wave are presented as well.

4.1 Green-Pumped CW SRO Based on MgO:PPLN

4.1.1 Experimental Setup

The experimental setup of the cw SRO based on MgO:PPLN is depicted in Fig. 4.1. The SRO cavity is a symmetric four-mirror bowtie ring resonator similar to the one

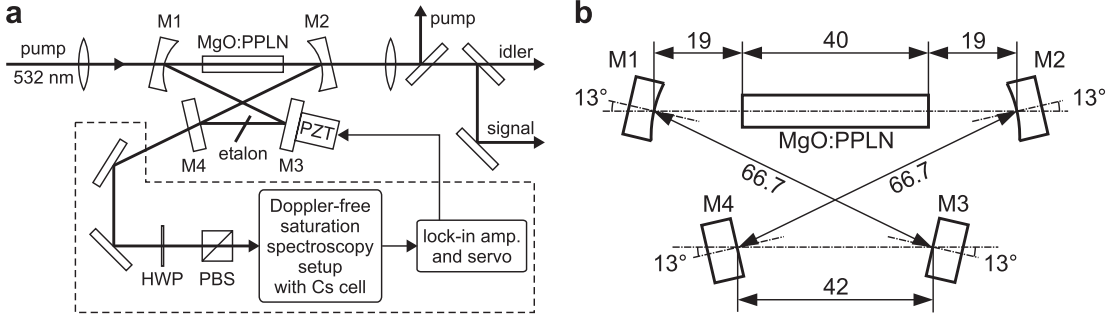


Figure 4.1: (a) Setup of the cw SRO (PZT: piezo actuator, HWP: half-wave plate, PBS: polarizing beamsplitter). The components enclosed by the dashed line are used for optional frequency stabilization. Figure after [128] (© Springer-Verlag 2009); with kind permission from Springer Science and Business Media. (b) Detailed sketch of the cavity design (all dimensions in mm).

used in [145]. It consists of two plano-concave mirrors M1 and M2 (radius of curvature $ROC = 50$ mm) and two plane mirrors M3 and M4. Each mirror is highly reflective at the signal wavelength (reflectivity $R > 99.8\%$ at 800–920 nm) and highly transmissive at the pump ($R < 8\%$ at 532 nm) and idler ($R < 10\%$ at 1250–1580 nm) wavelengths (mirror coatings by *Laseroptik GmbH*). Mirror M3 is mounted on a piezo actuator for scanning and controlling the cavity length. The temperature controlled MgO:PPLN crystal (*HC Photonics Corp.*) with dimensions 40 mm \times 8 mm \times 0.5 mm is placed at the center between mirrors M1 and M2. It contains six grating periods $\Lambda = 7.1, 7.2, \dots, 7.6 \mu\text{m}$ of which only $\Lambda = 7.3 \mu\text{m}$ is used in our experiments. Both crystal faces are antireflection coated at pump, signal, and idler wavelengths (532 nm, 750–950 nm, 1250–1650 nm). The SRO cavity including the crystal has a free spectral range (FSR) of more than 1.2 GHz. A frequency-doubled Nd:YVO₄ single-mode laser emitting at 532 nm (*Coherent Verdi-V10*) serves as the pump source. The pump beam is focused into the nonlinear crystal by a lens with focal length $f = 150$ mm, resulting in a beam waist of $w_0 \approx 35 \mu\text{m}$. This corresponds to a focusing parameter of $\xi = L/b = 1.22$ (see Sect. 3.2.2), where L denotes the crystal length and b is the confocal parameter of the pump beam. In order to obtain oscillation on a particular longitudinal mode, an uncoated glass etalon with a thickness of 30 μm (FSR: ~ 5 THz) is placed inside the resonator between mirrors M3 and M4. Behind output coupler M2, the pump, signal, and idler beams are collimated by a lens and subsequently separated by appropriate dichroic mirrors. The residual signal radiation leaking through mirror M4 is directed to a Doppler-free saturation spectroscopy setup (*TEM Messtechnik*

GmbH, model CoSy) that is optionally used for spectroscopy and frequency stabilization. It includes a glass cell filled with cesium at room temperature and optics to split up the incident beam into counterpropagating pump and probe beam along with the required photodetectors. A half-wave plate together with a polarizing beamsplitter allows for variable power attenuation. For frequency stabilization, the cavity length is slightly dithered by applying a 3-kHz modulation signal to the piezo. The Doppler-free absorption signal is phase corrected and mixed with the piezo modulation signal by a lock-in amplifier. The generated error signal is fed back to the M3 piezo actuator via a servo amplifier.

4.1.2 Basic Properties of the MgO:PPLN-Based SRO

Threshold and Output Power

Figure 4.2 shows the idler output power P_i and idler wavelength λ_i of the non-stabilized SRO as a function of the pump power P_p . Parametric oscillation occurs above a thresh-

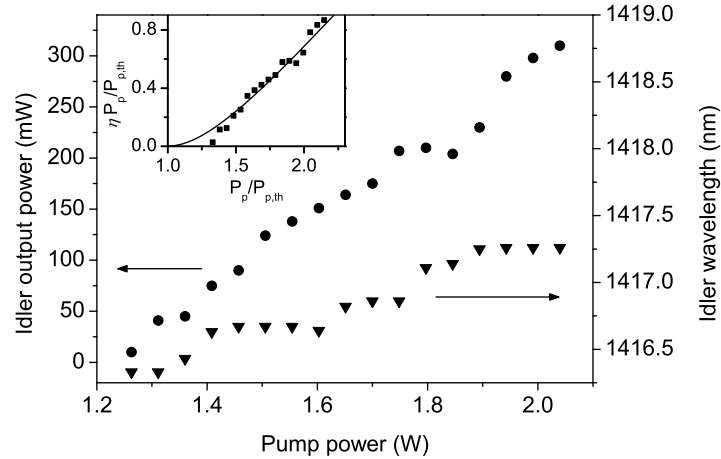


Figure 4.2: Idler output power (dots) and idler wavelength (triangles) vs. pump power. The inset shows the measured normalized idler output power vs. the normalized pump power (squares) together with the optimum theoretical curve $\eta_{\text{opt}}(\tilde{P}_p) \cdot \tilde{P}_p$ (solid line). Figure after [128] (© Springer-Verlag 2009); with kind permission from Springer Science and Business Media.

old pump power of $P_{p,\text{th}} \approx 1.2 \text{ W}$ (measured before the focusing lens). From Eq. (3.17), we estimate that the minimal threshold power could be $\sim 388 \text{ mW}$ under ideal conditions. For this estimation, we have assumed the following parameters: $\xi = 2.84$ (ideal focusing condition), $d_Q = 16 \text{ pm/V}$, 0.6% Fresnel losses at each crystal facet (given by the coating manufacturer), and 99.8% reflectivity for all four cavity mirrors, i.e., $1 - R_s e^{-\alpha_s L} = 1 - 0.998^4 \times 0.994^2 \approx 0.980$. The threshold pump power that was achieved experimentally is thus about three times larger than the theoretical prediction for ideal conditions. This can only be partly attributed to the non-ideal focusing and

suggests that a further loss mechanism is involved which was not taken into account in our estimation, e.g., absorption in the MgO:PPLN crystal (see discussion further below). The pump-to-idler conversion efficiency of the SRO is given by $\eta = \lambda_i P_i / (\lambda_p P_p)$. At a pump power of 2 W, we yield a single-mode idler power of 310 mW which corresponds to $\eta = 0.41$. In this case, the signal power is about 5 mW behind each cavity mirror. It is convenient for further considerations to introduce the normalized pump power $\tilde{P}_p = P_p / P_{p,\text{th}}$ and the normalized idler output power $\tilde{P}_i = \eta \tilde{P}_p$. Note that the efficiency η itself is a function of \tilde{P}_p , that means, it depends on how much the pump power exceeds the threshold pump power. For a SRO pumped by a Gaussian beam, the optimum theoretical conversion efficiency $\eta_{\text{opt}}(\tilde{P}_p)$ can be calculated numerically using the relation [110]

$$\eta_{\text{opt}}(\tilde{P}_p) = 1 - \left[\frac{1}{\tilde{P}_p} + \int_0^{\ln \tilde{P}_p} e^{-x} \cos^2 \Gamma(x) dx \right]. \quad (4.1)$$

Here $\Gamma(x)$ is a function which satisfies the equation

$$\frac{\sin^2 \Gamma(x)}{\Gamma^2(x)} = \frac{e^x}{\tilde{P}_p}. \quad (4.2)$$

The inset in Fig. 4.2 shows a plot of the normalized idler output power \tilde{P}_i vs. the normalized pump power \tilde{P}_p . As can be seen, the experimental data are close to the theoretical prediction. Figure 4.2 further shows that the idler wavelength slightly increases by 0.93 nm (139 GHz) when raising the pump power from $P_{p,\text{th}}$ to 2 W. Such an effect was previously observed for infrared-pumped SROs [146]. The cause was identified to be crystal heating due to the absorption of the resonant intracavity signal radiation. Depending on the circulating power in the cavity, which scales with the pump power, a rise in crystal temperature of 2 °C ($P_p = 3.6 \times P_{p,\text{th}}$) up to 30 °C ($P_p = 15 \times P_{p,\text{th}}$) was reported. Absorption-induced crystal heating, analogous to deliberate heating using the temperature control unit, changes the output frequencies of the cw SRO since it alters the refractive index of the nonlinear crystal and leads to thermal expansion. In the case of a green-pumped SRO, these effects shift the maximum of the parametric gain curve toward higher signal/lower idler frequencies (vice versa for 1- μm -pumped SROs). A 139-GHz shift of the gain maximum corresponds to an increase of ~ 0.8 °C in crystal temperature. At the same time, the cavity resonances are shifted toward lower frequencies because the effective length of the cavity increases. The shift of the gain curve is more significant since it is by an order of magnitude larger than the cavity frequency shift. This fact together with additional modulation of the gain curve by the intracavity etalon and several other residual resonances (e.g., from finite mirror reflectivity for pump and idler wavelength) prevent the signal/idler wavelength from continuously following the gain maximum. This is also evident from the steps in Fig. 4.2 where the idler wavelength jumps to higher levels at certain values of the pump power. The corresponding signal mode hops are on the order of 10 to 30 times the FSR of the cavity.

4.1.3 Tuning Range and Linewidths

By tuning the crystal temperature from 40.0 °C to 80.0 °C (temperature stability ~ 0.1 K) an idler wavelength range of 1406–1451 nm can be accessed. This corresponds to a signal wavelength from 840–856 nm. One can see from Fig. 4.3 that the measured data are in perfect agreement with curves calculated with Sellmeier coefficients from Gayer *et al.* [105]. We also compared our data to theoretical values obtained from the often used SNLO software [147]. Here we find a small offset of 2 °C. The tuning range of a

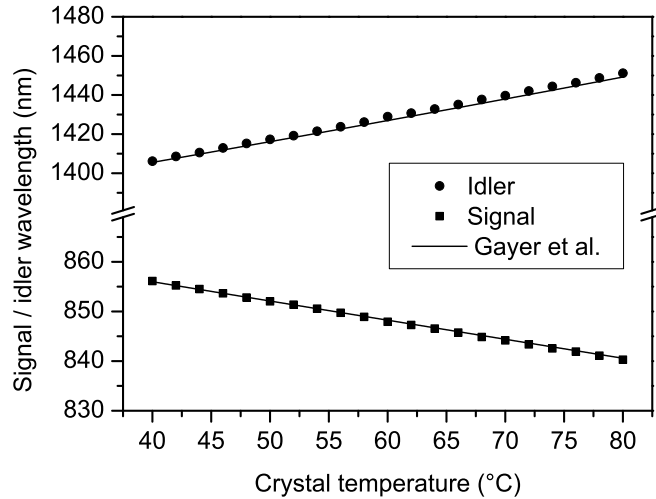


Figure 4.3: Temperature tuning curve from 40.0 °C to 80.0 °C for the grating period $\Lambda = 7.3 \mu\text{m}$. The experimental data are in perfect agreement with the theoretical curve calculated with Sellmeier coefficients from [105] (solid line). Figure after [128] (© Springer-Verlag 2009); with kind permission from Springer Science and Business Media.

green-pumped cw DRO based on the same crystal as the cw SRO presented here was investigated for the other five grating periods of the MgO:PPLN crystal in [148]. By utilizing all six poling periods from $7.1 \mu\text{m}$ to $7.6 \mu\text{m}$ and tuning the crystal temperature from 30.0 °C to 100.0 °C, a wavelength range from 800–920 nm (signal) and from 1250–1580 nm (idler) can be covered.

Single-mode operation is confirmed by monitoring the transmission of the signal wavelength through a scanning Fabry-Pérot interferometer (FPI, *Toptica FPI 100*, wavelength range: 615–885 nm, free spectral range: 1 GHz) as shown in Fig. 4.4(a). The linewidth of the signal radiation was determined to be less than 10 MHz, which is the resolution limit of the scanning FPI. Up to a pump power of approximately 2.1 W, reliable single-mode operation of the SRO is achieved. Above a pump power of 2.1 W, we often observe multi-mode operation of the SRO very similar to the behavior described in [131, 134]. The spectrum which was recorded during multi-mode operation with an optical spectrum analyzer (OSA, *Yokogawa AQ6370B*) is shown in Fig. 4.4(b). The characteristic spacing between two adjacent idler modes is ~ 0.4 nm (165 GHz). Kreuzer

has shown theoretically that SROs, in principle, oscillate on more than one longitudinal mode if the pump power exceeds a certain critical value P_c [149]. To this end, he has assumed a cw SRO in steady state operation which oscillates on a single longitudinal signal mode with angular frequency ω_s . He then investigated the stability of the steady state solution against perturbations caused by noise in another nearby signal mode at frequency ω'_s . It is found that the parametric gain G' at this mode is a function of $P_p/P_{p,\text{th}}$. Numerical calculation yields a critical value of $P_c \approx 4.61 P_{p,\text{th}}$. At pump powers exceeding this value, the parametric gain for the mode at ω'_s is high enough and this mode starts to oscillate in addition to the initial mode at ω_s . Although the analysis of Kreuzer is restricted to plane waves, it also seems to provide a good approximation for Gaussian beams in some cases [150]. While the theoretical model developed in [149] does not consider thermal effects, it has been reported [134] that crystal heating due to the absorption of intracavity signal power plays a role in oscillation in multiple longitudinal modes. In [134] the critical pump level for broadband oscillation was found to be 3.3 to 5 times the OPO threshold, depending on the cavity configuration. In our case, multi-mode operation readily occurs at pump powers which are well below this value. We hence assume that the multi-mode operation demonstrated in Fig. 4.4(b) originates

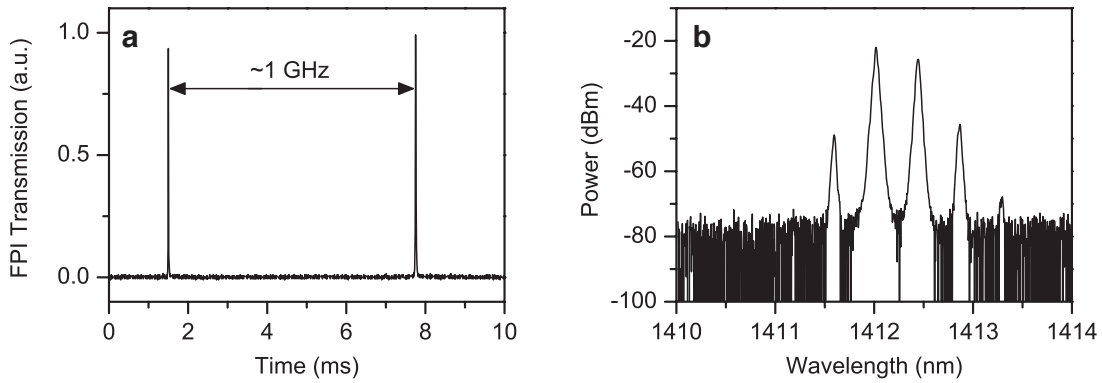


Figure 4.4: (a) The SRO spectrum measured with a scanning Fabry-Pérot interferometer clearly indicates single-mode operation at moderate pump powers. (b) Multi-mode operation of the SRO is observed above a pump power of 2.1 W. Figures after [128] (© Springer-Verlag 2009); with kind permission from Springer Science and Business Media.

from crystal heating caused by intracavity signal absorption. Yet, we could not determine in how far residual GRIIRA contributes to this or if the cavity configuration can favor the onset of multi-mode operation.

4.1.4 Spectroscopy of Cesium and Frequency Stabilization

Doppler-Free Spectroscopy of ^{133}Cs

Doppler-free saturation spectroscopy, particularly in alkali metal vapors, is a widely used technique of high-resolution spectroscopy [151]. It typically requires a tunable

and narrowband laser source in the visible to near-infrared, e.g., a diode laser or a Ti:sapphire laser. However, we can also use our SRO for such an application to prove its tunability, spectral purity, and narrow linewidth. This seems appealing since the D₂ line of Cs lies within the spectral window covered by the signal frequency. By stabilizing the signal frequency to one of the narrow hyperfine lines of the D₂ transition in Cs, the idler frequency is simultaneously stabilized because of energy conservation of the parametric conversion process. The stability of the idler frequency is only limited by the frequency stability of the pump laser. The signal wavelength of the SRO coincides with the cesium D₂ line (centroid at 852.347 nm [152]) at a crystal temperature of 50.0°C and a pump power of 1.79 W. In this case, the idler wavelength is about 1416 nm. For Doppler-free saturation spectroscopy, a signal power of 1.5 mW is used. By scanning the cavity length over more than 1.2 GHz, we measured the absorption spectra shown in Fig. 4.5. With a 25-Hz sweep rate applied to the piezo, it takes about 20 ms to acquire one spectrum. To scale the abscissae to frequency units, experimental data from a precision measurement [152] were used to determine the absorption peak frequencies. Figure 4.5(a) shows the hyperfine structure of the transition from the 6S_{1/2} ground state with total angular momentum $F = 3$ to the 6P_{3/2} excited states with $F' = \{2; 3; 4\}$. Likewise, Fig. 4.5(b) shows the hyperfine structure of the transition from the 6S_{1/2} ground state with $F = 4$ to the 6P_{3/2} excited states with $F' = \{3; 4; 5\}$. In addition, we observe six crossover resonances, denoted by two quantum numbers $F' = \{2, 3; 2, 4; 3, 4\}$ and $F' = \{3, 4; 3, 5; 4, 5\}$, respectively. Crossover resonances lie exactly midway between two resonances which share a common lower or upper level and overlap within their Doppler width. We bridged the frequency gap of 9.2 GHz between the $F = 3$ and $F = 4$ ground levels by adjusting the angle of the intracavity etalon. The linewidths of all resonances, which we calculated from Lorentzian fits, are given in Table 4.1. A recent theoretical prediction for the natural linewidth is $\Delta\nu = 5.23 \pm 0.01$ MHz (FWHM) calculated from the lifetime of the 6P_{3/2} state $\tau = 30.39 \pm 0.06$ ns [153]. This is in very good agreement with a previous precision measurement where a lifetime of $\tau = 30.57 \pm 0.07$ ns was determined yielding $\Delta\nu = 5.21 \pm 0.01$ MHz for the natural linewidth [154]. Our measured linewidths range from 7.1 MHz to 16.5 MHz. These deviations from the natural linewidth can be due to multiple reasons such as power broadening, residual Doppler broadening, or magnetic fields.

Table 4.1: Linewidths of D₂ hyperfine transitions determined from Lorentzian fits.

ground state: 6S _{1/2} ($F = 3$)						
F'	2	2,3	3	2,4	3,4	4
$\Delta\nu$ (MHz)	9.2	14.9	16.0	14.2	16.2	13.4
ground state: 6S _{1/2} ($F = 4$)						
F'	3	3,4	4	3,5	4,5	5
$\Delta\nu$ (MHz)	10.1	11.8	16.5	9.1	11.0	7.1

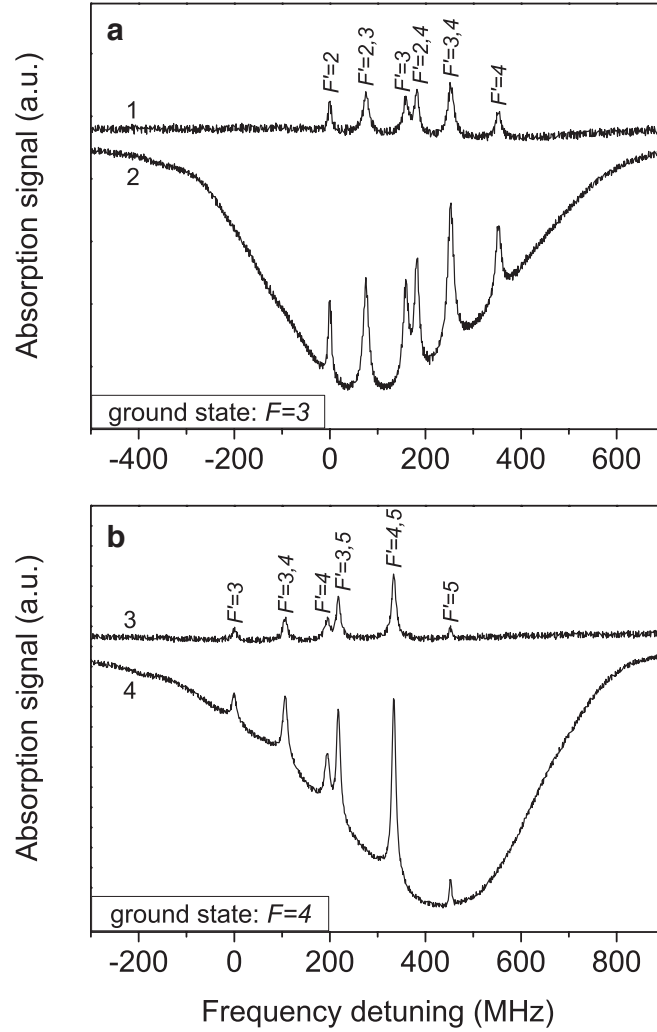


Figure 4.5: Doppler-free saturation spectroscopy of the cesium D_2 line hyperfine structure. (a) Transitions starting from the $F = 3$ ground state. (b) Transitions starting from the $F = 4$ ground state. Traces 2 and 4 show the Doppler broadened lines with lamb dips. In traces 1 and 3, the Doppler background has been subtracted. Lines labeled with two angular momentum numbers represent crossover resonances. Figures after [128] (© Springer-Verlag 2009); with kind permission from Springer Science and Business Media.

Frequency Stabilization

The narrow hyperfine transitions shown in Fig. 4.5 can be used as a frequency reference for frequency stabilization of the SRO. Frequency stabilization to an external reference was first applied to cw OPOs by Al-Tahtamouni *et al.* in 1998 [155]. We here achieved locking of the signal wave frequency to the $F = 3 \rightarrow F' = 3, 4$ crossover resonance in cesium for more than 9 minutes without interrupt. To this end, we used the technique

delineated in Sect. 4.1.1. Figure 4.6 shows the frequency fluctuations of the signal wave recorded during this time, derived from the saturation spectroscopy error signal, and given relative to the reference frequency of $\nu_{F=3 \rightarrow F'=3,4} = 351\,730\,801\,568$ kHz [152]. The distribution of the frequency fluctuations approximates a Gaussian (inset in

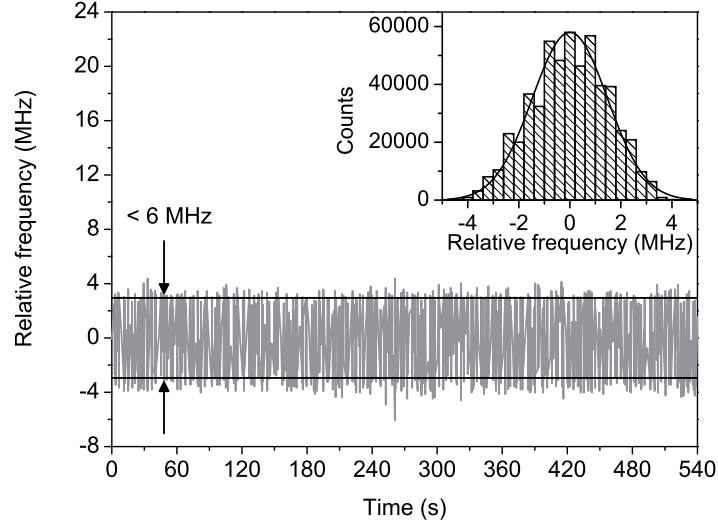


Figure 4.6: Frequency fluctuations relative to the atomic reference frequency $\nu_{F=3 \rightarrow F'=3,4}$ recorded over a time interval of 9 minutes. The 95% confidence interval 2σ is smaller than 6 MHz. Figure after [128] (© Springer-Verlag 2009); with kind permission from Springer Science and Business Media.

Fig. 4.6) with a standard deviation σ of less than 1.5 MHz. This corresponds to a 95% confidence interval ($\pm 2\sigma$) smaller than 6 MHz. The short-term stability is typically 0.5 MHz (1σ) over 1 ms. The average idler output power in frequency-locked operation exceeds 170 mW with a typical stability of 2% (rms) over 9 minutes. We also determined the linewidth of the pump laser with a high resolution FPI (*Sirah EagleEye*, resolution limit: 20 kHz) to be typically $\Delta\nu_p = 1$ MHz (on a time scale of 100 ms). Using this value together with the signal frequency stability during stabilized operation, we can estimate from

$$\Delta\nu_i \leq \Delta\nu_p + \Delta\nu_s \quad (4.3)$$

that the idler short-term frequency stability is ≤ 2 MHz.

To analyze the properties of the stabilized SRO in more detail, we calculated the Allan variance $\sigma_y^2(\tau)$ [156]. For a given set of data $\{y_k\}$ measured at times $\{t_k\}$, $\sigma_y^2(\tau)$ is defined as

$$\sigma_y^2(\tau) = \frac{1}{2(N-1)} \sum_{k=1}^{N-1} (y_{k+1} - y_k)^2. \quad (4.4)$$

N is the total number of samples, $\tau = t_{k+1} - t_k$ is the time interval between two measurements, and y_k is the frequency deviation from the reference frequency. The

square root of the Allan variance, the so-called Allan deviation, is plotted in Fig. 4.7. The curve is proportional to $\tau^{-1/2}$ which indicates that the fluctuations on the time

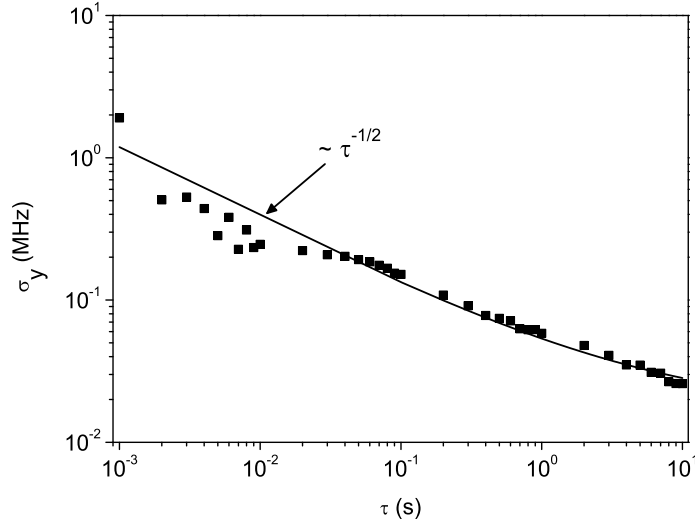


Figure 4.7: Square root of the Allan variance. The data were calculated from the frequency deviations recorded during frequency-stabilized operation of the SRO. To this end, a *MATLAB* code from [157] was used. Figure after [128] (© Springer-Verlag 2009); with kind permission from Springer Science and Business Media.

scale from 10 ms to 10 s are dominated by white frequency noise [158].

4.2 Green-Pumped CW SRO Based on MgO:PPSLT

Periodically poled MgO-doped stoichiometric LiTaO₃ (MgO:PPSLT) is a nonlinear material that was made commercially available during the time this work has been performed. Accordingly, its use in high power green-pumped cw SROs was investigated only in recent years [138–144]. Inspired by the promising results of other groups, we decided to test MgO:PPSLT as a material in our green-pumped SRO as well. The MgO:PPSLT-SRO was described and investigated in detail in the diploma thesis of C. Warschburger [159]. Therefore, we will only briefly recall the basic properties of this system in Sect. 4.2.1. After that, several new results which are not covered by [159] are presented. These comprise output coupling of the resonant signal wave, wavelength fine tuning by scanning the cavity length, and frequency stabilization to a wavemeter.

4.2.1 Basic Properties of the MgO:PPSLT-Based SRO

The SRO based on MgO:PPSLT was essentially build after the model of the MgO:PPLN-based device described in Sect. 4.1. Yet, minor changes and improvements were introduced. The length of the MgO:PPSLT crystal (*HC Photonics Corp.*) is only $L = 30$ mm

since this is the maximum length that was commercially available (width \times height = 6.9 mm \times 0.5 mm). Moreover, the input and output facets of the crystal are not polished plano-parallel but are angle-polished at 2° so that the crystal has the shape of a parallelogram. Potential residual reflections of light between the two facets of the crystal are eliminated in this way. The heating foil originally used to control the temperature of the QPM crystal was replaced by a thermoelectric Peltier module. This allows for controlling the temperature in both ways (heating and cooling), it is faster, and much more precise (typically better than 0.01 K for set points near room temperature). The cavity design is given in Fig. 4.8. For the MgO:PPSLT-based device, another

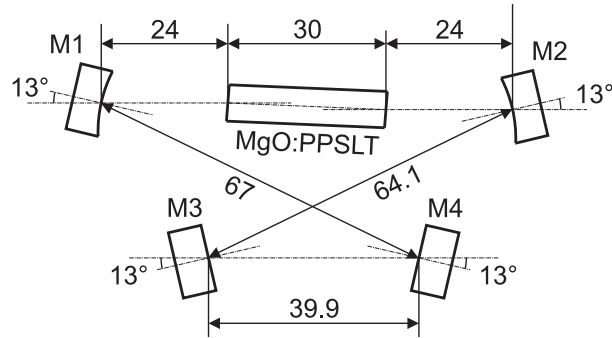


Figure 4.8: Cavity design of the SRO based on MgO:PPSLT. Mirrors M1 and M2 are plano-concave mirrors with $\text{ROC} = 50$ mm. Mirrors M3 and M4 are plane mirrors. The angle of incidence is 13° for all cavity mirrors.

set of mirrors was used (coatings by *Layertec GmbH*). According to the manufacturer, the mirrors provide a reflectivity of $R > 99.9\%$ for the signal wave (wavelengths between 790–995 nm). Due to the angle-polished facets, the crystal has to be tilted by an angle of $\sim 2.4^\circ$ to ensure that the pump beam traverses the crystal parallel to the 30-mm-long edge of the crystal. A plano-convex lens with $f = 150$ mm (not shown in Fig. 4.8) is used to focus the green pump beam into the nonlinear crystal. The presented cavity design guarantees a very good spatial idler beam profile with a beam quality factor [160] of $M_{x,y}^2 = 1.2$ in x and y direction [159] (as usual, the xy plane is the plane perpendicular to the propagation direction of the beam). With this configuration, idler output powers well exceeding 1 W can be reached as proven by Fig. 4.9(a). The plot exemplarily shows the idler power characteristic as a function of the pump power at 532 nm for a QPM grating period of $\Lambda = 8.2 \mu\text{m}$. The threshold is reached at a pump power of $P_{p,\text{th}} \approx 800$ mW. The lowest threshold ever achieved with this system was $P_{p,\text{th}} < 700$ mW with the 8.1- μm grating period. This is close to the threshold pump power of 564 mW predicted by Eq. (3.17) for our experimental parameters and under ideal focusing conditions. The following parameters were inserted into Eq. (3.17) to calculate the theoretical threshold: $\xi = 2.84$, $\lambda_s = 936.02$ nm, $\lambda_i = 1232.52$ nm, $d_Q = 8.79$ pm/V, 0.1% and 0.2% Fresnel losses at each crystal facet (given by the coating manufacturer), respectively, and 99.9% reflectivity for all four cavity mirrors,

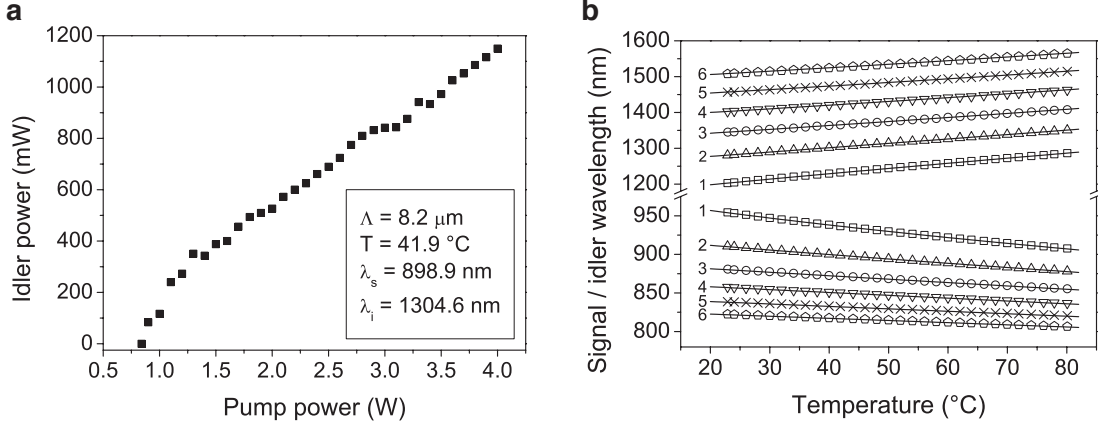


Figure 4.9: (a) Idler power vs. pump power (no intracavity etalon was inserted). (b) Coarse wavelength tuning by means of the crystal temperature. Curves {1, 2, 3, 4, 5, 6} correspond to QPM grating periods {8.1, 8.2, 8.3, 8.4, 8.5, 8.6} μm . Symbols: measured data, solid lines: fit.

i.e., $1 - R_s e^{-\alpha_s L} = 1 - 0.999^4 \times 0.998 \times 0.999 \approx 0.993$. The curves representing idler power vs. pump power for the other five QPM channels look similar to the one shown in Fig. 4.9(a), mostly differing in the threshold power (typically between 1.00 W and 1.75 W). Occasionally, we observe the same multi-mode effect as with the MgO:PPLN device (see Fig. 4.4(b)). However, this effect can be suppressed by placing a 1-mm-thick quartz etalon at the position of the second beam waist inside the cavity between mirrors M3 and M4. With this intracavity etalon, long-term stable single-mode operation is maintained up to a certain level of idler power, typically up to ~ 1.0 W. At this point, the multi-mode effect cannot be inhibited anymore. Therefore, the SRO is mostly operated below this critical point in later experiments.

By tuning the crystal temperature from 23–80 $^\circ\text{C}$, a spectral range from 806–954 nm (signal) and from 1203–1565 nm (idler) is accessed. The temperature tuning curves for all six QPM gratings are presented in Fig. 4.9(b). A fit using a Sellmeier equation from Dolev *et al.* [97] perfectly matches the experimental data. With this large idler tuning range, at least four telecom bands are fully covered (O-, E-, S-, and C-band). This would be an impossible task for any conventional laser system.

In comparison to other similar green-pumped SROs based on MgO:PPLT [139, 140, 143], our device exhibits a remarkable passive stability concerning output power and frequency. In a 5-h measurement, a long-term power stability with peak-to-peak fluctuations of $\Delta_{pp} P_i = 8.00 \text{ mW}$ (1.6%) and a standard deviation of $\sigma = 0.69 \text{ mW}$ (0.14%) could be achieved (see Fig. 4.10(a)). The average idler power was $\bar{P}_i = 495.2 \text{ mW}$ during this measurement. Simultaneously, the signal frequency fluctuates within a window of 250 MHz as seen from Fig. 4.10(b). The frequency trace, which was measured with a wavemeter (*High Finesse WS/6 200*, measurement range: 350–1120 nm, absolute accuracy: 200 MHz, measurement resolution: 50 MHz), is modulated with an oscillation period of roughly 15 min. This is mainly due to fluctuations of air humidity and pressure

in the laboratory [159].

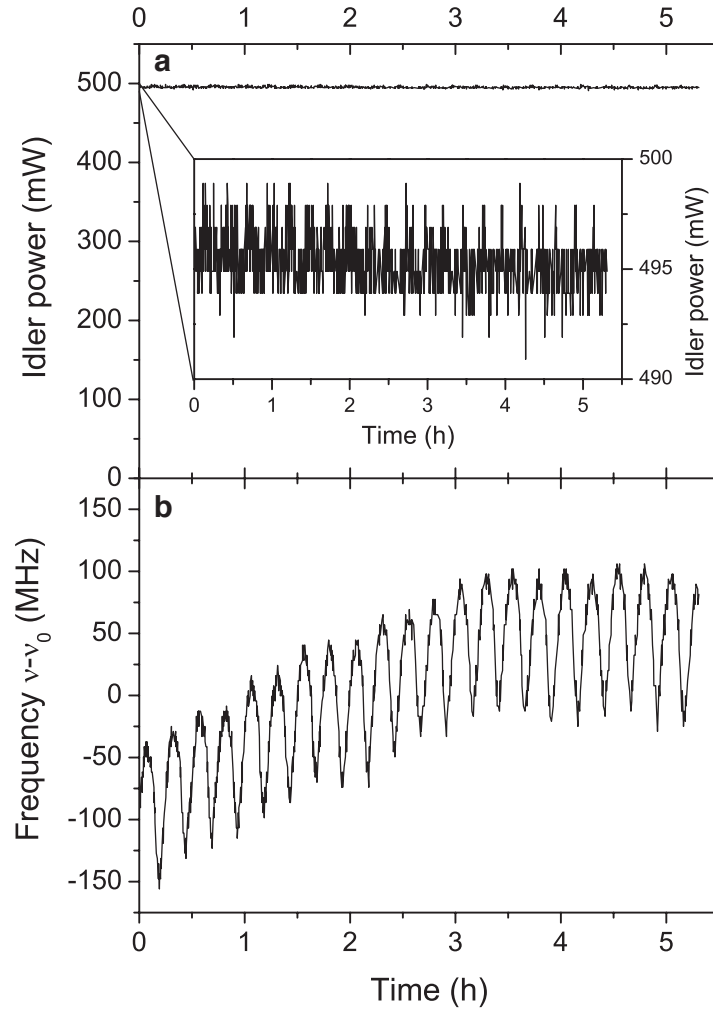


Figure 4.10: Simultaneous measurement of power and frequency stability over more than 5 h. (a) Idler power stability (the inset shows a magnified view). (b) Signal frequency stability relative to the average signal frequency of $\nu_0 = 350.34524$ THz (855.7058 nm).

4.2.2 Signal Extraction through Output Coupling

So far, we have always considered SRO ring cavities where all four mirrors are highly reflective for the signal wavelength and highly transmissive for the idler wavelength. This configuration ensures that a maximum of idler power is coupled out of the resonator. At the same time, we achieve a relatively low threshold with the singly resonant configuration. The signal power that can be extracted from such a system is modest, typically between several hundreds of μW and a few mW depending on the reflectivity

of the mirrors. For certain applications, though, it is desirable to provide higher levels of signal power. In analogy to a laser, this is accomplished by using an output coupling mirror. As shown in Fig. 4.11, mirror M2 is replaced by an output coupler (OC) with a transmission of $\sim 3\%$ at the signal wavelength. With this configuration, a signal (idler)

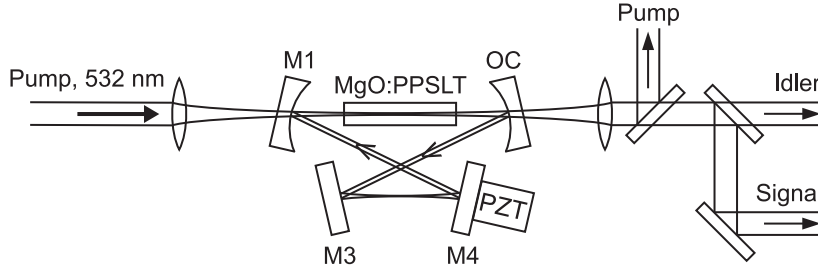


Figure 4.11: Similar resonator setup as in Fig. 4.1 but with mirror M2 replaced by a 3% output coupling mirror (OC) for signal extraction. At a pump power of 5.50 W, a signal (idler) power exceeding 1.1 W (1.0 W) can be generated with this configuration.

output power P_s (P_i) exceeding 1.1 W (1.0 W) was achieved. The SRO was pumped with a power of 5.50 W at 532 nm, a QPM grating period of $\Lambda = 8.2 \mu\text{m}$ was used, and the crystal temperature was set to 27.90 °C in this case. The signal (idler) wavelength was 907.5 nm (1286.9 nm). Signal and idler power were recorded over a time of 30 min (see Fig. 4.12) to prove that a good long-term stability can be maintained. During the time of 30 min, we observe periodic power fluctuations around average values of $\bar{P}_s = 1.109$ W (standard deviation $\sigma_s = 0.92\%$) and $\bar{P}_i = 1.022$ W ($\sigma_i = 0.89\%$). The peak-to-peak fluctuations are 4.7% and 6.0% for signal and idler, respectively. A fit according to a sine function (see inset in Fig. 4.12) reveals oscillation periods of $T = 465$ s and 484 s for the signal and idler power, respectively. In [159] oscillations of air humidity and pressure in the laboratory were identified to be the cause for periodic power fluctuations on such time scales. We put emphasis on the fact that the high power levels were achieved while the SRO was in constant single-frequency operation. We mention that, in our case, where we are particularly interested in a tunable telecom wavelength source for QFC experiments, it was not the primary goal to extract a maximum of signal power at wavelengths below 1 μm . The motivation for this experiment was rather to perform a proof-of-principle demonstration. Nevertheless, the obtained results on signal wave output coupling are interesting themselves. Future efforts could be directed toward finding the optimum point of signal output coupling (i.e., the optimum fraction of output-coupled signal power per cavity roundtrip) to maximize the signal output power.

The threshold of the SRO with output coupling is above 3 W. Aligning the setup at such power levels is inconvenient because optical components could be burned and damaged (especially the MgO:PPSLT chip) when hit by a reflected beam. Usually, it is no problem to align the setup at moderate power levels and, once the alignment is optimized, to increase the pump power then.

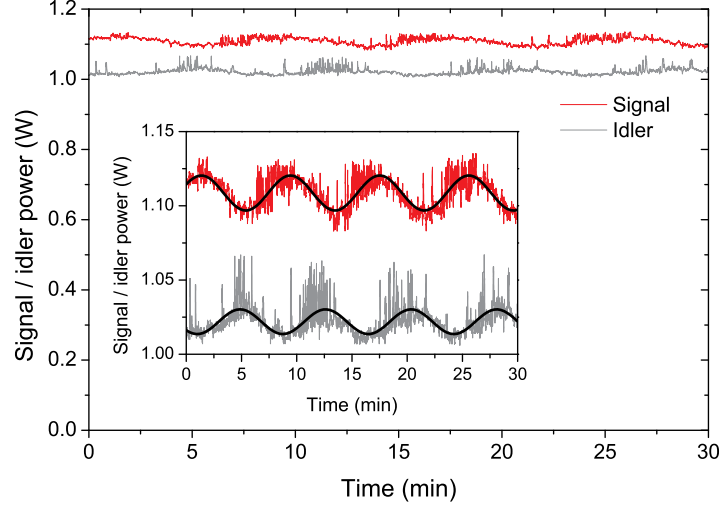


Figure 4.12: Signal and idler output power vs. time for the SRO based on MgO:PPSLT with signal wave output coupling. The inset shows a detailed view with a fit according to a sine function.

4.2.3 Frequency Stabilization Using a Wavemeter

Spectroscopy of Cs, as discussed in Sect. 4.1.4, was performed by tuning the signal wavelength of the SRO over an atomic resonance. This is done by scanning the SRO cavity length by means of a moveable cavity mirror that is mounted to a PZT. The SRO based on MgO:PPSLT offers the same possibility as seen in Fig. 4.13 which shows the signal wavelength and frequency as a function of time when a sawtooth voltage is applied to the PZT (frequency $f_{\text{scan}} = 100$ mHz, voltage: 0 to +80 V). The wavelength was measured with the wavemeter. We used a QPM grating period of $\Lambda = 8.6$ μm , a crystal temperature of $T_c = 52.35$ $^\circ\text{C}$, and a pump power of $P_p = 2.80$ W when recording the data in Fig. 4.13. This point of operation corresponds to an idler wavelength of $\lambda_i \approx 1537$ nm and an idler power of $P_i = 510$ mW. No output coupling was applied, i.e., the SRO cavity consisted of four mirrors that are all highly reflecting at the signal wavelength. For frequency tuning via the PZT, it is important that no etalon is inside the SRO cavity so that the signal frequency can freely follow the change of the cavity length. The maximum mode-hop-free tuning range (peak-to-peak value in Fig. 4.13) that was achieved is $\Delta\nu_s = 2.49$ GHz, corresponding to $\Delta\lambda_s = 0.00551$ nm (0.01959 nm) at 814 nm (1536 nm). A cavity length change of ΔL is related to a frequency change $-\Delta\nu$ of the resonant wave by $\Delta L/L_{\text{eff}} = -\Delta\nu/\nu_0$, where L_{eff} and ν_0 are the absolute (optical) length of the resonator and the absolute frequency, respectively. With $L_{\text{eff}} \approx 285$ mm and $\nu_0 = 368.1420$ THz, we find that a frequency variation of $\Delta\nu = \pm 2.49$ GHz corresponds to a length change of $\Delta L \approx \mp 1.9$ μm . The FSR of a ring cavity is given by $\text{FSR} = c/L_{\text{eff}}$, where c is the speed of light in vacuum. With L_{eff} as given above, we determine the FSR of our resonator to be ~ 1 GHz, i.e., the mode-hop-free tuning

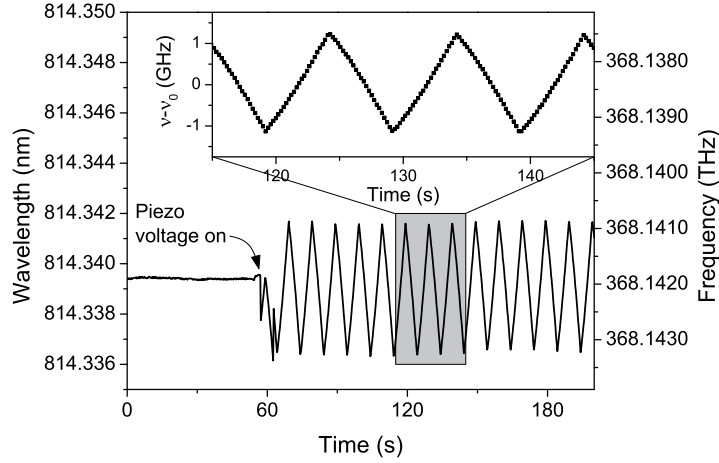


Figure 4.13: Wavelength fine tuning by scanning the cavity length of the SRO. Initially, no voltage is applied to the PZT and the signal wavelength is nearly constant. At $t = 56$ s, the sawtooth voltage is switched on and the signal wavelength starts to follow the periodic change of the cavity length. The inset shows a magnified view (frequency given relative to average frequency ν_0) proving that the tuning is mode-hop-free.

range is larger than two times the FSR of the cavity. This interesting observation has previously been reported for a 1064-nm-pumped MgO:PPLN-SRO and is explained by a thermal self-locking effect associated with the absorption of intracavity signal power [134]. By scanning the cavity length, the frequency of the signal mode is shifted with respect to the parametric gain curve. As a consequence, this mode experiences a change in parametric gain and the intracavity power changes. This leads to a small temperature change within the beam volume in the crystal (because more or less power is absorbed) and thus to a shift of the parametric gain curve. Suppose that the signal mode is initially (before scanning the cavity length) slightly red detuned from the maximum of the parametric gain. If the cavity length is decreased (i)/increased (ii), the effects that take place can be summarized as follows:

- (i) cavity length is decreased \rightarrow signal mode shifts to higher frequency \rightarrow it experiences a higher gain \rightarrow intracavity signal power increases \rightarrow absorbed power in the crystal increases \rightarrow increase of temperature in the beam volume \rightarrow parametric gain curve is shifted toward higher frequencies,
- (ii) cavity length is increased \rightarrow signal mode shifts to lower frequency \rightarrow it experiences a lower gain \rightarrow intracavity signal power decreases \rightarrow absorbed power in the crystal decreases \rightarrow decrease of temperature in the beam volume \rightarrow parametric gain curve is shifted toward lower frequencies.

The overall effect in both cases (i) and (ii) is that the maximum of the gain curve follows the shift of the signal mode to some extent which can explain why the observed mode-hop-free tuning range in our experiments is larger than the cavity FSR. If the

SRO initially oscillates on a signal mode which is blue detuned from the gain maximum, it tends to make a mode hop to the red-detuned side of the gain maximum according to [134]. This is because, in that case, the shift of the signal mode in one direction induces a shift of the parametric gain curve in the opposite direction. Note that the above arguments apply to our green-pumped SRO and that the situation is reversed for a 1- μm -pumped SRO as in [134]. In the latter case, the gain maximum has a tendency to follow the frequency shift if the initial signal frequency is blue detuned from the gain maximum and mode hops may occur if it is red detuned.

The method described above—cavity length scanning without an intracavity etalon—proves to be a simple and reliable technique of fine tuning the SRO's output frequencies in a deterministic way. With its tuning properties, the system is predestined for wavelength stabilization to an external reference. In Sect. 4.1.4 this was demonstrated for the MgO:PPLN-based SRO using a Doppler-free absorption line of Cs as an absolute frequency reference. In the present section, we study frequency stabilization to an interferometric reference (i.e., a wavemeter) with the setup depicted in Fig. 4.14. The

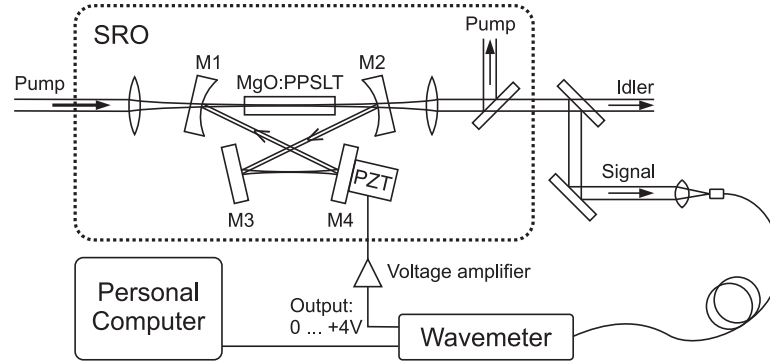


Figure 4.14: Schematic of the setup for frequency stabilization by means of a wavemeter.

residual signal light leaking through mirror M2 and the idler radiation are split up at a dichroic mirror and the signal light is guided to the wavemeter using a single-mode fiber. A software-based PID controller compares the measured frequency with a given set frequency and applies a voltage level between 0 V and +4 V to the control output of the wavemeter. This voltage is amplified (*TEM Messtechnik GmbH, model miniPiA103*, 0 ... +300 V max.) and fed to the PZT. The wavemeter records and controls the signal wavelength of the SRO simultaneously. With this technique, frequency stabilization over more than nine hours was achieved as shown in Fig. 4.15(a). After 9 h and 12 min, the control electronics obviously could no longer compensate for the long-term drift of the signal frequency. During frequency-stabilized operation, the average signal frequency was $\nu_{0,s} = 349.6040$ THz ($\lambda_{0,s} = 857.5200$ nm), the peak-to-peak fluctuations were $\Delta\nu_{pp,s} = 32.6$ MHz, and the standard deviation was $\sigma_s = 1.3$ MHz. Assuming a constant pump wavelength of $\lambda_p = 532.32$ nm (in fact this wavelength also fluctuates on the order of a few MHz), this corresponds to $\nu_{0,i} = 213.5769$ THz

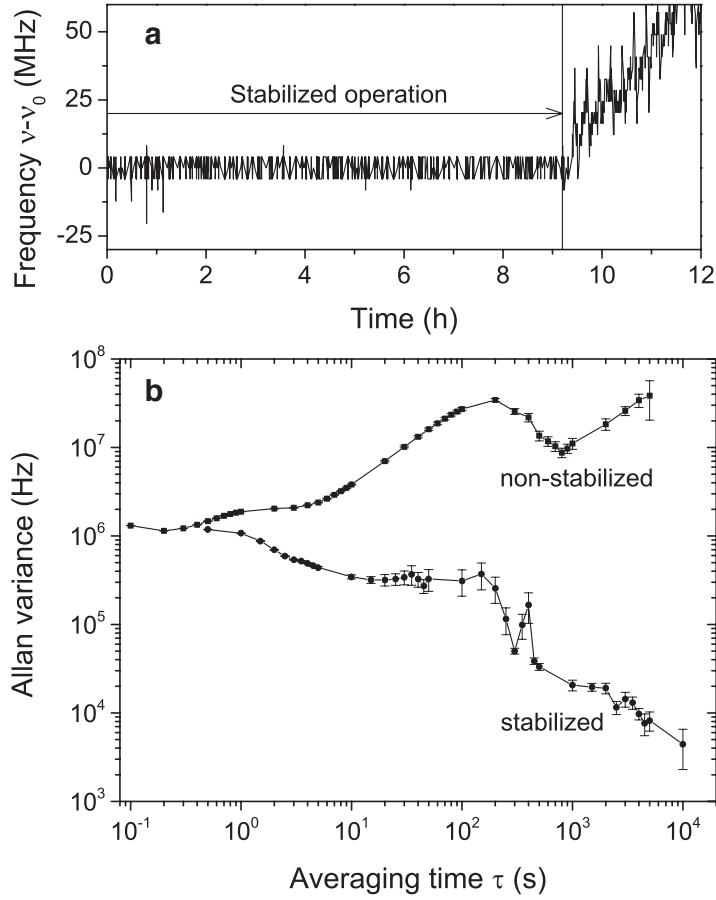


Figure 4.15: (a) Frequency vs. time in frequency-stabilized operation. Stabilization was achieved for more than 9 hours. The frequency is given relative to the time-averaged signal frequency of $\nu_0 = 349.6040$ THz (~ 857.52 nm). (b) Comparison of the Allan variance achieved in this work with that obtained from the same SRO but without active stabilization of the cavity length. Both curves were calculated with a software by T. Udem [161].

($\lambda_{0,i} = 1403.6748$ nm), $\Delta\nu_{pp,i} = \Delta\nu_{pp,s}$ and $\sigma_i = \sigma_s$ for the idler wave. Compared to the frequency scan measurement (Fig. 4.13), another point of operation was chosen for the long-term frequency stabilization shown in Fig. 4.15(a). The QPM grating period was $\Lambda = 8.4 \mu\text{m}$ at a crystal temperature of $T_c = 23.4^\circ\text{C}$. With the crystal temperature slightly above room temperature and a low threshold (< 1.0 W), this operating point was found to provide particularly stable conditions.

Long-term measurements of the signal frequency were also reported in [159] but not with an actively-stabilized SRO cavity. During 8 h, frequency fluctuations within a 260-MHz corridor were observed. In addition, the frequency trace was periodically modulated with a period of roughly 15 min and peak-to-peak fluctuations of 117 MHz on average. Comparing these results with those presented here, we find that the frequency stability

of the system was again improved by at least one order of magnitude with the help of a relatively simple stabilization scheme. This enhanced stability is also reflected by the Allan variance that was calculated from the data recorded during 9 h of frequency-stabilized operation (see Fig. 4.15(b)). The Allan variance plot from Ref. [159] is also shown in Fig. 4.15(b). As can be seen from comparison of the two plots, active stabilization to the wavemeter clearly reduces the wavelength drift on longer time scales ($1\text{--}10^4$ s).

4.3 Summary

In this chapter, we have presented two green-pumped cw SROs with similar signal-resonant ring cavity designs. One is based on a MgO:PPLN crystal (SRO #1), the other on a MgO:PPSLT crystal (SRO #2). SRO #1 has a pump threshold of about 1.2 W. It delivers a single-mode idler output power of more than 300 mW in non-stabilized operation. In principle, by tuning the crystal temperature, a spectral range between 1250–1580 nm can be accessed with the non-resonant idler wave (corresponding signal wavelength range: 800–920 nm) [148]. Although the device is operated at relatively low crystal temperatures from 40.0 °C to 80.0 °C, we observe no evidence of photorefractive damage. For SRO #2, introduced in Sect. 4.2, we find an even lower threshold of $P_p < 700$ mW. At first sight, this seems surprising because of the shorter crystal and the smaller nonlinear coefficient of LiTaO₃. One explanation is that, for SRO #2, the coatings of the cavity mirrors have a higher signal reflectivity and the antireflection coatings of the QPM crystal are better. Another reason could be that thermal effects (absorption of green pump light), which seem to be significantly weaker in MgO:PPSLT than in MgO:PPLN, play a role for the threshold pump power. Although multi-mode oscillation can be observed as well with SRO #2, it occurs at much higher idler output powers. Thus, with the help of an intracavity etalon, single-frequency operation is maintained up to idler power levels exceeding 1 W. The idler (signal) tuning range spans from 1203–1565 nm (806–954 nm). As an addition to the treatment of the MgO:PPSLT-SRO in [159] we have discussed a number of further applications in this chapter. Replacing one highly-reflective cavity mirror by a 3% signal output coupler allows for Watt-level single-frequency output at signal and idler wavelengths simultaneously. Frequency fine tuning can be realized not only by tilting the intracavity etalon (see [159]) but also by scanning the cavity length with a piezo mirror. No etalon is needed in this case. Deterministic frequency scans over 2.5 GHz are possible with this technique.

For applications which are demanding with respect to the frequency stability (e.g., high-resolution spectroscopy [135, 162]), the frequencies of the cw SRO can be stabilized to an external reference. Due to energy conservation of the parametric conversion process, frequency stabilization of the signal wave transfers to the frequency stability of the idler wave, at least within a range limited by the bandwidth of the pump source. As our cw SRO emits in the visible to near infrared we could use the established spectroscopic techniques for frequency stabilization to an atomic resonance. By scanning the

cavity length of SRO #1 over 1.2 GHz, Doppler-free saturation spectroscopy of the cesium D₂ line at 852 nm was performed. Frequency stabilization of the signal frequency to a crossover resonance was achieved. For a time of over 9 minutes, the frequency deviation from the reference frequency was less than 1.5 MHz (1σ). The idler radiation is simultaneously frequency stabilized with a short-term stability < 2 MHz. For SRO #2, we have demonstrated frequency stabilization to an interferometric reference: by controlling the cavity length with the piezo mirror, we achieve active stabilization of the signal frequency to a wavemeter. Frequency-stabilized operation of the system was possible over more than 9 hours. During this time, the standard deviation of the frequency fluctuations was 1.3 MHz with peak-to-peak deviations of 33 MHz.

The results show the potential of the devices for applications in spectroscopy and quantum optics. One goal of future efforts could be to achieve frequency stabilization to an atomic reference for longer times. To this end, the mechanical and thermal stability of the setup should be further improved. We have observed that mainly acoustic noise or slight changes in ambient temperature can interrupt active frequency stabilization. In case of SRO #1, it would also be essential to gain deeper understanding of the described thermal effects. This might help to further optimize the resonator (with regard to focusing parameter, output coupling etc.) to allow for a higher pumping ratio and a higher single-mode output power.

Table 4.2: Comparison of the properties of the two green-pumped SROs presented in this chapter.

	SRO #1	SRO #2
Nonlinear crystal	MgO:PPLN	MgO:PPSLT
Crystal dimensions	$40 \times 8 \times 0.5 \text{ mm}^3$	$30 \times 6.9 \times 0.5 \text{ mm}^3$
QPM gratings	7.1, 7.2, ... , 7.6 μm	8.1, 8.2, ... , 8.6 μm
Cavity FSR	$\sim 1 \text{ GHz}$	$\sim 1 \text{ GHz}$
Threshold power	1.2 W	$< 700 \text{ mW}$
Max. idler power*	310 mW	1.1 W
Max. signal power*	5 mW	1.1 W (3% OC)
Power stability	—	0.14% (1σ)
Idler tuning range	1250-1580 nm	1203-1565 nm
Signal tuning range	800-920 nm	806-954 nm
Frequency stabilization	$> 9 \text{ min}^{**}$	$> 9 \text{ h}^\dagger$

*in single-frequency operation

**reference: absorption line in Cs

† reference: wavemeter

Overall, MgO:PPLN can be considered an appropriate nonlinear material for green-pumped cw SROs in the regime of moderate pump powers. Nevertheless, compared to MgO:PPSLT, it has some clear disadvantages when used in green-pumped OPOs.

These handicaps have their origin in the strong thermal effects. We recognize from direct comparison that SRO #2 outperforms SRO #1 in every aspect (see Table 4.2). Both SROs could serve as a pump source in frequency down-conversion experiments. Naturally, due to its superior performance, SRO #2 was selected as a pump source for the down-conversion experiments presented in the next two chapters.

Chapter 5

Frequency Down-Conversion of Attenuated Laser Pulses

Copyright Notice:

The introduction of this chapter, Sect. 5.1, Sect. 5.2, and Sect. 5.4 contain material that was originally published in Ref. [49] (Copyright © 2011 Optical Society of America).

Color centers in diamond have attracted great interest in recent years as solid-state single-photon sources [163]. Unlike other single-photon emitters, like trapped atoms and ions or QDs, they offer the possibility of room temperature operation without the need for cryogenic or vacuum equipment. Integration of single color centers into photonic structures [164, 165] opens the perspective of diamond-based quantum networks in the future [166]. Apart from these attractive properties, one drawback with respect to long-distance fiber-based quantum communication is that color centers in diamond seem to have no strong emission lines above $1.0\ \mu\text{m}$ [167]. Therefore, QFC techniques are required for low-loss fiber transmission of photons generated by color centers in diamond. An experimental scheme which is aimed at efficient frequency down-conversion of single photons from a nitrogen-vacancy (NV) center (zero-phonon line at $637\ \text{nm}$ [163]) to the telecom C-band has been demonstrated [47, 168]. However, due to strong electron-phonon coupling, the emission spectrum of NV centers is very broad ($\sim 100\ \text{nm}$) compared to the acceptance bandwidth of the required DFG process in a PPLN WG crystal which is $< 0.5\ \text{nm}$ for typical interaction lengths. Recently, much progress has been made in the fabrication of single-photon sources based on silicon-vacancy (SiV) centers in diamond emitting around $738\ \text{nm}$ [60]. Compared to NV centers, they feature higher emission rates and significantly narrower spectral linewidths at room temperature ($\lesssim 2\ \text{nm}$). Motivated by these results we investigate the feasibility of frequency down-conversion of 738-nm photons in this chapter. To this end, attenuated laser pulses at $\lambda_a = 738\ \text{nm}$ are mixed with a strong classical pump field at $\lambda_p = 1403\ \text{nm}$ in a periodically poled Zn-doped LiNbO_3 (Zn:PPLN) ridge WG

to yield down-converted photons in the telecom C-band ($\lambda_b = 1557$ nm). We study the Raman noise spectrum generated by the strong 1403-nm pump light and investigate the conversion efficiency under realistic experimental conditions.

5.1 Experimental Design

5.1.1 Optical Setup

The optical setup is shown in Fig. 5.1(a). To simulate the single-photon source at

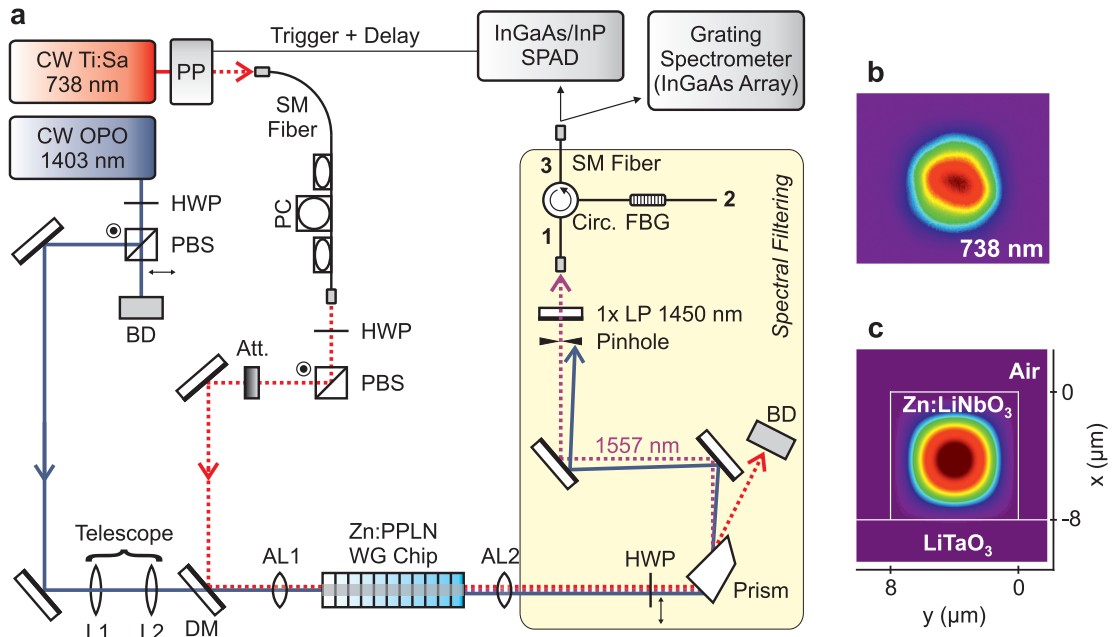


Figure 5.1: (a) Experimental setup for frequency down-conversion (PP: pulse picker, PC: polarization control, HWP: half-wave plate, PBS: polarizing beamsplitter, Att.: attenuator, AL1 and AL2: aspheric lenses, BD: beam dump, L1 and L2: plano-convex lenses, DM: dichroic mirror, LP: longpass filter, Circ.: fiber-optic circulator, FBG: fiber Bragg grating). (b) CCD image of the mode profile of the collimated 738-nm beam behind the WG. (c) Calculated intensity distribution of the 738-nm fundamental mode inside the WG. Figures after [49] (Copyright © 2011 Optical Society of America).

738 nm, a cw Ti:sapphire laser (*Sirah GmbH, Matisse TX*; linewidth < 100 kHz) together with a pulse picker and an attenuator is used. The 738-nm light is guided to the experiment by a single-mode optical fiber. The MgO:PPSLT-based cw SRO described in Sect. 4.2 is used to generate the strong field at 1403 nm. Its wide tunability from 1202–1564 nm adds an enormous flexibility to the setup: the cw SRO can also be employed as a pump source for frequency down-conversion of light emitted by other types of color centers in diamond (e.g., from a chromium-related color center [169]) or from a semiconductor QD [170] as we shall see in Chap. 6. The attenuated pulses at

738 nm and the strong pump field at 1403 nm are combined on a dichroic mirror and coupled into a Zn:PPLN WG (*NTT Electronics Corp., Japan*) by a single aspheric lens. A detailed description of the WG chip is given in Sect. 5.1.2. As the two wavelengths, λ_a and λ_p , are spectrally separated by 665 nm it is necessary to use an additional telescope in the beam line of the pump light to compensate for chromatic aberration. The telescope consists of two plano-convex lenses L1 (*Thorlabs LA1433*, $f = 150$ mm) and L2 (*Thorlabs LA1509*, $f = 100$ mm). The optimum distances d_{L1-L2} between L1 and L2 and d_{L2-AL1} between L2 and AL1 can be calculated from the requirement that the two light beams at λ_a and λ_p must have the same focus point behind AL1. For the calculation, it can be assumed that the two collimated beams have the same diameter at AL1. This diameter can be chosen such that the smallest aperture of the system (AL1 in this case) is filled. We find optimum distances of $d_{L1-L2} = 267$ mm and $d_{L2-AL1} = 228$ mm. In practice, the input coupling efficiency could be optimized by choosing a slightly shorter distance of $d_{L1-L2} = 261$ mm between L1 and L2. We tested two types of aspheric lenses for input coupling (AL1), one is uncoated (*Thorlabs A220TM*) and the other one has an antireflection coating from 650–1050 nm (*Thorlabs C220TME-B*). Apart from the coating, both lenses are almost identical and have an effective focal length of $f_{\text{eff}} = 11$ mm. The numerical aperture for the coated (uncoated) asphere is NA = 0.25 (0.26). For output coupling (AL2), we use an asphere with an antireflection coating from 1050–1620 nm for telecom wavelengths (*Thorlabs C220TME-C*, $f_{\text{eff}} = 11$ mm, NA = 0.25). The AR coating of AL1 seems to have only a marginal effect on the transmission through the system AL1–WG–AL2 at 738 nm: we measure a typical value of 60 % transmission, no matter if the coated or the uncoated lens is employed. Yet, at 1403 nm, the transmission through AL1–WG–AL2 can be improved by using the uncoated lens for input coupling. Here we obtain 53 % with the coated asphere compared to 65 % with the uncoated model. Since AL2 has an AR coating for telecom wavelengths, it should add only minimal losses at 1403 nm and the stated 65 % can be considered as the fraction of the pump power that can be coupled into the WG. At 738 nm, we have to take into account that the transmission through AL2 is only 64.5 %, i.e., a measured throughput of 60 % through AL1–WG–AL2 corresponds to an input coupling efficiency of 93 % into the WG.

What can be given as a conclusion after testing several lenses is that, by properly choosing input and output coupling optics, the coupling losses at 738 nm are minimized at the WG input while at the same time losses at telecom wavelengths are minimized at the WG output. In this way, we simultaneously yield a maximum coupling efficiency of 93 % and 65 % for 738 nm and 1403 nm, respectively. No efforts were made to discriminate between Fresnel losses at the facets, input coupling losses, and propagation losses of the WG. Propagation losses in this context refer to any losses experienced by the light field while it is transmitted through the WG from the input to the output facet. It includes losses that may be induced by WG imperfections (e.g., by scattering due to finite surface roughness) or by absorption in the WG material. From the transmission through the WG of 93 % we can quote 0.08 dB/cm as an upper bound for the propagation losses at 738 nm. The dimensions of the ridge WG are designed to support only the

fundamental spatial mode at telecom wavelengths which usually implicates that higher order spatial modes can be excited in the visible. This leads to a poor mode overlap and thus reduces the conversion efficiency (see Sect. 3.2.3). Nevertheless, by carefully optimizing the mode matching, it is possible to excite only the fundamental WG mode at λ_a . This is proven by Fig. 5.1(b) which shows the mode profile of the collimated 738-nm beam after being transmitted through the WG. The image was recorded using a CCD camera. For comparison, Fig. 5.1(c) shows the calculated intensity distribution of the fundamental mode at 738 nm for a ridge WG with $8 \times 8 \mu\text{m}^2$ cross section. The calculations were performed following the method described in Sect. 3.2.3. Note that for the measurement shown in Fig. 5.1(b) the beam was collimated with an aspheric lens (effective focal length $f_{\text{eff}} = 11$ mm) and had to pass several neutral density filters before it hit the CCD chip of the camera (measurement was performed at mW power level). This may explain the slight distortion of the CCD image compared to the perfect mode profile shown in Fig. 5.1(c). After collimation behind the WG, the three wavelengths λ_a , λ_p , and λ_b are spatially separated by a Pellin–Broca prism in combination with a pinhole. By rotating the prism, we can select which of the three beams is coupled into a single-mode optical fiber to guide it to a commercial InGaAs/InP single-photon avalanche diode (SPAD; *id Quantique id201*) or a grating spectrometer (*Princeton Instruments SP2500A* with *OMA V* InGaAs linear array and *Spec-10* CCD camera) for spectral analysis. For detection with the SPAD, we eliminate residual pump light after the pinhole employing a 1450-nm longpass filter and a fiber-optic circulator together with a fiber Bragg grating (FBG; *AOS GmbH, S/N: 05111002*; center wavelength: 1557.025 nm, -1.0 dB reflection bandwidth: 0.769 nm). Insertion losses for the whole filtering system are 10 % (prism and two mirrors) plus 30 % (longpass filter). The input coupling efficiency into the circulator is ~ 50 %. All together, this results in a total transmission coefficient of $T_{\text{tot}} \approx 0.3$ (-5.2 dB), i.e., on the way from the WG exit to the active area of the detector 70 % of the generated C-band photons are lost due to spectral filtering. We estimate the suppression of pump light at $\lambda_p = 1403$ nm by the filtering system to be better than 130 dB.

5.1.2 Zn:PPLN Waveguide Chip

For down-conversion from 738 nm to the telecom C-band, a Zn:PPLN WG chip from *NTT Electronics Corp., Japan*, is used (*WD-1550-000-A-C-C-S001, S/N 3079044*). It was fabricated using a technique in which a periodically poled Zn:LiNbO₃ wafer is directly bonded onto a LiTaO₃ substrate. Subsequently, the Zn:LiNbO₃ layer is mechanically thinned and ridge WGs are cut with a dicing saw or fabricated via dry etching. The LiTaO₃ substrate (lower-index material) serves as a cladding layer for the Zn:PPLN WGs (higher-index material). For further details on the fabrication process see [118, 172, 173]. The chip is 40 mm long, 6 mm wide, and 0.5 mm thick. It contains a total of 12 WGs that are arranged in six groups of two as delineated in Fig. 5.2(a) and (b). The QPM grating periods have been tailored to cover a set of wavelengths around 738/1409/1550 nm. They are different for each group, i.e., $\Lambda_1 = 16.04$, $\Lambda_2 = 16.08$, ... ,

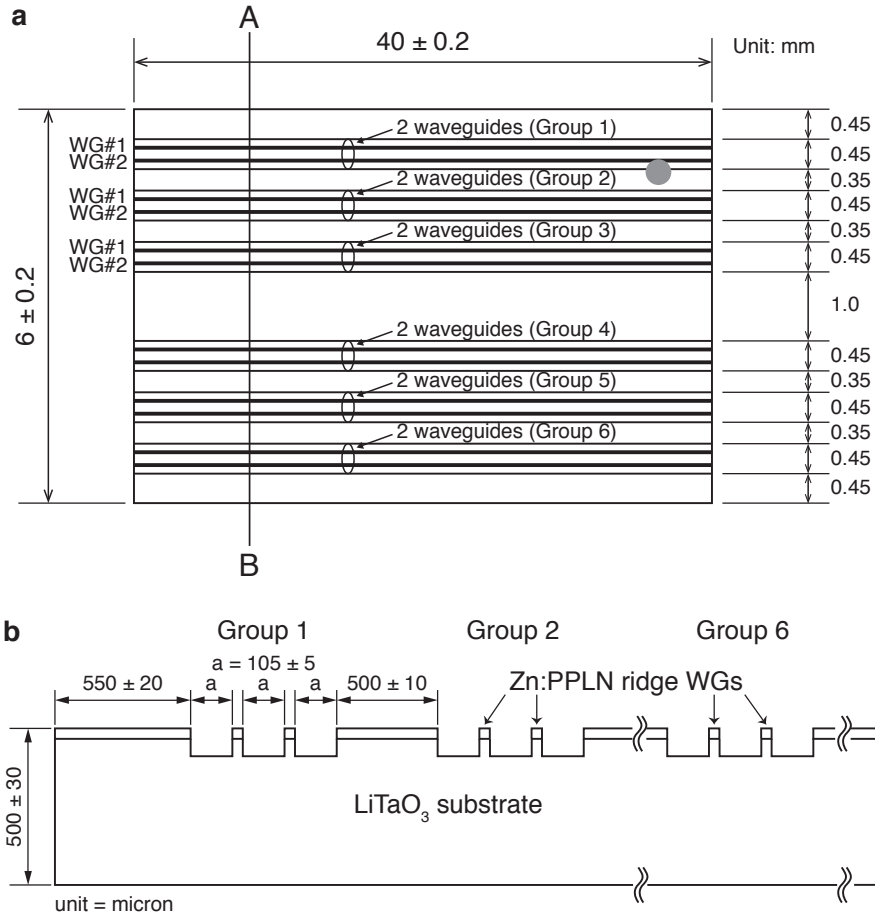


Figure 5.2: Dimensions and layout of the Zn:PPLN sample after [171] (Copyright © 2010 NTT Electronics Corp.). (a) Top view. (b) Cross section A–B.

$\Lambda_6 = 16.24 \mu\text{m}$, which allows for coarse wavelength tuning by choosing a certain WG. All WGs feature antireflection coatings for the spectral windows around λ_a , λ_p , and λ_b on the input and output facets. Figure 5.3(a) shows a photograph of the sample. The converter chip is fixed to a gold-plated copper mount on top of a 5-axis fiber alignment stage (*Newport M-562F-XYZ* with tilt platform *M-562F-TILT*) which allows for precise positioning of the sample. The WG temperature is controlled with a Peltier module to fulfill the QPM condition. A photograph of the sample on the stage can be seen in Fig. 5.3(b). For the experiments described in the following sections, WG #1, group 5 ($\Lambda_5 = 16.20 \mu\text{m}$) was chosen and the temperature was set to 21.3°C .

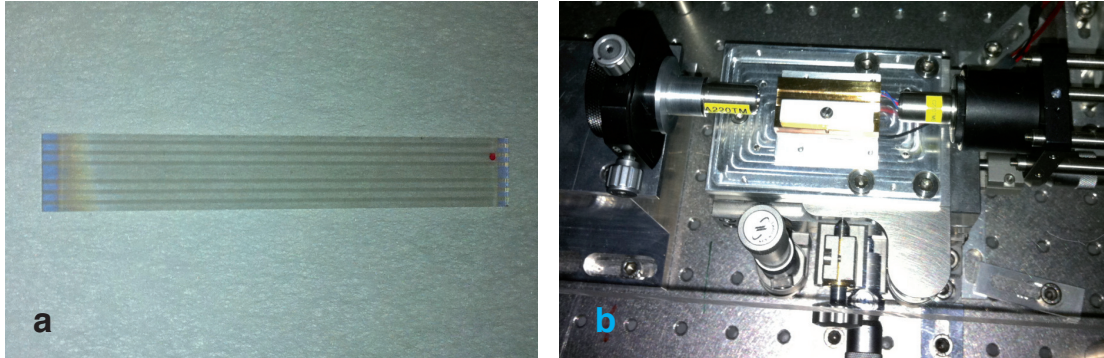


Figure 5.3: (a) Photograph of the Zn:PPLN sample. The 6 WG groups can well be recognized. The blueish gloom on the edges of the chip is due to the antireflection coating. (b) Photograph of the sample mounted on top of the 5-axis stage together with the aspheric lenses used for input and output coupling.

5.2 Down-Conversion from 738 nm to the C-Band: Experimental Results

5.2.1 Performance of the Frequency Converter

Before we conducted down-conversion experiments with input at the single-photon level we tested the performance of the WG chip at macroscopic power levels (mW regime). In the following, we briefly discuss how SPDC can be used to determine the right point of operation for (quasi-)phasematching a desired process. We will also investigate the depletion of 738-nm input light by the DFG process which is a measure for the conversion efficiency that can be expected.

Finding the Optimum Operating Point Using SPDC

In contrast to SHG or OPOs, in SFG/DFG processes two wavelength components are inserted into the crystal to generate a third one. Thus, measurement of the phasematching curve is usually performed by keeping one input wavelength fixed and tuning the second one. It is favorable to use a rapidly wavelength-tunable laser for this purpose, such as an external cavity diode laser (ECDL). Unfortunately, this is not possible in the present case. For preliminary tests and alignment, we use the Ti:sapphire laser at 738 nm and the MgO:PPSLT SRO at 1409 nm, none of which are rapidly tunable over a wide range. Nevertheless, we can apply a method which is based on SPDC and works with the Ti:sapphire laser alone to determine sets of parameters $\{\lambda_a, \lambda_b, \lambda_p, \Lambda, T\}$ for which $\Delta\beta = 0$ is satisfied. In this section, we return to the ‘classical’ notation introduced in the context of OPA/OPO (see Sect. 3.2.1) and denote the strongest light field with the shortest wavelength as the pump (λ_3) and the two generated fields as signal (λ_1) and idler (λ_2). Substituting $\lambda_3 \rightarrow \lambda_a$, $\lambda_1 \rightarrow \lambda_{p,b}$, and $\lambda_2 \rightarrow \lambda_{b,p}$ returns the notation that is used within the framework of QFC. By pumping a WG with a continu-

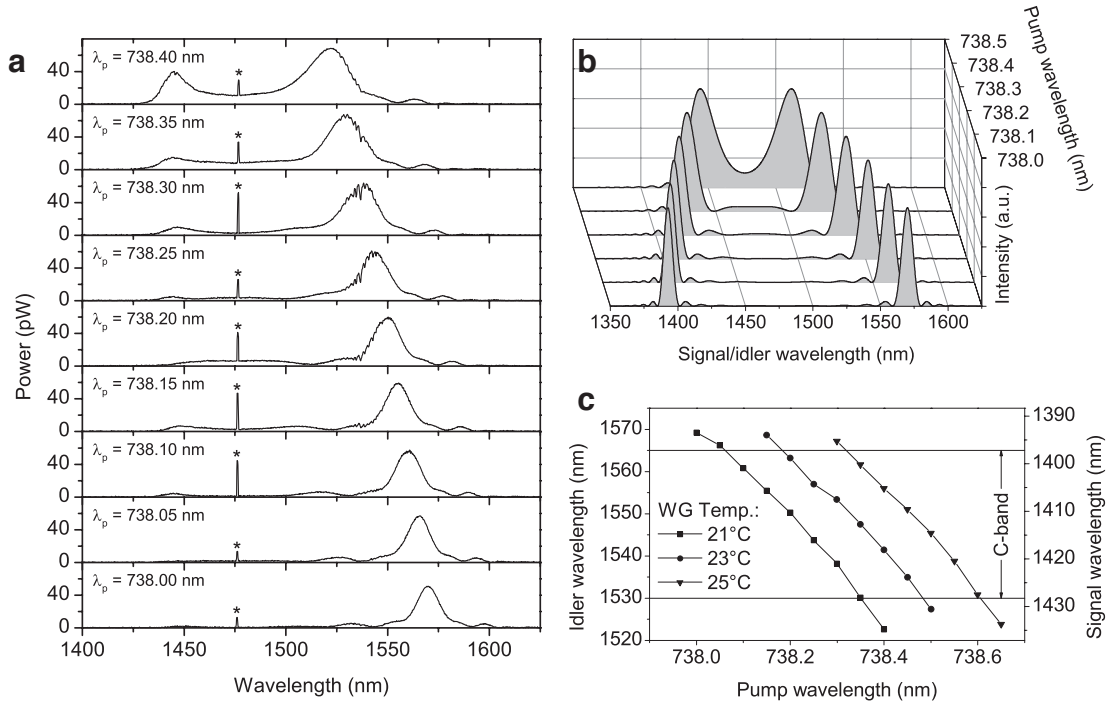


Figure 5.4: (a) SPDC spectra generated by 10 mW of pump power at different wavelengths around 738 nm. As we have used a longpass filter with a cut-on wavelength of 1450 nm, signal wavelengths that are shorter than this are blocked and only the idler spectrum is visible. The signal spectrum becomes clearly visible in the uppermost spectrum. The peak marked with an asterisk hardly changes its position at ~ 1476 nm and stems from second-order diffraction of the pump light in the OSA. It marks the point of wavelength degeneracy. The WG temperature was 21 °C in all measurements. (b) Calculated OPF spectra for a bulk crystal. (c) Points with $\Delta\beta = 0$ extracted from SPDC spectra. A slight variation of the input wavelength has big leverage at signal and idler wavelengths.

ous power of 10 mW around 738 nm, we generate OPF with an intensity that is strong enough to record the spectrum with the OSA. The spectra, obtained for different pump wavelengths around 738 nm, are exemplarily shown in Fig. 5.4(a) for WG #1, group 5. The Pellin–Broca prism in the experimental setup of Fig. 5.1 was removed for the measurements to avoid distortion of the spectra. The 1450-nm longpass filter is sufficient to block the 738-nm light in this case. The spectra in Fig. 5.4(a) are described by [66]

$$D(\Gamma, \Delta) = \Gamma^2 L^2 \left| \frac{\sinh(L\sqrt{\Gamma^2 - \Delta^2})}{L\sqrt{\Gamma^2 - \Delta^2}} \right|^2. \quad (5.1)$$

The above equation is the same as for the parametric gain in bulk crystals introduced in (3.8). For convenience, the phase mismatch Δ was written as

$$2\Delta = \beta_3 - \beta_1 - \beta_2 - 2\pi/\Lambda. \quad (5.2)$$

Note that, for waveguided SPDC, κ_1 and κ_2 in Eq. (3.4) must be calculated using (3.44) and (3.45). Since $\beta_m = k_m \times n_{\text{eff}}(\lambda_m, T)$, $m \in \{1, 2, 3\}$, and we do not know the exact function $n_{\text{eff}}(\lambda_m, T)$ for the WG modes, it is not possible to apply a proper curve fit to the spectra of Fig. 5.4(a). However, to see that the results are in qualitative agreement with theory, we consider calculated spectra for a bulk crystal in Fig. 5.4(b). Here we can use Sellmeier equations for LN to calculate analytic functions $n_{\text{eff}}(\lambda_m, T)$. From the measured and simulated curves we recognize that the central peaks of signal and idler spectrum become broader as they approach the point of wavelength degeneracy and eventually merge to one broad peak. For low gain ($\Gamma L \ll 1$), Eq. (5.1) can be approximated by [66]

$$D(\Gamma, \Delta) \approx \sinh^2 \left[\Gamma L \left(\frac{\sin \Delta L}{\Delta L} \right)^2 \right], \quad (5.3)$$

and for high gain ($\Gamma L \gg 1$) it becomes

$$D(\Gamma, \Delta) \approx \sinh^2 \Gamma L \exp(-(L/\Gamma)\Delta^2). \quad (5.4)$$

Thus, in the low gain regime the spectrum follows a sinc² function while for high gain the spectrum has a nearly Gaussian shape [66]. The measured and calculated spectra, shown in 5.4(a) and (b), respectively, correspond to the case of low to intermediate gain. The sidebands of the sinc² function are visible in both cases. For the calculated spectra $\Gamma L \approx 0.001$ was assumed. Figure 5.4(c) shows the parameter field $\{\lambda_3, \lambda_1, \lambda_2, T\}$ satisfying $\Delta = 0$ for WG #1, group 5. The data were extracted from the spectra in Fig. 5.4(a). As can be seen, slight variations of the pump wavelength have a large impact on signal and idler wavelength. With regard to single-photon down-conversion, this means that the visible emission wavelength of the single-photon source must be precisely controllable. We emphasize that the SPDC-based method that we have applied here is not as exact as methods based on SFG or DFG with input from tunable lasers. However, in our case it has turned out to be a fast and reliable way of finding a proper operating point.

We recall that the curves in Fig. 5.4(a) represent the parametric gain characteristics of the converter. If resonant feedback is provided in some way, e.g., by a reflective coating on the WG end facets [74] or by integration of the WG structure into a fiber loop [174], it is possible to build low-threshold and ultra-compact OPOs based on such devices. Besides, OPF from nonlinear WGs is commonly used to generate entangled photon pairs for quantum information and communication [175]. Apart from the applications discussed in the remainder of this thesis, our WG device could also be used for such applications.

Depletion of the 738-nm Input Signal

In the absence of propagation losses and competing nonlinear optical processes, the depletion of a weak input signal at λ_a by DFG must be equivalent to the generated

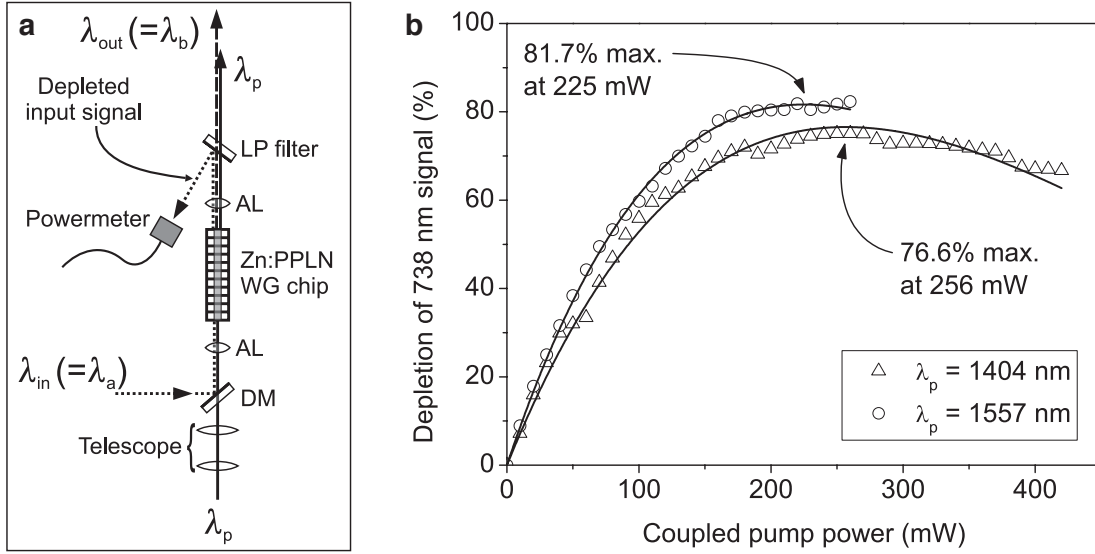


Figure 5.5: (a) Setup for measurement of the input signal depletion (DM: dichroic mirror, AL: aspheric lens, LP: longpass). (b) Depletion of the 738-nm input signal by DFG vs. coupled pump power for two different pump wavelengths. Solid lines are fits to the experimental data.

power at λ_b . This is a direct consequence of energy conservation. By competing nonlinear processes we mean that a significant amount of the input signal is converted to a wavelength other than λ_b . This can happen if another process is also quasi-phaseshifted by chance. In our case this could be excluded at least for the spectral range from 600–1700 nm. We recorded a complete spectrum of the unfiltered WG output with the OSA and found no further wavelength components except for the three expected lines at λ_a , λ_p , and λ_b .

We measured the depletion of a 1-mW input signal at $\lambda_a = 738$ nm in WG #1, group 5, as a function of the pump power in the WG. This was performed with the setup shown in Fig. 5.5(a). A 750-nm longpass filter (*Thorlabs FEL750*) is inserted behind the aspheric lens at the output of the WG. While 1404 nm and 1557 nm are transmitted by this filter, the 738-nm component is reflected and directed onto a Si-based powermeter (*Coherent OP-2 VIS*). With the pump beam blocked, the power at 738 nm is adjusted to $P_a(P_p = 0) = 1$ mW. Then, the pump beam is launched into the WG and the power $P_a(P_p)$ is recorded with the powermeter while the pump power is increased. The signal depletion is given by

$$\text{signal depletion} = 1 - \frac{P_a(P_p)}{P_a(0)}. \quad (5.5)$$

When propagation losses are neglected, Eq. (5.5) is equal to the internal conversion efficiency η_{int} . The measurement was performed twice. First, with $\lambda_p = 1404$ nm and $\lambda_b = 1557$ nm which is the wavelength combination for translation of the 738-nm signal to the C-band. Second, with interchanged λ_p and λ_b which is possible because the

cw SRO can be operated at both wavelengths. The result of both measurements is shown in Fig. 5.5(b). The data are fit using

$$\eta_{\text{int}}(P_p) = \eta_{\text{max}} \sin^2(\sqrt{\eta_{\text{nor}} P_p} L), \quad (5.6)$$

as derived at the end of Sect. 3.2.3. As compared with Eq. (3.67), the additional factor η_{max} was introduced to account for the non-unity efficiency. Both depletion curves in Fig. 5.5(b) show a maximum at a certain pump power level (hardly visible for the curve with $\lambda_p = 1557$ nm because of limited pump power). For values above this level the signal depletion decreases again. This is due to back-conversion via SFG between the fields at λ_p and λ_b and is in perfect agreement with theory. From the fits we determine $\eta_{\text{nor}} = 60.1$ %/W/cm² and $\eta_{\text{nor}} = 68.5$ %/W/cm² for $\lambda_p = 1404$ nm and $\lambda_p = 1557$ nm, respectively. Accordingly, the depletion maximum is reached at 256 mW (225 mW) with a maximum value of 76.6 % (81.7 %). It is interesting to note that these values seem to slightly depend on the pump wavelength. This is not expected from theory since the coupled mode equations are symmetric with respect to λ_p and λ_b . One possible explanation for this 5 % difference in signal depletion may be slightly different experimental conditions. Between the measurements, the idler wavelength of the cw SRO had to be set from 1404 nm to 1557 nm. This involves a translation of the PPSLT crystal inside the OPO cavity to change the QPM grating period, a different crystal temperature, and a re-alignment of the setup. As a result, the exact wavelengths were $\lambda_a = 738.226$ nm, $\lambda_p = 1403.576$ nm, $\lambda_b = 1557.310$ nm in the first measurement and $\lambda_a = 738.224$ nm, $\lambda_p = 1557.016$ nm, $\lambda_b = 1403.804$ nm in the second. In both runs, the WG temperature was $T = 22.4$ °C and the wavelength of the Ti:sapphire laser was optimized for maximum signal depletion. Visible wavelengths were measured with the wavemeter and telecom wavelengths with the OSA. As mentioned above, the influence of the slightly different operating points on the phasematching condition could be one reason for the difference in signal depletion. However, this explanation is not fully satisfying because the acceptance bandwidths (see Sect. 2.1.3) around 1404 nm and 1557 nm are broad (a calculation yields ~ 9 nm and ~ 11 nm, respectively) and thus the effect should be weak. Other explanations might be that a better spatial overlap of the WG modes was achieved in the second measurement ($\lambda_p = 1557.016$ nm) or that the WG attenuation is slightly different for 1404 nm compared to 1557 nm. A reliable test of the latter argument is difficult in practice because it requires a careful discrimination between input coupling losses and WG attenuation.

The results presented above indicate that the DFG process $1/\lambda_a - 1/\lambda_p = 1/\lambda_b$ in a nonlinear WG can be remarkably efficient—as expected from our theoretical considerations in Sect. 3.2.3. Depletion of the input signal between 77 % and 82 % is observed due to conversion of visible light to telecom light.

Phasematching Bandwidth

As we have seen in Sect. 2.1.3, second-order nonlinear processes feature a certain phasematching bandwidth which follows a sinc² law. This acceptance bandwidth can refer to

a number of parameters which determine the phasematching condition. For instance, in the context of QPM, the input wavelengths, crystal temperature, QPM grating period, or angle (between light beams and domain boundaries) are parameters which have to be within the acceptance bandwidth of a desired $\chi^{(2)}$ process [67]. Within this bandwidth, wavelength conversion happens efficiently and significant portions of the input power are distributed to light fields with other frequencies. We experimentally determined the signal wavelength acceptance bandwidth $\Delta\lambda_{\text{DFG}}$ for our frequency converter in the following way: a constant pump power of 27 mW at a fixed wavelength of 1403 nm was launched into the WG together with cw visible light from the Ti:sapphire laser. The wavelength of the Ti:sapphire laser was tuned from 737.816 nm to 738.616 nm while keeping the coupled power at a constant level of 0.8 mW. At the same time, we detected the generated power around 1557 nm with an InGaAs photodiode. The result is plotted in Fig. 5.6(a). In this figure, the data have been normalized with respect to the maximum of the central peak. From a sinc^2 fit we yield a spectral acceptance bandwidth of $\Delta\lambda_{\text{DFG}} = 0.16$ nm (FWHM). Note that the wavelength acceptance bandwidth for the visible input signal is two orders of magnitude narrower than the wavelength acceptance bandwidth for the infrared pump light. Evidently, the fit in Fig. 5.6(a) reproduces the data quite well around the central maximum while the tails of the measured curve significantly deviate from the fit. In general, such behavior indicates that the phase mismatch $\Delta\beta$ is not constant ($\Delta\beta = 0$ in the ideal case) along the propagation direction because of inhomogeneities (spatial fluctuations of the refractive index due to fluctuations in stoichiometry or WG imperfections, temperature variations along the crystal, etc.). This was studied for the first time by Nash *et al.* [176] for the case of SHG in bulk LiNbO₃. It was shown that the area under the sinc^2 -shaped phasematching curve divided by the height of the central peak can be considered a figure of merit for the effective nonlinear susceptibility of the crystal (while the phasematching curve can change its shape, the area under the curve is constant). The relation between the shape of the phasematching curve and the conversion efficiency was also studied for quasi-phasematched SHG in periodically poled materials [67] and has been experimentally observed for various $\chi^{(2)}$ processes in different types of QPM WG devices [118,177,178]. In our case, inhomogeneities could result, for example, from slightly imperfect WG structures or minimal variations in WG temperature. We calculated the sinc^2 curve for a 40-mm-long crystal using Sellmeier data from [101] (see Fig. 5.6(b)). From the theoretical curve we find a spectral acceptance bandwidth of $\Delta\lambda_{\text{DFG, theo}} = 0.11$ nm which is slightly narrower than the value determined from the measured data. In Fig. 5.6(b) we have normalized the experimental data from Fig. 5.6(a) such that the area under the measured curve and the area under the theoretical curve are identical. With this normalization method the maximum of the measured data drops to 0.65. According to [176], this means that the maximum intensity that can be generated at the target wavelength λ_b should be expected to be lower by a factor of 0.65 compared with the ideal situation (perfect sinc^2 function).

The temperature acceptance bandwidth ΔT_{DFG} was measured, too. This was performed by setting the two input wavelengths to fixed values and ramping the crystal

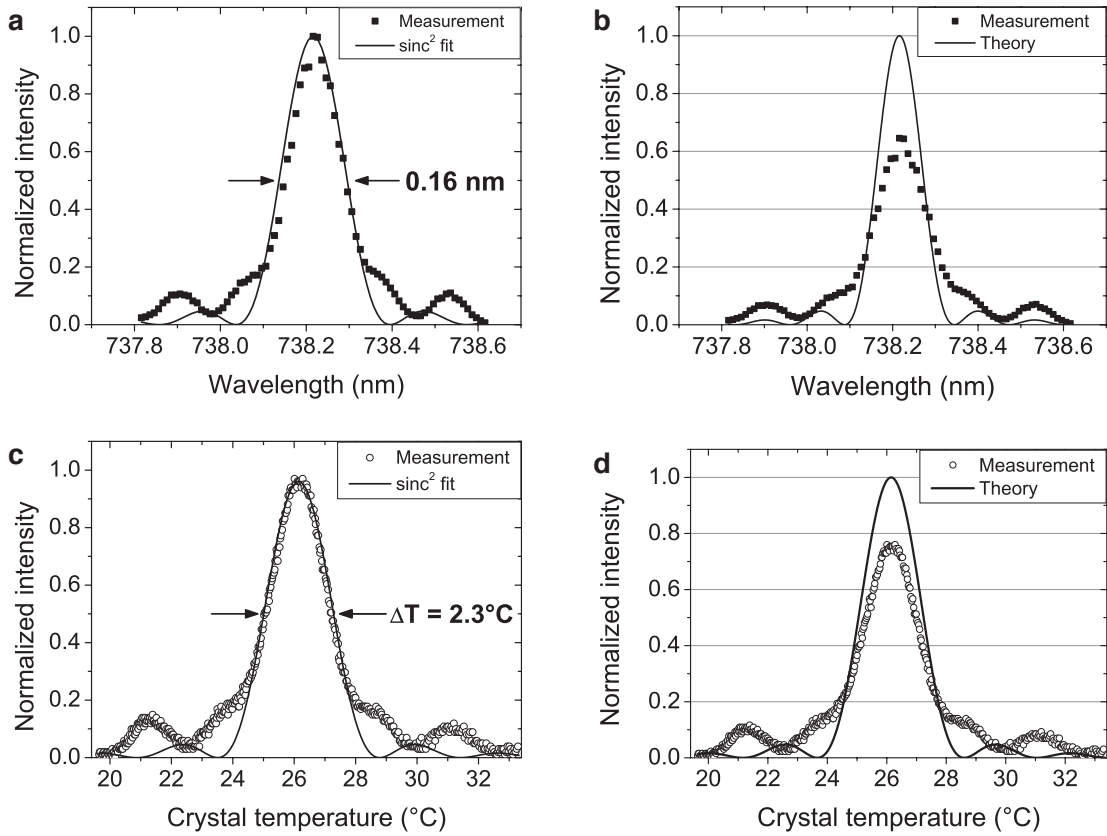


Figure 5.6: DFG acceptance bandwidths for the 40-mm-long WG. (a) Spectral acceptance bandwidth: measured data and sinc^2 fit. The data are normalized with respect to the central maximum. Figure after [49] (Copyright © 2011 Optical Society of America). (b) Same experimental data as in (a) but with different normalization for comparison with theory. The data are normalized such that the integrated area under the measured curve equals the area under the perfect sinc^2 curve predicted from theory (not a fit). (c) Measured temperature acceptance bandwidth and sinc^2 fit. (d) Same experimental data as in (c) but with normalization as in (b) for comparison with theoretical curve.

temperature with $\sim 1.7^\circ\text{C}/\text{min}$ (using the voltage input of the temperature controller for external control). The measurement was repeated several times at slightly different operating points. In all cases, we find $\Delta T_{\text{DFG}} = 2.3^\circ\text{C}$ from a sinc^2 fit. Exemplarily, Fig. 5.6(c) shows a recorded curve which attains its maximum at 26.2°C ($\lambda_a = 738.473\text{ nm}$, $\lambda_p = 1404.726\text{ nm}$). A temperature bandwidth of 2.3°C is not critical for later experiments since the accuracy of the temperature controller is typically 0.01°C . In analogy to the wavelength acceptance measurement in Fig. 5.6(a) and (b), we observe a discrepancy between experiment and theory concerning the tails of the sinc^2 function. In Fig. 5.6(d) the measured data have been normalized as in Fig. 5.6(b) for a comparison of the measured data with the ideal sinc^2 function. The FWHM

bandwidth of the theoretical function is $\Delta T_{\text{DFG, theo}} = 2.2^\circ\text{C}$ in good agreement with the measured value. The maximum of the central peak of the experimental data in Fig. 5.6(d) is 0.75. This factor is higher than the value of 0.65 obtained from the measurement of the wavelength acceptance bandwidth. We will comment on the reliability of estimating the expected conversion efficiency by the method described in [176] after we have discussed an experiment in which we have actually determined the conversion efficiency (see Sect. 5.2.4).

5.2.2 Investigation of Raman Noise

For quantum frequency converters, it is known that noise, i.e., unwanted photons at the target wavelength λ_b , can be generated by the strong driving field at λ_p . The reason is either spontaneous parametric down-conversion (SPDC) [47] or spontaneous Raman scattering [125] induced by the pump light. Figure 5.7 recalls the basic properties of Raman scattering. Stokes Raman scattering generates red-shifted photons and thus may be an issue in our experiment for $\lambda_p < \lambda_b$ while anti-Stokes Raman scattering generates blue-shifted photons and thus might cause problems for $\lambda_p > \lambda_b$. In the following sections we investigate the noise properties of our frequency converter in more detail.

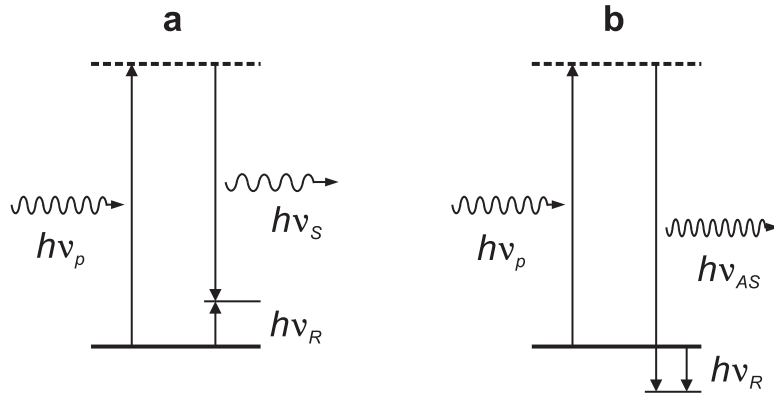


Figure 5.7: Virtual energy levels for Raman scattering in the photon/phonon picture (after [16]). (a) Stokes Raman scattering: the scattered photon has a lower frequency than the pump photon $\nu_S < \nu_p$, i.e., the scattered light is red-shifted with respect to the pump. A phonon with energy $h\nu_R = h(\nu_p - \nu_S)$ is created. (b) Anti-Stokes Raman scattering: opposite process as in (a). The scattered photon has a higher frequency than the pump photon $\nu_{AS} > \nu_p$, i.e., the scattered light is blue-shifted with respect to the pump. A phonon with energy $h\nu_R$ is destroyed and a photon at frequency $\nu_{AS} = \nu_p + \nu_R$ is created.

Stokes Raman Scattering

To record the noise spectrum, we coupled $P_p = 100\text{ mW}$ into the WG. Behind the collimation asphere, two mirrors are used to directly couple the light into a SMF-28

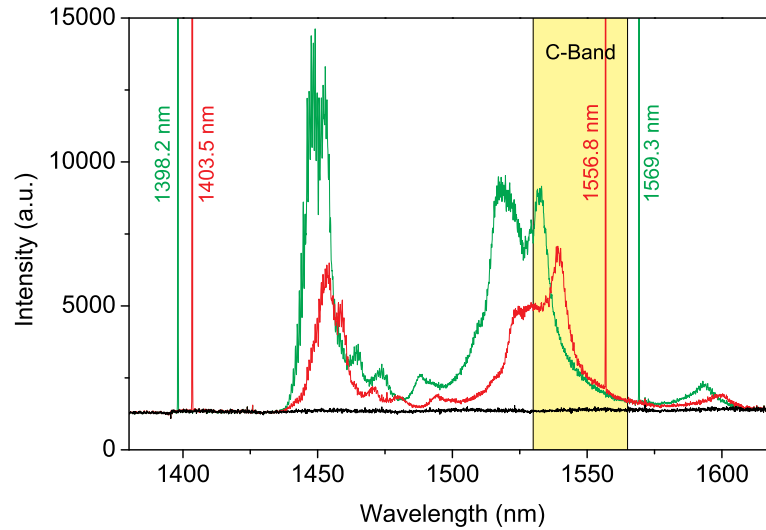


Figure 5.8: Raman spectra generated in the frequency converter by 100 mW of coupled power at 1398.2 nm (green) and 1403.5 nm (red). The black line represents the dark count level of the spectrometer’s InGaAs array. The yellow-shaded area indicates the telecom C-band. Lines at 1556.8 nm and 1569.3 nm are generated by DFG and are shown by way of illustration. Figure after [49] (Copyright © 2011 Optical Society of America).

fiber which guides it to the *Princeton Instruments* grating spectrometer. In this case, the whole spectral filtering system as described in Sect. 5.1.1 was bypassed to prevent distortion of the spectrum. Instead, two longpass filters (cut-on wavelength 1450 nm) were mounted in front of the fiber entrance to attenuate the intense light at λ_p . Thus, we avoid saturation of the spectrometer’s InGaAs array and the amount of spontaneous Raman scattering generated in the fiber [179] is kept negligibly low. We recorded the spectra at wavelengths > 1450 nm for two different pump wavelengths, 1398.2 nm and 1403.5 nm. The results are shown in Fig. 5.8. We see that the spectra exhibit several distinct peaks and that all spectral features shift with the pump wavelength. This is a first indication that Raman scattering is involved. To investigate this in more detail, Fig. 5.9 shows a comparison of the two spectra with a Raman spectrum of a bulk MgO:LiNbO₃ sample excited with laser light at 647 nm along the *c* axis of the crystal (note that the effect of different dopants, Zn or Mg, can be neglected here [180]). All three spectra were fit with a sum of N Lorentzian functions given by

$$I(\bar{\nu}) = \sum_{k=1}^N \frac{2A_k w_k}{4\pi(\bar{\nu} - \bar{\nu}_{c,k})^2 + w_k^2}, \quad (5.7)$$

where $I(\bar{\nu})$ denotes the intensity as a function of the wavenumber $\bar{\nu}$, and A_k , w_k , $\bar{\nu}_{c,k}$ are the amplitude, the width, and the center wavenumber of the k -th peak, respectively. The number of peaks N was chosen so as to achieve the best correlation between the fit and the measured data. The peak centers $\bar{\nu}_{c,k}$ determined from the fits are com-

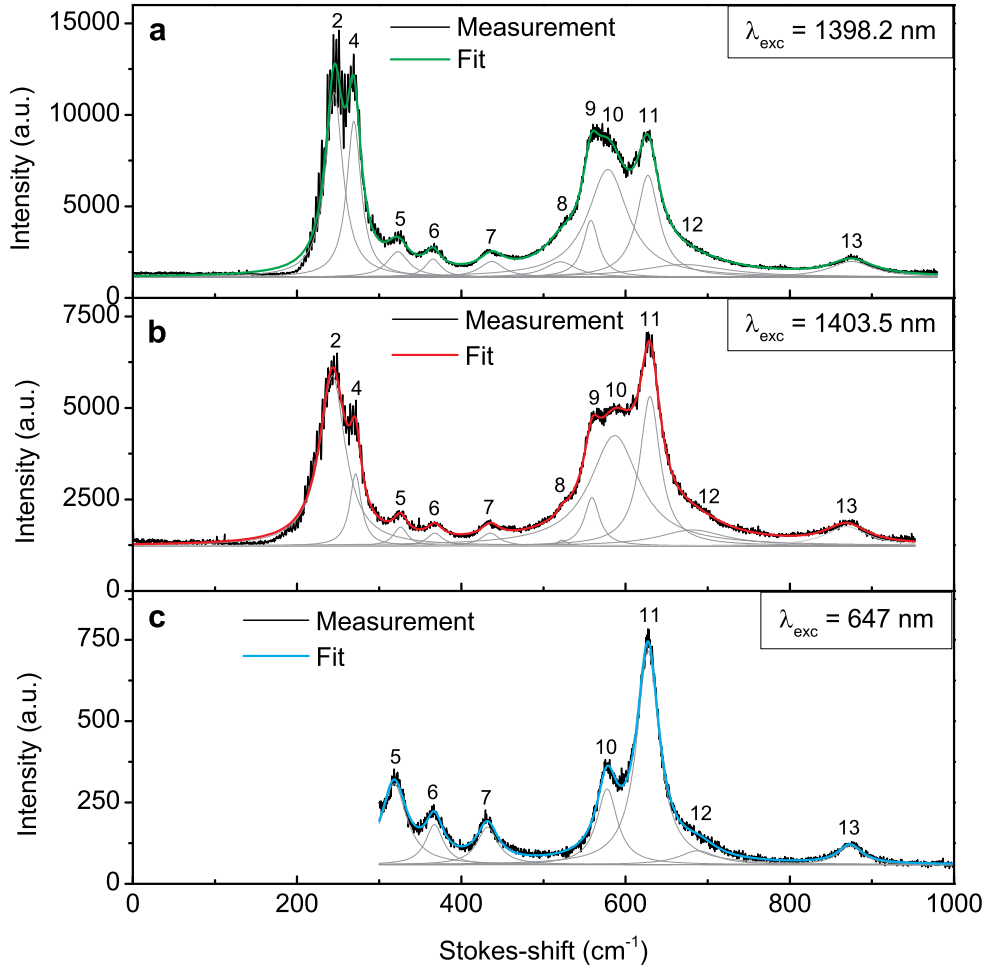


Figure 5.9: Comparison of Stokes Raman shifts. (a), (b) Stokes Raman spectra obtained using the Zn:PPLN WG. The excitation wavelengths are $\lambda_{\text{exc}} = 1398.2$ nm and 1403.5 nm. (c) Stokes Raman spectrum of a bulk MgO:PPLN sample excited at $\lambda_{\text{exc}} = 647$ nm (measurement by A. Lenhard). The offset for this spectrum is lower because it was measured with the Si CCD camera of the spectrometer which has a lower dark count level. Raman shifts < 300 cm^{-1} could not be measured for technical reasons. The center frequencies of the labeled peaks are given in Table 5.1.

pared to measured values for a stoichiometric LiNbO_3 single crystal [181] in Table 5.1. The spectra in [181] were recorded at an excitation wavelength of $\lambda_{\text{exc}} = 488$ nm in the $X(ZZ)Y$ and the $Z(YZ)X$ orientation.¹ Like Raman spectra obtained from other

¹The Porto notation is commonly used in Raman spectroscopy. It refers to the direction of wavevector and polarization of the excitation light and scattered light with respect to the crystallographic axis. For example, $Z(YZ)X$ means that the direction of the excitation beam is parallel to the Z axis and the scattered light is observed in X direction (first and fourth letter outside brackets) while the polarization of the excitation light is parallel to the Y axis and the polarization of the scattered light is parallel to

crystalline materials, the Raman spectrum of LiNbO_3 depends on the geometry of the experiment, i.e., on the direction and polarization of the excitation light and of the observed scattered light with respect to the crystallographic axes [182]. Compared to a bulk crystal, the situation is even more complicated in the case of a WG crystal. Here light that would otherwise exit the crystal in another direction is guided to the WG output and we have to consider different geometries for the assignment of Raman lines. In our measured spectra, we can clearly identify the 238, 276, 325, 371, 431, 582, and 871 cm^{-1} lines of Ref. [181]. Note that a deviation of $\Delta\bar{\nu} = 5\text{ cm}^{-1}$ corresponds to a wavelength difference of only $\Delta\lambda \approx 1.2\text{ nm}$ at 1550 nm (even smaller for shorter wavelengths). The spectrometer was not calibrated with respect to an absolute reference in this wavelength range. Deviations on this order of magnitude can thus be considered as a combined effect of experimental and numerical (from the multi-peak fit) uncertainties. In the case of excitation at 1398.2 nm and 1403.5 nm , we observe three further lines at $\sim 520\text{ cm}^{-1}$, $\sim 560\text{ cm}^{-1}$, and around 680 cm^{-1} that are not reported for the stoichiometric LiNbO_3 single crystal. The 680 cm^{-1} peak is also found in the spectrum excited at 647 nm . The origin of these extra features is unclear. However, they only have a subliminal effect on the shape of the spectra. In general, the exact shape and intensity of spectral features in Raman spectra excited in LiNbO_3 or its various doped derivatives depend on multiple factors. For example, it can be influenced by the composition of the crystal (congruent or stoichiometric) [183, 184], the temperature of the sample [185], the dopants (undoped, MgO-doped, Zn-doped, ...) [184], or, obviously from Fig. 5.9(a)–(c), by the wavelength of the excitation light. A more detailed study is beyond the scope of this work. Nevertheless, the Stokes Raman shifts for the peaks No. 2, 4–7, 10, 11, 13 of the measured spectra are in good agreement. This observation and the comparison with the Raman spectra reported for a stoichiometric LiNbO_3 single crystal provide convincing evidence that the dominating noise source in our experiment is spontaneous Stokes Raman scattering. We assume that SPDC of the pump light [47] can be excluded as a noise source in our case since the splitting of a 1403-nm pump photon into a 1550-nm and a $14.8\text{-}\mu\text{m}$ photon is extremely inefficient because of the strong absorption of the crystal at wavelengths $> 5\text{ }\mu\text{m}$.

Anti-Stokes Raman Scattering

So far, we have considered Stokes Raman scattering since it is the relevant noise process for a scheme where $\lambda_p < \lambda_b$. This short-wavelength pumping is inevitable if we want to perform frequency down-conversion from 738 nm to the C-band in a single conversion step. However, it is worthwhile to briefly discuss the strength of anti-Stokes Raman scattering which can be the reason for noise in the case of long-wavelength pumping, i.e., $\lambda_p > \lambda_b$ [46, 48]. As shown in Fig. 5.10, anti-Stokes Raman scattering is observed in our device as well. To obtain the spectrum of Fig. 5.10, the cw SRO was tuned to 1535.8 nm and 185 mW of excitation power were coupled into the WG at this wavelength. The filtering system for the anti-Stokes measurement consists of a shortpass

the Z axis (second and third letter in brackets). The analogue applies for $X(ZZ)Y$.

Table 5.1: Comparison of measured Stokes and anti-Stokes Raman shifts (in $[\text{cm}^{-1}]$) with values from Ref. [181].

Peak No. ↓	This work			Ref. [181]	
λ_{exc} [nm] →	Stokes		Anti-Stokes	Stokes	
	1398.2	1403.5	1535.8	488	
	Waveguide		Waveguide	$X(ZZ)Y$	$Z(YZ)X$
1	—	—	—	160	155
2	245	243	—	233	238
3			—	260	255
4	269	271	—	273	265
5	323	326	318	321	325
6	366	368	367	373	371
7	437	435	432	436	431
*8	521	523			
*9	558	559			
10	579	587	577	574	582
11	627	630	627		633
*12	671	681	688		
13	875	869	873		871

*The origin of these peaks is unclear.

filter (cut-off wavelength: 1470 nm) and a FBG (*TeraXion Inc.*, S/N : C098720; center wavelength: 1535.822 nm, -0.5 dB reflection bandwidth: ± 10 GHz) which suppress the intense excitation light. As for the Stokes Raman spectrum, we apply function (5.7) with $N = 9$ to fit the anti-Stokes spectrum. The center peak positions are found at 160, 233, 260, 273, 321, 373, 436, 574 cm^{-1} and are also compiled in Table 5.1. Each of the peaks can be assigned to lines that are also reported for single crystal stoichiometric LiNbO_3 in Ref. [181]. We notice that the peak at $\sim 630 \text{ cm}^{-1}$ (and also the smaller peak at $\sim 870 \text{ cm}^{-1}$) does not seem to exist in the anti-Stokes spectrum although it is present in all Stokes spectra in Fig. 5.9(a)–(c) and is also reported in Ref. [181]. In addition to what was mentioned before on the several factors that influence the exact shape and intensity of LiNbO_3 Raman spectra, there are two possible explanations for this phenomenon. First, as the steep slope at $\sim 600 \text{ cm}^{-1}$ resembles the characteristic of an edge-pass filter, one could speculate that the peaks do exist but are not transmitted due to absorption by one or more optical components in the setup. This was carefully checked and can be excluded. A second explanation, which better fits into the whole picture, is that the integrated intensity of the individual Raman peaks depends on the excitation wavelength. This phenomenon is also observed in the Stokes spectra of Fig. 5.9(a)–(c) where the relative heights of the peaks at $\sim 580 \text{ cm}^{-1}$ and $\sim 630 \text{ cm}^{-1}$ depend on the excitation wavelength (cf. peaks No.10 and 11 in Fig. 5.9(a)–(c)). A variation of the relative amplitudes of the 580 cm^{-1} and 630 cm^{-1} Raman peaks, in-

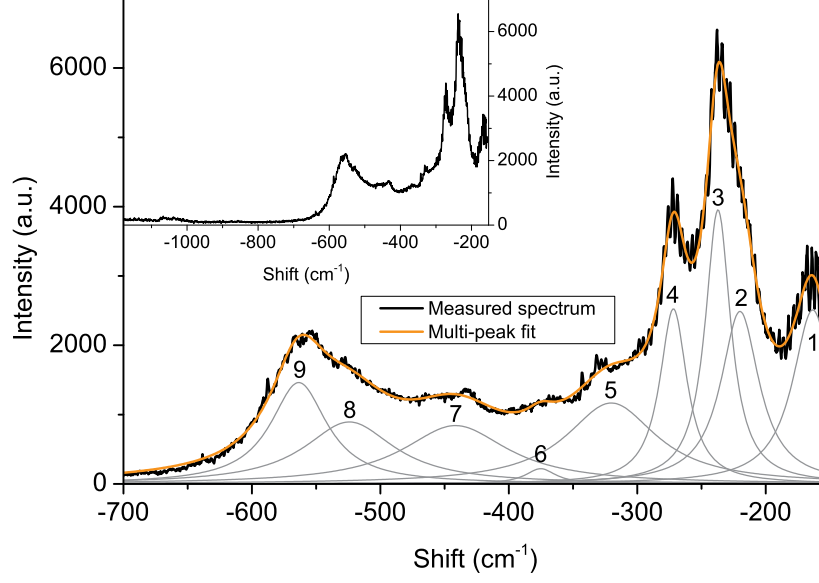


Figure 5.10: Spectrum of the anti-Stokes Raman light behind the WG and multi-peak fit. For excitation, a power of 185 mW at 1536 nm was inserted into the device. The inset shows a larger spectral interval from -1178 cm^{-1} to -152 cm^{-1} corresponding to a wavelength range of 1300–1500 nm. Dark counts were subtracted.

cluding a virtual suppression of the 630 cm^{-1} peak, has been previously observed by Sidorov *et al.* [184]. A resonance between Raman scattering and the electronic polaron absorption band is supposed to be responsible for varying Raman line intensities [184].

Stokes vs. Anti-Stokes Scattering

According to theory, the intensities $I_{AS}(\bar{\nu})$ and $I_S(\bar{\nu})$ of anti-Stokes and Stokes Raman bands measured at Raman shifts $\bar{\nu}$ (cm^{-1}) are related by the Boltzmann factor [186]

$$\exp(-hc\bar{\nu}/kT) = \frac{I_{AS}(\bar{\nu})/(\bar{\mu} + \bar{\nu})^4}{I_S(\bar{\nu})/(\bar{\mu} - \bar{\nu})^4}, \quad (5.8)$$

where $\bar{\mu}$ is the frequency (cm^{-1}) of the excitation source and T is the temperature (K) of the sample. To experimentally check relation (5.8), it would be desirable to record the full Raman spectrum (anti-Stokes and Stokes together) over 2000 cm^{-1} in a single sweep. Unfortunately, this turns out to be an intricate task because calibration of the setup's transmission properties in such a wide spectral range is quite involved. Thus, we restrict our experimental analysis to the peak around $\pm 580 \text{ cm}^{-1}$ which can be identified in both Figs. 5.9 and 5.10. Moreover, the measurement was performed with excitation light at 735 nm because at telecom wavelengths it is not possible to achieve proper alignment for anti-Stokes and Stokes Raman light simultaneously with the employed setup. By comparing the integrated intensities ($578\text{--}594 \text{ cm}^{-1}$) of anti-Stokes and Stokes Raman

peaks, we experimentally find $I_{AS}/I_S \approx 0.11$. This is in reasonable agreement with the theoretical prediction of $I_{AS}/I_S = 0.08$ calculated from relation (5.8) for $T = 295$ K and $\bar{\mu} = 13\,605$ cm^{-1} (735 nm). Assuming that similar conditions prevail for the case of telecom wavelength excitation, we would gain one order of magnitude in signal-to-noise ratio by interchanging λ_p and λ_b in our experiment. In the present case, this does not seem desirable as an ultimate goal since wavelengths around 1400 nm are critical in terms of fiber transmission losses (water peak). In general, however, we could exploit the reduced noise on the anti-Stokes side of the Raman spectrum and use a long-wavelength pumping scheme (see Chap. 6). In addition to that, our investigations suggest that it is always favorable (also in the case of short-wavelength pumping) to choose a large spectral separation between the pump and the target wavelength to suppress Raman noise. From the measured Raman spectra one could assume that all significant Raman peaks of LN can be found at Raman shifts below 1000 cm^{-1} . This conjecture is proven by a recent measurement of Pelc *et al.* [187] who recorded a (Stokes) Raman spectrum of a reverse-proton-exchanged PPLN WG for shifts from 200 cm^{-1} up to 1700 cm^{-1} . In their measurement, no further Raman peaks were found beyond 1000 cm^{-1} . In view of this fact, it would be favorable to select 1310 nm (telecom O-band) as the target wavelength in our experiment. With 738-nm input photons this would require a 1690-nm pump wavelength, meaning that the spectral separation between pump and target wavelength is > 1700 cm^{-1} .

5.2.3 Spectral Filtering

As can be seen from Fig. 5.8, the Stokes Raman noise stretches over hundreds of nanometers and no particular spectral interval, especially not in the C-band, can be identified which is not affected by a certain noise background. It is obvious that, without any spectral filtering, the amount of generated noise photons is not tolerable for QFC. For experiments at the single-photon level, we thus employ the spectral filtering system introduced in Sect. 5.1 which acts as a narrow bandpass filter. To illustrate its effect, we recorded the spectrum of the light exiting port 2 and port 3 of the circulator-FBG arrangement. This is shown in Fig. 5.11. The black curve represents the part of the spectrum as ‘seen’ by a single-photon detector when connected to port 3 while the grey curve is the part which is discarded at port 2. For this measurement, the coupled pump power at 1403 nm was 100 mW while the signal light field at 738 nm was attenuated to 2 pW. By comparing the integrated areas under the spectra in Fig. 5.11, we infer that a noise suppression by a factor of ~ 110 is achieved thanks to the circulator and the FBG. In the next section, we will investigate the influence of residual Raman noise on the performance of the frequency converter under realistic experimental conditions.

5.2.4 Conversion Efficiency with Single-Photon-Level Input

The frequency down-conversion will be most efficient if the spectral bandwidth $\Delta\lambda_a$ of the input photons satisfies the condition $\Delta\lambda_a \leq \Delta\lambda_{\text{DFG}}$. Considering typical interaction

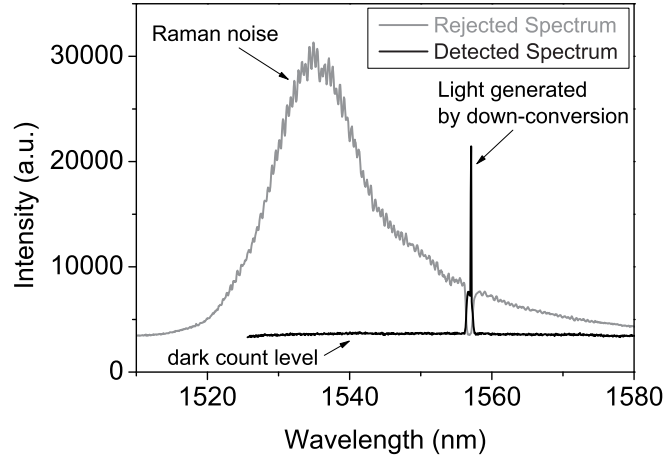


Figure 5.11: Spectra of the light leaving port 2 (rejected spectrum) and port 3 (detected spectrum) of the circulator–FBG arrangement (see optical setup in Fig. 5.1(a)). Figure after [49] (Copyright © 2011 Optical Society of America).

lengths of 10–60 mm, we can calculate $\Delta\lambda_{\text{DFG}}$ to be on the order of 0.1 nm in the case of our wavelength combination. In Sect. 5.2.1 we have measured $\Delta\lambda_{\text{DFG}} = 0.16$ nm for our 40-mm-long WG. For photons generated by a single color center in diamond at room temperature, this is hard to achieve. Currently, the emission linewidths of the narrowest color centers (SiV centers) are on the order of 1 nm at room temperature [60]. Consequently, the mismatch between $\Delta\lambda_a$ and $\Delta\lambda_{\text{DFG}}$ reduces the conversion efficiency. One solution to this problem can readily be implemented by cooling of the diamond sample to temperatures below 30 K where the emission linewidth of the SiV centers becomes as narrow as 0.17 nm [60]. Another promising approach which currently is subject to intensive research is the coupling of a color center to a cavity [164, 165, 188]. In the future, this may allow for much narrower emission linewidths even at room temperature. However, these concepts are not yet satisfactorily implemented. The emission linewidths of the bright SiV centers investigated in [60] were measured to be 0.7–2.2 nm at room temperature while count rates up to $4.8 \times 10^6 \text{ s}^{-1}$ were observed. Assuming a Lorentzian lineshape and perfect phasematching, we can estimate that the flux of photons lying within the measured 0.16-nm phasematching bandwidth is on the order of a few 10^5 s^{-1} . Thus, we simulate realistic experimental conditions by setting the repetition rate of the pulse picker to $\nu_{\text{rep}} = 500 \text{ kHz}$ and attenuating the 738-nm light to an average photon number per pulse of $\langle n_a \rangle \approx 0.76 < 1$ (this corresponds to an optical power of $\sim 100 \text{ fW}$). The temporal width of the generated pulses, limited by the resolution of the pulse picker, was determined to be 9.4 ns (FWHM) as shown in Fig. 5.12.

Using the setup as in Fig. 5.1(a) with the InGaAs/InP SPAD, the conversion efficiency of the setup can be determined. We define $N_{\text{dc+R}}$ as the count rate of the detector at 1557 nm when only pump light is present in the WG (signal light blocked). In this case,

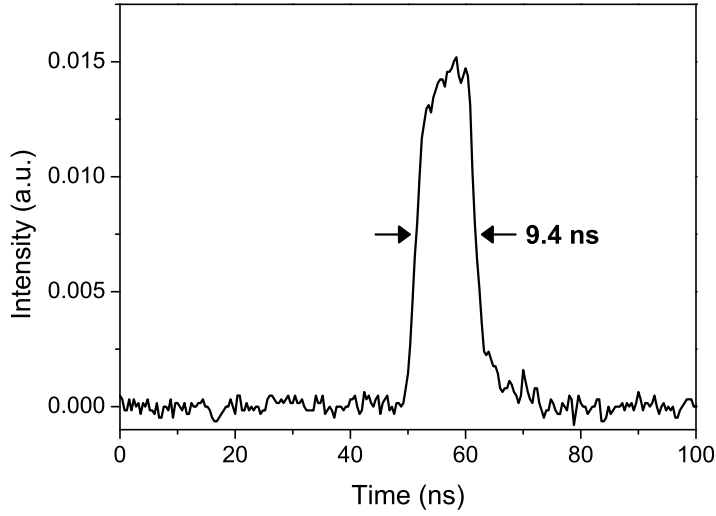


Figure 5.12: Temporal shape of the pulses at 738 nm recorded with a Si photodetector (1 ns rise time). Figure after [49] (Copyright © 2011 Optical Society of America).

a detection event can either be caused by a detector dark count (dc) or by a Raman photon (R) that was generated by the strong pump. We further define $N_{\text{dc+R+b}}$ as the count rate when both, pump and signal light, are coupled into the WG. In this situation, a detection event can additionally be caused by a photon at λ_b which was generated by DFG. We measured the count rates $N_{\text{dc+R}}$ and $N_{\text{dc+R+b}}$ as a function of the pump power. The result is shown in Fig. 5.13(a). The number of photons N_b generated by DFG (net count rate) is easily obtained from $N_b = N_{\text{dc+R+b}} - N_{\text{dc+R}}$ and is also shown in the plot. In this measurement, the parameters of the InGaAs/InP detector were set to the following values: detection efficiency $\eta_{\text{det}} = 0.25$, trigger rate $\nu_t = \nu_{\text{rep}} = 500$ kHz (external from pulse picker), gate width $\tau_g = 5$ ns, dead time $\tau_d = 1$ μs . With these settings, the dark count rate of the detector is about $N_{\text{dc}} = 107$ s^{-1} corresponding to a dark count probability of 2.14×10^{-4} within a gate time. From the count rates given in Fig. 5.13(a), the maximum total conversion efficiency of our setup is readily calculated to be

$$\eta_{\text{tot}}^{\text{max}} = \frac{N_b}{\langle n_a(0) \rangle \nu_{\text{rep}}} \approx \frac{8000 \text{ s}^{-1}}{0.76 \times 500000 \text{ s}^{-1}} \approx 0.02 \quad (5.9)$$

including detection and $0.02/\eta_{\text{det}} = 0.08$ without detection. The internal conversion efficiency is given by $\eta_{\text{int}} = \langle n_b(L) \rangle / \langle n_a(0) \rangle$, where $\langle n_a(0) \rangle$ is the average number of signal photons per pulse coupled into the WG and $\langle n_b(L) \rangle$ is the average number of converted photons per pulse exiting the WG. Since the transmission of the attenuator is known, $\langle n_a(0) \rangle$ can be determined by measuring the optical power before the attenuator. $\langle n_b(L) \rangle$ is calculated from the measured net count rate N_b using $\langle n_b(L) \rangle \nu_{\text{rep}} = N_b / (T_{\text{tot}} \times \eta_{\text{det}} \times 0.86 \times 0.47)$, where the factor 0.86×0.47 takes into account the non-perfect extinction ratio of the pulse picker and the mismatch between the

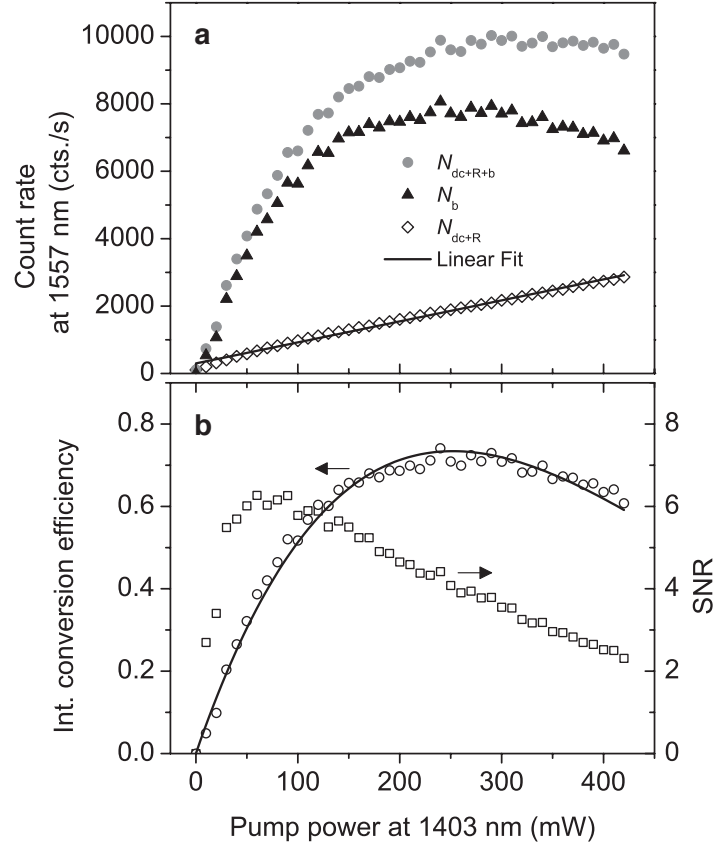


Figure 5.13: (a) Count rates with only pump light (open squares) and with pump + signal light (grey dots) coupled into the WG. Filled triangles represent the net count rate. (b) Internal conversion efficiency (open circles) and signal-to-noise ratio (open squares) of our setup vs. pump power. Figures after [49] (Copyright © 2011 Optical Society of America).

temporal width of the signal pulses and the gate width of the detector. Figure 5.13(b) shows η_{int} of our frequency converter as a function of the coupled pump power P_p . The data are fit according to relation (5.6). A maximum of $\eta_{\text{int}}^{\text{max}} > 0.73$ at 240 mW of pump power is achieved with the normalized efficiency $\eta_{\text{mor}} = 61\%/\text{W}/\text{cm}^2$. This is in good agreement with the values of $\eta_{\text{int}}^{\text{max}} = 0.77$ at 256 mW and $\eta_{\text{mor}} = 60\%/\text{W}/\text{cm}^2$ which were determined in the depletion measurement at a macroscopic signal power level (see Sect. 5.2.1). The slight deviation between the optimum pump powers can be explained by uncertainties in the fit function.

It is clear that the above method of measuring the internal conversion efficiency may also be affected by several experimental uncertainties. For example, to calculate $\langle n_b(L) \rangle$ we have to multiply a number of quantities that are subject to measurement errors themselves. Further, we have chosen a relatively short dead time of $1\ \mu\text{s}$ for the InGaAs/InP detector. This might cause additional detection events generated by the detector after-

pulsing effect [189] which could lead to an over-estimation of the conversion efficiency. To evaluate the potential impact of this effect, the afterpulsing probability was independently measured by means of an autocorrelation technique [190]. The measured probability shows a nearly exponential decay in time. For the parameters of our experiment, we yield an upper limit for the afterpulsing probability of 4.4 % which could add a maximum error of 4.4 % to the count rate N_b and thus to the calculated conversion efficiency [190]. To further verify that our results are reliable, we additionally investigated the depletion of signal photons at the single-photon level with a free running Si SPAD (*Perkin Elmer SPCM-AQR-14*, $\sim 65\%$ quantum efficiency at 738 nm). Here we get $\eta_{\text{int}}^{\text{max}} \approx 0.8$ at a pump power around 240 mW. All together, we find that, within measurement accuracy, the results obtained with the InGaAs/InP SPAD are confirmed by the depletion measurements at macroscopic power and at the single-photon level.

In the absence of any propagation losses, the internal conversion efficiency that is expected from theory (see Sect. 3.2.3) is 1, i.e., perfect conversion. We have given 7 % as an upper limit for the propagation losses of our device assuming an input coupling efficiency of 1 and zero Fresnel losses at the input coupling lens, at both facets of the WG, and at the output coupling lens. These assumptions are obviously not fulfilled in practice. Consequently, pure propagation losses will be less than 7 % and we would theoretically expect $0.93 < \eta_{\text{int}}^{\text{max}} < 1$ for the maximum internal conversion efficiency. In general, non-perfect spatial mode overlap within the WG might be a reason for reduced conversion efficiency. However, in our case we suppose the deviations of the measured phasematching curves from the ideal sinc^2 shape to be mainly responsible for the fact that the internal conversion efficiency is about 15–20 % less than the theoretical prediction. The effect of distorted phasematching curves was already analyzed in Sect. 5.2.1 using the method of Nash *et al.* [176]. We can now evaluate the usefulness of this method by comparing the results of the present section with those from Sect. 5.2.1. The factor of 0.75 obtained from the temperature acceptance curve (Fig. 5.6(d)) is in good agreement with the measured efficiency of ~ 0.73 . However, the factor of 0.65 obtained from the wavelength acceptance curve (Fig. 5.6(b)) underestimates the actual conversion efficiency. There is no obvious reason why the two measurements (wavelength and temperature acceptance bandwidth) should yield different results. Therefore, we assume that the method of Nash *et al.* provides an idea of the conversion efficiency that can be expected but cannot replace a more accurate measurement. Further systematic investigations (beyond the scope of this work) would be necessary to find out under what circumstances an accurate prediction of the conversion efficiency can be made from a measurement of the sinc^2 phasematching curves.

To complete the discussion, we consider the signal-to-noise ratio $\text{SNR} = N_b/N_{\text{dc+R}}$ which is an important figure of merit for a QFC device. The data are plotted in Fig. 5.13(b). The SNR reaches its maximum at $P_p \approx 60$ mW yielding a value of about 6:1. This is comparable to what was achieved in another frequency down-conversion experiment using long-wavelength pumping [46]. Note that due to the linearly rising Raman background, the SNR attains its maximum before the point of maximum conversion efficiency is reached.

5.3 Successive DFG and SFG in a Double-Pass Configuration

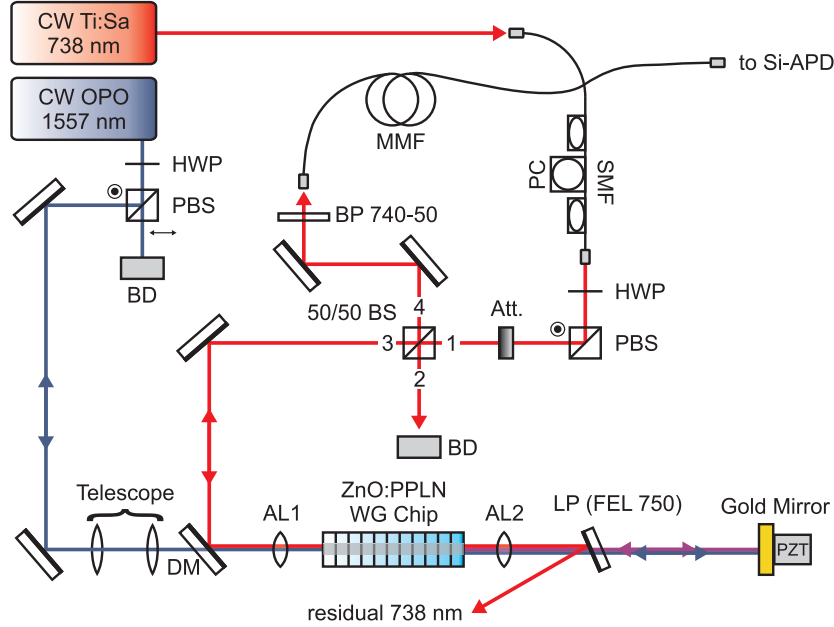


Figure 5.14: Setup for combined down- and up-conversion in one WG. HWP: half-wave plate, PBS: polarizing beamsplitter, BD: beam dump, DM: dichroic mirror, BS: beamsplitter, BP: bandpass filter, Att.: attenuator, PC: polarization control, SMF: single-mode fiber, MMF: multi-mode fiber, AL: aspheric lens, LP: longpass filter, PZT: piezoelectric transducer.

From the results discussed in the previous sections we have learned that QFC from 738 nm to the C-band brings some difficulties that are mostly attributed to Raman noise and the poor performance of the InGaAs/InP detectors. In this section, we review a bi-directional scheme that might have the potential to alleviate at least the detection problem. It is related to an idea proposed and implemented in the context of up-conversion of arbitrarily polarized light [191, 192]. The modified experimental setup is depicted in Fig. 5.14. The underlying principle of this configuration is that the visible input signal is first down-converted via DFG to a telecom wavelength and then up-converted again to the visible wavelength via SFG. In this way, we realize frequency down-conversion and subsequent up-conversion detection using one and the same WG. As shown in Fig. 5.14, the 738-nm input is split into two beams by a nonpolarizing 50/50 beamsplitter. One half is directed into a beam dump, the other half is sent through the WG and is mainly converted to a telecom wavelength. Residual visible light that has not been converted is blocked by a 750-nm longpass filter and is thus not involved in further interactions. Converted light and pump light are reflected by a plane mirror and traverse the frequency converter again in the opposite direction leading to an up-conversion to λ'_a (the prime indicates that this light has undergone two conver-

sion steps albeit $\lambda'_a = \lambda_a$). The plane reflector is mounted to a piezoelectric transducer that is wobbled at a frequency of 100 Hz by applying a sawtooth voltage. In doing so, we avoid perturbing interference effects that are otherwise observed. Pump light and up-converted light are separated by the dichroic mirror. The up-converted light beam is again split into two halves when it hits the 50/50 beamsplitter. The portion that is reflected under 90° is coupled into a multi-mode optical fiber. We point out that the 50/50 beamsplitter is not the ideal component to separate the two counter-propagating beams because 75% of the photons are sacrificed. An optical isolator which allows to use the reflected beam would be a much better choice. However, such a device was not available and the beamsplitter is fairly sufficient for proof-of-principle experiments.

We conduct a preliminary efficiency test of the DFG–SFG setup by inserting 1.53 mW at 738 nm (measured behind port 3 of the 50/50 BS). Initially, the 750-nm longpass filter is removed and the pump light is blocked. When the 738-nm light travels undisturbed back and forth through the whole optical system (starting from port 3 to the gold mirror and back to port 3) it experiences losses of $(1 - 0.64^2) \times 100\% \approx 59\%$, i.e., the measured power at port 4 of the BS is $1.53 \text{ mW} \times 0.41/2 = 313 \mu\text{W}$. The distance between the WG and the collimation asphere AL2 was optimized to ensure maximum transmission at 738 nm. We now insert the longpass filter so that the power at port 4 nominally drops to zero (in reality, faint reflections amount to $\sim 8 \mu\text{W}$). If the pump beam is coupled into the converter, the power at port 4 increases again since 738-nm light is generated in the consecutive DFG–SFG process. The converter is now pumped in both directions. The transmission coefficient of the longpass filter is 0.875 at 1404 nm and 1557 nm in single pass, i.e., the filter introduces losses of $\sim 23\%$ at these wavelengths in double pass. A measurement of the 738-nm power behind port 4 vs. the coupled pump power at 1404 nm (measured behind AL2 after a single pass) is presented in Fig. 5.15.

The noise floor of $8 \mu\text{W}$ was subtracted from the data. The highest power that was measured is about $150 \mu\text{W}$. By comparison with the power that is transmitted without down- and up-conversion, we find $150 \mu\text{W} / (0.875^2 \times 313 \mu\text{W}) \approx 0.63$ internal conversion efficiency, where the factor of 0.875^2 was introduced to correct for the transmission of the longpass filter. Assuming that DFG and SFG are equally efficient, we calculate $\eta_{\text{int}} = \sqrt{0.63} \approx 0.79$ for a single conversion step. This value matches the results that were obtained in Sect. 5.2.1 and 5.2.4. Figure 5.15 also shows the external efficiency that is about 20% at its maximum. The data are fit with the square of function (5.6). Since the efficiency test at the mW-power level was quite promising, we next investigate to what extent noise photons at 738 nm are generated when the crystal is pumped in the double-pass configuration. To this end, the laser power of the Ti:sapphire laser is attenuated to a power of 97 fW corresponding to $\sim 360,000$ photons/s behind the single-mode fiber. This power was measured directly with a Si APD. To minimize the possible noise background, we use long-wavelength pumping and choose $\lambda_p = 1557 \text{ nm}$. Behind port 4 of the BS, photons at 738 nm are coupled into the multi-mode fiber connected to a Si APD (see Fig. 5.14). Figure 5.16 shows the count rate of the Si APD with and without the single-photon level input signal at 738 nm. Evidently, the bi-directional pumping generates a massive number of noise photons in the 20-nm detection inter-

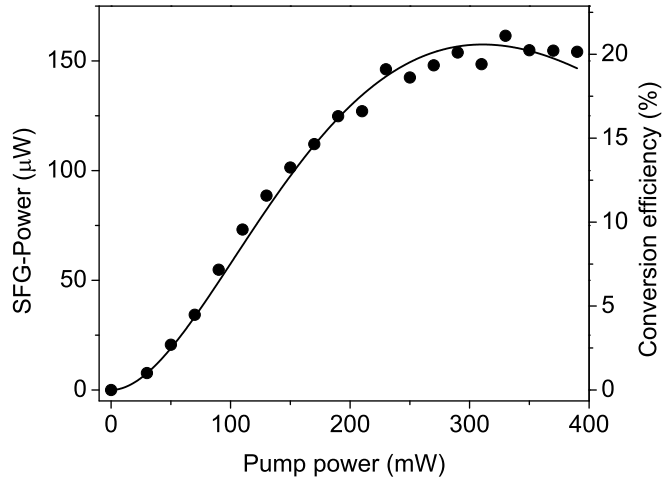


Figure 5.15: Power at 738 nm as a function of coupled pump power at 1404 nm and external efficiency of the two-step conversion process $738 \text{ nm} \rightarrow 1557 \text{ nm} \rightarrow 738 \text{ nm}$. Note that a factor of 2 was introduced in the efficiency calculation to account for the 50/50 BS. The dots are the measured data, the solid line is a fit.

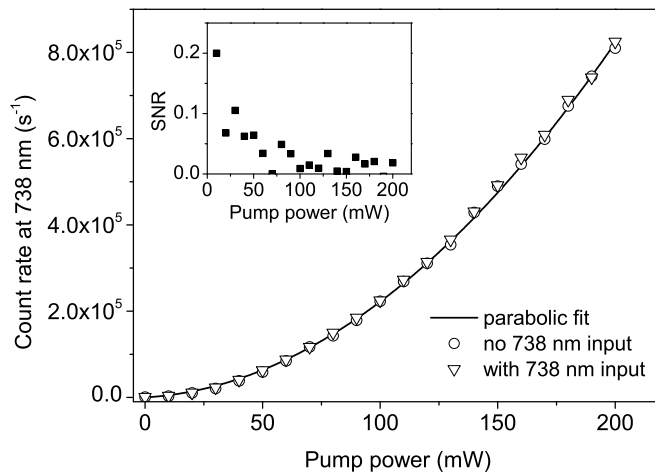


Figure 5.16: Count rate at 738 nm with and without weak signal input at 738 nm. Even when there is no signal input we observe considerable count rates in this wavelength range. The inset shows the SNR calculated from the measured data.

val around 740 nm given by the bandpass filter in front of the APD. From analysis of the data, we recognize a general tendency that the count rate with signal input is higher than without (up to 15,000 cts./s). However, the data are much too noisy to enable a reliable interpretation. Apparently, the noise floor in the double-pass scheme increases quadratically. This is in contrast to the results obtained in the single-pass DFG experiment described in Sect. 5.2.4 where a linear rise was observed (as expected

for Raman scattering). Only a poor SNR $< 1:10$ for relevant pump power levels is achieved. Spectral analysis in the 730–760 nm interval reveals eight peaks at 738.2,

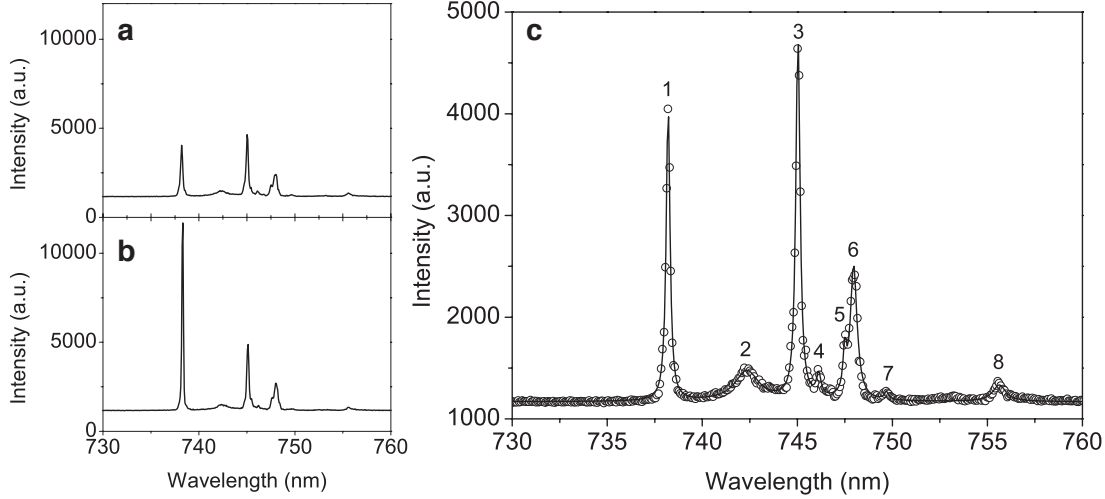


Figure 5.17: (a) Spectrum when the WG is bi-directionally pumped with a power of 100 mW at 1557 nm and no input at 738 nm. (b) Same conditions as in (a) but with additional weak input at 738 nm ($\sim 4.1 \times 10^6$ photons/s). (c) Detailed view of the spectrum shown in (a) with multi-Lorentz-peak fit (solid line). (Spectra measured by A. Lenhard.)

742.3, 745.0, 746.1, 747.5, 748.0, 749.7, and 755.6 nm when only pump light is coupled into the WG without any signal input (see Fig. 5.17). These peaks are supposed to be generated by SFG of ASR peaks with the strong pump light at 1557 nm. This could be understood as follows: when the strong pump field traverses the WG it generates ASR bands at center wavelengths $\lambda_{AS,1}, \lambda_{AS,2}, \dots, \lambda_{AS,N}$ as discussed in Sect. 5.2.2. Once a photon is created at a wavelength around $\lambda_{AS,j}$ it can be up-converted by sum frequency mixing with the 1557-nm pump light to a wavelength near 738 nm according to $1/\lambda_{AS/SFG,j} = 1/\lambda_p + 1/\lambda_{AS,j}$. The probability of this happening is doubled for bi-directional pumping since ASR noise generated in the first pass is reflected by the mirror and coupled into the WG again. The involvement of two processes, ASR and subsequent SFG, would explain the observed quadratic rise of noise photons with increasing pump power. Unlike the phasematching bandwidth around 738 nm for the DFG process, the phasematching bandwidth is much broader for the SFG process. ASR wavelength components generated in the 1400–1470 nm spectral region ($720\text{--}380\text{ cm}^{-1}$ from 1557 nm) would lead to up-converted photons in the 737–765 nm interval.

It is clear that the current performance of the bi-directional setup is even worse than one-step down-conversion and detection with InGaAs/InP single-photon detectors. We have tested the configuration with long-wavelength pumping. Interchanging λ_p and λ_b would certainly generate even more noise photons. A further improvement of the double-pass setup is beyond the scope of this work, though. Yet, it is worthwhile to shortly discuss to what extent the successive DFG–SFG scheme could be optimized. A

replacement of the 730–750 nm bandpass filter by a filter with a much narrower pass band (1-nm bulk bandpass filters are commercially available) could bring an enormous noise reduction. Additionally, it would also be possible to apply narrowband filtering after the first pass through the WG to prevent Raman noise from entering the converter again. Moreover, substitution of the 50/50 BS by an optical isolator which allows to use the reflected beam could minimize the losses at 738 nm in both directions. Finally, we note that insertion of a dual-wavelength quarter-wave plate between AL2 and the long-pass filter would allow for polarization-independent frequency conversion as described in [191, 192]. This is of relevance for QFC of polarization-entangled photons [52, 56]. A significant improvement of the signal-to-noise ratio in single-photon detection can also be achieved by using the lock-in technique in data postprocessing reported by Lenhard *et al.* [193].

5.4 Summary and Discussion

In this chapter, we have primarily studied frequency down-conversion from 738 nm to the telecommunications C-band (1557 nm). This particular wavelength combination was chosen to match the emission wavelength of the SiV center in diamond, a bright, narrowband quantum emitter that can be operated at room temperature [60]. The frequency conversion setup was introduced and the Zn:PPLN WG chip, as the most important part of this setup, was described. Experimental methods to test its performance were presented as well. To deliver the strong pump fields at ~ 1400 nm and around 1550 nm that are required for our experiments, we have used the home-built cw SRO based on MgO:PPSLT described in Sect. 4.2. Since the SRO is widely tunable, it can serve as a pump source in a variety of frequency conversion experiments with different input wavelengths (see also Chap. 6). We achieved a remarkably high input coupling efficiency of 90 % at 738 nm. A single-photon source based on a diamond SiV center was emulated with attenuated pulses from a Ti:sapphire laser. With this single-photon-level input a total conversion efficiency of 2 % (including filtering and detection) was achieved, corresponding to an internal conversion efficiency of 73 %. Maximizing the input coupling efficiency is an important task since it dramatically increases the overall efficiency of the conversion setup. The dominating noise source in the short-wavelength-pumped frequency converter was unambiguously identified to be spontaneous Stokes Raman scattering induced by the strong pump field at 1403 nm. We also studied the noise spectrum that is generated by anti-Stokes Raman scattering. This is of interest for evaluation of the expected noise level in frequency down-conversion experiments that use long-wavelength pumping. DFG processes according to $1/795 \text{ nm} - 1/1632 \text{ nm} = 1/1550 \text{ nm}$ ($^{87}\text{Rb } D_1$ line \rightarrow C-band) as proposed in [46] or $1/711 \text{ nm} - 1/1550 \text{ nm} = 1/1313 \text{ nm}$ as presented in Chap. 6 are examples for such schemes. Despite the strong Stokes Raman noise background in the down-conversion from 738 nm to 1557 nm, a signal-to-noise ratio of 6:1 was achieved using temporal and narrow spectral filtering. In principle, the lower limit for the filtering bandwidth is

given by the frequency bandwidth $\Delta\nu_b$ of the down-converted light. Since for SiV centers currently $\Delta\nu_b \geq \Delta\nu_{\text{DFG}}$, the minimum filtering bandwidth is actually given by the frequency phasematching bandwidth $\Delta\nu_{\text{DFG}} \approx 88$ GHz corresponding to a bandwidth of 0.7 nm at 1557 nm. If we would consider a single-photon source with a much narrower emission linewidth, e.g., a trapped atom coupled to a high-finesse cavity [20], we could employ even narrower spectral filtering achieving a much better signal-to-noise ratio.

At the end of this chapter, a bi-directional conversion scheme that utilizes two conversion steps, namely DFG and subsequent SFG, was discussed. This configuration was tested with the goal of employing free running Si-based single-photon detectors instead of their InGaAs counterparts that have to be operated in gated mode. With the twofold conversion, a considerable conversion efficiency of 0.63 could still be obtained but the noise problem was massively aggravated by the double-pass pumping. Even though these results seem disappointing at first sight, a number of technical improvements (as outlined in Sect. 5.3) could certainly bring a significant noise reduction. However, efforts in this direction are beyond the scope of this work.

As Ref. [47] and this work indicate, it is not the limited conversion efficiency but the noise problems that are a major challenge in quantum frequency down-converters. Narrowband spectral filtering and temporal gating can be a remedy but do not eliminate the cause of the converter noise. Temporal gating even brings some new difficulties as discussed further below. An alternative concept, which is attractive in the context of SiV centers, is to choose long-wavelength pumping [46, 48]. When aiming at the telecom O-band, i.e., $\lambda_b \approx 1310$ nm, the required pump wavelength has to be around 1690 nm which could be generated, e.g., by a 1- μm -pumped SRO.² As our measurements clearly reveal, this should exclude any SPDC or (anti-Stokes) Raman noise at the expense of only slightly higher fiber transmission losses at 1310 nm compared to 1550 nm. In situations where $\lambda_a < \lambda_b/2$ long-wavelength pumping is not an option. Then, a more elaborate approach must be chosen such as the cascaded scheme which was proposed for down-conversion [47] and demonstrated for up-conversion [194] by Pelc *et al.*. In our particular case with $\lambda_a = 738$ nm, the cascaded scheme would consist of two DFG processes that are both pumped with a wavelength of $\lambda_p = 2.8 \mu\text{m}$. In the first step, the input photons are down-converted to an intermediate wavelength according to $\lambda_{\text{int}} = (1/738 \text{ nm} - 1/2.8 \mu\text{m})^{-1} \approx 1.0 \mu\text{m}$, and in the second step, the so-generated photons at λ_{int} are down-converted to a C-band wavelength according to $\lambda_b = (1/1.0 \mu\text{m} - 1/2.8 \mu\text{m})^{-1} \approx 1.56 \mu\text{m}$. Again, the 2.8- μm pump wavelength could be generated by a 1- μm -pumped SRO.

In conclusion, we have assessed the chances of successful QFC from 738 nm to the C-band using single-photon-level input. With a SNR of 6:1, investigation of the photon statistics and demonstration of photon antibunching after the conversion process seem within reach. However, we must not ignore that several conditions are idealized in the presented experiment. In a realistic scenario, a single SiV center will emit only 2×10^5

²An experiment of this kind is currently set up. However, at the time this work was performed, no appropriate WG crystal and no pump source at 1700 nm were available. Hence, conversion from 738 nm to the O-band using long-wavelength pumping could not be performed.

to 3×10^5 photons/s under 80-MHz pulsed excitation due to the non-perfect quantum efficiency of the emitter [195]. This is in contrast to the record-high 6.2×10^6 counts/s that were reported for an SiV center under cw excitation [196]. The InGaAs SPADs cannot be gated with the 80-MHz repetition rate of the excitation laser but have to be gated at a lower rate of 0.5 MHz (corresponding to a $2\text{-}\mu\text{s}$ detector dead time) to keep the detector dark counts at a reasonable level. Taking into account the 2% total conversion efficiency, we estimate that only $3 \times 10^5 \times 0.5/80 \times 0.02 = 37.5$ counts/s are detected on average at 1550 nm when starting with an optimistic value of 3×10^5 input photons/s at 738 nm. In view of the noise floor generated in the converter, it would be impossible to verify photon antibunching after the frequency conversion under such conditions. The situation is even more complicated by the insufficiently reproducible spectral properties of the SiV center. It is difficult to find a center which shows bright and sufficiently narrowband single-photon emission at an appropriate center wavelength. For emission wavelengths of individual SiV centers in nanodiamonds, a broad distribution reaching from 730–750 nm has been observed [197].

All of the aforementioned issues are overcome by the experiments presented in Chap. 6. Here we have chosen a semiconductor QD as a single-photon source and have further improved important details of our setup.

Chapter 6

Quantum Frequency Down-Conversion of Single Photons from a Quantum Dot

Copyright Notice:

Sect. 6.1, Sect. 6.2, and Sect. 6.3 of this chapter contain material that was originally published in Ref. [198] and the accompanying supplemental material (SM) (Copyright © 2012 by the American Physical Society).

In this chapter, we describe the experimental implementation of the central objective of this thesis: QFC of nonclassical light from a true single-photon source from the visible spectral range to a telecom wavelength band. We recall that QFC in this context means that the statistical properties of a nonclassical input light field are fully mapped to the frequency-converted output telecom light. However, the practical realization represents a challenge since a number of technical difficulties have to be overcome simultaneously:

1. Spontaneous Raman scattering as described in Sect. 5.2.2 can generate extra photons at the target wavelength, thus degrading the single-photon character of the output light field.
2. The spectral acceptance bandwidth of the DFG process (see Sect. 5.2.1) is quite narrow compared to the typical (room temperature) spectral emission bandwidth of solid-state single-photon emitters which potentially reduces the conversion efficiency.
3. The power of the pump field has to be 12–13 orders of magnitude stronger than the power of the quantum light field to achieve a significant conversion efficiency. Pump light has to be massively suppressed after the frequency converter to avoid flooding of the detectors with pump photons. At the same time, the components employed for spectral separation of pump and converted signal photons have to

feature a transmission that is high enough to ensure reasonable count rates at the target wavelength.

4. Single-photon detectors based on Si APDs are technically mature devices which are reliable and easy to handle. In contrast, single-photon detectors at telecom wavelengths have only improved in recent years and still cannot compete with Si APDs as they suffer from low detection efficiencies and/or high dark count rates and/or limited count rates.

Here we demonstrate that by carefully addressing each of the above points, visible-to-telecom QFC is practically feasible and may become an important technique for quantum communication and information applications. Section 6.1 gives an introduction into InP/GaInP QDs which we used as single-photon emitters in our experiments. The experimental setup and the obtained results are discussed in Sect. 6.2 and Sect. 6.3, respectively.

6.1 InP Quantum Dots as Single-Photon Emitters

It was one of the goals in this thesis to demonstrate visible-to-telecom QFC with an all-solid-state system. We have learned from the results discussed in Chap. 5 that the SiV center in diamond, despite its undisputed advantages, causes some difficulties with respect to QFC at the moment. These problems are likely to be solved in the future, e.g., by using single-crystalline diamond as a host material and coupling of an SiV center to a cavity [165]. These measures should allow for better spectral control and narrower emission linewidths. However, for the time being, we choose to employ a semiconductor QD as a solid-state single-photon source in the visible. Since the first demonstration of single-photon emission from a QD by Michler *et al.* [19], these devices have attracted wide attention as single-photon emitters and have been thoroughly investigated [78,199]. Before we discuss the characteristics of the InP/GaInP QD sample used in this thesis, we start with a brief outline on fundamental properties of semiconductor QDs.

6.1.1 Semiconductor Quantum Dots: Fundamentals

The following treatment is inspired by the book of Michler *et al.* [78]. A semiconductor QD is a three-dimensional structure which is several 10 nanometers in size and immersed into a semiconductor material with larger bandgap. The nanostructure locally modifies the electronic band structure of the surrounding semiconductor material and forms a potential well with dimensions comparable to the de Broglie wavelength of an electron. Thus, charge carriers (electrons and holes) can be spatially confined in a QD. As a consequence, the energy of the particles inside the QD can only take discrete values. This situation is analogous to an atom and explains why QDs are sometimes termed ‘artificial atoms’. Semiconductor QDs are fabricated by epitaxial growth, e.g., molecular beam epitaxy (MBE) or metalorganic vapour phase epitaxy (MOVPE). During epitaxial growth, self-organization phenomena play a vital role and QDs produced under such

conditions are called self-assembled. The most common growth mode for optically active semiconductor QDs based on self-organization is the Stranski–Krastanow growth mode. In this heteroepitaxial process, a thin film of QDs consisting of a narrow bandgap material is embedded in a material with a higher bandgap. During growth, only some monolayers (the so-called wetting layer) of the narrow-bandgap material are deposited on the wide-bandgap substrate before the self-organized formation of nano-islands (i.e., QDs) begins. The formation of the QDs is caused by the strain induced by the mismatch of the lattice constants of the two materials. A prominent example for this kind of fabrication are InAs QDs (bandgap energy: 0.351 eV at 297 K [200]) embedded in a GaAs matrix (bandgap energy: 1.424 eV at 297 K [201]). As a consequence of the self-organized growth, the individual position of single dots is random. The area density of the QDs as well as their average size is determined by the lattice mismatch (i.e., by the material system) and the growth conditions. The size of individual dots follows a random distribution around a certain mean value.

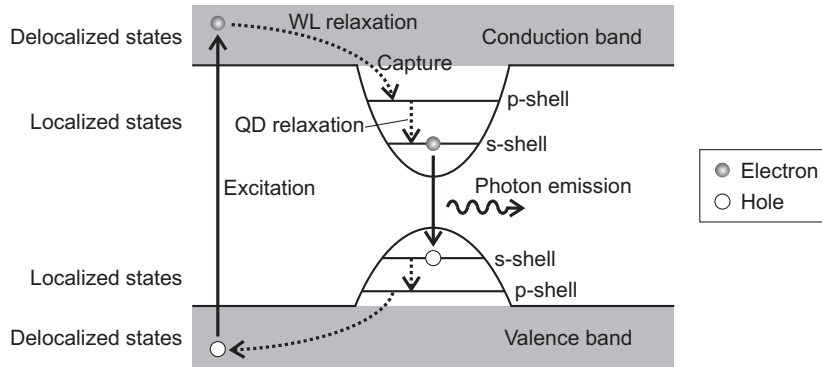


Figure 6.1: Typical energy level scheme of a semiconductor QD (after [78]). Non-resonant excitation generates electrons (holes) in the conduction (valence) band. After relaxation via carrier–carrier and carrier–phonon interactions, electrons and holes get trapped in the QD. Photons are emitted in a cascaded recombination of the electron–hole pairs. The sketch exemplarily shows the single exciton transition which corresponds to the recombination of the last electron–hole pair in the QD.

We can understand the generation of photons by a QD from the energy level structure depicted in Fig. 6.1. It represents a composition of both quasi-continuous (delocalized states in the conduction/valence band of the barrier) and discrete energy levels (localized states in the QD). In analogy to atoms, the lowest energy level in the dot is called *s*-shell and the second-lowest is called *p*-shell. To achieve light emission, electron–hole pairs are created by means of optical or electrical excitation. The excitation process can be non-resonant, quasi-resonant, or resonant. In the case of non-resonant excitation, the excitation energy is larger than the barrier bandgap. Quasi-resonant excitation takes place into one of the higher shells while resonant excitation means a direct excitation into the *s*-shell. We here consider non-resonant excitation since this type is used

in the experiments discussed in the following sections. After electron–hole pairs are created in the barrier, the electrons (holes) relax to the conduction (valence) band edge where they can get captured by a QD. Even or odd numbers of charge carriers can get trapped to form neutral or charged complexes, respectively. Neutral complexes formed by N electron–hole pairs are named N -excitons (X , $2X$ or XX , $3X$, ...). Each of these states corresponds to a certain energy E_X , E_{XX} , ... , E_{NX} . For applications as a single-photon source, the cases $N = 1$ and $N = 2$, i.e., the exciton (X) and the biexciton (XX) state, respectively, are the most important ones. Photon emission occurs via recombination of electron–hole pairs in the QD. We emphasize that not all N electron–hole pairs recombine at the same time to generate N photons. Instead, a cascaded emission takes place in which each change in configuration $NX \rightarrow (N - 1)X \rightarrow \dots \rightarrow X \rightarrow 0$ is associated with the emission of one photon at a time. The energy levels E_X , E_{XX} , ... , E_{NX} are not equally spaced because they depend on the Coulomb interaction between the charge carriers in the QD. As a consequence, each of the individual transitions has a slightly different energy leading to an anharmonic spectrum. In the experiment, this allows for resolving the spectral lines corresponding to each transition of a single QD. It is also important to note that different QDs in the same sample show different emission wavelengths due to their varying sizes.

6.1.2 Fabrication and Layout of the InP/GaInP Quantum Dot Sample

The QD sample that is employed in all experiments described in this thesis is labeled M4600-2 and was fabricated in the group of P. Michler at Universität Stuttgart by performing the following procedure [202]: it was grown by metal-organic vapor-phase epitaxy on a n-doped (100) GaAs substrate misorientated by 6° toward the $(111)_A$ direction (the subscript A indicates that the III-V semiconductor is terminated with a layer of Ga atoms, subscript B would stand for As). In order to enhance the collection efficiency, an n-doped distributed Bragg reflector (DBR) of 10 $\lambda/4$ -pairs of $\text{Al}_{0.50}\text{Ga}_{0.50}\text{As}/\text{AlAs}$ was placed below the active region. The InP QDs were grown self-assembled in the Stranski–Krastanow growth mode and were symmetrically embedded in 8.8-nm intrinsic $\text{Ga}_{0.51}\text{In}_{0.49}\text{P}$ barriers surrounded by 150-nm partially doped $(\text{Al}_{0.55}\text{Ga}_{0.45})_{0.51}\text{In}_{0.49}\text{P}$ cladding layers. On top, a p-doped aluminum rich oxidation layer was grown. The structure was terminated with a GaInP and a GaAs layer. After growth, standard processing techniques like lithography, thermal wet oxidation, and evaporation of ohmic contacts were applied to fabricate mesas of 100 μm diameter. A ring-shaped p-contact can be used to apply a DC bias voltage and the luminescence was collected inside a 20- μm opening window of this ring contact. A microscope image of the sample and a schematic of its layout are shown in Fig. 6.2(a) and (b), respectively. The sample consists of $4 \times 8 = 32$ mesas, each of them located on a rectangular contact pad which is $250 \times 250 \mu\text{m}^2$ in size. Due to space limitations, only three of these pads (B2, D4, B7) are provided with bonding wires which allow for applying a voltage to the QDs, i.e., investigation of QDs on the sample is effectively limited to three mesas. Light is emitted through circular apertures in the center of the mesas and is directed perpen-

pendicular to the sample surface. For easier handling, the sample shown in Fig. 6.2(a) is fixed on a larger circuit board which is mounted into a liquid helium (LHe) continuous flow cryostat (*Janis Research, Model ST-500LN*, see Fig. 6.2(c)) since the QDs have to be operated at cryogenic temperatures. The emission wavelengths of the QDs on the sample lie in a range of 690–715 nm and can be tuned by temperature and by Stark effect via the bias voltage. We employ a DC power supply (*Agilent E3643A*) to apply an adjustable bias voltage to the sample. In the conversion experiment, single QDs are optically addressed using a confocal microscope and an appropriate QD with an emission line around 710 nm is selected. Wavelength tuning and selection of the QDs are described in detail in Sect. 6.2.3.

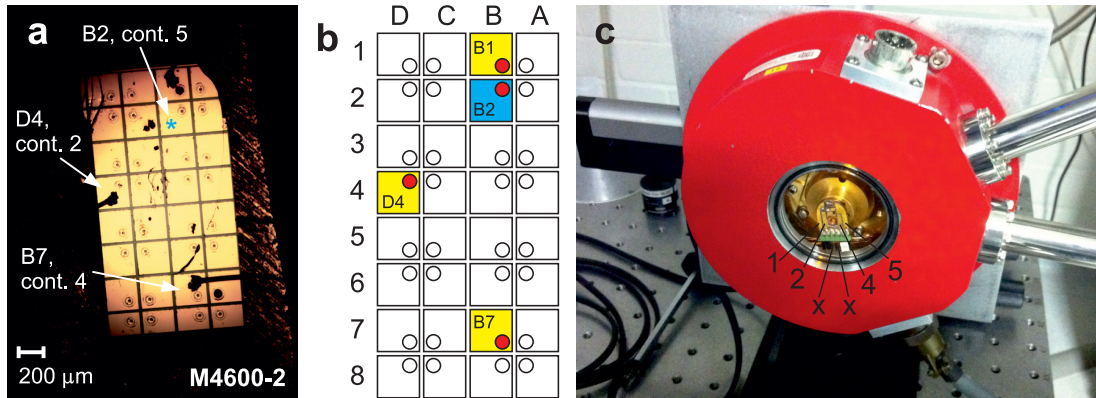


Figure 6.2: (a) Microscope image of the QD sample M4600-2. Initially, as shown here, mesas B1, D4, B7 were provided with bonding wires. After mounting the sample into the cryostat, evacuation of the system, and liquid helium cooling, mesa B1 did not show light emission anymore. Therefore, the B1 bonding wire was removed and a new one was bonded to the contact pad of mesa B2 (marked with blue star). The bonding wires are connected with contacts 2, 4, and 5 as marked in (c). (b) Schematic of the sample layout. Wire-bonded contact pads are filled yellow or blue (newly bonded). Red-filled circles are investigated mesas. (c) Sample with electrical contacts mounted in the LHe flow cryostat. Contact 1: ground; contacts 2, 4, 5: connected to mesas D4, B7, and B2, respectively; contacts X: not connected.

6.2 Experimental Setup and Preparatory Experiments

6.2.1 Experimental Setup

Figure 6.3 shows a detailed drawing of the complete experimental setup which is used for generation and frequency conversion of single photons from a QD. One part of it (Fig. 6.3(a)) consists of a confocal microscope, similar to the setup described in [82], for investigation of the QD sample. This setup is combined with the frequency conversion stage including the Zn:PPLN WG that, together with a spectral filtering stage, constitutes the second part of the setup (Fig. 6.3(b)). The two parts are located on different optical tables and are connected via optical fibers. An important component of the

confocal microscope consists of the cryostat containing the QD sample. The cryostat is mounted on a xy translation stage for precise sample positioning. A bias voltage on the order of several Volts can be applied to the QDs which are additionally optically excited using an average power of ~ 160 nW at 590 nm from a pulsed femtosecond (fs) OPO with 80 MHz repetition rate [73]. The yellow excitation light is spatially filtered by a single-mode fiber (SMF1) to create a perfect TEM₀₀ beam profile. The fs OPO is pumped by a fs Ti:sapphire laser (*Spectra Physics Tsunami*) at 773 nm which in turn is pumped by a cw frequency-doubled Nd:YVO₄ laser (*Spectra Physics Millennia*) at 532 nm. Optical excitation and collection of photoluminescence (PL) emitted by the QDs are performed using a 100 \times microscope objective with numerical aperture NA = 0.8 (*Olympus LMPLFLN100 \times*) mounted on a z translation stage. The microscope objective is integrated into the cryostat such that the PL from the QDs is first collimated by the objective and then passes through the cover glass of the cryostat. This increases the photon yield significantly compared with a configuration where the microscope objective is outside of the cryostat and the divergent light first has to pass through the cover glass and is then collimated by the objective. A glass substrate is used to separate excitation and PL light. The collected photons are coupled into a single-mode fiber (SMF2) that guides them to the frequency conversion setup. A specially coated silica etalon can be optionally inserted for narrowband filtering of the PL. Two long-pass filters prevent residual excitation light from entering SMF2. Using a mirror in a flip mount alternatively allows for bypassing the conversion setup and coupling the PL directly into a multi-mode fiber (MMF1). This proves to be convenient for coarse confocal scans and alignment of the setup. With the polarization control and the half-wave plate at the output of SMF2, we can adjust the power at the output ports ‘H’ and ‘V’ of the polarizing beamsplitter. For frequency down-conversion, the visible photons leaving port ‘V’ are coupled into the Zn:PPLN ridge WG together with a strong pump beam at 1550 nm provided by the MgO:PPSLT-SRO described in Sect. 4.2. To this end, we use an input coupling telescope similar to the one introduced in Sect. 5.1.1. The lenses L1 and L2 are the same but, in contrast to the setup in Sect. 5.1.1, we use an aspheric lens with a shorter effective focal length of $f_{\text{eff}} = 4.51$ mm (*Thorlabs A230TM*, NA = 0.55, uncoated). As a consequence, the distances L1–L2 and L2–AL1 have to be re-adjusted and become $d_{\text{L1-L2}} \approx 300$ mm and $d_{\text{L2-AL1}} \approx 235$ mm, respectively. The aspheric lens with the shorter f_{eff} was used because we found that it enables a more efficient excitation of the fundamental spatial WG mode at wavelengths around 710 nm. The use of an aspheric lens with $f_{\text{eff}} = 11$ mm—which was a good choice for input wavelengths around 740 nm—resulted in excitation of higher-order spatial modes at 710 nm. It is not clear if this is only due to the 30-nm wavelength difference or due to different numerical apertures of individual WGs.

The converted photons are spatially separated from the strong pump light and from residual visible photons by a Pellin–Broca prism and a pinhole and are coupled into a SMF-28 standard telecom fiber. To suppress residual pump light and noise background around the target wavelength λ_b , we additionally use a spectral filtering setup composed of a fiber-optic circulator (FOC), a fiber Bragg grating (FBG) centered

at 1312.714 nm (*AOS GmbH, S/N: 24040342*; -1.0 dB/ -20 dB reflection bandwidth: 0.755 nm/1.275 nm) and two 1310 nm/1550 nm wavelength division multiplexers ($2 \times$ *Thorlabs WD202B-FC*, WDM1 and WDM2). To analyze the spectrum of the visible QD emission, we employ a grating spectrometer with a CCD detector (*Horiba Jobin Yvon iHR 550*). The spectrum of the converted telecom signal can be recorded using another grating spectrometer (*Princeton Instruments SP2500A*) with an InGaAs linear array detector (*OMA V*). In both devices, we select a grating with 1800 lines/mm. For single-photon detection in the visible, we use Si APDs (*Perkin Elmer SPCM-AQR-14*) with 65 % detection efficiency around 700 nm, a dark count rate of ~ 300 s $^{-1}$, and 250 ps timing jitter (standard deviation of Gaussian envelope). Infrared photons are detected by two fiber-coupled NbN superconducting single-photon detectors (SSPDs, *SCONTEL, Russia*) [203,204]. These devices are integrated in a dip stick that is inserted into a LHe storage dewar. In this way, operation at temperatures below 2 K is possible. The timing jitter of the detectors is < 25 ps (standard deviation). With the optimal setting of the bias current, the detection efficiency has been measured to be 12.2 ± 0.7 % using an attenuated 1310-nm diode laser [205]. At the same time, we observe less than 10 dark counts per second.

Before discussing the results that were obtained in single-photon frequency conversion (see Sect. 6.3), we first investigate the performance of the WG chip that was used in the above-described setup and explain how an appropriate QD can be selected.

6.2.2 Performance of the Waveguide Chip

For the frequency down-conversion from 710 nm to the telecom O-band (1310 nm) another Zn:PPLN WG chip from *NTT Electronics Corp., Japan*, is used (*model WD-1550-000-A-C-C-S002, S/N 3079045*); it is called chip 2 in the following. Apart from the QPM grating periods, which are specifically tailored for the 710/1310/1550 nm wavelength set, it is very similar to the converter device described in Sect. 5.1.2. The chip also has dimensions of length \times width \times height = $40 \times 6 \times 0.5$ mm 3 and its layout is as drawn in Fig. 5.2. It contains 12 ridge WGs with 6 different QPM grating periods $\Lambda_1 = 14.72, \Lambda_2 = 14.76, \dots, \Lambda_6 = 14.92$ μ m. Before the device was employed for experiments with single-photon input, its performance was tested with cw laser light from a Ti:sapphire laser at the mW-level.

Depletion of a Coherent Input Signal

In Sect. 5.2.1 we have seen that the depletion of a coherent input signal is a good estimate for the DFG conversion efficiency that can be expected. If propagation losses are low and competing nonlinear processes can be neglected, the conversion efficiency should be a few percent less than the signal depletion. The depletion measurement was performed for the converter chip 2 in the same manner as described in Sect. 5.2.1. The result is presented in Fig. 6.4. A maximum coupled pump power of 310 mW was available in this experiment. Initially, the power of the weak 710-nm input was 543 μ W.

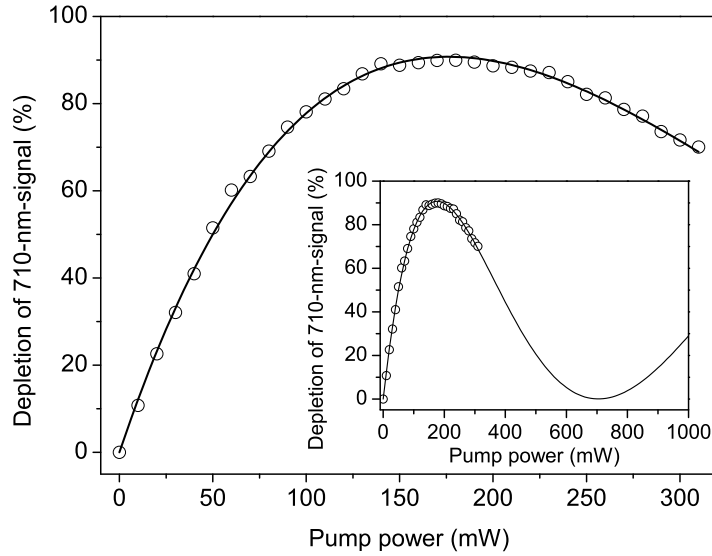


Figure 6.4: Depletion of a coherent 710-nm input signal due to frequency down-conversion. The exact wavelength combination was 710.3120 nm/1551.600 nm/1310.0560 nm and the WG temperature was 21.35 °C (chip 2, group 5, WG1, $\Lambda = 14.88 \mu\text{m}$). Open circles are measured data, solid lines are fits according to Eq. (5.6). The inset shows the same plot but with an extended pump power axis. It illustrates the expected trace of the function if the measurement would be performed with pump powers up to 1 W.

At the point of maximum depletion, a residual power of only 55 μW is observed behind the WG corresponding to a depletion of 90%. A fit according to Eq. (5.6) yields $\eta_{\text{nor}} = 87.5\%/W/\text{cm}^2$. Maximum depletion is attained at $P_p = 175 \text{ mW}$. It should be noted that Fig. 6.4 shows the best result of several measurements. The high 90% depletion was not routinely achieved because this value is very sensitive to the alignment of the setup. However, a signal depletion of 80% was a typical value that could be reached on a daily basis.

Judging from the depletion measurement, the performance of chip 2 is even better than that of chip 1 ($S/N\ 3079044$) investigated in Sect. 5.2.1. In the best case, the maximum depletion is 8–13% higher and it is reached at a pump power that is at least 50 mW lower. This could be a hint that the coupling to the fundamental WG mode is even more efficient at 710 nm with the $f_{\text{eff}} = 4.51 \text{ mm}$ aspheric lens than at 740 nm with the $f_{\text{eff}} = 11 \text{ mm}$ aspheric lens. Favored by these conditions, the back-conversion effect is observed very clearly. We recall that, considering noise issues, it is advantageous if the pump power required for maximum conversion efficiency is as low as possible. The cause for the discernable difference in the performance of the two converter chips is also assumed to lie in the quality of the WGs itself. In Sect. 5.2.1 and Sect. 5.2.4 we have discussed the influence of a deviation of the spectral acceptance curve from the perfect sinc^2 characteristic. We will see in Sect. 6.3.1 that the measured acceptance curve for chip 2 comes closer to a sinc^2 function than that of chip 1 (see Fig. 5.6(a)).

Total Conversion Efficiency at Macroscopic Power Levels

In addition to measuring the signal depletion, we determined the total power conversion efficiency $\eta_{\text{total}}^{(\text{power})}$ and the total photon-to-photon conversion efficiency η_{total} of our setup at macroscopic power levels (see Fig. 6.5). We define $\eta_{\text{total}}^{(\text{power})} = P_{\text{out}}^{(1313\text{ nm})} / P_{\text{in}}^{(711\text{ nm})}$,

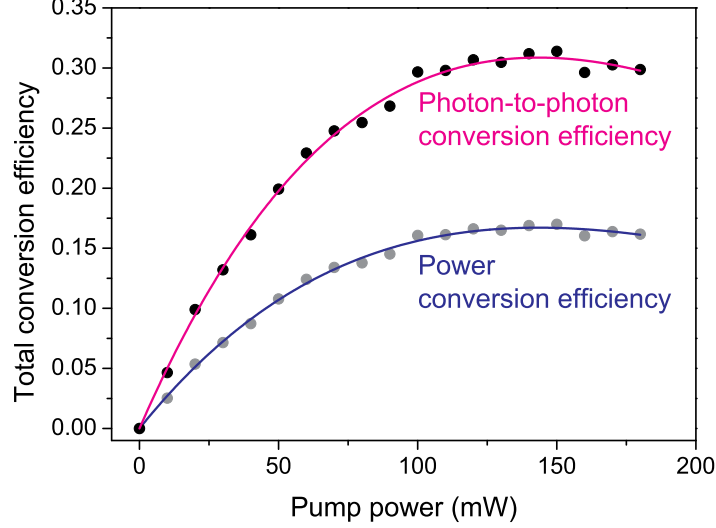


Figure 6.5: Total power conversion efficiency $\eta_{\text{total}}^{(\text{power})}$ (grey data points) and total photon-to-photon conversion efficiency η_{total} (black data points) as a function of the pump power at 1550 nm. These efficiencies refer to the complete conversion setup (from point E to point I in Fig. 6.3(b)) including spectral filtering. η_{total} was calculated from $\eta_{\text{total}}^{(\text{power})}$ by multiplication with a factor of $1312.668\text{ nm} / 710.74\text{ nm} \approx 1.85$. The blue and the pink solid lines are least square fits to the data according to Eq. (5.6).

where $P_{\text{out}}^{(1313\text{ nm})}$ is the power of the telecom light that leaves the setup at point I and $P_{\text{in}}^{(711\text{ nm})}$ is the power of the visible input light at point E (see Fig. 6.3(b)). The photon-to-photon conversion efficiency η_{total} is the ratio of the rate of telecom photons at point I to the rate of visible photons at point E. The definition of $\eta_{\text{total}}^{(\text{power})}$ and η_{total} is expedient as it describes the effect of the whole conversion setup as if it was a single component in a fiber network. To determine $\eta_{\text{total}}^{(\text{power})}$, we send a constant signal power of $P_{\text{in}}^{(711\text{ nm})} = 1\text{ mW}$ at 710.74 nm into the frequency converter. This power was measured at point E with a Si-based powermeter. The power $P_{\text{out}}^{(1313\text{ nm})}$ of the converted signal at 1312.668 nm (point I) was determined by integrating the power spectral density recorded with the OSA (the 50/50 FBS was removed and the SSPDs were replaced by the OSA in this experiment). The ratio $\eta_{\text{total}}^{(\text{power})}$ is shown as a function of the 1550-nm pump power in the lower plot of Fig. 6.5. The values of η_{total} (upper plot in Fig. 6.5) can be calculated from $\eta_{\text{total}}^{(\text{power})}$ by taking into account the wavelength factor $1312.668\text{ nm} / 710.74\text{ nm} \approx 1.85$. The data in Fig. 6.5 were fit according to Eq. (5.6).

From the fit of the upper plot, we yield a maximum of $\eta_{\text{total}}^{(\text{max})} = 0.31$ at a pump power of $P_{\text{opt}} = 143$ mW. The signal depletion at P_{opt} was measured to be 0.8 in this case. The deviation compared with the value $P_{\text{opt}} = 175$ mW determined in the depletion measurement is believed to be mainly due to uncertainties in the fit function. In contrast to the measurement in Fig. 6.5, the one in Fig. 6.4 contains data points beyond 180 mW which are taken into account in the fitting procedure.

Phasematching Curves

Individual QDs in the same sample vary in size. As a consequence, the wavelength of the exciton or biexciton line of each of them is slightly different. Hence, it is crucial to adapt the settings of our conversion setup to the wavelength of one particular emitter. Doing this in a deterministic way requires knowledge of the phasematching curves of the WGs on the chip, i.e., the set of parameters $\{\lambda_a, \lambda_b, \lambda_p, \Lambda, T\}$ for which $\Delta\beta = 0$ is satisfied. To find a suitable point of operation, we use the OPF-based method presented in Sect. 5.2.1. To this end, the Ti:sapphire laser is tuned to ~ 710 nm. The phasematching curves obtained from OPF spectra for 6 WGs are plotted in Fig. 6.6 for temperatures between 21°C and 35°C. The QPM grating periods are designed in such a way that the spectral intervals of acceptable input wavelengths are overlapping, i.e., WG #1 of group 4 is suitable for input wavelengths between 709.2–710.1 nm, WG #2, group 4 covers the region from 709.84–710.62 nm and so on. All together, the six WGs of groups 4–6 are suitable for input wavelengths in a spectral range from 709.20–712.52 nm. This interval is broad enough to find a QD on the sample whose properties fulfill all requirements for QFC: bright, narrowband, and low-background single-photon emission.

6.2.3 Preselection and Wavelength Tuning of Quantum Dots

As indicated at the end of the previous section, a solid-state system that should serve as a single-photon emitter in a QFC experiment has to fulfill several demanding conditions. The QD emission has to be bright (count rate $> 100,000$ cts./s), narrowband (< 0.1 nm) and should contain only low-noise background all at the same time. Additionally, since fast adjustment of the phasematching condition through variation of experimental parameters (WG temperature, pump wavelength, QPM grating period) is limited in our experiment, the wavelength of the emitted light should lie in a certain spectral region around 710 nm and should be slightly tunable. All three mesas of sample M4600-2 were carefully investigated in order to identify QDs which satisfy all of the aforementioned requirements. Figure 6.7 shows a confocal scan over the whole aperture of mesa B2. In this mesa, an appropriate single QD could be located. This specific emitter is used in the experiments described in the following where two methods of tuning the PL wavelength are introduced. In order to achieve perfect phasematching in the DFG process, one has to either optimize the operating point of the QPM WG crystal (temperature, grating period), adapt the pump wavelength, or tune the emission wavelength of the single emitter. In our experiment we apply the last method, i.e., we

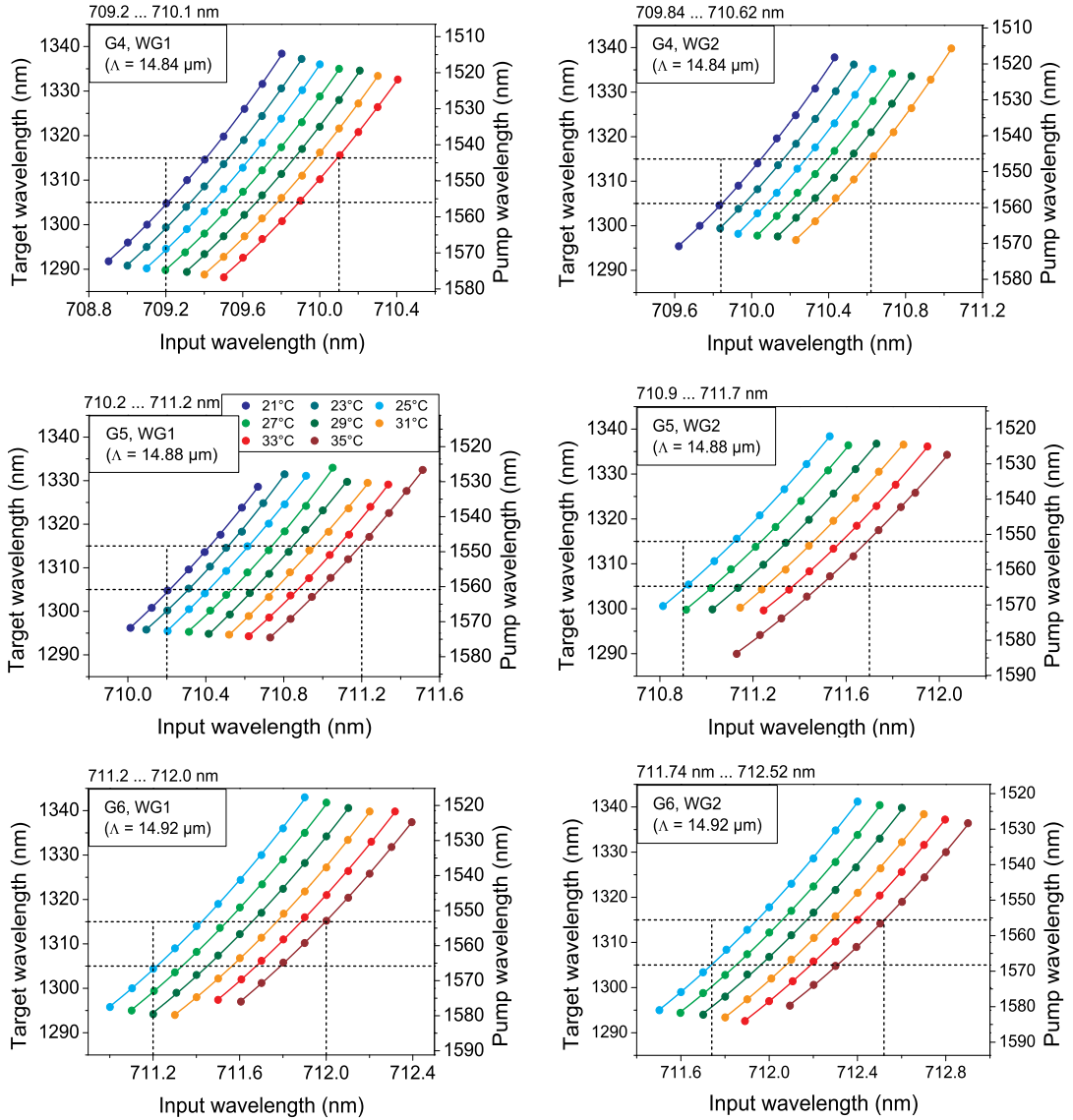


Figure 6.6: Phasematching curves for six different WGs at temperatures between 21°C and 35°C . The dashed lines mark regions where the target wavelength lies within a 1310 ± 5 nm interval, i.e., in the center of the O-band.

tune the exciton wavelength of the QD till we reach a maximum count rate at 1313 nm while all other parameters are kept fixed. In the following, we discuss two techniques how this can be performed: temperature tuning and bias voltage tuning.

It is well-known that the emission wavelengths of a QD tune with temperature. This is due to the temperature dependence of the bandgap energy in semiconductors. The bandgap energy decreases if the temperature is increased. According to Varshni [206],

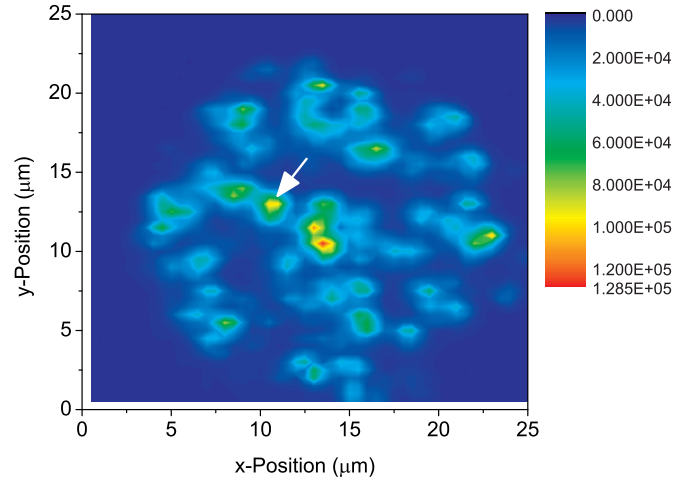


Figure 6.7: Confocal scan over the aperture of mesa B2. The fluorescence was coupled into a single-mode fiber and detected within a 710 ± 5 nm spectral window. The marked spot (white arrow) is fluorescence from the QD that is used in our QFC experiments.

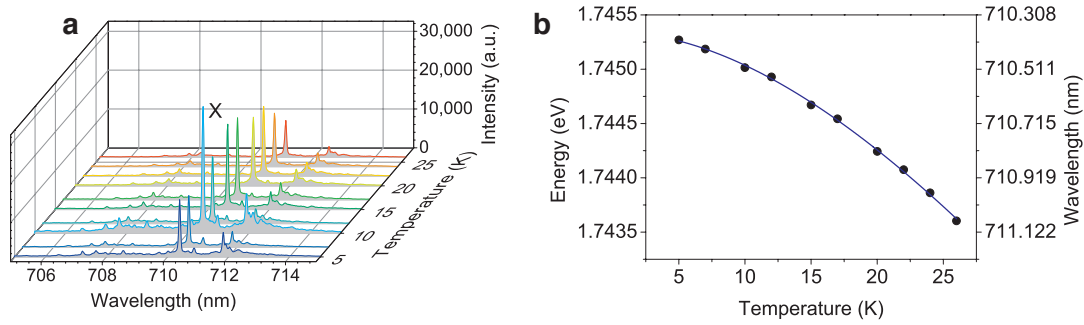


Figure 6.8: Wavelength tuning by means of the temperature. (a) Spectra of the QD at different temperatures. X denotes the single exciton line. All spectra were recorded at a bias voltage of 3.2 V and an excitation power of 120 nW at 590 nm. A spectrometer grating with 1800 lines/mm was used and the integration time was 10 s for each spectrum. (b) Center wavelength of the single exciton line vs. temperature. Figures after [198], SM (Copyright © 2012 by the American Physical Society.)

this can be explained by two effects. A shift in the relative position of the conduction and valence bands is caused, first, by a dilatation of the crystal lattice with increasing temperature and, second, by a temperature dependence of the interaction between electrons (holes) and phonons (whereas the second effect provides the major contribution). To investigate the temperature dependence of the emission wavelength for the QD used in our QFC experiment, we recorded the spectra of the QD for different temperatures between 5 K and 26 K. The measured spectra, shown in Fig. 6.8(a), consist of differ-

ent components. The main component is attributed to the single exciton line (labeled with X) because its intensity depends linearly on the excitation power (the intensity of the biexciton transition would show a quadratic power dependence). Additional lines and background can originate from biexciton and charged exciton transitions or other nearby QDs. With increasing temperature, all spectral features shift to longer wavelengths. The positions of the single exciton line were extracted from the spectra and plotted as a function of temperature in Fig. 6.8(b). The data are fit using the equation [206]

$$E_g(T) = E_0 - \alpha T^2 / (T + \beta), \quad (6.1)$$

which describes the bandgap E_g in semiconductors as a function of temperature T . E_0 is the energy gap at $T = 0$ K, α and β are constants. We obtain $E_0 = 1.74534 \pm 1.9 \times 10^{-5}$ eV, $\alpha = -2.42162 \pm 5.7 \times 10^{-5}$ eV/K, and $\beta = 69.2 \pm 22.7$ K from the fit. By varying the temperature in a range of $\Delta T = 21$ K we can tune the wavelength of the exciton line by $\Delta \lambda_X = 0.679$ nm. However, wavelength tuning by temperature is rather inconvenient for our purposes since it is slow and affects the alignment of the confocal microscope due to thermal expansion of the sample. The influence on the alignment can be seen from Fig. 6.8(a). All spectra were recorded under the same experimental conditions. The alignment of the confocal setup was done once before the measurement at a sample temperature of 10 K and was not optimized during the measurement. For temperatures above or below 10 K, the intensity of the exciton line in the spectrum decreases. Thus, when tuning the exciton wavelength via temperature, the alignment of the setup has to be optimized for each temperature value when maximum intensity is desired. A much

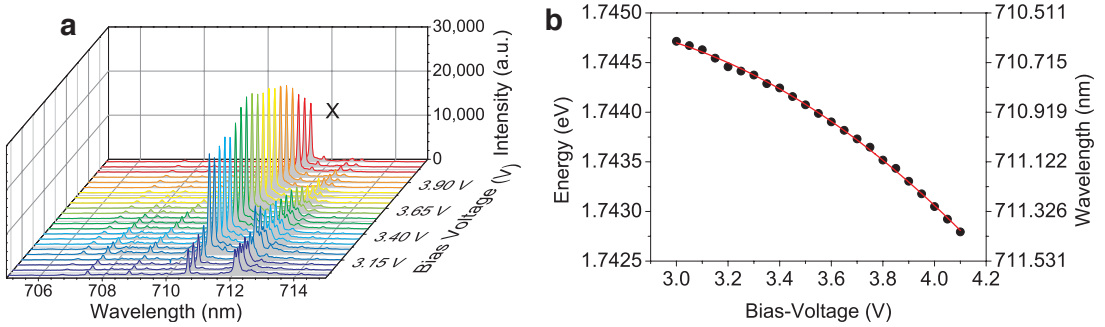


Figure 6.9: Wavelength tuning using the bias voltage. (a) Spectra of the QD for different bias voltages at $T = 12$ K. All other conditions are equal to those given for Fig. 6.8. (b) Center wavelength of the single exciton line as a function of the bias voltage. Figures after [198], SM (Copyright © 2012 by the American Physical Society.)

faster and more reliable way of tuning the exciton emission wavelength is provided by tuning the bias voltage applied to the QD sample. Emission spectra of the QD that were recorded at different bias voltages between 3.0 V and 4.1 V are displayed in Fig. 6.9(a). The temperature was held fixed at $T = 12$ K. From Fig. 6.9(a), we see that the intensity level of the spectra is roughly constant within a certain voltage range, i.e., tuning the wavelength of the exciton line is possible while collecting a high rate of photons without

performing any re-alignment of the setup. The center energy/wavelength of the exciton line as a function of the bias voltage is shown in Fig. 6.9(b). Similar to the case of temperature tuning, the curve follows a quadratic law. The data are well fit using the empirical formula

$$E(U_b) = A + BU_b + CU_b^2, \quad (6.2)$$

where $E(U_b)$ denotes the energy associated with the exciton transition, U_b is the bias voltage, and $A = 1.74002 \pm 4.7 \times 10^{-4}$ eV, $B = 0.00396 \pm 2.7 \times 10^{-4}$ eV/V, and $C = 7.99 \times 10^{-4} \pm 0.37 \times 10^{-4}$ eV/V² are constants. Tuning the bias voltage by $\Delta U_b = 1.1$ V results in an exciton wavelength change of $\Delta \lambda_X = 0.783$ nm.

6.3 QFC from 711 nm to 1313 nm: Experimental Results

6.3.1 Spectral Filtering

The fluorescence map shown in Fig. 6.7 was obtained by coupling the QD fluorescence into a single-mode fiber to guide it to the Si APD. A QD density of 1.5×10^{10} cm⁻² was determined in AFM measurements of InP QDs embedded in $(Al_xGa_{1-x})_{0.51}In_{0.49}P$ ($x \in [0, 1]$) barriers grown under the same conditions as the sample used in our experiments [207]. Although not all of the QDs show light emission, with such high QD density, it is crucial to employ confocal rejection using a single-mode fiber to spatially isolate PL from single emitters. However, this spatial filter is not sufficient to reduce the noise background of the visible fluorescence to a tolerable level. In fact, we have to apply narrow spectral filtering in addition. This is accomplished by inserting a coated 56- μ m-thick silica etalon into the beamline of the visible fluorescence light. The etalon (Finesse $\mathcal{F} = 42$, FSR = 1.85 THz/0.0753 nm) serves as a tunable narrow bandpass filter for the exciton line of the QD around 710.7 nm. The effect of spectral filtering can be studied by comparing the confocal scans and the corresponding spectra shown in Fig. 6.10(a), (c) and Fig. 6.10(b), (d), respectively. Figure 6.10(a) and Fig. 6.10(b) were recorded without narrow spectral filtering. Several QDs can be identified on the map in Fig. 6.10(a) and it is evident from the spectrum in Fig. 6.10(b) that a certain amount of background is still collected through the single-mode fiber. In order to select a single emission line from a single QD, we insert the etalon as a narrow bandpass filter into the beamline of the visible PL light. This situation is represented in the map in Fig. 6.10(c) and the spectrum in Fig. 6.10(d). The etalon clearly suppresses PL from other QDs and is applied in measurements where we directly detect visible photons. As will be explained below, etalon filtering of the visible fluorescence is not necessary when detecting down-converted light. Nevertheless, the etalon is an indispensable component for pre-alignment of the conversion setup: first, we identify a proper point of operation for the QD (temperature, bias voltage, optical excitation power) that delivers bright, narrowband emission into the single exciton line. Second, the angle of the etalon is tilted for maximum transmission of the single exciton line. We then temporarily replace the QD light source by the cw Ti:sapphire laser and insert light from this

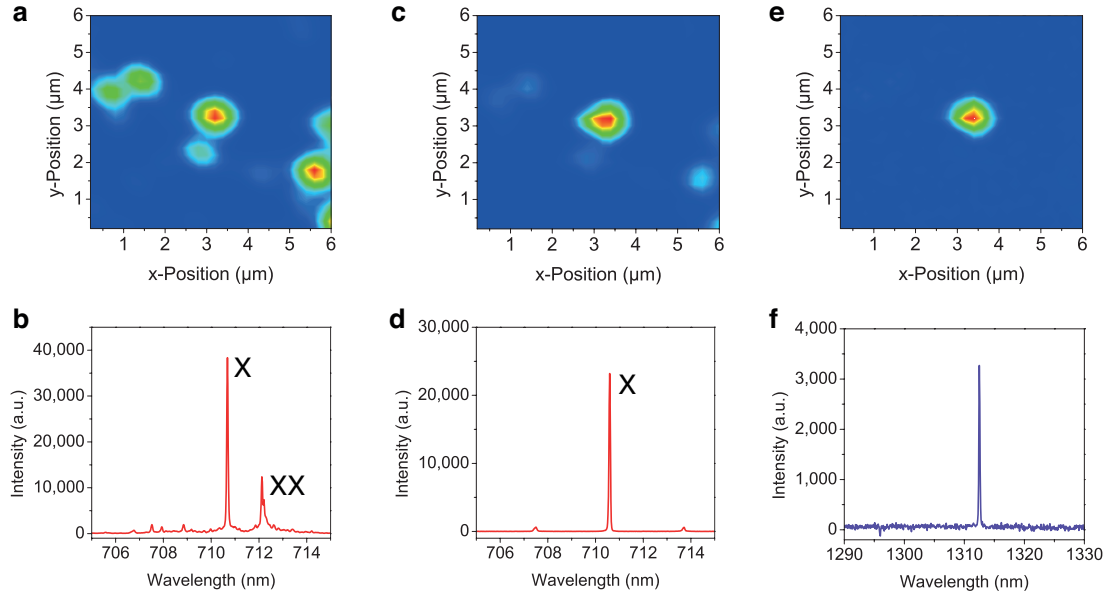


Figure 6.10: Photoluminescence (PL) maps with corresponding spectra. (a), (c), (e) Same $6 \times 6 \mu\text{m}^2$ detail of the QD sample. Maps (a) and (c) were recorded by scanning the xy position of the sample and directly detecting the visible PL from the QD using a Si APD, (a) without and (c) with etalon filtering. Map (e) was obtained by scanning the same sample area but detecting the down-converted light at 1313 nm with a SSPD. (b), (d), (f) Spectra that were measured by setting the xy position of the sample to the maximum intensity of the central QD. (b), (d) Visible PL spectrum without and with etalon filtering. The two prominent lines in (b), separated by 1.45 nm (3.54 meV), are attributed to exciton (X) and biexciton (XX) transitions. (f) Converted spectrum illustrating the effect of spectral filtering by a combination of DFG acceptance curve and FBG. Figures after [198] (Copyright © 2012 by the American Physical Society.)

laser into SMF2. The laser wavelength is set to match the transmission maximum of the etalon. Thus, the visible input wavelength is given. All parameters (QPM grating period, WG temperature, pump wavelength) can now be adjusted conveniently at macroscopic power levels to satisfy the quasi-phases-matching condition. Finally, SMF2 is again connected to the confocal microscope for launching single photons into the frequency converter. After the alignment procedure, the complete setup as given in Fig. 6.3 is ready for operation. Maximizing the count rate at 1313 nm can be achieved by fine tuning the exciton wavelength via the bias voltage as described in Sect. 6.2.3. The map in Fig. 6.10(e) was recorded by detecting converted IR light employing a SSPD. Figure 6.10(f) shows the corresponding spectrum. In this case, no etalon filtering of the visible input light is needed. From Fig. 6.10(f), one recognizes that no background or further emission lines are found in the IR spectrum. The acceptance bandwidth of the DFG process in combination with the FBG represents a narrow and efficient bandpass filter with high sideband suppression. To get a deeper insight in this effect, we regard

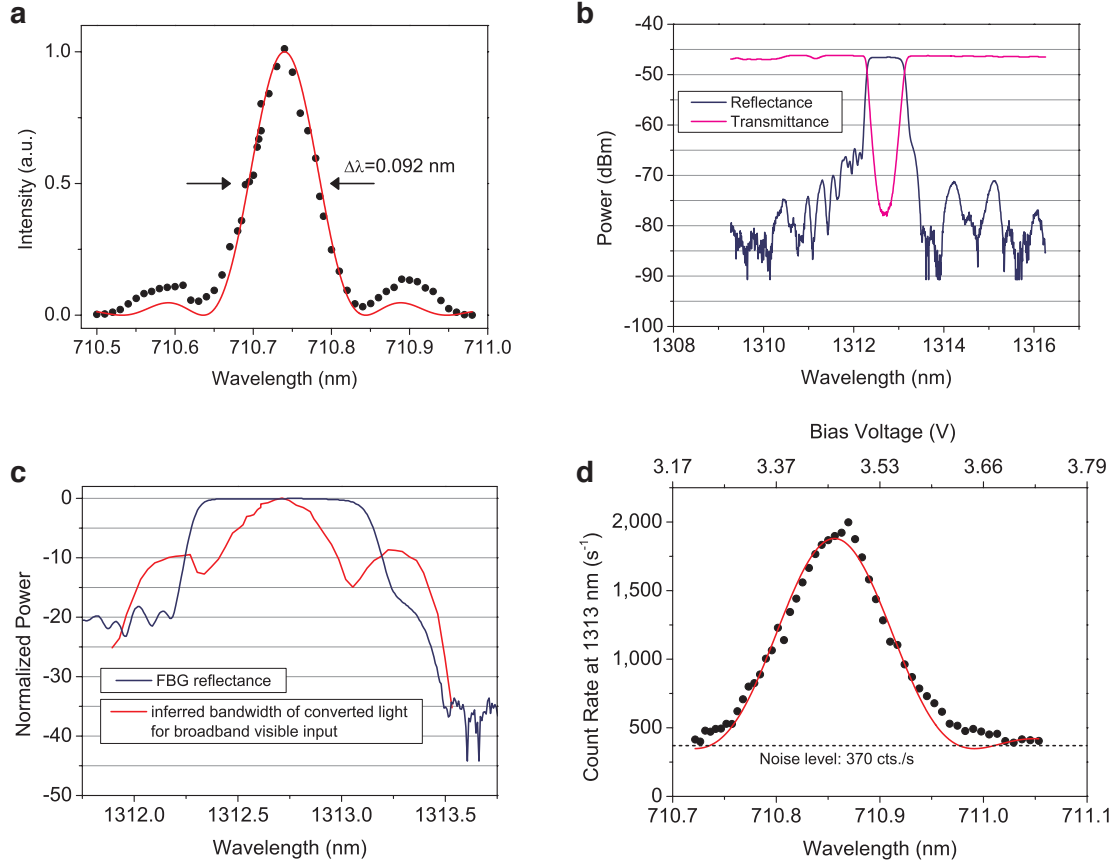


Figure 6.11: DFG acceptance bandwidth and FBG reflectance. (a) Spectral acceptance bandwidth of the DFG process measured with an OSA for 2 mW of input power around 710.74 nm from a tunable cw Ti:sapphire laser. Figure after [198] (Copyright © 2012 by the American Physical Society.) (b) Transmittance and reflectance of the FBG measured by the manufacturer [208]. (c) The spectrum of a converted broadband visible input (inferred from the DFG acceptance bandwidth) together with the FBG reflectance. For comparison, the curves have been normalized and plotted on a logarithmic scale. (d) DFG acceptance bandwidth measured with single-photon input from the QD. The wavelength of the input light was tuned by varying the applied bias voltage. The wavelength scale shows a slight offset with respect to (a) because the grating spectrometer used in this measurement was calibrated to another reference than the OSA.

Fig. 6.11(a) and (b) which show the acceptance curve of the DFG process and the reflectance (transmittance) characteristic of the FBG, respectively. The DFG acceptance bandwidth $\Delta\lambda_{\text{DFG}}$ is determined to be 0.092 nm from a sinc^2 fit to the measured data. Using $\Delta\nu_{\text{IR}} = \Delta\nu_{\text{vis}} + \Delta\nu_{\text{p}} \approx \Delta\nu_{\text{vis}}$ (since $\Delta\nu_{\text{p}} \ll \Delta\nu_{\text{vis}}$) this translates to a bandwidth of $\Delta\lambda_{\text{IR}} \approx 0.31$ nm. Together with a -20 dB reflection bandwidth of 1.275 nm for the FBG this essentially means that only IR light which lies in a spectral interval that corresponds to the converted central peak of the acceptance curve is transmitted. The

situation is illustrated in Fig. 6.11(c) where the inferred converted spectrum of a (hypothetical) broadband visible input is presented together with the reflectance of the FBG in one plot. As can be seen from the logarithmic plot, the sidebands of the sinc² curve are intrinsically one order of magnitude weaker than the central peak. Spectral filtering by means of the FBG additionally leads to a sideband suppression by at least two orders of magnitude. The above considerations are well confirmed by a measurement of the acceptance bandwidth using single-photon input (see Fig. 6.11(d)). Comparing Fig. 6.11(a) and 6.11(d) shows that the acceptance curve of the nonlinear interaction is correctly described by the sinc² function, no matter if the visible input power is on the order of mW or fW.

6.3.2 Conversion Efficiency with Single-Photon Input

In every experiment involving classical nonlinear wavelength conversion, the conversion efficiency is always an important parameter. This is even more true for QFC because, in the ideal case, we aim at translating the complete information carried by visible photons to telecom photons. Every photon that is not converted means a loss of information. To determine the conversion efficiency of our setup as shown in Fig. 6.3(b) with single photons, we send a constant rate of single photons from the QD into the converter. We measure the count rate N_{IR} at 1313 nm for different pump power levels between 0 and 230 mW. For each value of the pump power, we also determine the noise count rate N_{noise} by recording the count rate at 1313 nm without inserting any signal at 711 nm into the converter. In this way, we obtain the data plotted in Fig. 6.12(a). At the maximum pump power of 230 mW we find $N_{\text{noise}} \approx 560 \text{ s}^{-1}$. Noise counts are generated

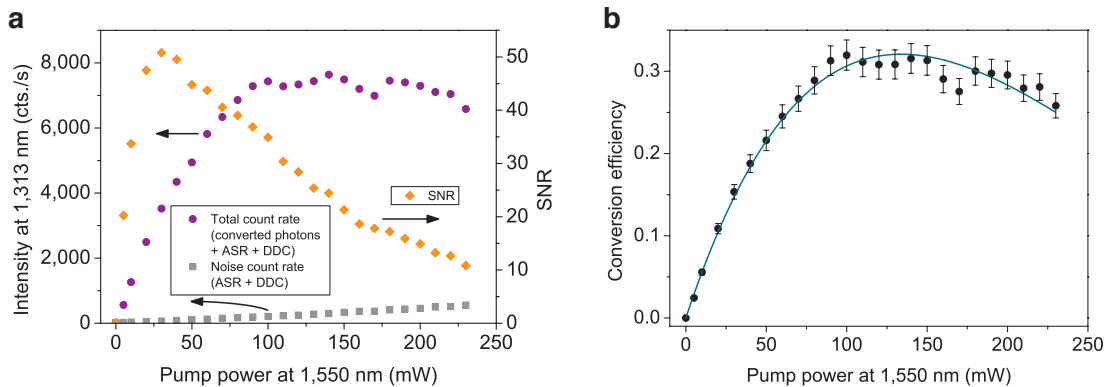


Figure 6.12: (a) Single-photon counting at 1313 nm using one SSPD. Total count rate (violet) including ASR noise and detector dark counts, noise background (grey) due to ASR noise and detector dark counts and SNR (orange). Each data point is a time average over 10 s. The highest count rate that is achieved at the optimum pump power is $\sim 7600 \text{ s}^{-1}$. Figure after [198], SM (Copyright © 2012 by the American Physical Society.) (b) Total efficiency of the frequency conversion setup calculated from the measured data in (a). Figure after [198] (Copyright © 2012 by the American Physical Society.)

either by ASR scattering (see Sect. 5.2.2 and Refs. [49,187]) induced by the strong 1550-nm pump field or by detector dark counts (DDC), such that $N_{\text{noise}} = N_{\text{ASR}} + N_{\text{DDC}}$, where N_{ASR} and N_{DDC} are the pure ASR and DDC rates, respectively. While the DDC rate of the SSPD is at a constant level of $N_{\text{DDC}} \approx 20 \text{ s}^{-1}$ in this measurement, N_{ASR} linearly scales with the pump power in the WG. The signal-to-noise ratio, given by

$$\text{SNR} = \frac{\text{count rate converted photons}}{\text{count rate noise photons}} = \frac{N_{\text{IR}} - N_{\text{noise}}}{N_{\text{noise}}} \quad (6.3)$$

is also shown in Fig. 6.12(a). We yield a maximum SNR of about 50 for 30 mW of pump power. This value is more than eight times higher than the maximum SNR of 6 determined for the 738 nm/1403 nm/1557 nm wavelength combination in Sect. 5.2.4 where the number of photocounts per second is comparable. At a first glance, the significant increase of the SNR seems surprising because the SSPDs are operated in free running mode (unlike the InGaAs/InP SPADs in Sect. 5.2.4 which are operated in gated mode) and also have a lower detection efficiency than the InGaAs/InP SPADs (SSPD: 12%, InGaAs/InP SPAD: 25%). One might expect that these factors should result in a SNR that is even worse. However, the advantages of long-wavelength pumping become clearly apparent here. Since the pump wavelength is significantly larger than the target wavelength (spectral separation $> 1100 \text{ cm}^{-1}$), Raman noise is dramatically reduced leading to a much better SNR. For the point of maximum conversion at $P_{\text{p}}^{(\text{opt})} \approx 150 \text{ mW}$ we still find $\text{SNR} \approx 21$, which is sufficient to perform a measurement of the photon statistics at 1313 nm in less than 4 hours (see next section). From the measured data in Fig. 6.12(a), we calculate the total conversion efficiency η_{total} as described in the following. The number of telecom photons per second $\Phi_{\text{out,IR}}$ that hit the SSPD (position I in Fig. 6.3) is given by $\Phi_{\text{out,IR}} = (N_{\text{IR}} - N_{\text{noise}})/\eta_{\text{SSPD}}$ where $\eta_{\text{SSPD}} = 0.122 \pm 0.007$ is the detection efficiency of the SSPD. To calculate η_{total} , we need to know the photon flux $\Phi_{\text{in,vis}}$ at position E which we regard as the entrance of our conversion setup. The (time-averaged) exciton emission of the QD is almost completely unpolarized since the excitonic line is composed of two fine structure components with orthogonal linear polarizations [78]. Thus, optimizing the polarization control and the half-wave plate behind the fiber exit (position A) with the goal of maximizing the output at port ‘V’ of the PBS is very limited: we achieve a ratio of $\eta_{\text{PBS}} = 1.15$ (power leaving port ‘V’/power leaving port ‘H’). However, we exploit this fact by coupling the 711-nm photons that leave port ‘H’ of the PBS into a multi-mode fiber (MMF) and counting them with one of the Si APDs. In this way, we can perform frequency conversion and monitor the count rate in the visible simultaneously. The coupling efficiency into the MMF is $\eta_{\text{MMF}} = 0.88$ (transmission B \rightarrow C). After the MMF, the photons pass a $710 \pm 5 \text{ nm}$ bandpass filter with a transmission coefficient of $\eta_{\text{BP}} = 0.66$ (transmission C \rightarrow D) at 711 nm and are focused onto the active area of the Si APD by an antireflection-coated lens. The detection efficiency of the Si APD at 711 nm is $\eta_{\text{APD}} = 0.65$. All together, we can deduce the photon flux $\Phi'_{\text{in,vis}}$ at position

E from the detected count rate N_{vis} in the visible via

$$\Phi'_{\text{in, vis}} = \frac{\eta_{\text{PBS}} N_{\text{vis}}}{\eta_{\text{APD}} \eta_{\text{BP}} \eta_{\text{MMF}}}. \quad (6.4)$$

Note that $\Phi'_{\text{in, vis}}$ as given by equation (6.4) is related to photons within a 10-nm interval around 710 nm. Since the DFG acceptance bandwidth of the frequency converter is only $\Delta\lambda_{\text{DFG}} = 0.092$ nm (54.6 GHz), we are solely interested in the power in this narrow spectral interval. This power is almost completely concentrated in the single exciton line that has a spectral width of ~ 3.8 GHz. By measuring N_{vis} with and without the etalon filter, we find that 13.9% of the photons detected within the large 710 ± 5 nm interval can be assigned to the exciton line. We take account of this fact by introducing the factor $\eta_X = 0.139$ and obtain the photon flux $\Phi_{\text{in, vis}}$ related to photons belonging to the single exciton line of the QD:

$$\Phi_{\text{in, vis}} = \eta_X \Phi'_{\text{in, vis}} \approx 188,400 \text{ s}^{-1}. \quad (6.5)$$

Using this single-photon input, we measure the total efficiency $\eta_{\text{total}} = \Phi_{\text{out, IR}}/\Phi_{\text{in, vis}}$ of our frequency conversion setup as a function of the pump power P_p at 1550 nm that is coupled into the WG (see Fig. 6.12(b)). The data are fit using Eq. (5.6), i.e.,

$$\eta_{\text{total}}(P_p) = \eta_{\text{total}}^{(\text{max})} \times \sin^2(\sqrt{\eta_{\text{nor}} P_p L}). \quad (6.6)$$

We find $\eta_{\text{nor}} = 115 \text{ \%}/(\text{W cm}^2)$ and $\eta_{\text{total}}^{(\text{max})} \approx 0.32$, i.e., at the point of maximum conversion (at $P_p^{(\text{opt})} \approx 150$ mW), more than 30% of the fraction of the QD emission that can be coupled into a single-mode fiber is frequency down-converted in our setup. This result is in very good agreement with the one that was obtained for macroscopic power levels (see Sect. 6.2.2). In Sect. 6.2.2 we found that a total conversion efficiency of 31% corresponds to a signal depletion of 80%. In case of single-photon input from a QD, it is not possible to perform a simultaneous measurement of the conversion efficiency and the signal depletion for technical reasons. However, as the alignment of the setup was not changed significantly between the measurement at macroscopic power and the one with single photons, we assume that the signal depletion was around 80% also for the case of single-photon input.

The maximum internal conversion efficiency $\eta_{\text{int}}^{(\text{max})}$, that is, the fraction of photons that is converted within the Zn:PPLN crystal (F \rightarrow G), can be estimated from $\eta_{\text{total}}^{(\text{max})}$ by taking into account the input coupling efficiency $\eta_{\text{wg}} = 0.84$ into the WG (point F) and the transmission coefficient $\eta_{\text{filter}} \lesssim 0.6$ of the complete filtering stage (from G to I): $\eta_{\text{int}}^{(\text{max})} = \eta_{\text{total}}^{(\text{max})}/(\eta_{\text{filter}} \eta_{\text{wg}}) \gtrsim 0.64$. The factor η_{filter} is given as the product $\eta_{\text{filter}} = \eta_{\text{optics}} \times \eta_{\text{FC}} \times \eta_{\text{WDM}}$. Here $\eta_{\text{optics}} = 0.9$ describes the losses that result from the transmission through the half-wave plate and the Pellin–Broca prism and from the reflection from two gold mirrors. The coupling efficiency into the single-mode fiber after the pinhole is $\eta_{\text{FC}} \leq 0.7$ and the coefficient $\eta_{\text{WDM}} = 0.95$ includes the combined insertion loss of the system FOC–FBG–WDM1–WDM2. All coupling efficiencies and

transmission coefficients (η_{optics} , η_{FC} , η_{WDM} , η_{wg}) were measured independently at macroscopic power levels using either an InGaAs photodiode or the OSA. Note that the value of 64% is a conservative estimate and can be regarded as a lower bound for $\eta_{\text{int}}^{(\text{max})}$. In our calculations of η_{filter} , we have neglected the losses induced by several mechanical fiber-to-fiber connections. These losses are estimated to amount to a few percent. The value of $\eta_{\text{int}}^{(\text{max})} \geq 64\%$ is also supported by another measurement of the conversion efficiency using attenuated laser pulses (500 kHz repetition rate, 1.7 photons/pulse on average) and an InGaAs/InP SPAD [209] analogous to the experiment described in Sect. 5.2.4. Here $\eta_{\text{int}}^{(\text{max})} = 0.68$ was reached at $P_{\text{p}}^{(\text{opt})} = 150$ mW. The corresponding signal depletion was 77% measured with a macroscopic input power at 710 nm (optical attenuation filters removed).

To summarize, we achieve an *internal* conversion efficiency that is slightly lower than the one determined for the 738 nm/1403 nm/1557 nm wavelength combination in Sect. 5.2.4. However, the *total* conversion efficiency (corrected for detection efficiency) could be increased by a factor of 4 (32% compared with 8% in Sect. 5.2.4). This is due to improvements of the setup. The transmission from the WG output to the detector was enhanced by increasing the coupling efficiency into the fiber behind the pinhole and using only fiber-optic components (FOC, FBG, WDMs) instead of bulk filters for spectral filtering. Furthermore, we have used the free running SSPD instead of a gated InGaAs/InP SPAD. In contrast to the InGaAs/InP detector, the SSPD has the advantage that it does not ‘miss’ photons at arrival times that are not within an active detection window. This was a problem in the experiment described in Sect. 5.2.4 where the gate width was chosen to be shorter than the temporal width of the photons to achieve a better SNR.

6.3.3 Time-Correlated Single-Photon Counting

For applications in quantum communication and information, it is essential to control the temporal and spectral properties of single photons. One fundamental example is the absorption of a photon by a single atom or ion in free space. In this case, the absorption probability strongly depends on the temporal shape and the spectral bandwidth of the single-photon wavepacket [210, 211]. With regard to QFC, it is either desirable to not change the temporal and spectral properties of the input photons or to manipulate them in a controllable way [212]. Under the conditions chosen in our experiment, QFC should not have any influence on the temporal shape and width of the single-photon wavepackets. This was checked by measuring the temporal width of the photons before and after conversion using time-correlated single-photon counting (TCSPC) [213]. To this end, we use a two-channel TCSPC system (*PicoQuant, model PicoHarp 300*). A TTL signal synchronized with the optical pulses from the 590-nm excitation source is inserted into channel 1. The electronic output of a single-photon detector (Si APD for visible photons, SSPD for telecom photons) is input to channel 2. Each TTL pulse arriving at channel 1 starts a clock which is stopped by an electronic pulse in channel 2 signalling a photon detection event from the detector. The number of counts $N(t)$

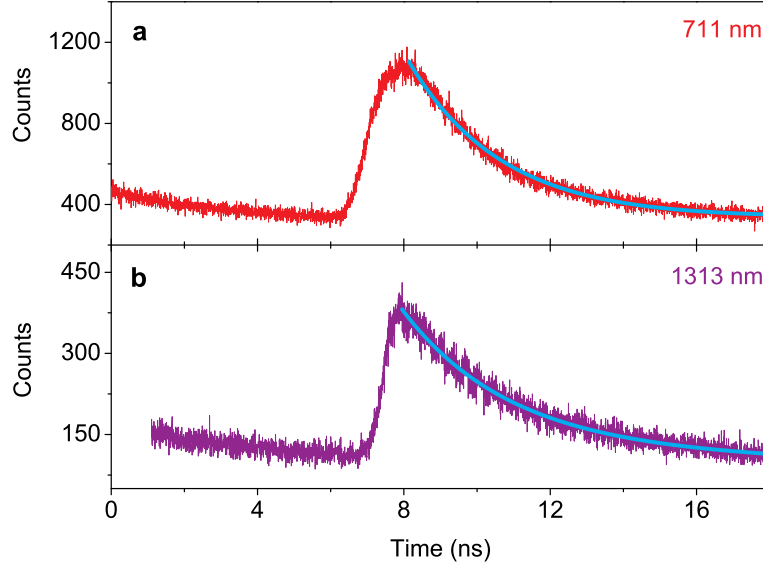


Figure 6.13: (a) TCSPC trace for the original input photons at 711 nm (red: measurement, cyan: fit). (b) Same measurement as in (a) but for converted telecom photons (violet: measurement, cyan: fit). The frequency translation process obviously does not deteriorate the shape and width of the temporal profile. Note that the histogram in (b) features a steeper rising edge due to the much better timing jitter of the SSPD compared to the Si APD.

accumulated during a certain time interval t between start and stop events is recorded in a histogram. These TCSPC traces for visible input photons and converted telecom photons are presented in Fig. 6.13(a) and (b), respectively. The data are fit using a bi-exponential function

$$N(t) = A_1 e^{-(t-t_0)/\tau_1} + A_2 e^{-(t-t_0)/\tau_2} + N_0. \quad (6.7)$$

A_1 and A_2 are the amplitudes of the two exponential functions, t_0 is a time shift accounting for the fact that the maxima of the exponentials are not at $t = 0$ for experimental reasons, and N_0 is an offset. The first decay constant τ_1 is associated with the lifetime of the excited state of the QD and τ_2 describes a much slower recapture process which has been reported earlier for InP QDs [214]. Figure 6.14 delineates the processes that can happen when the QD is optically excited and how they are related to the constants τ_1 and τ_2 . The model was proposed by Aichele *et al.* [214]. After electron-hole pairs are created by a non-resonant optical excitation pulse, two processes can take place: (i) electrons and holes are immediately captured by the QD to recombine and emit a photon or (ii) they get trapped by trapping sites in the vicinity of the QD. Trapped carriers can be released at a later time and get recaptured by the QD to recombine and generate a photon. The first process is governed by the time constant τ_1 which is the average lifetime of the excited state in the QD. The second process is determined by the much longer time constant τ_2 which is the average lifetime of a trapped carrier. It is

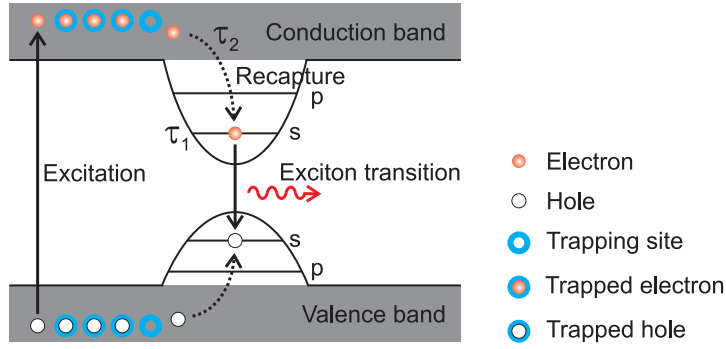


Figure 6.14: Illustration of the re-excitation process observed for InP QDs. Only the single exciton transition is drawn in the picture because only this transition is important for our experiments.

assumed that the recapture effect is connected to the MOVPE growth process applied to create InP QDs. Compared with MBE, the MOVPE technique creates much more defects in the crystal lattice which can act as trapping sites for charge carriers. This also explains why the recapture process does not play a role for InAs QDs that are grown by MBE. From the fits we obtain $\tau_{1, \text{vis}} = 2.6 \pm 0.1 \text{ ns}$ before and $\tau_{1, \text{IR}} = 2.9 \pm 0.4 \text{ ns}$ after conversion. Taking into account the error margins, these results indicate that the temporal width of the single-photon wavepacket remains unchanged under QFC. For the second decay constant we find $\tau_{2, \text{vis/IR}} \approx 2.5 \mu\text{s}$ for both visible and converted photons.

As a supplement to the TCSPC results discussed above, it should be added that also the preservation of temporal coherence has been investigated by A. Lenhard [198]. To this end, the degree of first-order coherence $g^{(1)}(\tau)$ was measured using a Michelson interferometer with an adjustable pathlength difference between the two arms. From a series of measurements with varying pathlength differences one can deduce the coherence time T_2 . The obtained results are $T_{2, \text{vis}} = 42 \pm 17 \text{ ps}$ before and $T_{2, \text{IR}} = 49 \pm 13 \text{ ps}$ after conversion [198], i.e., within the error margins, the coherence time of the photons remains unchanged during QFC. This is expected from theory and can be understood as follows. For a Lorentzian lineshape, the instantaneous linewidth $\Delta\nu$ is related to the coherence time by

$$T_2 = 1/(\pi\Delta\nu). \quad (6.8)$$

Due to energy conservation, the linewidths $\Delta\nu_{\text{IR}}$, $\Delta\nu_{\text{vis}}$, and $\Delta\nu_{\text{p}}$ of the converted field, the visible input field and the pump field, respectively, must satisfy $\Delta\nu_{\text{IR}} \leq \Delta\nu_{\text{vis}} + \Delta\nu_{\text{p}}$. On short timescales ($\sim 100 \mu\text{s}$), the linewidth of the pump light is far below 1 MHz [159]. Thus, assuming a Lorentzian lineshape and using Eq. (6.8), it follows that the influence of the pump light on the coherence of the converted single photons is negligible because $T_{2, \text{p}} > 0.32 \mu\text{s} \gg T_{2, \text{vis}}$.

Table 6.1: Parameters R_1 , R_2 , t_{int} used for normalization of the coincidence counts $G^{(2)}(\tau)$.

Measurement	R_1 [s ⁻¹]	R_2 [s ⁻¹]	t_{int} [s]
visible photons	27,800	28,981	745
telecom photons	3,300	4,461	6,085
cross correlation	9,922	2,234	9,440

6.3.4 Conservation of Photon Antibunching

Their nonclassical photon statistics make single quantum emitters, like QDs or single atoms, unique among all light sources. Therefore, it is crucial to test to what extent these fragile properties can be conserved during QFC. To this end, we measure the degree of second-order coherence $g^{(2)}(\tau)$ (see Sect. 2.2.2) before and after the conversion process. To determine $g^{(2)}(\tau)$ for the light emitted directly by the QD, we use a HBT interferometer (see Sect. 2.2.2 and Ref. [83]) consisting of a non-polarizing 50/50 beam-splitter cube and two Si APDs. In the case of telecom light, a fiber-based HBT setup composed of a 50/50 fiber beamsplitter and two SSPDs is applied. For measurements of the second-order photon correlation, the TCSPC module is operated in time-tagged mode, meaning that every detection event is stored in a list together with a time stamp. Using these lists, software-assisted correlation of the events can be performed on a PC during the measurement or at any later time. Each channel of the TCSPC unit features a constant fraction discriminator (CFD). On the one hand, the output pulses of the Si APDs associated with the detection of a photon are well adapted (concerning voltage level and shape) for the requirements of the TCSPC electronics. On the other hand, for the SSPD output pulses, the CFD sometimes produces irregular pulse bursts. Due to channel crosstalk, these pulse bursts appear on both input channels and thus can easily be identified and discarded by the data acquisition software. Figures 6.15(a)–(f) show a comparison of the correlation measurements that have been performed: the unnormalized coincidence counts $G^{(2)}(\tau)$ are given in Fig. 6.15(a) and 6.15(b) for visible input photons and converted output photons, respectively. The plot in Fig. 6.15(c) was obtained from a cross-correlation measurement with a hybrid HBT setup, i.e., one half of the visible photons is sent directly to a Si APD, the other half undergoes frequency down-conversion and is then detected with a SSPD. To ensure comparability, all calculations of the unnormalized correlation functions were performed with a time binning of $t_{\text{bin}} = 512$ ps. The $g^{(2)}(\tau)$ functions in Fig. 6.15(d)–(f) are calculated from the data presented in Fig. 6.15(a)–(c) by making use of relation (2.51). This corresponds to a normalization with respect to the correlation function of a perfect cw Poissonian light source of equal average intensity. The parameters R_1 , R_2 , and t_{int} that have been used for normalization in all three cases are summarized in Table 6.1. We underline that the $G^{(2)}(\tau)$ data have been normalized as if a cw excitation was applied to the QD albeit we have used pulsed excitation. This is justified by the fact that the data much more resemble a cw intensity correlation function than a pulsed one (a mod-

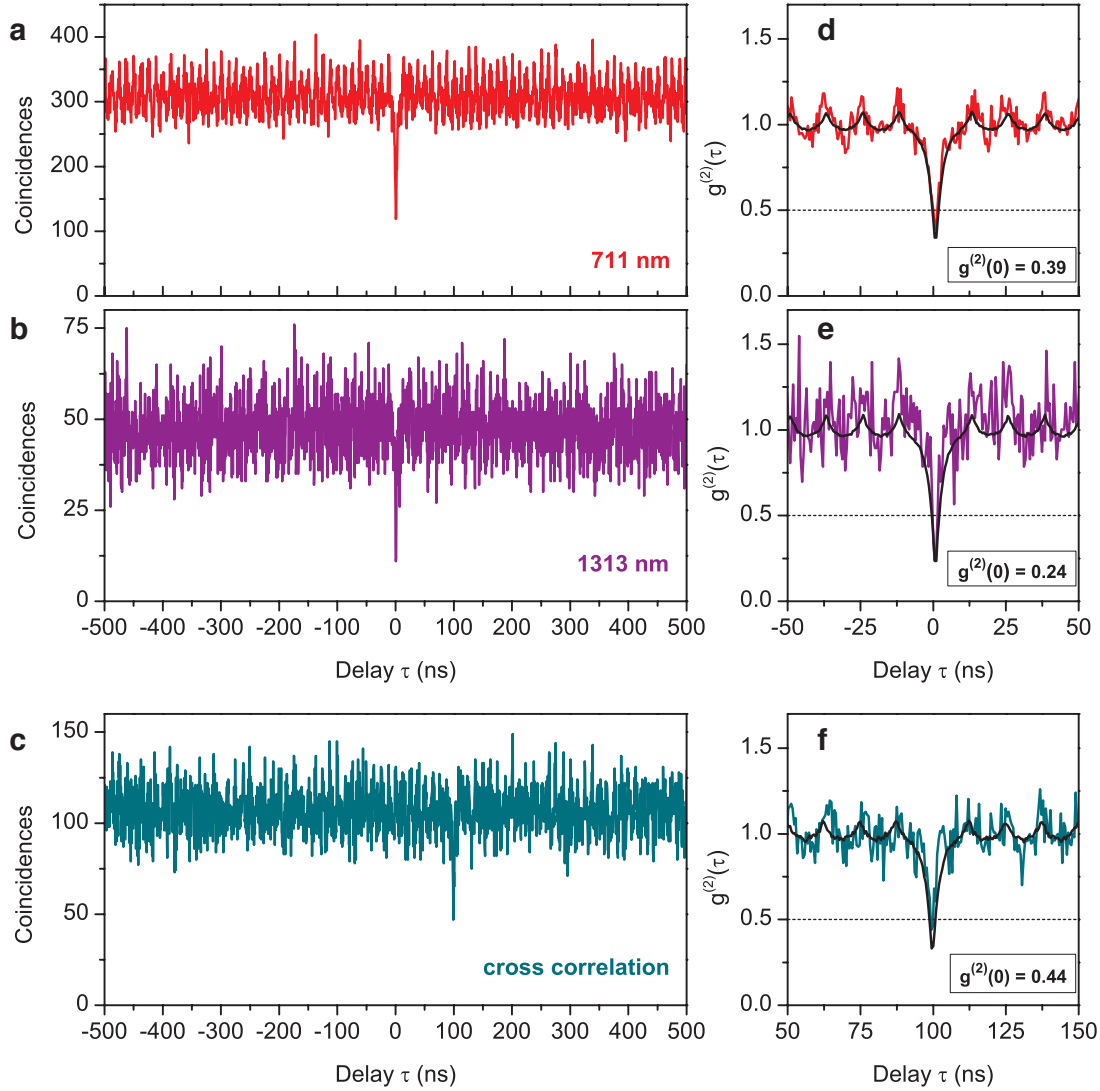


Figure 6.15: Conservation of photon antibunching under frequency down-conversion. (a) Coincidence counts vs. time delay τ for the input photons at 711 nm measured with a HBT setup for visible light. (b) Same as (a) but for the down-converted photons at 1313 nm measured with a fiber-integrated HBT setup for telecom light. (c) Coincidence counts measured with a hybrid HBT setup. (d)–(f) $g^{(2)}$ correlation functions calculated by normalization of the data plotted in (a)–(c). In each case, the detection events at the two individual detectors of the HBT setup are anti-correlated and the dip in the $g^{(2)}$ function drops below 0.5. The black curves in (d)–(f) were obtained from Monte Carlo simulations based on a theoretical model. No background has been subtracted from the experimental data in all plots.

ulation with the 80-MHz periodicity of the excitation pulses is still visible, though). This is due to the recapture effect described in the previous section and is a well-known

phenomenon for InP/GaInP QDs [214]. Monte Carlo simulations which perfectly reproduce the peculiar shape of the measured intensity correlation functions were performed by A. Lenhard [198] (see Fig. 6.15(d)–(f)). The simulations are based on the model sketched in Fig. 6.14. Three parameters are used as input to the simulations: the time constants τ_1 and τ_2 and the branching ratio r_1/r_2 of the two excitation paths. Here r_1 denotes the fraction of electron–hole pairs that are immediately captured by the QD and r_2 is the fraction of electron–hole pairs that are first trapped at trapping sites before they get captured by the QD. The branching ratio is the only free parameter in the simulations because τ_1 and τ_2 are known from the TCSPC measurements (see previous section). The branching ratio is adjusted such that the ratio of peak-to-valley values of the simulated $g^{(2)}$ functions match those of the measured $g^{(2)}$ functions (tested by a least squares fit). It is important to stress that the filling between the peaks of the $g^{(2)}(\tau)$ function is a specific property of the QD and has nothing to do with the QFC process. The authors of Ref. [214] have pointed out that re-excitation processes can be a severe problem for applications where it is essential to generate single photons on demand. Importantly, however, the effect does not destroy the antibunching dip at $\tau = 0$ and is thus irrelevant for our proof-of-principle experiment: to check whether the down-conversion process has corrupted the quantum properties of the input light field, we focus on the value of the intensity correlation function at zero delay $g^{(2)}(\tau = 0)$. The measured $g_{\text{vis}}^{(2)}(0) = 0.39 \pm 0.02 < 0.5$ for the original PL of the QD clearly proves single-photon emission from a single quantum emitter. The simulation of the emission process reproduces the measured data very well and reveals that $g_{\text{vis}}^{(2)}(0) > 0$ due to the timing jitter of the APDs and uncorrelated photon emission from background passing the etalon filter (SNR $\approx 7:1$ determined from the spectrum in Fig. 6.10(d)/Fig. 6.16). For the down-converted light field at 1313 nm we obtain a value of $g_{\text{IR}}^{(2)}(0) = 0.24 \pm 0.04$. The Monte Carlo simulation closely reproduces the measured data for SNR = 12:1 of the light field and a smaller timing jitter of the SSPD, indicating that the sub-Poissonian statistics of the input light field have been fully preserved or even improved. This can be understood from the fact that the SNR of the QFC process is much higher than the SNR of the light source, i.e., the SNR of the converted light is increased compared to the input light thanks to the strong spectral filtering effect of the QFC setup. This is consistent with the results from an up-conversion experiment published by Ates *et al.* very recently [57]. The $g^{(2)}$ cross-correlation function shown in Fig. 6.15(f) of original and converted photons exhibits a dip as well and we find $g_{\text{vis/IR}}^{(2)}(\tau') = 0.44 \pm 0.02$. The observed anti-correlation again proves the conservation of the single particle character of the light upon QFC. The fact that the dip occurs at $\tau' \approx 100$ ns perfectly matches the difference of the path lengths the photons of different color have to travel to the respective detectors.

Lastly, it should be mentioned that the minimum bin size compatible with our correlation electronics is $t_{\text{bin, min}} = 4$ ps. We have artificially increased this to $128 \times t_{\text{bin, min}} = 512$ ps to speed up data acquisition which was inevitable since constant experimental conditions could only be maintained over a few hours. The increase of t_{bin} generally

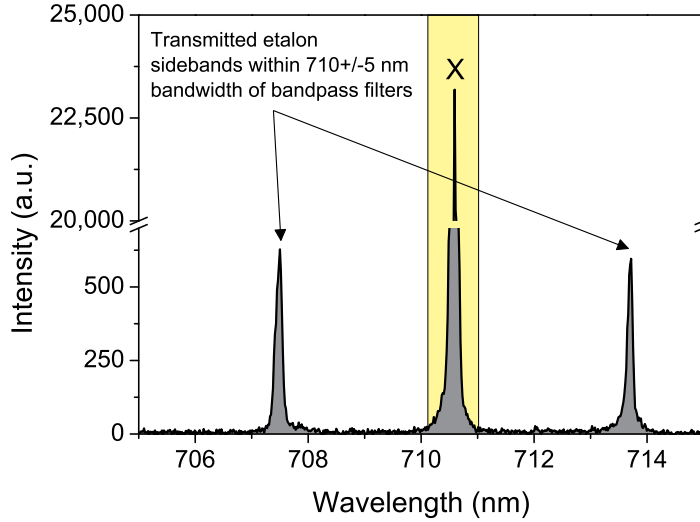


Figure 6.16: Same spectrum as in Fig. 6.10(d) but with a different scaling to better illustrate the effect of background due to transmitted etalon sidebands. A SNR of ~ 7 was determined by comparing the area under the full spectrum (grey area) with the area under the exciton line (yellow shaded). Figure after [198], SM (Copyright © 2012 by the American Physical Society).

leads to an overestimation of the $g^{(2)}(0)$ values. For perfect timing resolution, the measured data would correspond to $g_{\text{vis}}^{(2)}(0) = 0.23$ and $g_{\text{IR}}^{(2)}(0) = 0.15$ for the input photons and converted photons, respectively.

6.4 Summary and Discussion

The technical challenges stated at the beginning of this chapter were met in the experiments described in the previous sections. The detrimental influence of Raman scattering was drastically reduced by using a long-wavelength pumping scheme and narrow spectral filtering. The narrow acceptance bandwidth of the DFG process is a potential issue when using broadband light emitted by solid-state systems, e.g., diamond NV centers. This obstacle was avoided, however, by choosing a QD with a narrow single exciton line as a single-photon emitter. This means no limitation with respect to future applications because narrowband emission of single photons is definitely a prerequisite for the implementation of many fundamental protocols in the context of quantum information, e.g., the coupling of disparate quantum systems [215]. Suppression of the strong pump light has been accomplished by almost exclusively using fiber-optic components (FOC, FBG, WDMs). As opposed to most bulk optics, these allow to build narrow bandpass filters while at the same time providing a high transmission level within the passband. Finally, SSPDs were used for single-photon detection at the telecom wavelength. At present, these devices are most suitable for photon correlation measurements at telecom wavelengths as they combine reasonable detection efficiency with unprecedentedly

low dark count rates (even compared to Si APDs) [216, 217]. All in all, the aforementioned methods made it possible to prove that photon antibunching is conserved in our experiment. To the best of our knowledge, within the framework of this thesis, this has been demonstrated for the first time for visible-to-telecom QFC with single photons from a true quantum emitter. Table 6.2 again gives an overview on the results that have been obtained from the experiments on single-photon frequency down-conversion.

Table 6.2: Summary of the results obtained in single-photon frequency down-conversion.

			before conversion	after conversion
Photon flux	Φ	[s ⁻¹]	~188,400	~62,300
External efficiency	η_{ext}		0.32	
Internal efficiency	η_{int}			
TCSPC	τ_1	[ns]	2.6 ± 0.1	2.9 ± 0.4
	τ_2	[μs]	2.5	2.5
Coherence time	T_2	[ps]	42 ± 17 [198]	49 ± 13 [198]
Second-order coherence	$g^{(2)}(0)$		0.39* ± 0.02 (0.23**)	0.24* ± 0.04 (0.15**)

* time bin width of 512 ps

** perfect timing resolution

We close this chapter with several concluding remarks on the impact and future perspectives of the performed experiments. The motivation that stood at the very beginning of this thesis was to use visible-to-telecom QFC in order to minimize fiber transmission losses. It is evident from Fig. 6.17 that this goal has been reached. Assuming a realistic fiber attenuation of 3 dB/km at 711 nm and 0.3 dB/km at 1313 nm, QFC pays off for distances larger than 1.9 km when taking into account the actual overall efficiency of 32 % in our experiment. Note that after 16.8 km still 10 % of the telecom photons arrive at the fiber exit while this is true only for a poor 9×10^{-4} % of the visible photons. The actual performance of single-photon sources directly emitting at telecom wavelengths [218–222] (all based on QDs) is quite modest. The photon yield of these sources is low—at best, they produce detector count rates of a few 1000 cts./s—and it seems uncertain if this can be improved significantly in the future. Currently, such count rates are still comparable to those achieved with our hybrid approach consisting of a QD (emitting in the visible to near-infrared spectral range) in combination with quantum frequency down-conversion in a PPLN WG crystal. However, the telecom photon rate in our experiment could be dramatically increased by using a QD with a higher photon generation rate. Such devices already exist, e.g., Strauf *et al.* [223] have achieved single-photon count rates of up to 4.0 MHz (10.1 MHz) with an InAs QD in a high-Q microcavity under pulsed (cw) excitation. Therefore, the hybrid scheme seems to be a promising alternative to sources directly emitting at telecom wavelengths. The technique is very flexible as it allows for tuning the target wavelength by experimental

parameters that are easily adjustable, such as the pump wavelength, the QPM grating period, or the WG temperature. This paves the way for new kinds of applications, e.g., single-photon WDM [224]. Analogous to classical WDM techniques, two single-photon signals of different wavelengths could be converted to the same target wavelength to create indistinguishable photons emitted by two independent sources. Very recently, promising results in erasing distinguishability have been obtained by up-conversion of photons from the single exciton and the biexciton transition of the same QD [57]. Conversely, single-photon WDM could also be used to transmit photons from multiple emitters with identical emission wavelengths through a single optical fiber by distributing them to different wavelength channels via QFC. In this way, channel capacity could be greatly enhanced in QKD experiments with true single photons.

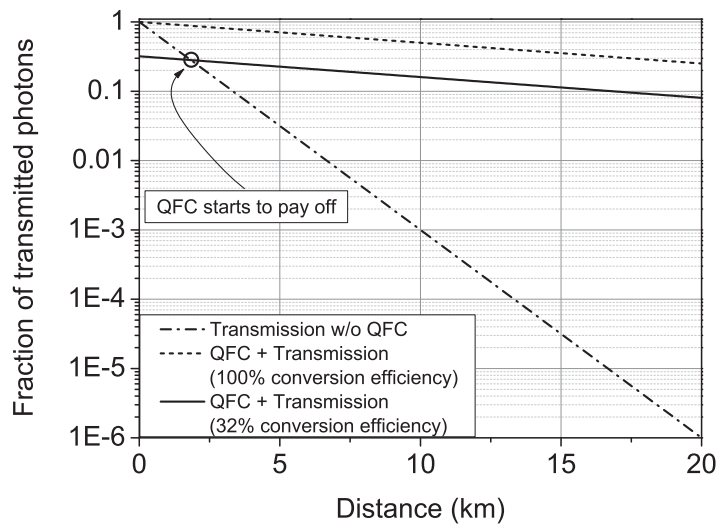


Figure 6.17: Fiber attenuation vs. fiber length for the case of direct transmission at 711 nm compared to transmission at 1313 nm with previous frequency down-conversion for 100 % (ideal case) and 32 % total conversion efficiency (achieved experimentally in this work). Although in our experiment 68 % of the photons are lost due to non-perfect frequency conversion and lossy spectral filtering, QFC is beneficial for distances larger than 1.9 km.

Finally, a few technical improvements of our setup could be made in the future. For example, as long as only C-band wavelengths are required, the cw SRO could be replaced by a less complex laser system consisting of an 1.55- μm ECDL and an erbium-doped fiber amplifier (EDFA). These systems are routinely used in classical fiber-optic communication. They are rapidly tunable over the whole C-band and can deliver more than 1 W of single-frequency output power. Furthermore, the internal conversion efficiency could be further increased to almost unity by an enhancement of the spatial mode overlap inside the WG (e.g., by mode matching tapers [225]). Additionally, external losses could be reduced by using a volume Bragg grating for spectral filtering as

in [57]. Altogether, this would lead to an increased overall conversion efficiency. Apart from optimizing the conversion setup, the quality of the visible single-photon source could also be improved in future experiments. Increased photon collection efficiency into a single-mode fiber, cavity coupling of emitters, resonant optical excitation, or all-electrical excitation are among the points that should be addressed. Higher count rates, smaller bandwidths (ideally Fourier-limited photons), and avoidance of detrimental effects, such as the carrier recapture process, would become possible in this way. It is also worthwhile to consider other wavelength combinations than the one we have used here. For instance, an interesting process would be the down-conversion from $\lambda_{\text{in}} \approx 900 \text{ nm}$ to $\lambda_{\text{out}} \approx 1550 \text{ nm}$ as demonstrated by Pelc *et al.* in a very recent paper [59]. This would require a pump wavelength around $2.15 \mu\text{m}$. The assets of this particular scheme are the following: first, to generate the input photons at 900 nm one could use InAs QDs which are probably the best QDs for quantum optics at the moment. They have been used in a number of pathbreaking experiments, including the first demonstration of a QD-based single-photon source [19], Hong–Ou–Mandel-type two-photon interference [226], coupling of a single QD to nano- and microcavities [223,227], and generation of subnatural linewidth single photons [228]. Second, with the target wavelength lying in the C-band, ultimate low-loss fiber transmission of the converted photons is guaranteed (world’s lowest attenuation record is 0.1484 dB/km at 1570 nm [229]). And, third, the pump wavelength is much longer than the target wavelength (spectral separation: 1800 cm^{-1}) enabling noise-free QFC. The pump wavelength could be provided by a Tm-doped fiber laser/amplifier or by a semiconductor disc laser [230].

Chapter 7

Summary and Future Prospects

In this work, we have experimentally studied quantum frequency down-conversion from the visible spectral range to the telecommunications O- and C-band. As outlined in the introduction, the motivation for these experiments was to implement an efficient visible-to-telecom photonic interface for single photons emitted by solid-state quantum emitters such as SiV color centers in diamond or semiconductor QDs. With the current performance of our setup, frequency down-conversion already allows for more efficient long-distance fiber transmission compared with a direct transmission of visible photons. Down-conversion interfaces together with the complementary up-conversion devices might become an important tool to connect dissimilar elements (quantum memories or processors, optical fibers, ...) of a quantum network in the future.

From the beginning, a number of experimental boundary conditions were determined by our goal to efficiently translate visible photons to telecom photons with an all solid-state system. We have chosen to use DFG in WG-based frequency converters made from Zn:PPLN because of the high conversion efficiency that can be obtained with these devices. Historically, nonlinear optics has mostly been a research area in which high laser powers are employed to achieve efficient frequency conversion. However, from our analysis and the work published by others [47, 52] it is evident that the three-wave mixing process can happen with very high efficiencies (theoretically 100 %) even if one of the two input fields is very weak (at the single-photon level) and the other input field has a moderate power on the order of 100 mW. Since the DFG process should be tailored to convert light from a specific single-photon source (SiV center in diamond and InP QD in our case), one of the input wavelengths λ_a is always dictated by the emission wavelength of that source. The target wavelength λ_b should lie in one of the telecom bands and thus also could not be chosen freely (although this allowed a bit more flexibility). Since energy conservation always has to be fulfilled in DFG and we wanted to investigate different combinations of input and target wavelengths, these requirements led to the development of two 532-nm-pumped signal-resonant cw SROs as widely tunable pump sources. Two different nonlinear materials were tested in the SROs, a 40-mm-long MgO:PPLN crystal and a 30-mm-long MgO:PPLT crystal, to determine which of

them is better suited for our purposes. While MgO:PPLN was well known, MgO:PPSLT was a relatively new crystal that became commercially available during this work was conducted. Similar to earlier publications on cw OPOs, we have chosen a bow-tie ring cavity design for both of our devices. With the MgO:PPLN-based SRO, a minimum pump power at threshold of 1.2 W and a maximum single-frequency idler (signal) output power of 310 mW at 1417 nm was achieved. The demonstrated idler (signal) tuning range was 1406–1451 nm (856–840 nm) with one QPM grating period. In principle, by using all six grating periods an idler tuning range of 1250–1580 nm (920–800 nm) would be possible. With the MgO:PPLN-SRO, we achieved Doppler-free spectroscopy of the cesium D_2 line hyperfine structure. This is believed to be the first demonstration of Doppler-free spectroscopy using an OPO at wavelengths shorter than $1\ \mu\text{m}$. In principle, it proves that the device has the level of stability and spectral purity required for such demanding applications. Frequency stabilization to one of the hyperfine lines was also tested but could not be maintained for times longer than ~ 10 minutes due to thermal and acoustic noise. Better shielding of the SRO resonator from such noise could improve the stability and should allow for frequency stabilization on longer time scales. Despite its negative reputation in terms of green-pumped OPOs, our results show that MgO:PPLN can be used as a nonlinear material in these devices as long as operation at low to moderate (cw) pump powers is considered. However, even better results—both concerning output power and stability—were obtained with the MgO:PPSLT-based SRO. For this device, the minimum threshold pump power was below 700 mW and we achieved a maximum single-frequency idler output power of 1.1 W. Approximately the same output power level can be reached simultaneously for the signal radiation if one highly reflecting mirror of the signal-resonant SRO cavity is replaced by a 3% output coupling mirror. The idler (signal) tuning range spans from 1203–1565 nm (954–806 nm). The output power of the MgO:PPSLT-SRO was observed to be very stable with peak-to-peak fluctuations of 1.6% (0.14% standard deviation) over more than 5 h of operation. By stabilization of the signal frequency to a wavemeter, we could compensate for periodic frequency fluctuations and long-term drifts caused by slight variations of ambient conditions in the laboratory. Frequency stabilization to the wavemeter could be maintained over more than 9 h without interrupt. Due to its superior performance, the SRO based on MgO:PPSLT was eventually adopted as a pump source for our visible-to-telecom down-conversion experiments.

We have investigated frequency down-conversion from $\lambda_a = 738\ \text{nm}$ to the C-band ($\lambda_b = 1557\ \text{nm}$) pumped at $\lambda_p \approx 1.4\ \mu\text{m}$. From our measurements with a weak coherent input signal, we found that the process was quite efficient (77% depletion of the red input photons). However, the amount of noise photons generated by the frequency converter around the target wavelength gave rise to concern. A careful inspection of the spectra that were measured behind the WG revealed that the noise photons were produced by spontaneous Stokes Raman scattering of the strong $1.4\text{-}\mu\text{m}$ pump light. In parallel with our findings, there were other reports about noise in PPLN frequency converters [46, 47, 187]. Important conclusions are that the noise is generated either by spontaneous Raman scattering or by SPDC. While the first phenomenon preferably oc-

curs if pump and target wavelengths are relatively close together (as in our case $1.4\ \mu\text{m}$ and $1.56\ \mu\text{m}$), the second can play a role if the spectral separation between the two is larger (e.g., $\lambda_p = 1.06\ \mu\text{m}$ and $\lambda_b = 1.56\ \mu\text{m}$ as in [47]). By choosing a pump wavelength that is longer than the target wavelength, SPDC noise can be completely eliminated because the pump photons can only decay into photons with even longer wavelengths. Long-wavelength pumping also helps to reduce Raman noise since anti-Stokes Raman lines are much less intense than Stokes Raman lines. This is well known in Raman spectroscopy and was confirmed by our measurements. Nevertheless, as interchanging λ_p and λ_b was not an option in our case ($1.4\ \mu\text{m}$ is not the best choice for fiber-optic communication), we applied narrow spectral and temporal filtering to get rid of the Stokes Raman noise. In this way, we managed to perform a down-conversion experiment with 738-nm input at the single-photon level (0.5 MHz repetition rate with an average of 0.76 photons/pulse) and to discriminate the converted signal photons from the Raman noise floor. The maximum internal (external) conversion efficiency in this experiment was $> 73\%$ ($\sim 8\%$ without detection) at a pump power of 240 mW (SNR of 4:1). The best SNR was 6:1 reached at a pump power of 60 mW. As discussed in the summary at the end of Chap. 5, several technical difficulties prevented us from performing the down-conversion experiment with true single photons from an SiV center. With the current performance, single-photon sources based on diamond SiV centers do not reach the required level of predictability (in terms of deterministic single-photon emission) and reproducibility (in terms of the zero-phonon line wavelength). A second difficulty which is also related to the performance of the SiV centers has to do with triggered single-photon detection at telecom wavelengths. On the one hand, triggered detection at a rate of 0.5 MHz (or less) was inevitable to keep the photocounts caused by Raman noise at a reasonable level. On the other hand, an excitation rate of 0.5 MHz (matching the trigger rate of the detector) is far too low to yield an input photon flux from the SiV center such that the output flux at the telecom wavelength is sufficiently high. Another point which makes the situation even worse, because it reduces the conversion efficiency, is that the emission spectrum of SiV centers is usually not narrow enough. In the best case, at cryogenic temperatures, it approximately matches the acceptance bandwidth of the 40-mm-long frequency converter (0.16 nm) [60]. Nevertheless, it seems worthwhile to undertake further efforts in the future regarding the down-conversion of photons emitted by single color centers in diamond. Of course, the SiV center is not the only eligible candidate in this context. Other color centers like the well-investigated NV center should also be reconsidered. Currently, promising research is going on in our group to make the zero-phonon emission of diamond color centers narrower and brighter. Research in this direction includes near-resonant and resonant optical excitation of SiV centers for narrower emission linewidths and coupling of single NV centers to fiber-based microcavities for narrower emission linewidths and enhanced collection efficiency. In the conversion experiment with 738-nm input, the massive amount of noise photons resulting from the short-wavelength pumping at $1.4\ \mu\text{m}$ could be significantly reduced by selecting an O-band wavelength as the target wavelength. Then, long-wavelength pumping at a wavelength around $1.69\ \mu\text{m}$ could be

applied. This experiment is being set up in our laboratory at the moment. For conversion to the lowest-loss C-band, the cascaded scheme of Pelc *et al.* [47] may be an option both for 637-nm (NV) and 738-nm (SiV) input. This requires a pump wavelength of $2.15\ \mu\text{m}$ ($2.8\ \mu\text{m}$) for an input wavelength of 637 nm (738 nm) and a PPLN WG with two sections that feature different QPM grating periods. In the first section, photons at 637 nm (738 nm) are converted to an intermediate wavelength of 905 nm (1002 nm) by difference frequency mixing with the pump light and in the second section, the photons are converted from the intermediate wavelength to $1.56\ \mu\text{m}$, again by DFG with the pump light at $2.15\ \mu\text{m}$ ($2.8\ \mu\text{m}$).

Compared with SiV centers in diamond, semiconductor QDs have been investigated longer and more intensively and are thus better understood. For our proof-of-principle QFC experiment, we have chosen InP QDs fabricated by Peter Michler's group at Universität Stuttgart. These QDs showed single-photon emission in a wavelength range of 690–715 nm. A hybrid excitation scheme using combined electrical (DC bias voltage) and pulsed optical excitation (80 MHz at 590 nm) was applied. A particular bright emitter at 711 nm was selected to deliver the input photons for our frequency conversion device. The 711-nm input wavelength is perfectly suited to apply the long-wavelength pumping scheme with a pump wavelength at $1.55\ \mu\text{m}$ and a target wavelength at 1313 nm. The pump light was again provided by the home-built MgO:PPLN-SRO. Key achievements in this experiment were an external (internal) maximum conversion efficiency of 32 % ($\geq 64\%$), a SNR of 20:1 at optimum pump power (150 mW), preservation of single-photon lifetime and coherence during down-conversion, and, most importantly, the preservation of photon antibunching. The latter was proved by measuring the second-order correlation function $g^{(2)}(\tau)$ before and after wavelength translation ($g^{(2)}(0) = 0.39 \pm 0.02$ before and $g^{(2)}(0) = 0.24 \pm 0.04$ after conversion). To the best of our knowledge, this kind of measurement had not been done before for frequency down-converted photons from a triggered single-photon source. Note that it is the reversal of the experiment reported by the NIST group in 2010 [51]. The $g^{(2)}$ measurement was greatly facilitated by using free running SSPDs. Owing to the long-wavelength pumping scheme, the noise counts were greatly reduced and triggered single-photon detection was obsolete. Compared to the experiments on down-conversion from 738 nm to 1557 nm, the external conversion efficiency could be improved by using all-fiber components for spectral filtering.

Very recently, there were other interesting reports about new achievements in QFC using PPLN WGs. Ates *et al.* [57] performed up-conversion of 980-nm single photons from an InAs QD to 600 nm by SFG pumped at 1550 nm. This process is essentially noiseless because of the large spectral separation between pump and target wavelength. The authors demonstrated the preservation of photon antibunching by measuring the $g^{(2)}$ functions before and after frequency conversion. Furthermore, they showed how QFC can be used to achieve Hong–Ou–Mandel-type interference of photons that initially have a different wavelength. To this end, photons generated by the recombination of single excitons and biexcitons in the same QD were converted to a common wavelength and subsequently interfered. Erasing distinguishability is particularly interesting for

quantum networks based on solid-state qubits which do not emit/absorb photons at perfectly identical wavelengths (such as QDs). In this context, the latest report of success came from a collaboration at Stanford University [58]. They performed QFC of 910-nm single photons from an InAs QD to 1560 nm (pumped by sub-10-ps pulses at $2.2\ \mu\text{m}$) and used this process as a quantum eraser [231]. In this way, they managed to demonstrate entanglement between an InAs QD electron spin qubit and a photonic qubit at 1560 nm. In a related paper, the authors also demonstrate the preservation of photon antibunching under the 910 nm-to-1560 nm down-conversion [59].

QFC now seems to be a vital research area which attracts more and more interest among researchers in the fields of nonlinear optics and quantum optics (see, e.g., the recent coverage in the November 2012 issue of *Physics Today* [232]). Nearly all the necessary proof-of-principle experiments (including the present work) have been performed in recent years proving that QFC is indeed an enabling technique for long-distance quantum networks. Now, one goal of future work could be to use QFC in order to establish entanglement between two remote matter qubits of the same kind or of different kinds (e.g., electronic states of a trapped atom and spin states of an electron in a QD). The latter seems very challenging because the single-photon wavepackets emitted by dissimilar quantum systems do not only have different color but also have a different spectral and temporal shape [215]. However, these issues can also be tackled by QFC [58, 59, 212, 232]. Rakher *et al.* [212] have demonstrated how QFC with a pulsed 1550-nm pump laser can be used to up-convert 1300-nm single photons from a QD to 710 nm (using SFG in a PPLN WG) and simultaneously manipulate the temporal shape of the up-converted single-photon wavepackets. The waveform of the 1550-nm pump pulses is tailored in a desired way and ‘imprinted’ on the up-converted photons. A similar method was also applied in [58, 59] to erase frequency distinguishability and create the spin–photon entanglement. These experiments suggest how entanglement between two (possibly disparate) quantum systems at remote locations A and B could be achieved in a future experiment. It would require two QFC devices (one at A , one at B) which convert the emitted photons from the quantum systems to a common telecom wavelength at each location. Then, the telecom photons can be sent through kilometers of optical fiber cable from one location to the other (or to an intermediate location). Entanglement between the two quantum systems can be created by the joint detection of two photons (one coming from A , the other from B) at the output ports of a beamsplitter [46, 233]. As this scheme relies on two-photon interference, it is crucial that the photons coming from locations A and B are indistinguishable. Regarding the creation of entanglement between disparate quantum systems, photon–phonon interfaces based on cavity optomechanics (see [234] and references therein) might bring further flexibility. These devices enable microwave-to-optical (and vice versa) as well as optical-to-optical frequency conversion. Thus, on the one hand, they could be used as an interface between superconducting qubits and optical photons and, on the other hand, they are an alternative to QFC devices based on intrinsic $\chi^{(2)}$ or $\chi^{(3)}$ nonlinearities.

Frequency *down*-conversion in particular, as demonstrated in this thesis, could also be

used to build a heavily sought-after bright triggered single-photon source at telecom wavelengths. Such sources could find application in device-independent QKD [21,24] or in integrated quantum optical circuits for on-chip quantum information processing [235]. Again, the second application requires indistinguishable photons from two or more different sources and QFC could be used to overcome this difficulty. From our experiments we anticipate that a hybrid approach, i.e., the combination of a bright single-photon emitter in the visible with frequency down-conversion, has the potential to outperform any current source based on direct emission of photons at telecom wavelengths.

Appendix A

Refractive Indices of Nonlinear Materials

Sellmeier Equation for Undoped CLN and 5 % MgO-doped CLN

A temperature-dependent Sellmeier equation for the extraordinary index of refraction n_e in congruent LiNbO₃ (CLN) was derived by Jundt [101]. It is given by

$$n^2(\lambda, T) = a_1 + b_1 f + \frac{a_2 + b_2 f}{\lambda^2 - (a_3 + b_3 f)^2} + \frac{a_4 + b_4 f}{\lambda^2 - a_5^2} - a_6 \lambda^2, \quad (\text{A.1})$$

with

$$f = (T - T_0)(T + T_0 + 2 \times 273.16) \quad (\text{A.2})$$

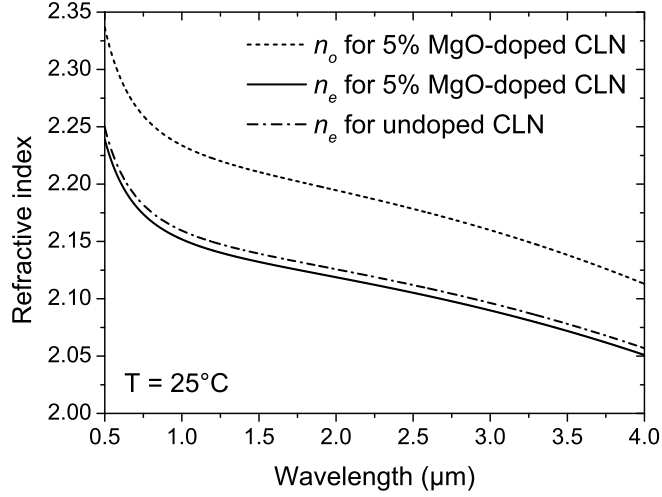
$$= (T - 24.5^\circ\text{C})(T + 570.82). \quad (\text{A.3})$$

The Sellmeier coefficients $\{a_i\}$ and $\{b_i\}$ are given in the first column of Table A.1. The temperature must be inserted in °C. Equation (A.1) is valid in a spectral range of 0.4–5 μm and for temperatures between room temperature and 250 °C.

Based on Eq. (A.1), Gayer *et al.* [105] have experimentally determined the Sellmeier coefficients for 5 % MgO-doped CLN, both for the ordinary and the extraordinary index of refraction. These parameters are listed in the second and third column of Table A.1. The n_e (n_o) equation is valid for the 0.5–4 μm (0.5–1.62 μm) spectral range and 20–200 °C (20–100 °C) temperature range. The indices n_e and n_o for MgO-doped CLN as well as n_e for undoped CLN are plotted in Fig. A.1 for $T = 25^\circ\text{C}$.

Table A.1: Sellmeier coefficients for undoped CLN and 5% MgO-doped CLN.

Parameter	CLN [101]	MgO-doped CLN [105]	
	n_e	n_e	n_o
a_1	5.35583	5.756	5.653
a_2	0.100473	0.0983	0.1185
a_3	0.20692	0.2020	0.2091
a_4	100	189.32	89.61
a_5	11.34927	12.52	10.85
a_6	1.5334×10^{-2}	1.32×10^{-2}	1.97×10^{-2}
b_1	4.629×10^{-7}	2.860×10^{-6}	7.941×10^{-7}
b_2	3.862×10^{-8}	4.700×10^{-8}	3.134×10^{-8}
b_3	-0.89×10^{-8}	6.113×10^{-8}	-4.641×10^{-9}
b_4	2.657×10^{-5}	1.516×10^{-4}	-2.188×10^{-6}

**Figure A.1:** Refractive indices of undoped CLN (n_e) and of 5% MgO-doped CLN (n_e , n_o) calculated with Eq. (A.1) and the parameters given in Table A.1.

Sellmeier Equation for SLT

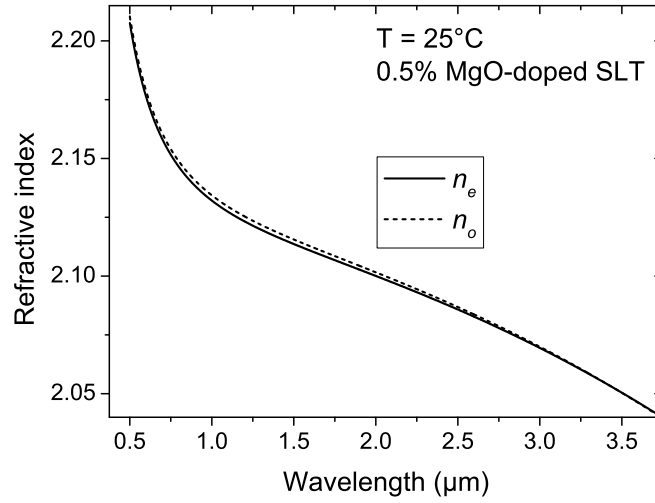
A modified version of Eq. (A.1) with an additional parameter b_5 has been introduced by Dolev *et al.* [97] for 0.5% MgO-doped SLT. They found the relation

$$n^2 = a_1 + b_1 f + \frac{a_2 + b_2 f}{\lambda^2 - (a_3 + b_3 f)^2} + \frac{a_4 + b_4 f}{\lambda^2 - (a_5 + b_5 f)^2} - a_6 \lambda^2, \quad (\text{A.4})$$

with the Sellmeier coefficients given in Table A.2. Figure A.2 shows $n_{e,o}(\lambda, T = 25^\circ)$ according to (A.4).

Table A.2: Sellmeier coefficients for 0.5 % MgO-doped stoichiometric LiTaO₃ according to [97].

Parameter	n_e	n_o
a_1	4.5615	4.5082
a_2	0.08488	0.084888
a_3	0.1927	0.19552
a_4	5.5832	1.1570
a_5	8.3067	8.2517
a_6	0.021696	0.0237
b_1	4.782×10^{-7}	2.0704×10^{-8}
b_2	3.0913×10^{-8}	1.4449×10^{-8}
b_3	2.7326×10^{-8}	1.5978×10^{-8}
b_4	1.4837×10^{-5}	4.7686×10^{-6}
b_5	1.3647×10^{-7}	1.1127×10^{-5}

**Figure A.2:** Refractive indices n_e and n_o as a function of λ for SLT calculated with Eq. (A.4) and parameters from Table A.2.

Appendix B

Supplemental Equations and Formulas

E_{pq}^x Modes in the Regions 2–5 According to Ref. [120, 121]

Region 2:

$$E_z = A \cos \kappa_x(\xi - d) \cos \kappa_y(y + \eta) \exp[\gamma_2(x + d)] \quad (\text{B.1})$$

$$H_z = -A \sqrt{\frac{\epsilon_0}{\mu_0}} n_2^2 \frac{\kappa_y}{\gamma_2} \frac{k}{\beta} \cos \kappa_x(\xi - d) \sin \kappa_y(y + \eta) \exp[\gamma_2(x + d)] \quad (\text{B.2})$$

$$E_x = +iA \frac{\gamma_2^2 + n_2^2 k^2}{\gamma_2 \beta} \cos \kappa_x(\xi - d) \cos \kappa_y(y + \eta) \exp[\gamma_2(x + d)] \quad (\text{B.3})$$

$$E_y \approx 0 \quad (\text{B.4})$$

$$H_x = 0 \quad (\text{B.5})$$

$$H_y = iA \sqrt{\frac{\epsilon_0}{\mu_0}} n_2^2 \frac{k}{\gamma_2} \cos \kappa_x(\xi - d) \cos \kappa_y(y + \eta) \exp[\gamma_2(x + d)] \quad (\text{B.6})$$

Region 3:

$$E_z = A \cos \kappa_x \xi \cos \kappa_y(y + \eta) \exp(-\gamma_3 x) \quad (\text{B.7})$$

$$H_z = A \sqrt{\frac{\epsilon_0}{\mu_0}} n_3^2 \frac{\kappa_y}{\gamma_3} \frac{k}{\beta} \cos \kappa_x \xi \sin \kappa_y(y + \eta) \exp(-\gamma_3 x) \quad (\text{B.8})$$

$$E_x = -iA \frac{\gamma_3^2 + n_3^2 k^2}{\gamma_3 \beta} \cos \kappa_x \xi \cos \kappa_y(y + \eta) \exp(-\gamma_3 x) \quad (\text{B.9})$$

$$E_y \approx 0 \quad (\text{B.10})$$

$$H_x = 0 \quad (\text{B.11})$$

$$H_y = -iA \sqrt{\frac{\epsilon_0}{\mu_0}} n_3^2 \frac{k}{\gamma_3} \cos \kappa_x \xi \cos \kappa_y(y + \eta) \exp(-\gamma_3 x) \quad (\text{B.12})$$

Region 4:

$$E_z = A \frac{n_1^2}{n_4^2} \cos \kappa_y(b + \eta) \cos \kappa_x(x + \xi) \exp[-\gamma_4(y - b)] \quad (\text{B.13})$$

$$H_z = -A \sqrt{\frac{\epsilon_0}{\mu_0}} n_1^2 \frac{\gamma_4}{\kappa_x} \frac{k}{\beta} \cos \kappa_y(b + \eta) \sin \kappa_x(x + \xi) \exp[-\gamma_4(y - b)] \quad (\text{B.14})$$

$$E_x = iA \frac{n_1^2}{n_4^2} \frac{n_4^2 k^2 - \kappa_x^2}{\kappa_x \beta} \cos \kappa_y(b + \eta) \sin \kappa_x(x + \xi) \exp[-\gamma_4(y - b)] \quad (\text{B.15})$$

$$H_y = iA \sqrt{\frac{\epsilon_0}{\mu_0}} n_1^2 \frac{k}{\kappa_x} \cos \kappa_y(b + \eta) \sin \kappa_x(x + \xi) \exp[-\gamma_4(y - b)] \quad (\text{B.16})$$

Region 5:

$$E_z = A \frac{n_1^2}{n_5^2} \cos \kappa_y \eta \cos \kappa_x(x + \xi) \exp(\gamma_5 y) \quad (\text{B.17})$$

$$H_z = A \sqrt{\frac{\epsilon_0}{\mu_0}} n_1^2 \frac{\gamma_5}{\kappa_x} \frac{k}{\beta} \cos \kappa_y \eta \sin \kappa_x(x + \xi) \exp(\gamma_5 y) \quad (\text{B.18})$$

$$E_x = iA \frac{n_1^2}{n_5^2} \frac{n_5^2 k^2 - \kappa_x^2}{\kappa_x \beta} \cos \kappa_y \eta \sin \kappa_x(x + \xi) \exp(\gamma_5 y) \quad (\text{B.19})$$

$$H_y = iA \sqrt{\frac{\epsilon_0}{\mu_0}} n_1^2 \frac{k}{\kappa_x} \cos \kappa_y \eta \sin \kappa_x(x + \xi) \exp(\gamma_5 y) \quad (\text{B.20})$$

Equations of Motion for the Operators \hat{a} and \hat{b}

$$\begin{aligned} \frac{d\hat{a}}{dt} &= \frac{i}{\hbar} [\hat{H}, \hat{a}] \\ &= \frac{i}{\hbar} \left\{ \left(i\hbar \eta \hat{a} \hat{b}^\dagger A_p^* - i\hbar \eta^* A_p \hat{b} \hat{a}^\dagger \right) \hat{a} - \hat{a} \left(i\hbar \eta \hat{a} \hat{b}^\dagger A_p^* - i\hbar \eta^* A_p \hat{b} \hat{a}^\dagger \right) \right\} \\ &= \left(-\eta \hat{a} \hat{b}^\dagger A_p^* + \eta^* A_p \hat{b} \hat{a}^\dagger \right) \hat{a} - \hat{a} \left(-\eta \hat{a} \hat{b}^\dagger A_p^* + \eta^* A_p \hat{b} \hat{a}^\dagger \right) \\ &= \underline{-\eta \hat{a}^2 \hat{b}^\dagger A_p^* + \eta^* A_p \hat{b} \hat{a}^\dagger \hat{a}} + \underline{\eta \hat{a}^2 \hat{b}^\dagger A_p^* - \eta^* A_p \hat{b} \hat{a}^\dagger} \\ &= \eta^* A_p \hat{b} \hat{a}^\dagger \hat{a} - \eta^* A_p \hat{b} \hat{a} \hat{a}^\dagger \\ &= \eta^* A_p \hat{b} [\hat{a}^\dagger, \hat{a}] \\ &= -\eta^* A_p \hat{b}. \end{aligned}$$

In the last step, the boson commutation relation $[a, a^\dagger] = 1$ was used.

The derivation of the equation of motion for \hat{b} is analogous:

$$\begin{aligned}
\frac{d\hat{b}}{dt} &= \frac{i}{\hbar} [\hat{H}, \hat{b}] \\
&= \frac{i}{\hbar} \left\{ \left(i\hbar\eta\hat{a}\hat{b}^\dagger A_p^* - i\hbar\eta^* A_p \hat{b}\hat{a}^\dagger \right) \hat{b} - \hat{b} \left(i\hbar\eta\hat{a}\hat{b}^\dagger A_p^* - i\hbar\eta^* A_p \hat{b}\hat{a}^\dagger \right) \right\} \\
&= \left(-\eta\hat{a}\hat{b}^\dagger A_p^* + \eta^* A_p \hat{b}\hat{a}^\dagger \right) \hat{b} - \hat{b} \left(-\eta\hat{a}\hat{b}^\dagger A_p^* + \eta^* A_p \hat{b}\hat{a}^\dagger \right) \\
&= -\eta\hat{a}\hat{b}^\dagger \hat{b} A_p^* + \eta^* A_p \hat{b}^2 \hat{a}^\dagger + \eta\hat{a}\hat{b}\hat{b}^\dagger A_p^* - \eta^* A_p \hat{b}^2 \hat{a}^\dagger \\
&= \eta\hat{a}\hat{b}\hat{b}^\dagger A_p^* - \eta\hat{a}\hat{b}^\dagger \hat{b} A_p^* \\
&= \eta A_p^* \hat{a} [\hat{b}, \hat{b}^\dagger] \\
&= \eta A_p^* \hat{a}.
\end{aligned}$$

To summarize, we have the equations of motion

$$\frac{d\hat{a}}{dt} = -\eta^* A_p \hat{b}, \quad (\text{B.21})$$

$$\frac{d\hat{b}}{dt} = \eta A_p^* \hat{a}. \quad (\text{B.22})$$

Expectation Values of Photon Number Operators

For comparison with classical results, we determine the expectation values of the photon number operators $\hat{n}_a^{(\text{out})}$, $\hat{n}_b^{(\text{out})}$ at the WG output. Using (3.57) and (3.58), the number operator for the signal field (mode a) reads

$$\begin{aligned}
\hat{n}_a^{(\text{out})} &= \hat{a}^{(\text{out})\dagger} \hat{a}^{(\text{out})} \\
&= \left(\hat{a}^\dagger(0) \cos(|\eta A_p| \tau) - e^{i\phi_p} \hat{b}^\dagger(0) \sin(|\eta A_p| \tau) \right) \left(\hat{a}(0) \cos(|\eta A_p| \tau) - e^{-i\phi_p} \hat{b}(0) \sin(|\eta A_p| \tau) \right) \\
&= \hat{a}^\dagger(0) \hat{a}(0) \cos^2(|\eta A_p| \tau) - e^{-i\phi_p} \hat{a}^\dagger(0) \hat{b}(0) \cos(|\eta A_p| \tau) \sin(|\eta A_p| \tau) \\
&\quad - e^{i\phi_p} \hat{b}^\dagger(0) \hat{a}(0) \sin(|\eta A_p| \tau) \cos(|\eta A_p| \tau) + \hat{b}^\dagger(0) \hat{b}(0) \sin^2(|\eta A_p| \tau).
\end{aligned} \quad (\text{B.23})$$

Using the relations

$$\begin{aligned}
\hat{a} |n_a, n_b\rangle &= \sqrt{n_a} |n_a - 1, n_b\rangle, \\
\hat{a}^\dagger |n_a, n_b\rangle &= \sqrt{n_a + 1} |n_a + 1, n_b\rangle, \\
\hat{b} |n_a, n_b\rangle &= \sqrt{n_b} |n_a, n_b - 1\rangle, \\
\hat{b}^\dagger |n_a, n_b\rangle &= \sqrt{n_b + 1} |n_a, n_b + 1\rangle,
\end{aligned}$$

we have

$$\begin{aligned}
\langle n_a, n_b | \hat{a}^\dagger \hat{a} | n_a, n_b \rangle &= \langle \hat{n}_a \rangle, \\
\langle n_a, n_b | \hat{a}^\dagger \hat{b} | n_a, n_b \rangle &= \sqrt{n_b(n_a + 1)} \langle n_a, n_b | n_a + 1, n_b - 1 \rangle = 0, \\
\langle n_a, n_b | \hat{b}^\dagger \hat{a} | n_a, n_b \rangle &= \sqrt{n_a(n_b + 1)} \langle n_a, n_b | n_a - 1, n_b + 1 \rangle = 0, \\
\langle n_a, n_b | \hat{b}^\dagger \hat{b} | n_a, n_b \rangle &= \langle \hat{n}_b \rangle.
\end{aligned}$$

So the mixed terms in (B.23) vanish when we calculate the expectation value and we have

$$\begin{aligned}\langle \hat{n}_a^{(\text{out})} \rangle &= \langle n_a, n_b | \hat{n}_a^{(\text{out})} | n_a, n_b \rangle \\ &= \langle \hat{n}_a(0) \rangle \cos^2(|\eta A_p| \tau) + \langle \hat{n}_b(0) \rangle \sin^2(|\eta A_p| \tau).\end{aligned}\quad (\text{B.24})$$

The calculation for $\langle \hat{n}_b^{(\text{out})} \rangle$ is quite similar and we get the result

$$\langle \hat{n}_b^{(\text{out})} \rangle = \langle \hat{n}_b(0) \rangle \cos^2(|\eta A_p| \tau) + \langle \hat{n}_a(0) \rangle \sin^2(|\eta A_p| \tau).\quad (\text{B.25})$$

Bibliography

- [1] “Nicolaas Bloembergen – Banquet Speech”. Nobelprize.org. 18 Feb 2013. http://www.nobelprize.org/nobel_prizes/physics/laureates/1981/bloembergen-speech.html.
- [2] S. Wiesner, “Conjugate Coding,” *ACM SIGACT News* **15**, 78–88 (1983).
- [3] C. H. Bennett and G. Brassard, “Quantum Cryptography: Public Key Distribution and Coin Tossing,” in *Proceedings of IEEE International Conference on Computers, Systems and Signal Processing*, p. 175 (Bangalore, India, 1984).
- [4] C. H. Bennett, F. Bessette, G. Brassard, L. Salvail, J. Smolin, “Experimental Quantum Cryptography,” *J. Cryptology* **5**, 3–28 (1992).
- [5] M. A. Nielsen and I. L. Chuang, *Quantum Computation and Quantum Information* (Cambridge University Press, Cambridge, 2000).
- [6] T. D. Ladd, F. Jelezko, R. Laflamme, Y. Nakamura, C. Monroe, and J. L. O’Brien, “Quantum computers,” *Nature* **464**, 45–53 (2010).
- [7] H. J. Kimble, “The quantum internet,” *Nature* **453**, 1023–1030 (2008).
- [8] B. Schumacher, “Quantum coding,” *Phys. Rev. A* **51**, 2738–2747 (1995).
- [9] J. S. Bell, “On the Einstein Podolsky Rosen Paradox,” *Physics* **1**, 195–200 (1964).
- [10] J. F. Clauser, M. A. Horne, A. Shimony, and R. A. Holt, “Proposed Experiment to Test Local Hidden-Variable Theories,” *Phys. Rev. Lett.* **23**, 880–884 (1969).
- [11] D. F. V. James, P. G. Kwiat, W. J. Munro, and A. G. White, “Measurement of qubits,” *Phys. Rev. A* **64**, 052312 (2001).
- [12] M. B. Plenio and S. Virmani, “An Introduction to Entanglement Measures,” *Quantum Inf. Comput.* **7**, 1–51 (2007).
- [13] T. Monz, P. Schindler, J. T. Barreiro, M. Chwalla, D. Nigg, W. A. Coish, M. Harlander, W. Hänsel, M. Hennrich, and R. Blatt, “14-Qubit Entanglement: Creation and Coherence,” *Phys. Rev. Lett.* **106**, 130506 (2011).

- [14] A. Steane, “Quantum computing,” *Rep. Prog. Phys.* **61**, 117–173 (1998).
- [15] J. I. Cirac, P. Zoller, H. J. Kimble, and H. Mabuchi, “Quantum State Transfer and Entanglement Distribution among Distant Nodes in a Quantum Network,” *Phys. Rev. Lett.* **78**, 3221–3224 (1997).
- [16] B. E. A. Saleh and M. C. Teich, *Fundamentals of Photonics* (Wiley, Hoboken, N.J., 2007), 2nd ed.
- [17] A. K. Ekert, “Quantum cryptography based on Bell’s theorem,” *Phys. Rev. Lett.* **67**, 661–663 (1991).
- [18] R. Loudon, *The Quantum Theory of Light* (Oxford University Press, Oxford, 2000), 3rd ed.
- [19] P. Michler, A. Kiraz, C. Becher, W. V. Schoenfeld, P. M. Petroff, L. Zhang, E. Hu, and A. Imamoglu, “A Quantum Dot Single-Photon Turnstile Device,” *Science* **290**, 2282–2285 (2000).
- [20] M. Hijlkema, B. Weber, H. P. Specht, S. C. Webster, A. Kuhn, and G. Rempe, “A single-photon server with just one atom,” *Nature Phys.* **3**, 253–255 (2007).
- [21] N. Sangouard and H. Zbinden, “What are single photons good for?” *J. Mod. Opt.* **59**, 1458–1464 (2012).
- [22] H. J. Kimble, M. Dagenais, and L. Mandel, “Photon Antibunching in Resonance Fluorescence,” *Phys. Rev. Lett.* **39**, 691–695 (1977).
- [23] H.-K. Lo, X. Ma, and K. Chen, “Decoy State Quantum Key Distribution,” *Phys. Rev. Lett.* **94**, 230504 (2005).
- [24] N. Gisin, S. Pironio, and N. Sangouard, “Proposal for Implementing Device-Independent Quantum Key Distribution Based on a Heralded Qubit Amplifier,” *Phys. Rev. Lett.* **105**, 070501 (2010).
- [25] N. Gisin, G. Ribordy, W. Tittel, and H. Zbinden, “Quantum cryptography,” *Rev. Mod. Phys.* **74**, 145–195 (2002).
- [26] W. K. Wootters and W. H. Zurek, “A single quantum cannot be cloned,” *Nature* **299**, 802–803 (1982).
- [27] H.-J. Briegel, W. Dür, J. I. Cirac, and P. Zoller, “Quantum Repeaters: The Role of Imperfect Local Operations in Quantum Communication,” *Phys. Rev. Lett.* **81**, 5932–5935 (1998).
- [28] L.-M. Duan, M. D. Lukin, J. I. Cirac, and P. Zoller, “Long-distance quantum communication with atomic ensembles and linear optics,” *Nature* **414**, 413–418 (2001).

- [29] C. Simon, M. Afzelius, J. Appel, A. Boyer de la Giroday, S. J. Dewhurst, N. Gisin, C. Y. Hu, F. Jelezko, S. Kröll, J. H. Müller, J. Nunn, E. S. Polzik, J. G. Rarity, H. De Riedmatten, W. Rosenfeld, A. J. Shields, N. Sköld, R. M. Stevenson, R. Thew, I. A. Walmsley, M. C. Weber, H. Weinfurter, J. Wrachtrup, and R. J. Young, “Quantum memories,” *Eur. Phys. J. D* **58**, 1–22 (2010).
- [30] C. H. Bennett, G. Brassard, C. Crépeau, R. Jozsa, A. Peres, and W. K. Wootters, “Teleporting an Unknown Quantum State via Dual Classical and Einstein-Podolsky-Rosen Channels,” *Phys. Rev. Lett.* **70**, 1895–1899 (1993).
- [31] N. Sangouard, C. Simon, H. de Riedmatten, and N. Gisin, “Quantum repeaters based on atomic ensembles and linear optics,” *Rev. Mod. Phys.* **83**, 33–80 (2011).
- [32] C. Simon, H. de Riedmatten, M. Afzelius, N. Sangouard, H. Zbinden, and N. Gisin, “Quantum Repeater with Photon Pair Sources and Multimode Memories,” *Phys. Rev. Lett.* **98**, 190503 (2007).
- [33] N. Sangouard, C. Simon, J. Minář, H. Zbinden, H. de Riedmatten, and N. Gisin, “Long-distance entanglement distribution with single-photon sources,” *Phys. Rev. A* **76**, 050301(R) (2007).
- [34] P. Kumar, “Quantum frequency conversion,” *Opt. Lett.* **15**, 1476–1478 (1990).
- [35] J. Huang and P. Kumar, “Observation of Quantum Frequency Conversion,” *Phys. Rev. Lett.* **68**, 2153–2156 (1992).
- [36] G. Giorgi, P. Mataloni, and F. De Martini, “Frequency Hopping in Quantum Interferometry: Efficient Up-Down Conversion for Qubits and Ebits,” *Phys. Rev. Lett.* **90**, 027902 (2003).
- [37] A. P. VanDevender and P. G. Kwiat, “High efficiency single photon detection via frequency up-conversion,” *J. Mod. Opt.* **51**, 1433–1445 (2004).
- [38] M. A. Albota and F. N. C. Wong, “Efficient single-photon counting at 1.55 μm by means of frequency upconversion,” *Opt. Lett.* **29**, 1449–1451 (2004).
- [39] R. V. Roussev, C. Langrock, J. R. Kurz, and M. M. Fejer, “Periodically poled lithium niobate waveguide sum-frequency generator for efficient single-photon detection at communication wavelengths,” *Opt. Lett.* **29**, 1518–1520 (2004).
- [40] D. A. Kleinman and G. D. Boyd, “Infrared Detection by Optical Mixing,” *J. Appl. Phys.* **40**, 546–566 (1969).
- [41] S. Tanzilli, W. Tittel, M. Halder, O. Alibart, P. Baldi, N. Gisin, and H. Zbinden, “A photonic quantum information interface,” *Nature* **437**, 116–120 (2005).
- [42] J. D. Franson, “Bell Inequality for Position and Time,” *Phys. Rev. Lett.* **62**, 2205–2208 (1989).

- [43] Z. Y. Ou, “Efficient conversion between photons and between photon and atom by stimulated emission,” *Phys. Rev. A* **78**, 023819 (2008).
- [44] A. G. Radnaev, Y. O. Dudin, R. Zhao, H. H. Jen, S. D. Jenkins, A. Kuzmich, and T. A. B. Kennedy, “A quantum memory with telecom-wavelength conversion,” *Nature Phys.* **6**, 894–899 (2010).
- [45] Y. O. Dudin, A. G. Radnaev, R. Zhao, J. Z. Blumoff, T. A. B. Kennedy, and A. Kuzmich, “Entanglement of Light-Shift Compensated Atomic Spin Waves with Telecom Light,” *Phys. Rev. Lett.* **105**, 260502 (2010).
- [46] H. Takesue, “Single-photon frequency down-conversion experiment,” *Phys. Rev. A* **82**, 013833 (2010).
- [47] J. S. Pelc, C. Langrock, Q. Zhang, and M. M. Fejer, “Influence of domain disorder on parametric noise in quasi-phase-matched quantum frequency converters,” *Opt. Lett.* **35**, 2804–2806 (2010).
- [48] N. Curtz, R. Thew, C. Simon, N. Gisin, and H. Zbinden, “Coherent frequency-down-conversion interface for quantum repeaters,” *Opt. Express* **18**, 22099–22104 (2010).
- [49] S. Zaske, A. Lenhard, and C. Becher, “Efficient frequency downconversion at the single photon level from the red spectral range to the telecommunications C-band,” *Opt. Express* **19**, 12825–12836 (2011).
- [50] H. J. McGuinness, M. G. Raymer, C. J. McKinstrie, and S. Radic, “Quantum Frequency Translation of Single-Photon States in a Photonic Crystal Fiber,” *Phys. Rev. Lett.* **105**, 093604 (2010).
- [51] M. T. Rakher, L. Ma, O. Slattery, X. Tang, and K. Srinivasan, “Quantum transduction of telecommunications-band single photons from a quantum dot by frequency upconversion,” *Nature Photon.* **4**, 786–791 (2010).
- [52] R. Ikuta, Y. Kusaka, T. Kitano, H. Kato, T. Yamamoto, M. Koashi, and N. Imoto, “Wide-band quantum interface for visible-to-telecommunication wavelength conversion,” *Nat. Commun.* **2**, 537 (2011).
- [53] H. Takesue, K. Inoue, O. Tadanaga, Y. Nishida, and M. Asobe, “Generation of pulsed polarization-entangled photon pairs in a 1.55- μm band with a periodically poled lithium niobate waveguide and an orthogonal polarization delay circuit,” *Opt. Lett.* **30**, 293–295 (2005).
- [54] H. Takesue and Y. Noguchi, “Implementation of quantum state tomography for time-bin entangled photon pairs,” *Opt. Express* **17**, 10976–10989 (2009).
- [55] G. Berlín, G. Brassard, F. Bussi eres, N. Godbout, J. A. Slater, and W. Tittel, “Experimental loss-tolerant quantum coin flipping,” *Nat. Commun.* **2**, 561 (2011).

- [56] S. Ramelow, A. Fedrizzi, A. Poppe, N. K. Langford, and A. Zeilinger, “Polarization-entanglement-conserving frequency conversion of photons,” *Phys. Rev. A* **85**, 013845 (2012).
- [57] S. Ates, I. Agha, A. Gulinatti, I. Rech, M. T. Rakher, A. Badolato, and K. Srinivasan, “Two-Photon Interference Using Background-Free Quantum Frequency Conversion of Single Photons Emitted by an InAs Quantum Dot,” *Phys. Rev. Lett.* **109**, 147405 (2012).
- [58] K. De Greve, L. Yu, P. L. McMahon, J. S. Pelc, C. M. Natarajan, N. Y. Kim, E. Abe, S. Maier, C. Schneider, M. Kamp, S. Höfling, R. H. Hadfield, A. Forchel, M. M. Fejer, and Y. Yamamoto, “Quantum-dot spin–photon entanglement via frequency downconversion to telecom wavelength,” *Nature* **491**, 421–425 (2012).
- [59] J. S. Pelc, L. Yu, K. De Greve, P. L. McMahon, C. M. Natarajan, V. Esfandyarpour, S. Maier, C. Schneider, M. Kamp, S. Höfling, R. H. Hadfield, A. Forchel, Y. Yamamoto, and M. M. Fejer, “Downconversion quantum interface for a single quantum dot spin and 1550-nm single-photon channel,” *Opt. Express* **20**, 27510–27519 (2012).
- [60] E. Neu, D. Steinmetz, J. Riedrich-Möller, S. Gsell, M. Fischer, M. Schreck, and C. Becher, “Single photon emission from silicon-vacancy colour centres in chemical vapour deposition nano-diamonds on iridium,” *New J. Phys.* **13**, 025012 (2011).
- [61] R. W. Boyd, *Nonlinear Optics* (Academic Press, Burlington, MA, 2008), 3rd ed.
- [62] D. A. Kleinman, “Nonlinear Dielectric Polarization in Optical Media,” *Phys. Rev.* **126**, 1977–1979 (1962).
- [63] P. A. Franken and J. F. Ward, “Optical Harmonics and Nonlinear Phenomena,” *Rev. Mod. Phys.* **35**, 23–39 (1963).
- [64] J. E. Midwinter and J. Warner, “The effects of phase matching method and of uniaxial crystal symmetry on the polar distribution of second-order non-linear optical polarization,” *Br. J. Appl. Phys.* **16**, 1135–1142 (1965).
- [65] F. Zernike and J. E. Midwinter, *Applied Nonlinear Optics* (Dover Publications, Mineola, N.Y., 2006).
- [66] T. Suhara and M. Fujimura, *Waveguide Nonlinear-Optic Devices* (Springer, Berlin, 2003).
- [67] M. M. Fejer, G. A. Magel, D. H. Jundt, and R. L. Byer, “Quasi-Phase-Matched Second Harmonic Generation: Tuning and Tolerances,” *IEEE J. Quantum Electron.* **28**, 2631–2654 (1992).
- [68] S. W. Smith, *The Scientist and Engineer’s Guide to Digital Signal Processing* (California Technical Publishing, San Diego, 1997).

- [69] J. A. Armstrong, N. Bloembergen, J. Ducuing, and P. S. Pershan, “Interactions between Light Waves in a Nonlinear Dielectric,” *Phys. Rev.* **127**, 1918–1939 (1962).
- [70] G. D. Miller, “Periodically Poled Lithium Niobate: Modeling, Fabrication, and Nonlinear-Optical Performance,” Ph.D. thesis, Stanford University (1998).
- [71] S. Zelt, “Erzeugung von periodischen Domänen in ferroelektrischen Kristallen und deren Anwendung in der nichtlinearen Optik,” Ph.D. thesis, TU Kaiserslautern (2003).
- [72] W. R. Bosenberg, J. I. Alexander, L. E. Myers, and R. W. Wallace, “2.5-W, continuous-wave, 629-nm solid-state laser source,” *Opt. Lett.* **23**, 207–209 (1998).
- [73] F. Ruebel, P. Haag, and J. A. L’huillier, “Synchronously pumped femtosecond optical parametric oscillator with integrated sum frequency generation,” *Appl. Phys. Lett.* **92**, 011122 (2008).
- [74] W. Sohler, H. Hu, R. Ricken, V. Quiring, C. Vannahme, H. Herrmann, D. Büchter, S. Reza, W. Grundkötter, S. Orlov, H. Suche, R. Nouroozi, and Y. Min, “Integrated Optical Devices in Lithium Niobate,” *Opt. Photonics News* **19**, 24–31 (2008).
- [75] R. J. Glauber, “Coherent and Incoherent States of the Radiation Field,” *Phys. Rev.* **131**, 2766–2788 (1963).
- [76] M. D. Eisaman, J. Fan, A. Migdall, and S. V. Polyakov, “Invited Review Article: Single-photon sources and detectors,” *Rev. Sci. Instrum.* **82**, 071101 (2011).
- [77] B. Lounis and M. Orrit, “Single-photon sources,” *Rep. Prog. Phys.* **68**, 1129–1179 (2005).
- [78] P. Michler, ed., *Single Semiconductor Quantum Dots*, NanoScience and Technology (Springer, Berlin, 2009), 1st ed.
- [79] E. K. Neu, “Silicon vacancy color centers in chemical vapor deposition diamond: New insights into promising solid state single photon sources,” Ph.D. thesis, Universität des Saarlandes (2012).
- [80] S. Singh, “Antibunching, sub-poissonian photon statistics and finite bandwidth effects in resonance fluorescence,” *Opt. Commun.* **44**, 254–258 (1983).
- [81] G. A. Steudle, S. Schietinger, D. Höckel, S. N. Dorenbos, I. E. Zadeh, V. Zwiller, and O. Benson, “Measuring the quantum nature of light with a single source and a single detector,” *Phys. Rev. A* **86**, 053814 (2012).
- [82] D. Steinmetz, “Ni/Si-basierte Farbzentren in Diamant als Einzelphotonenquellen,” Ph.D. thesis, Universität des Saarlandes (2011).

- [83] R. Hanbury Brown and R. Q. Twiss, "Correlation between Photons in two Coherent Beams of Light," *Nature* **177**, 27–29 (1956).
- [84] A. M. Fox, *Quantum Optics* (Oxford University Press, Oxford, 2006).
- [85] R. S. Weis and T. K. Gaylord, "Lithium Niobate: Summary of Physical Properties and Crystal Structure," *Appl. Phys. A* **37**, 191–203 (1985).
- [86] R. C. Miller and A. Savage, "Temperature Dependence of the Optical Properties of Ferroelectric LiNbO₃ and LiTaO₃," *Appl. Phys. Lett.* **9**, 169–171 (1966).
- [87] S. C. Abrahams, E. Buehler, W. C. Hamilton, and S. J. Laplaca, "Ferroelectric Lithium Tantalate—III. Temperature Dependence of the Structure in the Ferroelectric Phase and the Paraelectric Structure at 940°K," *J. Phys. Chem. Solids* **34**, 521–532 (1973).
- [88] P. Lerner, C. Legras, and J. P. Dumas, "Stoechiométrie des monocristaux de métaniobate de lithium," *J. Cryst. Growth* **3–4**, 231–235 (1968).
- [89] A. Ashkin, G. D. Boyd, J. M. Dziedzic, R. G. Smith, A. A. Ballman, J. J. Levinstein, and K. Nassau, "Optically-Induced Refractive Index Inhomogeneities in LiNbO₃ and LiTaO₃," *Appl. Phys. Lett.* **9**, 72–74 (1966).
- [90] R. G. Batchko, G. D. Miller, A. Alexandrovski, M. M. Fejer, and R. L. Byer, "Limitations of high-power visible wavelength periodically poled lithium niobate devices due to green-induced infrared absorption and thermal lensing," in *Summaries of papers presented at the Conference on Lasers and Electro-Optics, 1998. CLEO 98. Technical Digest*, pp. 75–76 (1998).
- [91] J. Hirohashi, V. Pasiskevicius, S. Wang, and F. Laurell, "Picosecond blue-light-induced infrared absorption in single-domain and periodically poled ferroelectrics," *J. Appl. Phys.* **101**, 033105 (2007).
- [92] T. R. Volk, V. I. Pryalkin, and N. M. Rubinina, "Optical-damage-resistant LiNbO₃:Zn crystal," *Opt. Lett.* **15**, 996–998 (1990).
- [93] Y. Furukawa, K. Kitamura, S. Takekawa, A. Miyamoto, M. Terao, and N. Suda, "Photorefraction in LiNbO₃ as a function of [Li]/[Nb] and MgO concentrations," *Appl. Phys. Lett.* **77**, 2494–2496 (2000).
- [94] Y. Furukawa, K. Kitamura, A. Alexandrovski, R. K. Route, M. M. Fejer, and G. Foulon, "Green-induced infrared absorption in MgO doped LiNbO₃," *Appl. Phys. Lett.* **78**, 1970–1972 (2001).
- [95] I. Shoji, T. Kondo, A. Kitamoto, M. Shirane, and R. Ito, "Absolute scale of second-order nonlinear-optical coefficients," *J. Opt. Soc. Am. B* **14**, 2268–2294 (1997).

- [96] R. C. Miller, W. A. Nordland, and P. M. Bridenbaugh, "Dependence of Second-Harmonic-Generation Coefficients of LiNbO_3 on Melt Composition," *J. Appl. Phys.* **42**, 4145–4147 (1971).
- [97] I. Dolev, A. Ganany-Padowicz, O. Gayer, A. Arie, J. Mangin, and G. Gadret, "Linear and nonlinear optical properties of $\text{MgO}:\text{LiTaO}_3$," *Appl. Phys. B* **96**, 423–432 (2009).
- [98] D. S. Hum, R. K. Route, G. D. Miller, V. Kondilenko, A. Alexandrovski, J. Huang, K. Urbanek, R. L. Byer, and M. M. Fejer, "Optical properties and ferroelectric engineering of vapor-transport-equilibrated, near-stoichiometric lithium tantalate for frequency conversion," *J. Appl. Phys.* **101**, 093108 (2007).
- [99] L. E. Myers, R. C. Eckardt, M. M. Fejer, R. L. Byer, W. R. Bosenberg, and J. W. Pierce, "Quasi-phase-matched optical parametric oscillators in bulk periodically poled LiNbO_3 ," *J. Opt. Soc. Am. B* **12**, 2102–2116 (1995).
- [100] H. Ishizuki and T. Taira, "Mg-doped congruent LiTaO_3 crystal for large-aperture quasi-phase matching device," *Opt. Express* **16**, 16963–16970 (2008).
- [101] D. H. Jundt, "Temperature-dependent Sellmeier equation for the index of refraction, n_e , in congruent lithium niobate," *Opt. Lett.* **22**, 1553–1555 (1997).
- [102] D. E. Zelmon, D. L. Small, and D. Jundt, "Infrared corrected Sellmeier coefficients for congruently grown lithium niobate and 5 mol. % magnesium oxide-doped lithium niobate," *J. Opt. Soc. Am. B* **14**, 3319–3322 (1997).
- [103] M. Nakamura, S. Higuchi, S. Takekawa, K. Terabe, Y. Furukawa, and K. Kitamura, "Optical Damage Resistance and Refractive Indices in Near-Stoichiometric MgO-Doped LiNbO_3 ," *Jpn. J. Appl. Phys.* **41**, L49–L51 (2002).
- [104] O. Paul, A. Quosig, T. Bauer, M. Nittmann, J. Bartschke, G. Anstett, and J. A. L'huillier, "Temperature-dependent Sellmeier equation in the MIR for the extraordinary refractive index of 5% MgO doped congruent LiNbO_3 ," *Appl. Phys. B* **86**, 111–115 (2007).
- [105] O. Gayer, Z. Sacks, E. Galun, and A. Arie, "Temperature and wavelength dependent refractive index equations for MgO-doped congruent and stoichiometric LiNbO_3 ," *Appl. Phys. B* **91**, 343–348 (2008).
- [106] K. S. Abedin and H. Ito, "Temperature-dependent dispersion relation of ferroelectric lithium tantalate," *J. Appl. Phys.* **80**, 6561–6563 (1996).
- [107] M. Nakamura, S. Higuchi, S. Takekawa, K. Terabe, Y. Furukawa, and K. Kitamura, "Refractive Indices in Undoped and MgO-Doped Near-Stoichiometric LiTaO_3 Crystals," *Jpn. J. Appl. Phys.* **41**, L465–L467 (2002).

- [108] Y. Nishida, “personal communication,” (2012).
- [109] R. L. Byer, “Optical Parametric Oscillators,” in *Quantum Electronics*, H. Rabin and C. L. Tang, ed. (Academic Press, New York, 1975).
- [110] R. L. Sutherland, *Handbook of Nonlinear Optics* (Marcel Dekker, New York, 2003).
- [111] J. A. Giordmaine and R. C. Miller, “Tunable Coherent Parametric Oscillation in LiNbO_3 at Optical Frequencies,” *Phys. Rev. Lett.* **14**, 973–976 (1965).
- [112] M. H. Dunn and M. Ebrahimzadeh, “Parametric Generation of Tunable Light from Continuous-Wave to Femtosecond Pulses,” *Science* **286**, 1513–1517 (1999).
- [113] L. Mandel and E. Wolf, *Optical coherence and quantum optics* (Cambridge University Press, 1995), chap. 22, p. 1074 et seq.
- [114] G. D. Boyd and D. A. Kleinman, “Parametric Interaction of Focused Gaussian Light Beams,” *J. Appl. Phys.* **39**, 3597–3639 (1968).
- [115] H. Kogelnik and T. Li, “Laser Beams and Resonators,” *Appl. Opt.* **5**, 1550–1567 (1966).
- [116] M. E. Klein, “Wavelength tunable, diode laser pumped optical parametric oscillators based on quasi-phase-matching,” Ph.D. thesis, Universität Kaiserslautern (2000).
- [117] A. K. Y. Ngai, S. T. Persijn, G. von Basum, and F. J. M. Harren, “Automatically tunable continuous-wave optical parametric oscillator for high-resolution spectroscopy and sensitive trace-gas detection,” *Appl. Phys. B* **85**, 173–180 (2006).
- [118] T. Nishikawa, A. Ozawa, Y. Nishida, M. Asobe, F.-L. Hong, and T. W. Hänsch, “Efficient 494 mW sum-frequency generation of sodium resonance radiation at 589 nm by using a periodically poled Zn:LiNbO_3 ridge waveguide,” *Opt. Express* **17**, 17792–17800 (2009).
- [119] J. E. Goell, “A Circular-Harmonic Computer Analysis of Rectangular Dielectric Waveguides,” *Bell Syst. Tech. J.* **48**, 2133–2160 (1969).
- [120] D. Marcuse, *Theory of Dielectric Optical Waveguides* (Academic Press, New York, 1974).
- [121] E. A. J. Marcatili, “Dielectric Rectangular Waveguide and Directional Coupler for Integrated Optics,” *Bell Syst. Tech. J.* **48**, 2071–2102 (1969).
- [122] H. Herrmann, “Optisch nichtlineare Differenzfrequenzerzeugung abstimmbarer, kohärenter Strahlung im mittleren Infrarotbereich in Ti:LiNbO_3 -Streifenwellenleitern,” Ph.D. thesis, Universität-Gesamthochschule Paderborn (1991).

- [123] J. Bures, *Guided Optics* (Wiley-VCH, Weinheim, 2009).
- [124] A. Messiah, *Quantenmechanik* (de Gruyter, Berlin, 1976).
- [125] C. Langrock, E. Diamanti, R. V. Roussev, Y. Yamamoto, M. M. Fejer, and H. Takesue, “Highly efficient single-photon detection at communication wavelengths by use of upconversion in reverse-proton-exchanged periodically poled LiNbO₃ waveguides,” *Opt. Lett.* **30**, 1725–1727 (2005).
- [126] J. S. Pelc, “Frequency conversion of single photons: physics, devices, and applications,” Ph.D. thesis, Stanford University (2012).
- [127] S. Blum, “Theoretische und experimentelle Untersuchungen der nichtlinearen Frequenzkonversion einzelner Photonen,” diploma thesis, Universität des Saarlandes (2011).
- [128] S. Zaske, D.-H. Lee, and C. Becher, “Green-pumped cw singly resonant optical parametric oscillator based on MgO:PPLN with frequency stabilization to an atomic resonance,” *Appl. Phys. B* **98**, 729–735 (2010).
- [129] W. R. Bosenberg, A. Drobshoff, J. I. Alexander, L. E. Myers, and R. L. Byer, “93% pump depletion, 3.5-W continuous-wave, singly resonant optical parametric oscillator,” *Opt. Lett.* **21**, 1336–1338 (1996).
- [130] P. Gross, M. E. Klein, T. Walde, K.-J. Boller, M. Auerbach, P. Wessels, and C. Fallnich, “Fiber-laser-pumped continuous-wave singly resonant optical parametric oscillator,” *Opt. Lett.* **27**, 418–420 (2002).
- [131] A. Henderson and R. Stafford, “Spectral broadening and stimulated Raman conversion in a continuous-wave optical parametric oscillator,” *Opt. Lett.* **32**, 1281–1283 (2007).
- [132] J. Kiessling, R. Sowade, I. Breunig, K. Buse, and V. Dierolf, “Cascaded optical parametric oscillations generating tunable terahertz waves in periodically poled lithium niobate crystals,” *Opt. Express* **17**, 87–91 (2009).
- [133] M. M. J. W. van Herpen, S. E. Bisson, and F. J. M. Harren, “Continuous-wave operation of a single-frequency optical parametric oscillator at 4–5 μm based on periodically poled LiNbO₃,” *Opt. Lett.* **28**, 2497–2499 (2003).
- [134] M. Vainio, J. Peltola, S. Persijn, F. J. M. Harren, and L. Halonen, “Thermal effects in singly resonant continuous-wave optical parametric oscillators,” *Appl. Phys. B* **94**, 411–427 (2009).
- [135] T. Petelski, R. S. Conroy, K. Bencheikh, J. Mlynek, and S. Schiller, “All-solid-state, tunable, single-frequency source of yellow light for high-resolution spectroscopy,” *Opt. Lett.* **26**, 1013–1015 (2001).

- [136] B. Arora, M. S. Safronova, and C. W. Clark, “Magic wavelengths for the np - ns transitions in alkali-metal atoms,” *Phys. Rev. A* **76**, 052509 (2007).
- [137] R. G. Batchko, D. R. Weise, T. Plettner, G. D. Miller, M. M. Fejer, and R. L. Byer, “Continuous-wave 532-nm-pumped singly resonant optical parametric oscillator based on periodically poled lithium niobate,” *Opt. Lett.* **23**, 168–170 (1998).
- [138] G. K. Samanta, G. R. Fayaz, Z. Sun, and M. Ebrahim-Zadeh, “High-power, continuous-wave, singly resonant optical parametric oscillator based on MgO:sPPLT,” *Opt. Lett.* **32**, 400–402 (2007).
- [139] J.-M. Melkonian, T.-H. My, F. Bretenaker, and C. Drag, “High spectral purity and tunable operation of a continuous singly resonant optical parametric oscillator emitting in the red,” *Opt. Lett.* **32**, 518–520 (2007).
- [140] G. K. Samanta, G. R. Fayaz, and M. Ebrahim-Zadeh, “1.59 W, single-frequency, continuous-wave optical parametric oscillator based on MgO:sPPLT,” *Opt. Lett.* **32**, 2623–2625 (2007).
- [141] G. K. Samanta and M. Ebrahim-Zadeh, “Continuous-wave singly-resonant optical parametric oscillator with resonant wave coupling,” *Opt. Express* **16**, 6883–6888 (2008).
- [142] T.-H. My, O. Robin, O. Mhibik, C. Drag, and F. Bretenaker, “Stimulated Raman scattering in an optical parametric oscillator based on periodically poled MgO-doped stoichiometric LiTaO₃,” *Opt. Express* **17**, 5912–5918 (2009).
- [143] G. K. Samanta, S. Chaitanya Kumar, Ritwick Das, and M. Ebrahim-Zadeh, “Continuous-wave optical parametric oscillator pumped by a fiber laser green source at 532 nm,” *Opt. Lett.* **34**, 2255–2257 (2009).
- [144] G. K. Samanta and M. Ebrahim-Zadeh, “High-power, continuous-wave, optical parametric oscillator pumped by an optically pumped semiconductor laser at 532 nm,” *Opt. Lett.* **35**, 1986–1988 (2010).
- [145] M. E. Klein, C. K. Laue, D.-H. Lee, K.-J. Boller, and R. Wallenstein, “Diode-pumped singly resonant continuous-wave optical parametric oscillator with wide continuous tuning of the near-infrared idler wave,” *Opt. Lett.* **25**, 490–492 (2000).
- [146] A. Henderson and R. Stafford, “Intra-cavity power effects in singly resonant cw OPOs,” *Appl. Phys. B* **85**, 181–184 (2006).
- [147] A. V. Smith, “SNLO software, version 4.0,” .
- [148] D.-H. Lee, S. K. Kim, S.-N. Park, H. S. Park, J. Y. Lee, and S.-K. Choi, “Continuous-wave 532 nm pumped MgO:PPLN optical parametric oscillator with external power regulation and spatial mode filtering,” *Appl. Opt.* **48**, 37–42 (2009).

- [149] L. B. Kreuzer, “Single and multimode oscillation of the singly resonant optical parametric oscillator,” in “Proceedings of the Joint Conference on Lasers and Opto-electronics,” (Institution of Electronic and Radio Engineers, 1969), pp. 52–63.
- [150] R. Sowade, I. Breunig, J. Kiessling, and K. Buse, “Influence of the pump threshold on the single-frequency output power of singly resonant optical parametric oscillators,” *Appl. Phys. B* **96**, 25–28 (2009).
- [151] W. Demtröder, *Laser Spectroscopy* (Springer, Berlin, 2003).
- [152] Th. Udem, J. Reichert, T. W. Hänsch, and M. Kourogi, “Absolute optical frequency measurement of the cesium D_2 line,” *Phys. Rev. A* **62**, 031801(R) (2000).
- [153] A. Derevianko and S. G. Porsev, “Determination of lifetimes of $6P_J$ levels and ground-state polarizability of Cs from the van der Waals coefficient C_6 ,” *Phys. Rev. A* **65**, 053403 (2002).
- [154] R. J. Rafac, C. E. Tanner, A. E. Livingston, and H. G. Berry, “Fast-beam laser lifetime measurements of the cesium $6p^2P_{1/2,3/2}$ states,” *Phys. Rev. A* **60**, 3648–3662 (1999).
- [155] R. Al-Tahtamouni, K. Bencheikh, R. Storz, K. Schneider, M. Lang, J. Mlynek, and S. Schiller, “Long-term stable operation and absolute frequency stabilization of a doubly resonant parametric oscillator,” *Appl. Phys. B* **66**, 733–739 (1998).
- [156] D. W. Allan, “Statistics of atomic frequency standards,” *Proc. IEEE* **54**, 221–230 (1966).
- [157] H. Langfischer, “Frequenzstabilisierung eines Diodenlasers bei 650 nm zur Spektroskopie an einzelnen Barium-Ionen,” diploma thesis, Universität Innsbruck (1998).
- [158] F. G. Major, *The Quantum Beat: Principles and Applications of Atomic Clocks* (Springer, New York, 2007).
- [159] C. Warschburger, “Aufbau eines Optisch Parametrischen Oszillators basierend auf PPLT für Experimente zur Frequenzkonversion einzelner Photonen,” diploma thesis, Universität des Saarlandes (2010).
- [160] J. Eichler, L. Dünkel, and B. Eppich, “Die Strahlqualität von Lasern – Wie bestimmt man Beugungsmaßzahl und Strahldurchmesser in der Praxis?” *Laser Tech. J.* **1**, 63–66 (2004).
- [161] Available at <http://www.mpq.mpg.de/~haensch/comb/people/thomas.html>.

- [162] E. V. Kovalchuk, D. Dekorsy, A. I. Lvovsky, C. Braxmaier, J. Mlynek, A. Peters, and S. Schiller, “High-resolution Doppler-free molecular spectroscopy with a continuous-wave optical parametric oscillator,” *Opt. Lett.* **26**, 1430–1432 (2001).
- [163] I. Aharonovich, S. Castelletto, D. A. Simpson, C.-H. Su, A. D. Greentree, and S. Praver, “Diamond-based single-photon emitters,” *Rep. Prog. Phys.* **74**, 076501 (2011).
- [164] A. Faraon, P. E. Barclay, C. Santori, K.-M. C. Fu, R. G. Beausoleil, “Resonant enhancement of the zero-phonon emission from a colour centre in a diamond cavity,” *Nature Photon.* **5**, 301–305 (2011).
- [165] J. Riedrich-Möller, L. Kipfstuhl, C. Hepp, E. Neu, C. Pauly, F. Mücklich, A. Baur, M. Wandt, S. Wolff, M. Fischer, S. Gsell, M. Schreck, and C. Becher, “One- and two-dimensional photonic crystal microcavities in single crystal diamond,” *Nature Nanotech.* **7**, 69–74 (2012).
- [166] I. Aharonovich, A. D. Greentree, and S. Praver, “Diamond photonics,” *Nature Photon.* **5**, 397–405 (2011).
- [167] L. Rogers, “How far into the infrared can a colour centre in diamond emit?” *Phys. Procedia* **3**, 1557–1561 (2010).
- [168] J. S. Pelc, C. Langrock, Q. Zhang, and M. M. Fejer, “Efficient Down-Conversion of Single Photons for Quantum Communication,” in *Nonlinear Optics: Materials, Fundamentals and Applications*, OSA Technical Digest (CD) (Optical Society of America, 2009), paper NTuB1.
- [169] I. Aharonovich, S. Castelletto, B. C. Johnson, J. C. McCallum, and S. Praver, “Engineering chromium-related single photon emitters in single crystal diamonds,” *New J. Phys.* **13**, 045015 (2011).
- [170] M. Reischle, C. Kessler, W.-M. Schulz, M. Eichfelder, R. Roßbach, M. Jetter, and P. Michler, “Triggered single-photon emission from electrically excited quantum dots in the red spectral range,” *Appl. Phys. Lett.* **97**, 143513 (2010).
- [171] Y. Nishida, *Datasheet: PPLN Waveguide for 1550 nm DFG, WD-1550-000-A-C-C-S001, S/N 3079044*, NTT Electronics Corp. (2010).
- [172] Y. Nishida, H. Miyazawa, M. Asobe, O. Tadanaga, and H. Suzuki, “Direct-bonded QPM-LN ridge waveguide with high damage resistance at room temperature,” *Electron. Lett.* **39**, 609–611 (2003).
- [173] T. Umeki, O. Tadanaga, and M. Asobe, “Highly Efficient Wavelength Converter Using Direct-Bonded PPZnLN Ridge Waveguide,” *IEEE J. Quantum Electron.* **46**, 1206–1213 (2010).

- [174] C. Langrock and M. M. Fejer, “Fiber-feedback continuous-wave and synchronously-pumped singly-resonant ring optical parametric oscillators using reverse-proton-exchanged periodically-poled lithium niobate waveguides,” *Opt. Lett.* **32**, 2263–2265 (2007).
- [175] S. Tanzilli, A. Martin, F. Kaiser, M. P. De Micheli, O. Alibart, and D. B. Ostrowsky, “On the genesis and evolution of integrated quantum optics,” *Laser & Photon. Rev.* **6**, 115–143 (2012).
- [176] F. R. Nash, G. D. Boyd, M. Sargent, and P. M. Bridenbaugh, “Effect of Optical Inhomogeneities on Phase Matching in Nonlinear Crystals,” *J. Appl. Phys.* **41**, 2564–2576 (1970).
- [177] H. Jiang, G. Li, and X. Xu, “Highly efficient single-pass second harmonic generation in a periodically poled MgO: LiNbO₃ waveguide pumped by a fiber laser at 1111.6 nm,” *Opt. Express* **17**, 16073–16080 (2009).
- [178] K.-D. F. Büchter, H. Herrmann, C. Langrock, M. M. Fejer, and W. Sohler, “All-optical Ti:PPLN wavelength conversion modules for free-space optical transmission links in the mid-infrared,” *Opt. Lett.* **34**, 470–472 (2009).
- [179] R. H. Stolen and E. P. Ippen, “Raman gain in glass optical waveguides,” *Appl. Phys. Lett.* **22**, 276–278 (1973).
- [180] U. T. Schwarz and M. Maier, “Asymmetric Raman lines caused by an anharmonic lattice potential in lithium niobate,” *Phys. Rev. B* **55**, 11041–11044 (1997).
- [181] Y. Repelin, E. Husson, F. Bennani, and C. Proust, “Raman spectroscopy of lithium niobate and lithium tantalate. Force field calculations,” *J. Phys. Chem. Solids* **60**, 819–825 (1999).
- [182] X. Yang, G. Lan, B. Li, and H. Wang, “Raman Spectra and Directional Dispersion in LiNbO₃ and LiTaO₃,” *Phys. Status Solidi B* **141**, 287–300 (1987).
- [183] A. Ridah, P. Bourson, M. D. Fontana, and G. Malovichko, “The composition dependence of the Raman spectrum and new assignment of the phonons in LiNbO₃,” *J. Phys.: Condens. Matter* **9**, 9687–9693 (1997).
- [184] N. V. Sidorov, A. A. Yanichev, P. G. Chufyrev, M. N. Palatnikov, and B. N. Mavrin, “Raman spectra of photorefractive lithium niobate single crystals,” *J. Appl. Spectrosc.* **77**, 110–114 (2010).
- [185] R. M. Khafagy, “Detection of Two Phases Coexisting at the Phase Transition Temperature in LiNbO₃ Single Crystal by using Raman Spectroscopy,” *Egypt. J. Solids* **31**, 171–180 (2008).

- [186] M. Malyj and J. E. Griffiths, “Stokes/Anti-Stokes Raman Vibrational Temperatures: Reference Materials, Standard Lamps, and Spectrophotometric Calibrations,” *Appl. Spectrosc.* **37**, 315–333 (1983).
- [187] J. S. Pelc, L. Ma, C. R. Phillips, Q. Zhang, C. Langrock, O. Slattery, X. Tang, and M. M. Fejer, “Long-wavelength-pumped upconversion single-photon detector at 1550 nm: performance and noise analysis,” *Opt. Express* **19**, 21445–21456 (2011).
- [188] C. H. Su, A. D. Greentree, and L. C. L. Hollenberg, “Towards a picosecond transform-limited nitrogen-vacancy based single photon source,” *Opt. Express* **16**, 6240–6250 (2008).
- [189] G. Ribordy, N. Gisin, O. Guinnard, D. Stucki, M. Wegmuller, and H. Zbinden, “Photon counting at telecom wavelengths with commercial InGaAs/InP avalanche photodiodes: current performance,” *J. Mod. Opt.* **51**, 1381–1398 (2004).
- [190] A. Lenhard, “personal communication,” (2011).
- [191] M. A. Albota, “Single-Photon Frequency Upconversion for Long-Distance Quantum Teleportation and Communication,” Ph.D. thesis, Massachusetts Institute of Technology (2006).
- [192] M. A. Albota, F. N. C. Wong, and J. H. Shapiro, “Polarization-independent frequency conversion for quantum optical communication,” *J. Opt. Soc. Am. B* **23**, 918–924 (2006).
- [193] A. Lenhard, S. Zaske, and C. Becher, “Lock-in detection of single photons after two-step frequency conversion,” *Opt. Lett.* **37**, 4254–4256 (2012).
- [194] J. S. Pelc, Q. Zhang, C. R. Phillips, L. Yu, Y. Yamamoto, and M. M. Fejer, “Cascaded frequency upconversion for high-speed single-photon detection at 1550 nm,” *Opt. Lett.* **37**, 476–478 (2012).
- [195] C. Arend, “personal communication,” (2011).
- [196] E. Neu, M. Agio, and C. Becher, “Photophysics of single silicon vacancy centers in diamond: implications for single photon emission,” *Opt. Express* **20**, 19956–19971 (2012).
- [197] E. Neu, M. Fischer, S. Gsell, M. Schreck, and C. Becher, “Fluorescence and polarization spectroscopy of single silicon vacancy centers in heteroepitaxial nanodiamonds on iridium,” *Phys. Rev. B* **84**, 205211 (2011).
- [198] S. Zaske, A. Lenhard, C. A. Keßler, J. Kettler, C. Hepp, C. Arend, R. Albrecht, W.-M. Schulz, M. Jetter, P. Michler, and C. Becher, “Visible-to-Telecom Quantum Frequency Conversion of Light from a Single Quantum Emitter,” *Phys. Rev. Lett.* **109**, 147404 (2012).

- [199] S. Buckley, K. Rivoire, and J. Vučković, “Engineered quantum dot single-photon sources,” *Rep. Prog. Phys.* **75**, 126503 (2012).
- [200] Z. M. Fang, K. Y. Ma, D. H. Jaw, R. M. Cohen, and G. B. Stringfellow, “Photoluminescence of InSb, InAs, and InAsSb grown by organometallic vapor phase epitaxy,” *J. Appl. Phys.* **67**, 7034–7039 (1990).
- [201] D. D. Sell, H. C. Casey Jr., and K. W. Wecht, “Concentration dependence of the refractive index for n - and p -type GaAs between 1.2 and 1.8 eV,” *J. Appl. Phys.* **45**, 2650–2657 (1974).
- [202] C. A. Keßler, “personal communication,” (2012).
- [203] A. D. Semenov, G. N. Gol’tsman, and A. A. Korneev, “Quantum detection by current carrying superconducting film,” *Physica C: Superconductivity* **351**, 349–356 (2001).
- [204] C. Zinoni, B. Alloing, L. H. Li, F. Marsili, A. Fiore, L. Lunghi, A. Gerardino, Yu. B. Vakhtomin, K. V. Smirnov, G. N. Gol’tsman, “Single-photon experiments at telecommunication wavelengths using nanowire superconducting detectors,” *Appl. Phys. Lett.* **91**, 031106 (2007).
- [205] J. Kettler, “personal communication,” (2012).
- [206] Y. P. Varshni, “Temperature dependence of the energy gap in semiconductors,” *Physica* **34**, 149–154 (1967).
- [207] W.-M. Schulz, R. Roßbach, M. Reischle, G. J. Beirne, M. Bommer, M. Jetter, and P. Michler, “Optical and structural properties of InP quantum dots embedded in $(\text{Al}_x\text{Ga}_{1-x})_{0.51}\text{In}_{0.49}\text{P}$,” *Phys. Rev. B* **79**, 035329 (2009).
- [208] T. Thiel (AOS GmbH), “personal communication,” (2012).
- [209] A. Lenhard, S. Zaske, S. Blum, G. Morigi, and C. Becher, “Low-Noise Frequency Down-Conversion at the Single Photon Level,” in *CLEO: QELS-Fundamental Science*, OSA Technical Digest (Optical Society of America, 2012), paper JTh1K.4.
- [210] M. Stobińska, G. Alber, and G. Leuchs, “Perfect excitation of a matter qubit by a single photon in free space,” *Europhys. Lett.* **86**, 14007 (2009).
- [211] N. Piro, F. Rohde, C. Schuck, M. Almendros, J. Huwer, J. Ghosh, A. Haase, M. Henrich, F. Dubin, and J. Eschner, “Heralded single-photon absorption by a single atom,” *Nature Phys.* **7**, 17–20 (2011).
- [212] M. T. Rakher, L. Ma, M. Davanço, O. Slattery, X. Tang, and K. Srinivasan, “Simultaneous Wavelength Translation and Amplitude Modulation of Single Photons from a Quantum Dot,” *Phys. Rev. Lett.* **107**, 083602 (2011).

- [213] W. Becker, *Advanced Time-Correlated Single Photon Counting Techniques*, Springer Series in Chemical Physics (Springer, Berlin, 2005), 1st ed.
- [214] T. Aichele, V. Zwiller, and O. Benson, “Visible single-photon generation from semiconductor quantum dots,” *New J. Phys.* **6**, 90 (2004).
- [215] G. S. Solomon, E. B. Flagg, S. V. Polyakov, T. Thomay, and A. Muller, “Manipulating single photons from disparate quantum sources to be indistinguishable [Invited],” *J. Opt. Soc. Am. B* **29**, 319–327 (2012).
- [216] T. Lunghi, C. Barreiro, O. Guinnard, R. Houlmann, X. Jiang, M. A. Itzler, and H. Zbinden, “Free-running single-photon detection based on a negative feedback InGaAs APD,” *J. Mod. Opt.* **59**, 1481–1488 (2012).
- [217] Z. Yan, D. R. Hamel, A. K. Heinrichs, X. Jiang, M. A. Itzler, and T. Jennewein, “An ultra low noise telecom wavelength free running single photon detector using negative feedback avalanche diode,” *Rev. Sci. Instrum.* **83**, 073105 (2012).
- [218] C. Zinoni, B. Alloing, C. Monat, V. Zwiller, L. H. Li, A. Fiore, L. Lunghi, A. Gerardino, H. de Riedmatten, H. Zbinden, and N. Gisin, “Time-resolved and antibunching experiments on single quantum dots at 1300 nm,” *Appl. Phys. Lett.* **88**, 131102 (2006).
- [219] K. Takemoto, M. Takatsu, S. Hirose, N. Yokoyama, Y. Sakuma, T. Usuki, T. Miyazawa, and Y. Arakawa, “An optical horn structure for single-photon source using quantum dots at telecommunication wavelength,” *J. Appl. Phys.* **101**, 081720 (2007).
- [220] P. M. Intallura, M. B. Ward, O. Z. Karimov, Z. L. Yuan, P. See, A. J. Shields, P. Atkinson, and D. A. Ritchie, “Quantum key distribution using a triggered quantum dot source emitting near 1.3 μm ,” *Appl. Phys. Lett.* **91**, 161103 (2007).
- [221] K. Takemoto, Y. Nambu, T. Miyazawa, K. Wakui, S. Hirose, T. Usuki, M. Takatsu, N. Yokoyama, K. Yoshino, A. Tomita, S. Yorozu, Y. Sakuma, and Y. Arakawa, “Transmission Experiment of Quantum Keys over 50 km Using High-Performance Quantum-Dot Single-Photon Source at 1.5 μm Wavelength,” *Appl. Phys. Express* **3**, 092802 (2010).
- [222] M. D. Birowosuto, H. Sumikura, S. Matsuo, H. Taniyama, P. J. van Veldhoven, R. Nötzel, and M. Notomi, “Fast Purcell-enhanced single photon source in 1,550-nm telecom band from a resonant quantum dot-cavity coupling,” *Sci. Rep.* **2**, 321 (2012).
- [223] S. Strauf, N. G. Stoltz, M. T. Rakher, L. A. Coldren, P. M. Petroff, and D. Bouwmeester, “High-frequency single-photon source with polarization control,” *Nature Photon.* **1**, 704–708 (2007).

- [224] Y. Ding and Z. Y. Ou, “Frequency downconversion for a quantum network,” *Opt. Lett.* **35**, 2591–2593 (2010).
- [225] M. H. Chou, J. Hauden, M. A. Arbore, and M. M. Fejer, “1.5- μ m-band wavelength conversion based on difference-frequency generation in LiNbO₃ waveguides with integrated coupling structures,” *Opt. Lett.* **23**, 1004–1006 (1998).
- [226] C. Santori, D. Fattal, J. Vučković, G. S. Solomon, and Y. Yamamoto, “Indistinguishable photons from a single-photon device,” *Nature* **419**, 594–597 (2002).
- [227] A. Badolato, K. Hennessy, M. Atatüre, J. Dreiser, E. Hu, P. M. Petroff, and A. Imamoglu, “Deterministic Coupling of Single Quantum Dots to Single Nanocavity Modes,” *Science* **308**, 1158–1161 (2005).
- [228] C. Matthiesen, A. N. Vamivakas, and M. Atatüre, “Subnatural Linewidth Single Photons from a Quantum Dot,” *Phys. Rev. Lett.* **108**, 093602 (2012).
- [229] K. Nagayama, M. Kakui, M. Matsui, I. Saitoh, and Y. Chigusa, “Ultra-low-loss (0.1484 dB/km) pure silica core fibre and extension of transmission distance,” *Electron. Lett.* **38**, 1168–1169 (2002).
- [230] M. Rattunde, S. Kaspar, T. Töpper, C. Manz, K. Köhler, and J. Wagner, “GaSb-based 2-3 μ m Semiconductor Disk Lasers: Versatile Lasers for High-Power and Narrow-Linewidth Emission,” in *Lasers, Sources, and Related Photonic Devices*, OSA Technical Digest (CD) (Optical Society of America, 2012), paper AM5A.4.
- [231] M. O. Scully and K. Drühl, “Quantum eraser: A proposed photon correlation experiment concerning observation and “delayed choice” in quantum mechanics,” *Phys. Rev. A* **25**, 2208–2213 (1982).
- [232] M. G. Raymer and K. Srinivasan, “Manipulating the color and shape of single photons,” *Phys. Today* **65**, 32–37 (2012).
- [233] C. Simon and W. T. M. Irvine, “Robust Long-Distance Entanglement and a Loophole-Free Bell Test with Ions and Photons,” *Phys. Rev. Lett.* **91**, 110405 (2003).
- [234] J. T. Hill, A. H. Safavi-Naeini, J. Chan, and O. Painter, “Coherent optical wavelength conversion via cavity optomechanics,” *Nat. Commun.* **3**, 1196 (2012).
- [235] J. L. O’Brien, A. Furusawa, and J. Vučković, “Photonic quantum technologies,” *Nature Photon.* **3**, 687–695 (2009).

List of Publications

Journal Publications

1. A. Lenhard, S. Zaske, and C. Becher, “Lock-in detection of single photons after two-step frequency conversion,” *Opt. Lett.* **37**, 4254–4256 (2012).
2. S. Zaske, A. Lenhard, C. A. Keßler, J. Kettler, C. Hepp, C. Arend, R. Albrecht, W.-M. Schulz, M. Jetter, P. Michler, and C. Becher, “Visible-to-Telecom Quantum Frequency Conversion of Light from a Single Quantum Emitter,” *Phys. Rev. Lett.* **109**, 147404 (2012).
3. S. Zaske, A. Lenhard, and C. Becher, “Efficient frequency downconversion at the single photon level from the red spectral range to the telecommunications C-band,” *Opt. Express* **19**, 12825–12836 (2011).
4. I.-H. Bae, H. S. Moon, S. Zaske, C. Becher, S. K. Kim, S.-N. Park, and D.-H. Lee, “Low-threshold singly-resonant continuous-wave optical parametric oscillator based on MgO-doped PPLN,” *Appl. Phys. B* **103**, 311–319 (2011).
5. A. Lenhard, S. Zaske, J. A. L’huillier, and C. Becher, “Stabilized diode laser pumped, idler-resonant cw optical parametric oscillator,” *Appl. Phys. B* **102**, 757–764 (2011).
6. S. Zaske, D.-H. Lee, and C. Becher, “Green-pumped cw singly resonant optical parametric oscillator based on MgO:PPLN with frequency stabilization to an atomic resonance,” *Appl. Phys. B* **98**, 729–735 (2010).

Conference Papers¹

1. NOEKS 2012, Stuttgart, Germany:
 - C. Becher, A. Lenhard, S. Zaske, C. Keßler, J. Kettler, C. Arend, C. Hepp, R. Albrecht, W.-M. Schulz, M. Jetter, and P. Michler, “Quantum Frequency Conversion of Single Photons from a Quantum Dot to the Telecom Band,” *11th International*

¹A bullet (•) marks the presenter of the talk/poster.

Workshop on Nonlinear Optics and Excitation Kinetics in Semiconductors, paper Th1.1.

2. QELS 2012, San Jose, CA, USA:
 - A. Lenhard, S. Zaske, C. Kessler, J. Kettler, C. Arend, C. Hepp, R. Albrecht, W. Schulz, M. Jetter, P. Michler, and C. Becher, “Quantum Frequency Down-Conversion of Single Photons from a Quantum Dot to the Telecom Band,” in *CLEO: QELS-Fundamental Science*, OSA Technical Digest (Optical Society of America, 2012), postdeadline paper QTh5B.6.
3. QELS 2012, San Jose, CA, USA:
 - A. Lenhard, S. Zaske, S. Blum, G. Morigi, and C. Becher, “Low-Noise Frequency Down-Conversion at the Single Photon Level,” in *CLEO: QELS-Fundamental Science*, OSA Technical Digest (Optical Society of America, 2012), paper JTh1K.4.
4. NLO 2011, Kauai, HI, USA:
 - S. Zaske, A. Lenhard, and C. Becher, “Efficient Frequency Downconversion at the Single Photon Level from 738 nm to 1557 nm,” in *Nonlinear Optics: Materials, Fundamentals and Applications*, OSA Technical Digest (CD) (Optical Society of America, 2011), paper NMB3.
5. CLEO/Europe EQEC 2011, Munich, Germany:
 - S. Zaske, A. Lenhard, and C. Becher, “Highly Efficient Frequency Downconversion at the Single Photon Level,” in *CLEO/Europe and EQEC 2011 Conference Digest*, OSA Technical Digest (CD) (Optical Society of America, 2011), paper EF4.4.
6. QELS 2010, San Jose, CA, USA:

G. A. Olivares-Renteria, C. Ottaviani, G. Morigi, H. Ruetz, S. Zaske, J. A. L’huillier, and • C. Becher, “Frequency Down-Conversion of Single Photons into the Telecom Band,” in *Quantum Electronics and Laser Science Conference*, OSA Technical Digest (CD) (Optical Society of America, 2010), paper QFB3.
7. CLEO 2010, San Jose, CA, USA:
 - I.-H. Bae, H. S. Moon, S. Zaske, C. Becher, S. K. Kim, S. N. Park, and D.-H. Lee, “Self-Guided Operation of Green-Pumped Singly Resonant CW OPO Based on Bulk MgO:PPLN,” in *Conference on Lasers and Electro-Optics*, OSA Technical Digest (CD) (Optical Society of America, 2010), paper CThEE1.
8. CLEO 2010, San Jose, CA, USA:

A. Lenhard, S. Zaske, J. A. L’huillier, and • C. Becher, “Highly Stable Diode-Laser Pumped, Idler Resonant CW OPO Based on MgO:PPLN,” in *Conference on Lasers and Electro-Optics*, OSA Technical Digest (CD) (Optical Society of America, 2010), paper CThY5.

9. CLEO/Pacific Rim 2009, Shanghai, People's Republic of China:
 - I.-H. Bae, H. S. Moon, S. Zaske, C. Becher, S.-N. Park, and D.-H. Lee, "Continuous-Wave 532 nm Pumped Singly-Resonant Optical Parametric Oscillator based on MgO-doped PPLN," in *Conference on Lasers and Electro-Optics/Pacific Rim 2009*, (Optical Society of America, 2009), paper TUP5.45.
10. NLO 2009, Honolulu, HI, USA:
 - S. Zaske, D.-H. Lee, and C. Becher, "Green-Pumped CW Singly Resonant Optical Parametric Oscillator Based on MgO:PPLN with Frequency Stabilization," in *Nonlinear Optics: Materials, Fundamentals and Applications*, OSA Technical Digest (CD) (Optical Society of America, 2009), paper NThA1.
11. CLEO/Europe EQEC 2009, Munich, Germany:
 - S. Zaske, D.-H. Lee, and C. Becher, "Green-Pumped CW Singly Resonant Optical Parametric Oscillator Based on MgO:PPLN with Frequency Stabilization," in *CLEO/Europe and EQEC 2009 Conference Digest*, (Optical Society of America, 2009), paper CD_P14.
12. NEWRAD 2008, Daejeon, South Korea:
 - D.-H. Lee, S.-N. Park, H.-S. Park, S.-K. Choi, S. Zaske, and C. Becher, "Calibration of Si and InGaAs Single-Photon Counters using a Wavelength-Tunable CW Optical Parametric Oscillator Below Threshold", *10th International Conference on New Developments and Applications in Optical Radiometry* (NEWRAD 2008), paper TH-O-04.

Danksagung

An dieser Stelle möchte ich all jenen meinen Dank aussprechen, die zum Gelingen dieser Arbeit beigetragen haben. An erster Stelle sei mein Doktorvater Prof. Dr. Christoph Becher genannt. Ich danke ihm dafür, dass er mich als Doktorand in seiner Arbeitsgruppe aufgenommen und die interessante und herausfordernde Themenstellung zu dieser Arbeit geliefert hat. Er hat von Anfang an viel Vertrauen in mich gesetzt, mich stets gefördert und mir viele Freiheiten gewährt. Von den vielen Dingen, die ich in den vergangenen Jahren von ihm lernen durfte, werde ich zwei Weisheiten sicher nie vergessen: “Try again, try harder!” und “Es gibt keinen Plan B.”.

Dr. habil. Johannes L’huillier vom Photonik-Zentrum Kaiserslautern danke ich herzlich, dass er die Rolle als Zweitgutachter für diese Arbeit übernommen hat.

Ein weiterer Lehrer, dem ich zu großem Dank verpflichtet bin, ist Dr. Dong-Hoon Lee. Im Rahmen eines wissenschaftlichen Austauschs durfte ich vom Meister die Tricks und Kniffe lernen, die es braucht, um einen cw OPO stabil zum Laufen zu bringen (“Es ist immer schlecht, wenn man gar kein Signal hat...”). Ich danke Dong auch besonders für seine Gastfreundschaft während meiner beiden Aufenthalte in Südkorea und dafür, dass er mir so viel von diesem faszinierenden Land gezeigt hat. Es war fachlich und menschlich eine große Freude mit ihm zusammenzuarbeiten.

Natürlich dürfen die Kooperationspartner hier nicht unerwähnt bleiben. Ich danke Herrn Prof. Dr. Peter Michler von der Uni Stuttgart und seinen Gesandten, Christian Keßler und Jan Kettler, ganz herzlich für die erfolgreiche Kooperation. Die Weisen aus dem Schwabenland brachten uns leuchtende Quantenpunkte und supraleitende Detektoren als (Leih-)Gaben dar (ein Powermeter fiel den Räufern zum Opfer). “The greatest feeling you can get in a gym ... is the pump!” Christian und Jan wünsche ich alles Gute für die Zukunft.

Weiterhin gebührt großer Dank allen aktuellen und ehemaligen Mitgliedern der AG Becher, ohne deren fachliche und moralische Unterstützung diese Arbeit nicht möglich gewesen wäre. Besonders bedanke ich mich bei meinem Bürokollegen und Partner am Konversionsexperiment Andreas Lenhard für die gute Stimmung im Büro und Labor sowie die Top-Zusammenarbeit. Darüberhinaus danke ich den Pionieren der AG Quantenoptik, Dr. David Steinmetz und Dr. Elke Neu, die all das aufgebaut haben, was zukünftige Generationen von Doktoranden wahrscheinlich als gottgegeben ansehen werden. Danke sagen möchte ich auch den Kollegen Roland Albrecht (insb. Nespresso, Käsefondue, Skifahren, Modifikation des $g^{(2)}$ -Programms), Christian Hepp

(insb. nächtliche Optimierung des Konfokalmikroskops), Carsten Arend sowie den “Photonics Girls” Janine Riedrich-Möller und Laura Kipfstuhl. Die tägliche Arbeit, das Mittagessen, sowie die zahlreichen Konferenzen und privaten Unternehmungen mit euch haben mir großen Spaß gemacht. Ich wünsche allen Mitgliedern der AG Becher alles Gute für die Zukunft, viele Drittmittel und anhaltenden wissenschaftlichen Erfolg.

Andreas, Janine und Alexander Erwin Richard (“Entanglement”) Bommer danke ich insbesondere auch für das sorgfältige Korrekturlesen dieser Arbeit.

Meinen ehemaligen Diplomanden Helge Rütz und Claudia Warschburger sende ich ebenfalls ein Dankeschön nach Paderborn bzw. Mainz. Sie haben mir sehr beim Aufbau des Experiments geholfen. Ich hoffe, ich war als “Lehrer” nicht allzu streng und ungeduldig. Ich wünsche ihnen für die Zukunft alles Gute und viel Erfolg bei ihren aktuellen Experimenten.

Elke Huschens, der Sekretärin und guten Seele unserer AG, möchte ich recht herzlich danken und ihr zugleich ein großes Lob für ihre Arbeitseinstellung aussprechen. Sie macht sprichwörtlich in der halben Zeit die doppelte Arbeit und behält stets den Überblick, sei es bei Beschaffungsanträgen, Projektmitteln, oder (besonders wichtig) Arbeitsverträgen.

Die Experimente für diese Arbeit wären undenkbar gewesen ohne Meister Michael Schmidt und seine begabten Männer von der Metallwerkstatt. Ich danke der Werkstatt ganz herzlich für die Herstellung unzähliger Dreh- und Frästeile für meinen Versuchsaufbau. Die Teile wurden stets in kürzester Zeit und mit hoher Präzision gefertigt. Gerüchten zufolge plant Apple die Zusammenarbeit mit Foxconn zu beenden und das künftige iPhone 6 in Schmidts Werkstatt fertigen zu lassen (aus Titan).

Unserem AG-Techniker Rolf Kiefer und dem unvergleichlichen Monsieur Löw von der Elektronikwerkstatt danke ich für die Unterstützung bei der Bewältigung von größeren und kleineren (Elektronik-)Problemen.

Seit Beginn des Studiums ist die Phalanx meine seelische Heimat. Ich danke hiermit ausdrücklich den Herren Dr. Lars Rainer Bommer, Dr. Adrian Ferdinand, Dr. Ralf Jungmann und Dr. Andreas Ziehl für einfach alles und ziehe meinen Hut vor jedem einzelnen von ihnen.

Harald danke ich für die vielen guten und amüsanten Gespräche, seine stetige Anteilnahme und das stets vorzügliche Abendessen.

Dank gebührt auch meiner großen Schwester Katrin und meiner Oma Ella, und zwar dafür, dass es ihnen völlig wurscht ist, ob die Photonenstatistik bei der Frequenzkonversion erhalten bleibt. Sie beschäftigen sich mit ganz anderen Fragen im Zusammenhang mit meiner Person (beispielsweise ob der “Knecht” schon was gegessen hat oder ob er beim Friseur war).

Meinen Eltern danke ich dafür, dass sie mir das Studium und die Promotion ermöglicht haben. Sie haben immer an mich geglaubt, mich immer unterstützt (moralisch wie finanziell) und große Geduld mit mir gehabt. Ich kann das in diesem Leben nicht mehr zurückgeben, aber trotzdem: danke.

Zum Schluß möchte ich Lisa danken. Für ihre Liebe, Unterstützung und Geduld in all den Jahren sowie für stets kalten Vodka und warmen Hefezopf.